QUENCHING FACTOR MEASUREMENT OF NEON NUCLEI IN NEON GAS AND STUDY OF THE FEASIBILITY OF DETECTING COHERENT ELASTIC NEUTRINO-NUCLEUS SCATTERING AT A NUCLEAR REACTOR USING A SPHERICAL PROPORTIONAL COUNTER

by

MARIE VIDAL

A thesis submitted to the
Department of Physics, Engineering Physics and Astronomy
in conformity with the requirements for
the degree of Doctor of Philosophy

Queen's University
Kingston, Ontario, Canada
October 2021

Abstract

The NEWS-G collaboration uses Spherical Proportional Counters (SPCs) to search for weakly interacting massive particles (WIMPs) through direct detection. Due to their sensitivity to single electrons from ionization, SPCs are also considered for the detection of neutrinos via coherent elastic neutrino-nucleus scattering (CEνNS). We study the feasibility of an experiment conducted near a nuclear reactor, and provide estimates of the CEνNS event rate in four different targets, and provide preliminary event rates of backgrounds from materials intrinsic radioactivity. From these calculations, we propose xenon and argon as viable targets for a CEνNS experiment with SPCs at a nuclear power plant.

The detection of low-energy nuclear recoils induced by both CEνNS and WIMPs presents several challenges. One of them is the energy calibration to nuclear recoils in the sub-keV region. We explored the feasibility of measuring the nuclear quenching factor of neon nuclear recoils induced by a neutron beam, produced at the TUNL facility, in an SPC filled with 2 bar of Ne+CH_4 (3 %). A new analysis technique was developed to extract the quenching factor between 0.43 and 11 $\mathrm{keV_{nr}}$, by implementing a Bayesian analysis framework and simultaneously fitting multiple data sets recorded during the experimental campaign. The energy dependence of the nuclear quenching factor is modelled using a simple power law: $\alpha \mathrm{E}_{nr}^{\beta}$, whose parameters were measured to be $\alpha = 0.2801 \pm 0.0050$ (fit) $\pm$ 0.0045 (sys) and $\beta = 0.0867 \pm 0.020$ (fit) $\pm$ 0.006 (sys). These measurements provide the first estimation of the nuclear quenching factor in neon gas.

To my mother

Acknowledgements

I would like to acknowledge that the work presented in this thesis is not my accomplishment alone, but is the accomplishment of a scientific community and constant support from important people in my life.

First, I would like to express my deepest gratitude to Ryan Martin and Gilles Gerbier, my supervisors, who gave me this incredible opportunity to work within the NEWS-G collaboration. They taught me how to become an experimental physicist and guided me during my graduate career. Thank you both for your advice and your constant support, in particular during the tougher times. I will always be grateful.

I wish to thank all my colleagues of the NEWS-G collaboration, it was a real pleasure to work with each one of you. I would like to pay my special regards to my "Canadian" colleagues: Jean-Marie Coquillat, George Savvidis, Jean-François Caron, Guillaume Giroux, Dan Durnford, Philippe Gros, Alexis Brossard and Francisco (Paco) Vazquez de Sola Fernandez, for their kindness, assistance and support. I would like to take a moment to thank Alexis Brossard for being my Geant4 mentor and his endless knowledge about backgrounds, Philippe for his companionship at TUNL, Dan for his analysis expertise, and Paco for his many areas of expertise and in particular his endless support during the quenching factor analysis challenge. I would like to thank George, Guillaume, Dan, Philippe, Alexis, Paco and Ioannis Katsioulas for reviewing this manuscript. Because experimental physics is nothing without them, I would like to thank our engineers Sean Crawford and Koby Derring for their amazing work, and without whom NEWS-G could not be possible.

I would like to express my gratitude to Phil Barbeau, who opened the door of the TUNL facility to the NEWS-G collaboration, which lead to the first quenching factor measurements in neon gas. I would like to acknowledge the invaluable assistance and expertise of Phil during this quenching factor experiment and his team: Peibo An, Connor Awe, Sam Hedges, Long Li, and James Runge. It was an honor to work with all of you.

I wish to express my sincere gratitude to Calvin Howell [97], Grayson Rich [112], Alexis Brossard [82], and Paco Vazquez de Sola Fernandez [67], whose theses provided priceless guidance for the writing of this manuscript.

I also wish to take a moment to thank the Physics Department staff of Queen's University and in particular Loanne Meldrum, who provided practical guidance and endless kindness throughout all these years.

I would like to take this opportunity to thank all my internship supervisors, starting with Nathalie Besson, who gave me my first internship in particle physics in undergrad. I would like also to thank Thierry Lasserre, Ed Blucher, Alessandra Tonazzo and Anatael Cabrera for mentoring me and teaching me about research.

I would like to thank my "Canadian" friends for their support during these past four years: Vasu and Shivaji Basu, Ananthan Karunakaran, Kathy Adams, and Ingrida Semenec. I would like to thank my landlord Pat Babcock, for being more than a landlord to me, thank you for your endless kindness. You all made my life so much easier and nicer so far away from home.

Enfin, je voudrais remercier ma famille et mes amis en France. Ces quatre années loin de vous tous ont été une épreuve longue et difficile. Cependant, malgré la distance votre soutient et amitié m'ont accompagnés. Je souhaiterais en particulier remercier mes amis les plus proches: Cyndie, Carole, Giovanni et Timothée, ainsi que ma meilleure amie Thessalie pour son amitié sans faille, son soutient constant, et ses messages vocaux de 20 min sur WhatApp. Je souhaiterais remercier mes parents, ma grand-mère, mon oncle et mes tantes, pour leur soutient, leur gentillesse et d'être juste géniaux. Je voudrais en particulier remercier ma mère qui m'a élevée, soutenue et toujours encouragée. Maman, les mots me manquent pour exprimer toute la gratitude que j'éprouve.

I also wish to thank the LaTorre family, and in particular Shawn and Joe for welcoming me in their home, and made me feel like I had a family on this continent. At last but not least, I wish to thank Tony LaTorre. I have been encouraged, supported, and inspired by Tony since we met. He believed in me when others did not and I will always be grateful for this. Tony introduced me to the Bayesian world, this was quite a ride! He helped me review my analysis and parts of this thesis. Tony helped become a better scientist and overall a better person.

To all of you, thank you.

Contents

List of Figures

List of Tables

Chapter 1

Introduction

At the beginning of the 20^{th} century two new theories were developed: quantum mechanics and special relativity. Together, they established the basis of elementary particle interactions. In the 1960s and 70s a theory incorporating quantum chromodynamics, quantum electrodynamics and weak processes emerged allowing physicists to describe all particle interactions but gravity. This theory is called the Standard Model. It is based on two families of elementary particles: quarks and leptons, called fermions, and 13 bosons.

The neutrino is an elementary particle from the Standard Model first postulated by Pauli in 1930 [1] and is categorized as a neutral lepton. There are three flavors of neutrinos: the electronic neutrino, the muon neutrino and the tau neutrino. The electronic neutrino was detected for the first time by Reines and Cowan in 1956 [2], followed by the detection of the muon neutrino in 1962 by Steinberger, Lederman and Schwartz [3] and the tau neutrino detected by the DONUT experiment in 2000 [4]. Neutrinos interact only via the weak interaction, which makes them challenging to detect, with a cross section of the order of $1 \times 10^{-43}\,\mathrm{cm}^2$.

The Standard Model predicted a neutral interaction mediated by one boson. Emulating the well-established elastic electron-nucleus scattering [5], Freedman postulated in 1974 the existence of a similar interaction involving neutrinos: coherent elastic neutrino-nucleus scattering, or CEνNS [6]. Freedman noted first applications to CEνNS in probing the nuclear structure as well as in stellar evolution, as neutrino transport strongly impacts the mechanism of supernovae explosion. More details on the role of this neutral current can be found in [7]. Freedman also warned experimenters of the difficulty of detecting CEνNS, since it requires the detection of nuclei recoiling with low energies, a few keV.

One of the goals of this thesis is to investigate the feasibility of detecting CEνNS using a Spherical Proportional Counter (SPC) at a nuclear reactor. SPCs were developed by the New Experiments with Spheres-Gas collaboration (NEWS-G) in 2006 [8] in view to search for a low-mass dark matter candidate: WIMPs [9]. These particles are assumed to have a weak interaction cross section with the particles of the Standard Model. This technology consists of a grounded spherical metallic vessel filled with gas. At its center, a small spherical anode is set to a high voltage, which allows the ionization signal induced by a particle depositing energy in the gas to be collected. In SPCs, the signals from both direct dark matter detection and CEνNS consist of nuclear recoils from elastic scatters. The SPC detectors have appealing features for both searches, such as a sub-keV sensitivity, a low intrinsic electronic noise and the ability to easily change the target material. Due to the nature of the signals of interest, the calibration to nuclear recoils in our detectors is essential. To the best of our knowledge, only two measurements were performed in gas [10] [11], and there is no existing calibration for nuclear recoils in pure neon or mixture of neon and methane. The latter is the primary gas mixture used by the NEWS-G collaboration for its search for dark matter and target candidate for a CEνNS experiment with SPCs. For this reason, a nuclear recoil calibration experiment was organized at the Triangle Universities Nuclear Laboratory facility to extract the nuclear quenching factor of neon nuclei in the neon based gas mixture used by the NEWS-G collaboration. In this thesis, we present a new analysis approach to extract the quenching factor within 5 % uncertainty, in support of the dark matter and CEνNS communities.

In Chapter 2, we present the theory behind the CEνNS interaction, the applications of such an interaction and the state of the art of the CEνNS detection experiments. Chapter 3 describes the SPCs and their working principles. Chapters 4, 5, 6, and 7 represent the main work performed for this thesis. Chapter 4 covers the theory behind the nuclear quenching factor and the experimental procedures used or proposed as of today, to extract such quantity. Chapter 5 presents the nuclear quenching factor measurements performed in the scope of this thesis: the experimental set up, the energy calibration and stability of the detector. Chapter 6 covers the analysis approach to extract the nuclear quenching factor from that experiment: the model developed to describe the nuclear recoils, and the unbinned fit to the data in a Bayesian framework. Then, Chapter 7 presents the results of the quenching factor measurement. Finally, Chapters 8 and 9 cover the feasibility of an experiment using an SPC at a nuclear reactor. First, we estimate the induced CEνNS signal in four different targets, as to estimate the best candidates. And then, we present a preliminary study of the background induced by the materials used to build the detector and the shielding.

Chapter 2

Coherent elastic neutrino-nucleus scattering

2.1 cross section for CEνNS

Coherent elastic neutrino-nucleus scattering (CEνNS) involves an incident neutrino scattering coherently off of all the nucleons in the nucleus. For most medium A nuclei, a neutrino with an energy below roughly 50 MeV will scatter off of the nucleus as a whole. The nucleons in the nucleus thus recoil in phase, and we model this as the whole nucleus recoiling. For the coherence to be possible, the following condition must be met:

$$qr_n \leqslant 1 \tag{2.1}$$

with q the momentum transfer from the neutrino to the nucleus, and, r_n, the nuclear radius. The reduced Planck constant, $\hbar$, and the speed of light, c, are set to 1.

The Standard Model predicts a neutrino-nucleus differential cross section as a function of the recoil and the neutrino energies [6]:

$$\frac{d\sigma}{dE_{nr}}(E_\nu, E_n) = \frac{G_F^2}{2\pi} M \left(2 - \frac{2E_{nr}}{E_\nu} + \left(\frac{E_{nr}}{E_\nu}\right)^2 - \frac{ME_{nr}}{E_\nu^2} \right) \frac{Q_W^2}{4} F^2(Q^2), \tag{2.2}$$

where E_ν is the neutrino energy, E_{nr} is the recoil energy of the nucleus, M is the target nuclear mass, G_F is Fermi's constant, F is the nuclear form factor, Q is the 4-momentum transfer and Q_W is the weak nuclear charge, which can be written as follows:

$$Q_W = N - (1 - 4\sin^2\theta_W)Z, \tag{2.3}$$

where θ_W is the Weinberg angle, N is the number of neutrons, and Z is the number of protons. Because the recoil energy of the nucleus is much smaller than the energy of the neutrino, $E_{nr} \ll E_\nu$, then the differential cross section can be written as:

$$\frac{d\sigma}{dE_{nr}}(E_\nu, E_{nr}) = \frac{G_F^2}{2\pi} M \left(1 - \frac{ME_{nr}}{E_\nu^2}\right) Q_W^2 F^2(Q^2), \tag{2.4}$$

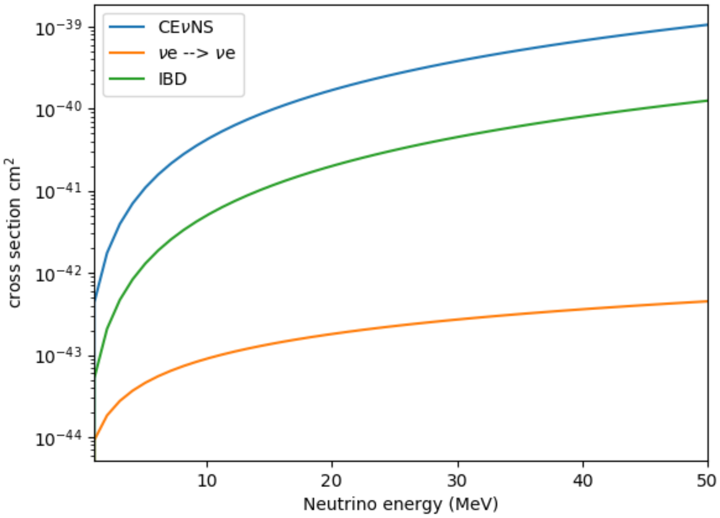

Figure 2.1: Comparison of cross section processes: CEνNS on Ne target in blue, elastic neutrino-electron scattering in orange and inverse beta decay in green. The CEνNS cross section is from [12].

The derivation of the nuclear form factor correction comes from Lewin and Smith [13] which uses the Helm form factor function [14]. The form factor describes the distribution of nucleons within the nucleus. The quantity depends on a dimensionless quantity Q=$qr_n/\hbar$. The coherence of the interaction breaks when $F(Q \geqslant 1)^2 \to 0$. The momentum transfer $q = \sqrt{2M_T E_{nr}}$ depends on the target mass and the nuclear recoil energy is in keV. r_n is an effective nuclear radius and is approximated by:

$$r_n = \sqrt{c^2 + \frac{7}{3}\pi^2 a^2 - 5s^2}, \tag{2.5}$$

with c = $1.23A^{1/3}$ - 0.6 fm, s = 0.9 fm is a measure of the nuclear skin thickness and a = 0.52 fm. The Helm factor is written as:

$$F(qr_n) = 3\frac{j_1(qr_n)}{qr_n} \times e^{-(qs)^2/2} \tag{2.6}$$

with:

$$j_1(qr_n) = \frac{\sin(qr_n) - qr_n\cos(qr_n)}{(qr_n)^2}. \tag{2.7}$$

The parameters in equation 2.6 are determined from experimental estimates, more details can be found in [13].

The cross section is relatively high compared to other neutrino processes, due to the N^2 term; see Figure 2.1. However, because the only detectable output of this interaction is the nuclear recoil of the nucleus (∼ few keV) and the technology available for the past 40 years did not allow an energy threshold low enough, the first detection of CEνNS was not made until 2017 by the COHERENT experiment [15].

Because of the cross section dependence on N^2, the choice of target is important. Figure 2.2a shows the comparison of cross sections of CEνNS for different targets: Xe, Ar, Ne and He. The cross section on He is by a factor 4 lower than the cross section of inverse beta decay (IBD), thus from a cross section point of view using He as target is not advantageous. The Xe, Ar and Ne target are more interesting target candidates.

The recoil energy of the nucleus ranges from 0 to a maximum value, E_{nr}^{max}:

$$E_{nr}^{max} = \frac{2E_\nu^2}{m_N + 2E_\nu}, \tag{2.8}$$

where m_N is the target mass nucleus. Figure 7.1 shows the maximum recoil energy reached for dif-

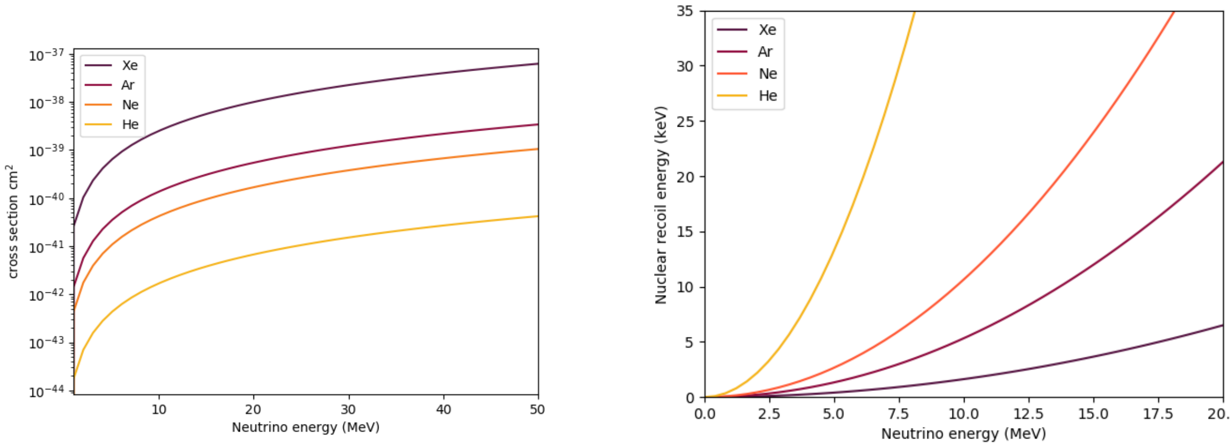

(a) Comparison of different targets' cross sections for CEνNS interaction: Xe in dark red, Ar in red, Ne in orange and He in yellow.

(b) Maximum nuclear recoil energy as a function of the incident neutrino energy for different targets: Xe, Ar, Ne and He.

Figure 2.2: Impact of the target on the CEνNS cross section and on the maximum nuclear recoils energy.

ferent targets: Xe, Ar, Ne and He. From this figure, one can see that for a neutrino of energy 5 MeV the maximum recoil energy from a He nucleus is about 14 keV$_{\text{nr}}$, Ne nucleus it is about 3 keV$_{\text{nr}}$, Ar nucleus it is about 2 keV$_{\text{nr}}$ and Xe nucleus it is about 0.5 keV$_{\text{nr}}$. Thus, the heavier nuclei which have a higher cross section are more difficult to detect because the signal output is below 0.5 keV$_{\text{nr}}$. It is also important to keep in mind that these energies will be "quenched" since most detectors can only detect a fraction of the total nuclear recoil energy deposited (e.g. in the form of ionization).

2.2 Sources of detectable neutrinos

In this section we describe the possible sources of neutrinos from which CEνNS could be detected. These tend to be sources that produce neutrinos in the intermediary energy regime (below hundreds of MeV). They are presented in two categories: natural and artificial sources.

2.2.1 Natural sources of neutrinos

The natural neutrinos cover solar, atmospheric and supernovae neutrinos. These sources of neutrinos constitute an ultimate background to the direct detection of dark matter: the so-called “neutrino floor” [16]. It is thus important for the dark matter search community to have a strong understanding of the CEνNS signal in their detectors. This section follows L. Strigari work [17], which looked into neutrino induced background for WIMP detection.

Solar neutrinos

The main contribution from solar neutrinos is coming from the *pp*-chain, see Figure 2.4. Considering the energies of the neutrinos generated in the chain, only two sources of neutrinos are considered for potential observations. Indeed, the nuclear recoil energies generated by such neutrinos would be below 30 eV [18]. The two neutrino reactions considered are: ^{8}B and *hep* neutrinos. The energy spectra of neutrinos produced in such reactions are shown in Figure 2.3, where the maximum neutrino energy reaches about 20 MeV, thus can generate a maximum nuclear recoil energy of about 5 keV$_{\mathrm{nr}}$ for heavy targets such as as Xe, see Figure 2.5. Their position in the *pp*-chain is shown in Figure 2.4.

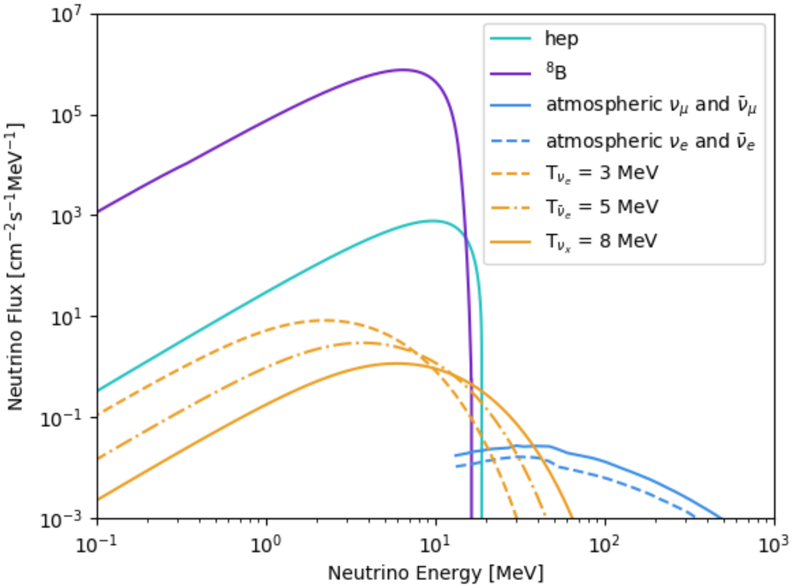

Figure 2.3: Dominant neutrino fluxes from astrophysical sources to observe CEνNS. The contribution from solar neutrinos is reduced to the *hep* and ^{8}B chains, in turquoise and purple. The different contributions from atmospheric and diffuse supernovae are shown in blue and orange respectively. [17] [19] [20].

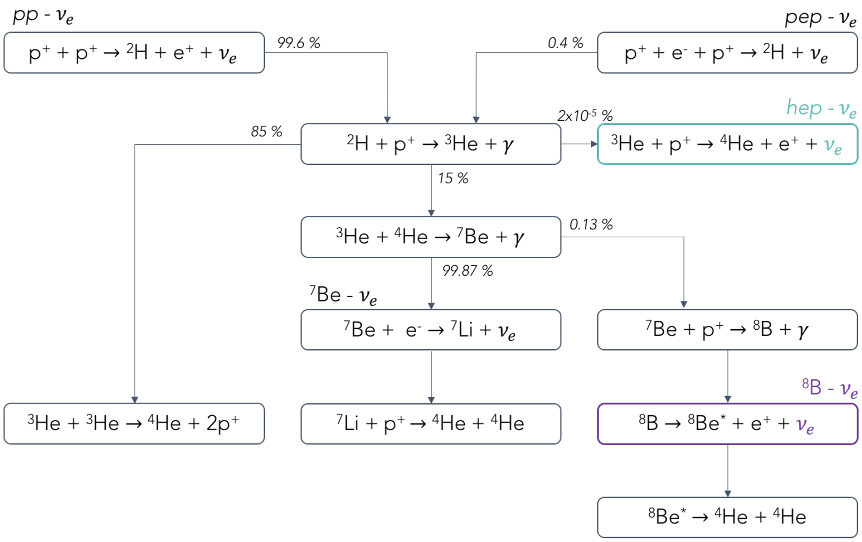

Figure 2.4: *pp* - chain with in turquoise and purple the *hep* and ^{8}B reactions [21].

Atmospheric neutrinos

When cosmic rays interact with the atmosphere they produce an intense flux of neutrinos going up to energies of few hundreds of GeV and down to few tens of MeV. Two flavors of neutrinos are created, electronic and muonic neutrinos, along with their respective antiparticle. Figure 2.3 shows the energy spectra for such neutrinos. The neutrinos with energies within the lower limit and 50 MeV constitute a source of CEνNS events, however quite a faint one.

Supernovae neutrinos

When a supernova takes place it generates a burst of about 10^{58} neutrinos of all flavors in a time window of about 10 s. The remnants of such explosions constitute a diffuse supernova neutrinos flux. The flux is calculated from the neutrino spectrum per supernova and the core-collapse supernova event rate as a function of redshift [17]. The neutrino energy spectrum of core-collapse supernovae is approximated as a Fermi-Dirac spectrum, with energy ranging from 3 to 8 MeV [20]. Each temperature corresponds to a neutrino flavor: $\mathrm{T}_{\nu_e} = 3\,\mathrm{MeV}$, $\mathrm{T}_{\bar{\nu}_e} = 5\,\mathrm{MeV}$ and $\mathrm{T}_{\nu_x} = 8\,\mathrm{MeV}$, where ν_x represents ν_μ, ν_τ and their respective antiparticles. The energy spectra of the three contributions are shown in Figure 2.3.

Figure 2.5 shows the expected event rates for the natural neutrinos sources: ^{8}B and *hep*, atmospheric and diffuse supernovae background in four different targets: xenon, argon, neon and helium. The contribution from ^{8}B solar neutrinos is expected to produce the most intense signal in the four targets. Considering an arbitrary energy threshold of $100\,\mathrm{eV_{nr}}$ the event rates are reaching 713, 220, 90 and 18.7 CEνNS events/t/year for xenon, argon, neon and helium, respectively. The other contributions to the signals are listed in Table 2.1. They seem to constitute a faint signal in the CEνNS channel.

Thus, in order to detect CEνNS, experimenters are opting for artificial neutrino sources, which have a higher neutrino flux and thus a higher expected event rate.

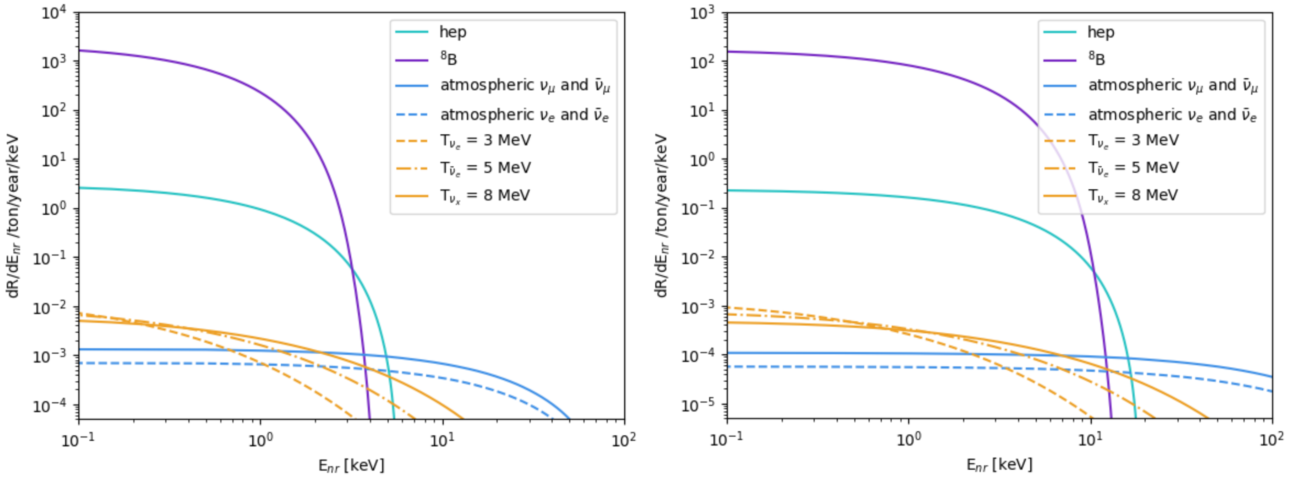

(a) Xenon.

(b) Argon.

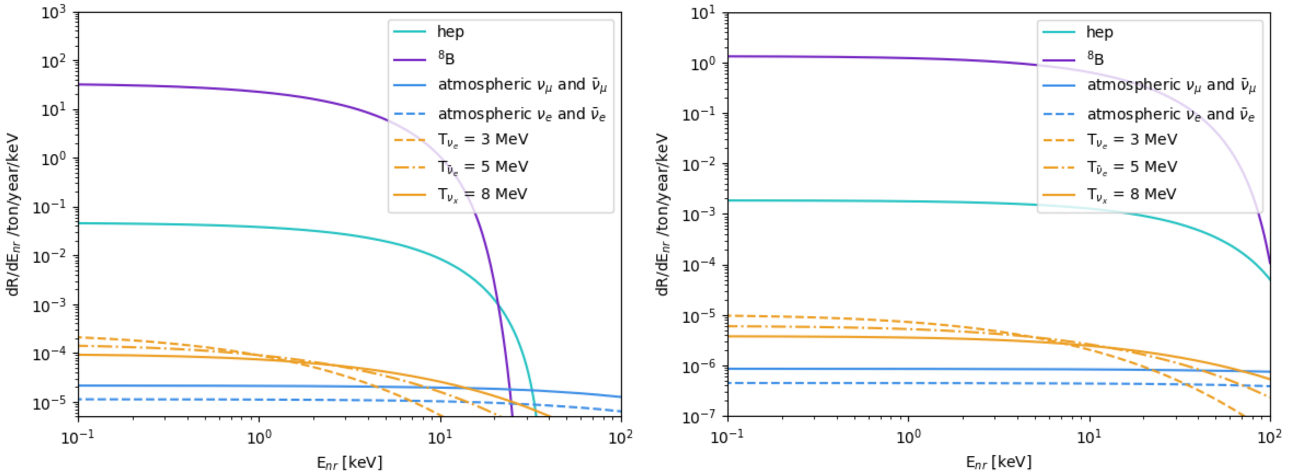

(c) Neon.

(d) Helium

Figure 2.5: Event rate as a function of the nuclear recoil energy for four target nuclei, considering the four astrophysical fluxes aforementioned: ^{8}B and *hep*, atmospheric and diffuse supernovae background neutrinos (DSNB).

2.2.2 Artificial sources of neutrinos

Neutrino beams

Neutrino beams can be produced from charged particle beams. For example, a beam of protons is aimed at a target generally made of graphite or mercury, producing pions and kaons. These

CEνNS /t/year	Xe	Ar	Ne	He
^{8}B	713	220.5	90.5	18.7
hep	2	0.63	0.25	5.1e-2
Atm. ν_μ, $\bar{\nu}_\mu$	2.e-2	6e-3	1.6e-3	7.9e-5
Atm. ν_e, $\bar{\nu}_e$	1.e-3	4e-3	8.2e-4	4.1e-5
DSNB T$_{\nu_e}$	2.3e-3	8e-4	3.6e-4	7.4e-5
DSNB T$_{\bar{\nu}_e}$	5e-3	1.5e-3	6.1e-4	1.1e-4
DSNB T$_{\nu_x}$	7.6e-3	2.36 e-3	9.3 e-4	1.3e-4

Table 2.1: Event rates above arbitrary energy threshold = 100 eV$_{\mathrm{nr}}$.

particles decay over several hundreds of meters mainly into muons and muon neutrinos [22]:

$$\pi^+ \rightarrow \mu^+ + \nu_\mu \tag{2.9}$$

Finally, the μ^+ in turn decay in:

$$\mu^+ \rightarrow e^+ + \nu_e + \bar{\nu}_\mu \tag{2.10}$$

These sources generate a wide range of energy between 0 and about 50 MeV, thus, producing recoils above 1 keV$_{\mathrm{nr}}$. An advantage of such a source is the beam timing for background rejection, more details are provided in Table 2.2.

Neutrino beams are used in varieties of neutrino physics experiments: the NuMI (Neutrino at the Main Injector) beamline is used for the NOνA experiment [23] and will undergo upgrades for DUNE [24], both focusing on studying neutrino oscillation. The SNS (Spallation Neutrino Source) used by the COHERENT experiment focuses on CEνNS detection [25].

Electron-capture neutrinos

Electron-capture (EC) takes place when a proton-rich nucleus absorbes an inner atomic electron, generally from the K and/or L shells, and then emits a neutrino:

$$^{\mathrm{A}}_{\mathrm{Z}}\mathrm{X}_{\mathrm{N}} + \mathrm{e}^- \longrightarrow \mathrm{Y}_{\mathrm{N+1}} + \nu_e \tag{2.11}$$

The neutrino carries almost all the energy of the decay, and generates a monochromatic electron neutrino source. The neutrino energy of such sources ranges between about 0.5 and 1.5 MeV. Most EC decays are visible thanks to one or more X-ray emitted after an outer electron replaces the inner atomic electron that was absorbed.

Mega-Curie (MCi) scale EC neutrino sources have been developed in the last three decades [26] [27], using ^{51}Cr and ^{37}Ar isotopes. If considering an ^{37}Ar source of 5 MCi, the resulting neutrino flux is of the order of $1 \times 10^{17}\,\nu$/MeV/s. These sources were developed primarily for calibration purposes by GALLEX and SAGE [26] [27]. However, other applications were proposed like sterile neutrino searches via short-baseline oscillations, neutrino magnetic moment searches, and searches beyond the Standard Model [28]. In 2012, the Ricochet experiment, which aims at detecting CEνNS, submitted a proposal in view of a possible CEνNS program [29].

Reactor neutrinos

Nuclear reactors provide the most intense artifcial source of neutrinos $\sim 2 \times 10^{20}$ GW^{-1}s^{-1}. The neutrinos are not the product of fission, but they result from the beta decay of the fission products; thus nuclear reactors only generate $\bar{\nu}_e$. The reactor neutrinos cover an energy range up to about 12 MeV. Section 8.1 will provide more details about $\bar{\nu}_e$ production at nuclear reactors.

Source	Flux [s^{-1}]	Flavor	Energy [MeV]	Pros	Cons
Reactor	$\sim 2 \times 10^{20}$ /GW	$\bar{\nu}_e$	0-10	large flux	- lower cross section - lower energy recoils
Stopped -pion	$\sim 10^{15}$	ν_μ ν_e $\bar{\nu}_\mu$	0-50	- higher cross section - higher energy recoils - pulsed beam	- lower flux - pulsed source (background)

Table 2.2: Summary of pros and cons for CEνNS detection with two different artificial sources: nuclear reactors and neutrino beam (stopped pion source) [30].

2.3 Applications of CEνNS

Once CEνNS is well characterized, the next phase is to use the process to probe further physics questions. The following sections highlight some of the most straightforward physics to explore as well as highlight directions for future research.

2.3.1 Application in monitoring reactor neutrino flux

The coherent elastic neutrino-nucleus scattering, as the inverse beta decay, can be used to probe the core fuel of nuclear power plant. Indeed, the flux of $\bar{\nu}_e$ depends on the nature of the fuel. Two main isotopes participate in the neutrino production of a reactor: ^{235}U and ^{239}Pu. The first represents about 5% of the total fuel and is directly fissile, while the other comes from the ^{238}U that form the rest of the core fuel. The plutonium emits less neutrinos per fission than the ^{235}U. One can directly probe the reactor fuel at a nuclear power plant and check for plutonium production. Currently, it is proposed to use inverse beta decay to probe the reactor fuel at a nuclear power plant [31].

Another interesting application of CEνNS is to probe the reactor neutrino spectrum as this spectrum is not well known. Indeed, inverse beta decay has a threshold of 1.8 MeV in order to take place, which is not the case of the CEνNS interaction. Thus, the CEνNS could provide complementary information, and help develop more accurate models to describe the neutrino flux.

2.3.2 Neutrino magnetic moment searches

The Standard Model predicts a magnetic moment of the neutrino to be [32]:

$$\mu_\nu \sim 3.2 \times 10^{-19} \left[\frac{m_\nu}{1\,\mathrm{eV}}\right] \mu_B \tag{2.12}$$

However, the current best limit is $\mu_{\nu_e} \leq 1.4 \times 10^{-12}\ \mu_B$, provided from solar neutrino data from the Borexino experiment [34]. Other experiments use reactor neutrinos and set limits at $2.9 \times 10^{-11} \mu_B$

for the GEMMA experiment [35]. The LSND experiment used the neutrino beam produced at Los Alamos and provided limits for $\mu_{\nu_\mu} < 6.8 \times 10^{-10}\mu_B$ [36]. All of these measurements took place using elastic ν-e$^-$ interactions. One could observe a non zero magnetic moment via a distortion of the nuclear recoil spectrum of coherent elastic neutrino-nucleus scattering. Figure 2.6 shows such distortion for Ge and CaWO$_4$ targets.

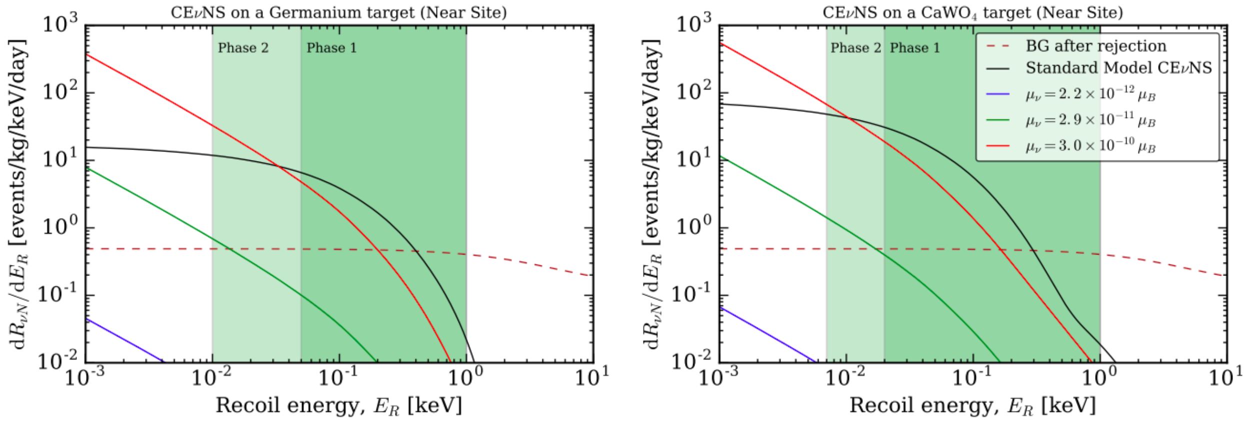

Figure 2.6: Expected distortion of the nuclear recoil rate due to the magnetic moment neutrino. In [33] the author worked out the expected distortion on nuclear recoil rate considering two targets at a nuclear reactor: Chooz reactor, in France, for the Standard Model in black, and with varying neutrino magnetic moment: $2.2 \times 10^{-12}\ \mu_B$, $2.9 \times 10^{-11}\ \mu_B$, and $3 \times 10^{-10}\ \mu_B$, in blue, green, and, red, respectively. The green shaded regions correspond to different detector phases with improved energy threshold: 50 and 10 eV$_{\text{ee}}$ for Ge and 20 and 7 eV$_{\text{ee}}$ for CaWo$_4$. The red dashed line shows the background after rejection.

The cross section can be expressed in terms of the neutrino magnetic moment:

$$\left(\frac{d\sigma}{dE_{nr}}\right)_\mu = \frac{\pi\alpha^2\mu_\nu^2 Z^2}{m_e^2}\left(\frac{1}{E_{nr}} - \frac{1}{E_\nu} + \frac{E_{nr}}{4E_\nu^2}\right)F^2(Q) \tag{2.13}$$

Massive Majorana and Dirac neutrinos have different magnetic moment values, so this could shed light on the nature of the neutrino [37].

2.3.3 Nuclear form factor measurements

The coherent elastic neutrino-nucleus cross section is predicted by the Standard Model; therefore investigations on the nuclear form factors could give information on the neutron spatial distribution in a nucleus, and also on its radius [38].

2.3.4 Supernovae neutrinos searches

As mentioned by Freedman [6] the CEνNS process could be, in part, responsible for supernovae explosions. The number of neutrino produced during a supernova is $\sim 10^{58}$, carrying roughly 6.2 $\times$ 10^{55} GeV [39]. It is thought that neutrinos play a key role in the shockwave leading to the explosion [39]. CEνNS could be responsible for the energy containment in the stellar matter, with neutrinos scattering off of nuclei that redeposit energy in the dense environment. However, the overall impact of CEνNS in supernovae could be reduced by ion-ion correlations where the densities are high.

The relatively large cross section of CEνNS could provide a way to observe supernova neutrinos. The interaction could give us an opportunity of studying fundamental physics such as neutrino oscillations and neutrino mass hierarchy for example [41].
As aforementioned, the densities in gravitational collapses are high, $1.0 \times 10^9\,\mathrm{g/cm^3}$ [40], which leads to electron captures, which in turn produces a large number of ν_e in the stellar medium. Thus, the number of neutrinos is so large that neutrino-neutrino scattering interactions, not only occur, but are thought to be a dominant process [41]. These effects and the propagation of the neutrinos through a high density medium can lead to flavor oscillations enhanced by matter by the Mikheyev-Smirnov-Wolfenstein (MSW) effect [42] [43]. Hence, the outgoing neutrinos have distinct spectral features depending on their flavor. Additionally, the flavor conversions by MSW depend on θ_{13} and the neutrino mass hierarchy.

The CEνNS process can not distinguish between neutrino flavors. However if CC supernova experiments and NC supernova experiments join their efforts, it could be made possible to extract energy spectra of the neutrinos emerging from the stellar environment. These could help increase our understanding of supernovae and supernovae neutrinos.

2.3.5 Weak mixing angle precision measurement

The weak mixing angle is related to the electroweak symmetry breaking in the cooling of the Universe, when the neutral electroweak W and B bosons "mixed" to create the γ and Z bosons. This electroweak symmetry breaking hypothesis is part of the Standard Model.

The value of $\sin^2\theta_W$ depends on the momentum transfer; hence, several measurements with different momentum transfer were performed. They are shown in Figure 2.7. Some existing measurements are in disagreement with the Standard Model prediction. However, there are not enough measurements with significant deviations to conclude to a disagreement with the Standard Model.

The coherent elastic neutrino-nucleus scattering cross section is predicted by the Standard Model and depends on the weak charge given in equation 2.3. Itself depends on the number of neutrons and protons inside the nucleus, which is known, and the weak mixing angle θ_W. Thus, it can be directly extracted from the cross section. A variation from the theory would indicate physics beyond the Standard Model. Reactor experiments can probe the momentum transfer of about 5 MeV [44], which has not any comparable existing measurement to this day. Accelerators, or stopped-pion neutrino source, experiments can probe a momentum transfer of about 40 MeV, which is comparable with measurements from proton and electron scattering experiments.

Thus, CEνNS proves to be an attractive tool towards weak mixing angle measurements in two different momentum transfer regions.

2.3.6 Sterile neutrino searches

The reason for a discrepancy between expected and observed reactor neutrinos flux (”reactor anti-neutrino anomaly”) is still unknown [47]. Other experiments using neutrino beams also have anomalous results [50] [51], as well as gallium experiments [48] [49]. To explain those anomalies a fourth species of neutrinos has been postulated. This additional neutrino does not interact via weak

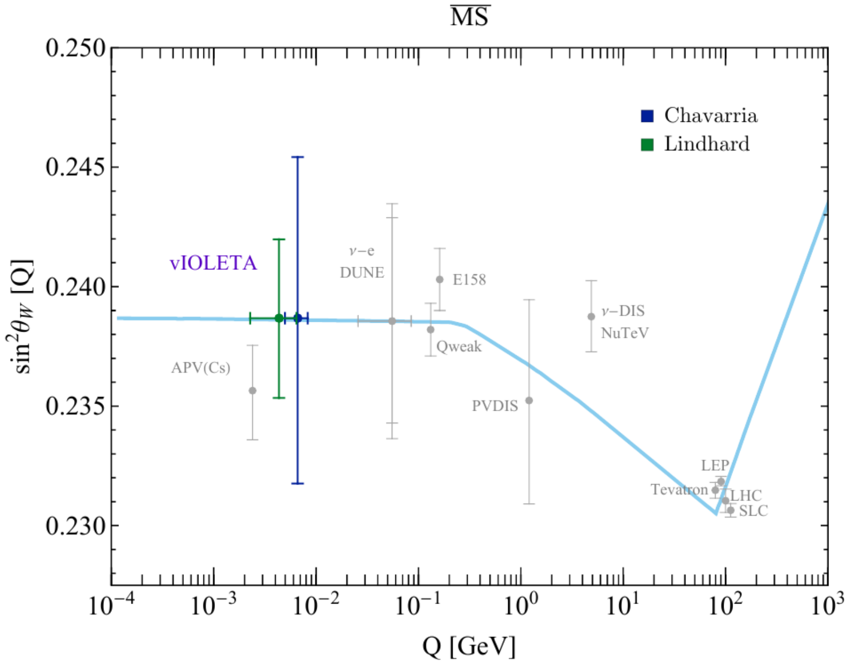

Figure 2.7: Existing $\sin^2\theta_W$ measurements and projections in the renormalization scheme $\overline{MS}$ as a function of the momentum transfer Q. The prediction from the Standard Model is shown in blue. The grey points correspond to past measurements [45], except for the projection for the DUNE experiment [46]. This plot is coming from Reference [44], from the νIOLETA collaboration, which is a future CEνNS experiment. In green and dark blue are the sensitivity of their experimental setup to the weak mixing angle with two different quenching factor models.

interaction like other neutrinos, and is called “sterile”. A way to look for a sterile neutrino, would be to compare the neutrino spectrum coming from a source in a short-baseline experiment with CEνNS, which is not flavor dependent, and thus comparing the total neutral current disappearance with CC current experiments. A significant disappearance in the neutral current would favor the existence of a sterile neutrino.

2.4 Current CEνNS experiments

The only detectable output of the CEνNS interaction is the nuclear recoil induced by the neutrino scattering. Depending on the neutrino incident energy the recoil energies cover a range below $1\,\text{keV}_{\text{nr}}$ and up to few keV_{nr}. Thus, the detection of such a faint signal is technologically challenging.

One of the first proposals to detect CEνNS came from Drukier and Stodolsky [12] in 1984, where they proposed to use superconducting grains detectors. The detector being held in a magnetic field and at a certain temperature, it allows a particle to deposit energy when it interacts with the medium. A temperature jump, δT, flips the grain from a superconducting state to a normal state, which results in a change of the magnetic field around the grain and thus to be detected. δT can be set to the desired value by tuning the magnetic field or the temperature at which the system is maintained, by using a phase diagram of the metal considered. The size of the grains depends on the nuclear recoil energy we want to detect. If the energy is of the order of the keV$_{\mathrm{nr}}$, then $10\,\mu$m grains can be flipped at a temperature of $-269.0\,^{\circ}$C, which is the liquid helium temperature. If the recoil energy is in the sub-keV$_{\mathrm{nr}}$ region, then a smaller grain is needed and/or lower temperatures are necessary, so that the δT is large in comparison of the temperature of the grain, and thus change the grain's state. The drawback of such a method is that the detected signal does not provide information on the energy of the detected particle.

Since then, we saw the proliferation of low-energy threshold detectors, making the detection possible. Depending on the technology used, one must also include a nuclear energy quenching factor, which makes the detection even more challenging.

Due to the signal constraint, an experiment aiming at detecting CEνNS wants to meet several requirements. Having a low background environment is necessary, and in particular in the region of interest. One need to have detectors having low-energy threshold in order to detect few keV down to the sub-keV region.

Finally, an intense source of neutrino is required satisfying the coherent energy range. As aforementioned in Section 2.2, there are currently two artificial sources that can satisfy both criteria: nuclear reactors and neutrino beams.

This section focuses on the experiments involved in CEνNS detection. The COHERENT experiment is described into more details due to its first detection of the interaction and achievements.

2.4.1 The COHERENT experiment

The COHERENT collaboration achieved its primary goal of detecting CEνNS in 2017 [15], using a neutrino beam produced at the Spallation Neutron source (SNS) at Oak Ridge National Laboratory (ORNL). The particularity of the COHERENT experiment is the deployment of four detectors with four different targets in order to show the N^2 nature of the cross section. The detectors are deployed in the neutrino alley at SNS, a location relatively neutron quiet. Details on the detectors are given below and in Table 2.3.

Target	Technology	Mass [kg]	Distance from source [m]	Recoil threshold [keV$_{nr}$]
CsI[Na]	Scintillation	14.6	20	6.5
Ge	Ionization	16	22	1
LAr	Scintillation	24.4/610	29	20
NaI[Tl]	Scintillation	185/3000	28	13

Table 2.3: Summary of the three COHERENT detector subsystems parameters. See [52]. Note that the CsI detector has been dismantled.

The 14 kg *CsI[Na] Scintillator* detector (cesium iodine crystals dopped with sodium) had several advantages to detect CEνNS: a low energy threshold and a large number of neutrons (Cs: 78 and I:74) which boosts the cross section of the CEνNS interaction. The two recoiling species have very similar masses (Cs: 132.9 u and I: 126.9 u). The commissioning of this detector took place in 2015, followed by 15 months of accumulated data. The detector was then decommissioned in 2019.

The P-Type Point Contact Germanium detectors combine several advantages for the CEνNS detection: low energy threshold, high energy resolution (below 1 keV$_{\text{ee}}$), a well known quenching factor and a low internal backgrounds. Its medium-A nucleus optimizes the coherence process and generates more energetic nuclear recoils than for heavier nuclei, which makes it a perfect candidate for CEνNS detection. The low intrinsic noise of about 150 eV$_{\text{ee}}$, allows detection of energies below 1 keV$_{\text{nr}}$. An array of 8 germanium modules of 2.2 kg each are deployed at the SNS with the goal of measuring the CEνNS spectrum, but also probe electromagnetic properties of neutrinos. The detector will be in commissioning phase in 2022.

The Liquid Argon single phase TPC, or CENNS-10 detector, has a relatively high light yield, roughly 40 photons/keV$_{\mathrm{ee}}$, moreover LAr presents a huge advantage of discrimination between nuclear recoils and electronic recoils. The detector is a 56.7 L cylindrical chamber filled with the scintillator liquid with two photomultipliers (PMTs) on each extremities with a fiducial mass of 24.4 kg. The detector will undergo an upgrade in 2023, and increase its fiducial mass to 610 kg.

The NaI[Tl] detector is the last detector that the COHERENT collaboration deployed. The sodium isotope has the lowest neutron value of all the experiment's target materials (N = 12 neutrons); therefore it will result in the highest nuclear recoil energies. The light yield is similar to the LAr TPC subsystem roughly 40 photons/keV$_{\mathrm{ee}}$. The NaI[Tl] subsystem consists of 7.7 kg NaI[Tl] rectangular modules sealed in aluminum and combined with PMTs. The first phase of this detector is to explore CC interactions (with I), and then several upgrades will be done to deploy a larger detector volume. In the second phase the detector will be a 2 tonnes NaI[Tl] subsystem sensitive to CEνNS and CC interactions. The detector will be in commissioning phase in 2022.

In August 2017, the COHERENT collaboration released a paper [15] showing the first observation of coherent elastic neutrino-nucleus scattering interaction. This result comes from 15 months of accumulated data with the CsI[Na] detector. Thanks to the pulsed beam the collaboration isolated the environmental backgrounds from neutrino signals and was able to compare signals from before protons-on-target triggers and after. They observed a high significance excess of events on the second signal group (beam ON), in both the energy spectrum and the arrival time distribution, see Figure 2.8. The excess signal follows the Standard Model prediction for both distribution. The measurement show a confidence with the theory with a level of 1 sigma (134 ± 22 events observed against 173 ± 48 predicted). Finally, the COHERENT collaboration observe the CEνNS process at a 6.7 σ confidence level. The uncertainties were dominated by uncertainties on the neutrino flux, 10 %, and the quenching factor, 25 %. Additional data were taken to increase the statistics by a factor 2 and the quenching factor was re-measured and estimated with a new analysis, decreasing its uncertainty contribution to 3.6 %. With these new data, and better understanding of the quenching factor, the COHERENT collaboration was able to set a new confidence level of 11.6 σ (results communicated at conferences and not yet published).

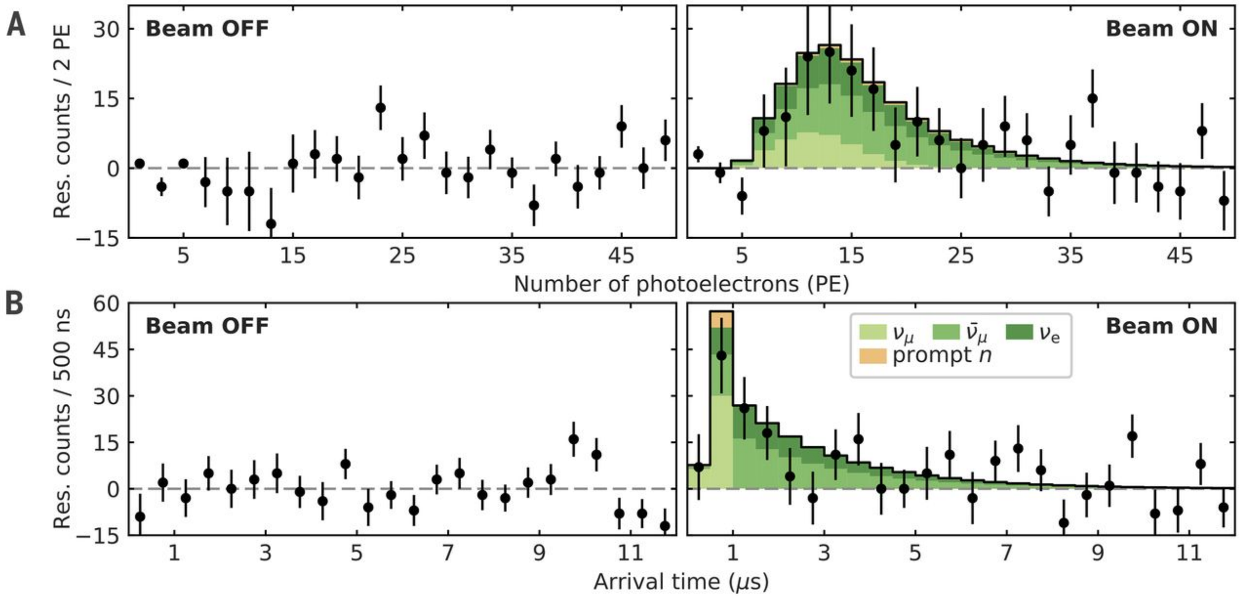

Figure 2.8: Figure from [25], which highlight the detection of the CEνNS interaction in the CsI detector of the COHERENT experiment. The left two plots correspond to the residual differences between signal events and background events. The top right plot shows the energy spectrum, in photoelectrons, expected in green from the different neutrino flavors and the data in black dots. The bottom right plot shows the arrival time spectrum, expected in green and in black dots the data.

In 2020, the COHERENT collaboration released new results showing first detection of CEνNS on argon [53]. The collaboration conducted two independent analyses that showed good agreement, showing detection at 3.5 σ confidence level. The other efforts of COHERENT are summarized in Table 2.4.

The two results of COHERENT are shown in Figure 2.9 in blue dots, and compared with the expected cross section averaged to the neutrino flux as a function of the neutron number. They agree within uncertainty with theory, in green.

2.4.2 Other experiments

There are international efforts in detecting CEνNS, and several experiments made their primary goal to detect and use the interaction to probe physics. In this section, we will talk about the main experiments involved in CEνNS detection, with a particular focus on those that already took data or will turn online in the next couple of years.

The experiments looking into detecting CEνNS are using different technologies and targets. The most part of these experiments use a nuclear reactor as neutrino source and are listed in Table 2.4: COνUS, CONNIE, Miner, Ricochet and Nu-CLEUS. The first two experiments: COνUS and CONNIE, set first limits in the detection of CEνNS for reactor experiments, in 2021 [54] and 2019 [55], respectively. These two limits are shown in Figure 2.9 by red arrows and compared with the expected cross section averaged to the neutrino flux as a function of the neutron number, in red.
A first limit from solar neutrinos was provided by the XENON1T experiment in early 2021 [56], which is shown in magenta in Figure 2.9. As for the previous results/limits, it is compared with the expected cross section averaged to the neutrino flux as a function of the neutron number in magenta.

Despite not listing them in Table 2.4, other experiments are expected to go online in the near future: RED-100, TEXONO, and Xenon, which are reactor experiments.

We want to point out that the achievements of the past four years by the CEνNS community are significant. All the efforts lead to two detections for accelerator experiments, using different targets, and three limits for reactor and solar experiments.

Experiment	Target	Technology	Distance	Energy threshold	QF	Status
Reactor						
COνUS [57]	Ge	HPGe	17 m	300 eV_{ee}	Yes	2018-20: Physics run 2021: 1^{st} limit [54]
CONNIE [58]	Si	CCD arrays	30 m	40 eV_{ee}	Yes	2019-20: Physics run 2019: 1^{st} limit [55] Upgrade: 7 eV_{ee} E_{th}
Miner [59]	Si & Ge	Cryogenic	2-10 m movable core	0.1 keV_{nr}	Yes	Phase-I: on-going Phase-II: hermetic 2022: Shielding
NU-CLEUS [60]	CaWO_4	Cryogenic	72-102 m	20 eV	No	2022: Physics run
Ricochet [61]	Zn & Ge	Semi-conductor	8 m	50 eV	No	2023: Physics run
Accelerator						
COHERENT	CsI	Scintillation	19.3 m		Yes	2017: Detection [15] 2019: Decommissioning
	Ge	HPGe	21.1 m	1 keV_{nr}	Yes	2021: Commissioning
	LAr	Scintillation	28.4 m	20 keV_{nr}	Yes	2020: Detection [53] 2022: Upgrade 750 kg
	NaI	Scintillation	22 m	13 keV_{nr}	Yes	2021: Commissioning
CCM	LAr	Scintillation	20 m	20 keV_{nr}	Yes	2021-22: Physics run
Solar						
XENON1T	LXe	TPC	-	0.5 keV_{nr}	Yes	2021: 1^{st} limit [56]

Table 2.4: Summary of the experiments involved in CEνNS detection. The target, the technology used, the distance from the source, the recoil energy threshold, the sensitivity to QF and the status of the experiments are listed. Based on the report of the experiment at the workshop The Magnificent CEνNS 2020 [62].

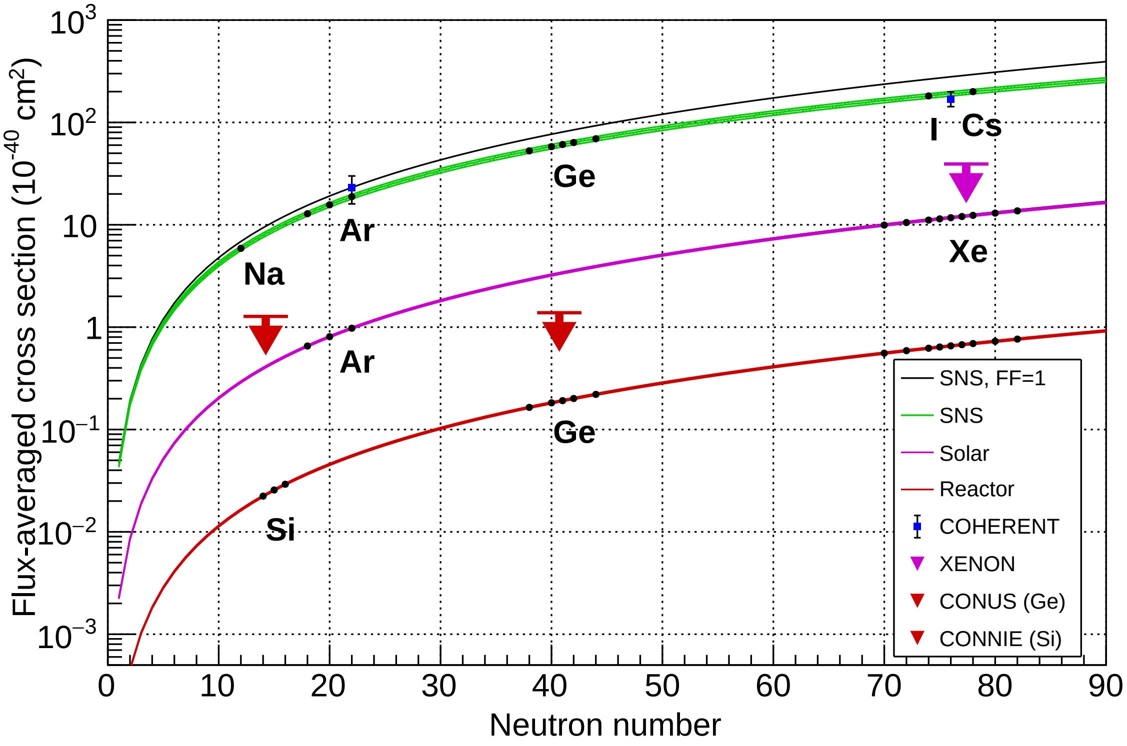

Figure 2.9: cross section averaged to the neutrino flux as a function of the neutron number. Are shown in green, magenta, and red the cross sections for accelerator, solar, and reactor, respectively. The blue points are the results from the COHERENT experiment on CsI [15] and LAr [53] targets. These results agree with the expected cross section, in green. The difference between the black and green curves is the corrections from incoherence, which have to be taken into account for accelerator experiments, due to the neutrino energy range produced. The red arrows are the limits from CONNIE [55] and COνUS [54], with Si and Ge targets, respectively. The red curve is the flux-averaged cross section for nuclear reactors. The magenta arrow is the limit of the XENON1T experiment [56] on LXe target and the magenta curve is the flux-averaged cross section for solar neutrinos experiment. Courtesy of K. Scholberg for the COHERENT Collaboration.

Chapter 3

Spherical proportional counters

This chapter describes the working principles of the Spherical Proportional Counters (SPCs). First, we start with an introduction to gaseous detectors and then we cover the specificities of the SPCs.

3.1 Introduction to gaseous particle detectors

3.1.1 Working principle

The gaseous particle detectors were invented in 1908 by E. Rutherford and H. Geiger [63]. They consisted of a volume filled with gas between an anode and a cathode. There are three modes for a gaseous detector, which depend on the high voltage (HV) applied on the anode: the ionization chamber, the proportional chamber and the Geiger-Muller counter. The ionization chamber mode uses low voltages producing low electric fields, which does not allow charge multiplication; the output signal is proportional to the charges from the primary ionization. The proportional counter mode operates in higher voltages and allow for a charge multiplication between 10^2 and 10^5, but generally 10^3. The output signal is also proportional to the charges produced during the primary ionization. The Geiger counter mode operates at even higher voltages than the proportional mode, inducing a strong electric field in the gas volume. As a result the charge multiplication reaches 10^6-10^8, but the Geiger mode loses the primary ionization dependence for the amplitude of the signal output.

When an incident particle interacts in the gas, it can deposit its energy through different processes depending on the particle and the gas: producing radiation, heat and/or ionizing the gas. The number of charges produced by the ionization process, called the primary ionization, is proportional to the total energy deposited in the gas. Thus, the estimation of the ionization energy is a good estimation of the energy deposited by the incident particle.

All interactions have an ionization yield, or quenching factor, which is the ratio of the mean ionization energy to the total kinetic energy of the incident particle. Depending on the incident particle (e.g. neutron, gamma), and respective target particle (e.g. electron or nucleus), the quenching factor will be close to 1, for electronic recoils, and smaller than 1 for nuclear recoils.

The primary electrons will drift toward the anode, and depending on the mode, proportional or Geiger, they will reach a high intensity field region, where each primary electron will gain enough kinetic energy between each collision that they can further ionize the gas. For each primary electron, hundreds or tens of millions of secondary ionizations take place, allowing very small signals (corresponding to single primary ionization electrons) to be amplified and detected thanks to the avalanche amplification process. For more details about gaseous detectors, the reader is encouraged to review [64].

3.1.2 Particle interactions in a gas

Different particles will create ionization signals in different ways. These are summarized in this section.

Charged particles

Charged particles interact with the electronic cloud of the gas atoms. By interacting with the electrons, charged particles lose energy in different ways.

Ion-electron pairs creation take place when the charged particle interacts with the electronic cloud of an atom, where the electron kinetic energy is equal to the energy deposited in the gas by the charged particle minus the ionization potential of the atomic electron.

Charged particles can excite an atom, which in turn releases a photon. The emitted photon can in turn ionize the gas, depending on the quencher concentration in the gas. The quenching gas, in general hydrocarbon molecules, prevents uncontrolled discharging.

Bremsstrahlung radiations can be created by β decays of the copper detector shell and lead shielding, which produce Bremsstrahlung γ. These radiations can be a substantial contamination as they can cross larger depth of material.

Heavy ions include all charged particles that are more massive than electrons. These particles can interact with the nuclei of a gas mixture through scattering, whose ionization is quenched.

Photons

Photons are neutral radiations, which interact primarily with electrons. Then, the electrons deposit their energy in the gas. The different processing involving photons energy loss are Compton scattering and photoelectric effect. The processes become dominant based on the energy of the photon and the atomic number of the target.

Compton scattering consists of a photon scattering off of an electron from an atom. The maximum energy transfer through Compton scattering takes place when the photon back scatters.

The photoelectric effect consists in the absorption of a photon by an atom, which in turn ejects an electron from the atomic cloud. The energy of the outgoing electron is equal to the energy of the incoming photon minus the binding energy of the atomic electron.

Finally, the pair, or electron-positron production has an energy threshold of 1.022 MeV, which is the sum of the masses of the electron and positron created. In the presence of a Coulomb field, like a nucleus of an atom, a photon is absorbed and it produces an electron-positron pair.

Neutral particles

In the hundreds of keVs up to MeVs the principal mechanism of energy loss by neutrons is elastic scattering off of nuclei. In this scenario, a small portion of the neutron energy is transferred to the recoiling nucleus (few keV) and is scattered with a certain angle from its initial trajectory. A neutron can also undergo inelastic scattering with a nucleus, which lead to a nucleus in an excited state followed by radiation. Neutrons can undergo capture from an atomic nucleus followed by an electromagnetic radiation.

Within the tens of MeV region, neutrinos scatter off of nuclei, through coherent elastic neutrino-nucleus scattering. There are many other interactions involving neutrinos, they will not be discussed in this document.

WIMPs scatter off of nuclei and create a nuclear recoil depositing energy through ionizations.

In the three cases mentioned above, it is the induced nuclear recoil that is the only signal output from the interaction, where the ionization energy is quenched in comparison to the total energy deposited in the gas.

3.2 Principle of SPC

This section describes the Spherical Proportional Counters, their working principle and their properties, which are common to all SPCs and independent of the size and gas used.

3.2.1 Description

SPCs consist in a grounded metallic spherical shell filled with gas [8]. At the center of the sphere, a small spherical electrode is held at high positive voltage ($\sim$ 700-2500 V) and used to read out signals. Particles are detected by the ionization charge that they deposit. The size of the detectors vary depending on their purpose, with typical diameters ranging from 15 cm to 140 cm. The size of the sensor varies as well from 1 mm to 16 mm of diameter. The sensor is kept at the centre of the sphere by a grounded rod which carries an HV wire, leading to an electric field that goes approximately as $1/\mathrm{r}^2$. We distinguish two regions in the electric field along the radius of the SPC. The main region of the volume, where the primary electrons are created, is the drift region, and a smaller region in the vicinity of the anode, where the electric field is large and the charge multiplication takes place.

When an ionizing particle interacts in the gas, it creates a cloud of "primary ionization" (e^-/ion pairs). The electrons then drift towards the sensor within a few hundreds of microseconds, for a SPC of 30 cm of diameter. They reach the high intensity electric field region within few hundreds of micrometers from the electrode, while the ions drift toward the surface of the sphere, see Figure 3.1.

Near the sensor, the electric field is strong enough for the electrons to gain enough kinetic energy to ionize more gas between each collision, which leads to an avalanche amplification process, known as a Townsend avalanche [65]. Thanks to this avalanche process, a single primary electron reaching the vicinity of the anode generates thousands of secondary e^-/ion pairs, allowing signals resulting from a single primary electron to be detectable.

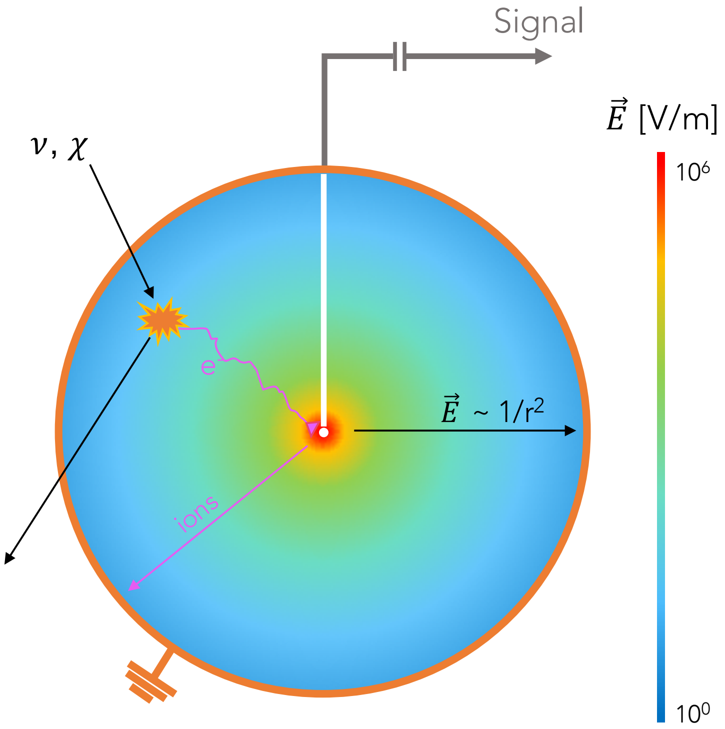

Figure 3.1: Cartoon showing the working principle of the SPC, with an ionizing incident particle interacting in the gas and the primary electrons drifting towards the anode. After the secondary ionization in the avalanche region the secondary ions are drifting towards the surface of the sphere, inducing a signal on the sensor. The $\vec{E}$ gradient is indicative and does not represent an accurate field, it is here to show the different zones of the electric field in the SPC: high and low $\vec{E}$ regions.

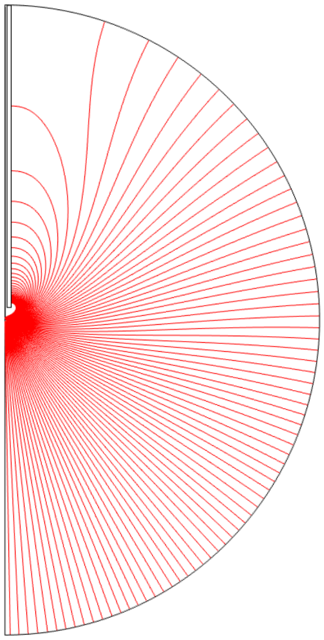

Figure 3.2: Electric field lines for a spherical proportional counter with a simple sensor design using the COMSOL software [68]. Courtesy of F. Vazquez de Sola Fernandez [67].

As shown in Figure 3.2, the electric field is disturbed by the presence of the rod. In order to resolve this anisotropy of the electric field lines in the northern hemisphere, a second electrode is added close to the sensor. This second electrode nicknamed an “umbrella” as it is designed to restore a near $1/\mathrm{r}^2$ field in the north hemisphere. Figure 3.3 shows two sensor designs: a simple one with no umbrella and a sensor with a bakelite umbrella that was used to estimate the single electron response of our detectors [66].

The gases used in the SPCs are mixtures of noble gases with another gas called a quencher gas. Noble gases are used because they do not form chemical bounds with other atoms, thus they allow the charges left by an incident particle to drift unimpeded toward the electrode. Noble gases used in the NEWS-G collaboration are mainly argon, neon, and helium. The role of the quencher is to absorb any UV radiation to slow down the avalanche and prevent sparks (discharging). The quencher used is CH_4, with a concentration of 2% of the total volume.

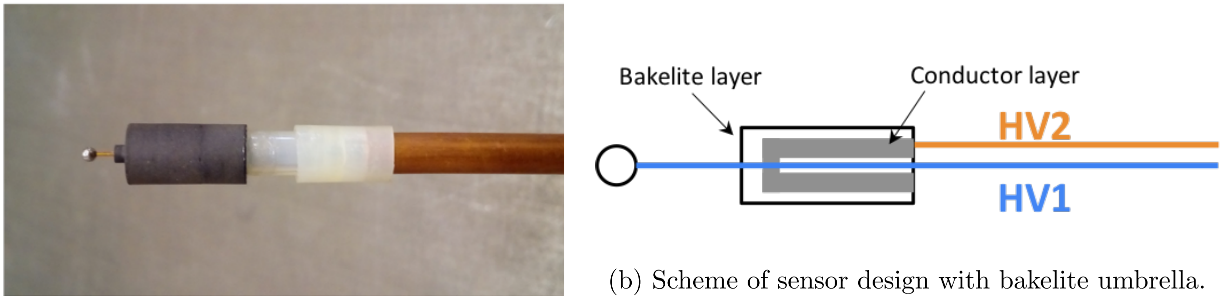

(a) Sensor design with bakelite umbrella.

(b) Scheme of sensor design with bakelite umbrella.

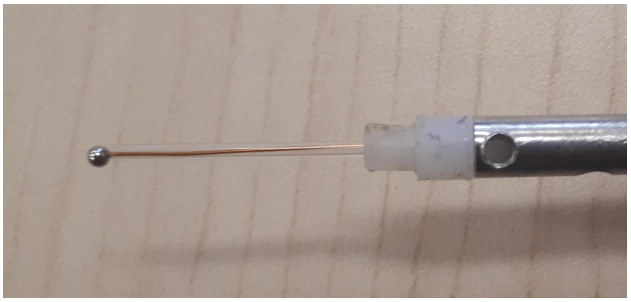

(c) “Simple” sensor design: no umbrella.

Figure 3.3: Different sensor designs.

3.2.2 Pulse formation

When the avalanche takes place and secondary ion/e- pairs are created, the electrons are collected within ns by the anode while the ions drift back toward the outer shell of the detector. As they move away from the avalanche region, the secondary ions induce a charge on the anode, described by the Shockley-Ramo theorem [69]. The induced charge is integrated by the preamp and a pulse is formed on the digitizer.

J. Derré developed the formalism to calculate signal induced by drifting ions in a SPC [71]. We consider the ideal case of a grounded metallic sphere of radius r_1 with a small electrode of radius r_2 in its center, kept at a voltage V_0. First we want to estimate the electric field in the SPC and then estimate the change of charge induced on the electrode by the drifting secondary ions.

The electric field can be found by using Gauss' law and the spherical symmetry. The voltage can be calculated from the electric field and depends on the charge, Q, contained in the electrode and the permittivity of the gas, ϵ:

$$V(r) = V_0\rho\left(\frac{1}{r} - \frac{1}{r_1}\right). \tag{3.1}$$

with $\frac{1}{\rho} = \frac{1}{r_2} - \frac{1}{r_1}$ and $V_0 = \frac{Q}{4\pi\epsilon\rho}$. Therefore, we can re-write the electric field in terms of V_0 as well:

$$E(r) = -\nabla V = \frac{V_0 \rho}{r^2} \tag{3.2}$$

Now, we want to know the current induced on the anode by the drifting ions. By using the Shockley-Ramo theorem [69], we know the change in charge induced by the drifting charges:

$$I_{ind} = \frac{dQ_{ind}}{dt} = -q_i \frac{E(r)}{V_0} v_i \tag{3.3}$$

with I_{ind} the current induced, Q_{ind} the charge induced, q_i the ions charge and v_i the ions' velocity. The Shockley-Ramo theorem can be interpreted with the conservation of energy [70]. The work done on the moving secondary ions comes from the energy stored in the electric field.

We can estimate the ions' velocity by using their mobility, μ, in the gas:

$$v_i = \mu E(r) \qquad \text{with} \qquad \mu = \frac{\mu_0}{P}$$

μ_0 is the mobility of the ions in the normal conditions of pressure and temperature and P is the pressure of the gas mixture. By substituting $E(r)$ and v_i in 3.3 we obtain:

$$dQ_{ind} = -q_i \, \frac{\rho^2 \mu}{r^4} \, V_0 \, dt \tag{3.4}$$

We want to re-write 3.4 to have the time contribution appear. By definition, we know that:

$$\mu = \frac{1}{E(r)} \frac{dr}{dt} \tag{3.5}$$

By substituting $E(r)$ and μ, we find that $\alpha \, dt = r^2 dr$, with $\alpha = \mu_0 V_0 \rho / P$. When we integrate over the time and the distance: the ions leave the surface of the sensor, r_2, at time $t = 0$ and reach the distance r from the sensor at time t.

$$\int_0^t \alpha \, dt = \int_{r_2}^{r} r^2 dr \tag{3.6}$$

Then, we can express r in terms of the time, t:

$$r = (3\alpha t + r_2^3)^{1/3} \tag{3.7}$$

By substituting 3.7 in 3.4 then we have the change in the charge and the current induced on the electrode:

$$I_{ind}(t) = \frac{dQ_{ind}}{dt} = -q_i \rho \alpha \, (3\alpha t + r_2^3)^{-4/3} \tag{3.8}$$

If we integrate between 0 and t, then the charge induced on the electrode is:

$$\begin{aligned} Q_{ind} &= \int_0^t -q_i \rho \alpha \, (3\alpha t + r_2^3)^{-4/3} dt \\ &= -q_i \rho \left[\frac{1}{r_2} - \frac{1}{(r_2^3 + 3\alpha t)^{1/3}} \right] \end{aligned} \tag{3.9}$$

Considering the time t_{max} when the ions reach the surface of the detector, r_1:

$$t_{max} = \frac{r_1^3 - r_2^3}{3\alpha} \tag{3.10}$$

Then the induced charge on the sensor is: $Q_{ind} = -q_i$.

The induced current is convolved with the response of the pre-amplifier:

$$f(t) = G_p e^{-t/\tau} \tag{3.11}$$

where τ is the preamplifier decay constant (47 μs for a Canberra 2006 and 140 μs for a CREMAT) and G_p is the gain of the preamplifier in V/C. Understanding the signal formation is primordial, it allows a proper extraction of the physical parameters we are interested in. The processing and analysis of the pulses will be described in Section 3.3.

3.2.3 Response of the detector

In this section we discuss how the statistics of primary and secondary ionization affect the detector response.

The number n of primary electrons created is subject to statistical fluctuation around an expected number of primary electrons:

$$\mu_{E_{ee}} = \frac{E_{ee}}{W(E_{ee})}, \tag{3.12}$$

with E_{ee} the observed energy in our detector (through ionization) and W, the mean ionization energy necessary to create an electron-ion pair. W depends on the energy deposited, it is often modelled with an asymptotic function to the minimum ionization potential of the medium. With increasing energies, W rapidly reaches a constant value, which is generally of the order of few tens of eV.

The observed number of events in particle scattering experiments is a particular case of the Binomial distribution in the limit that the number of incident particles N is large and the probability p of interaction and detection is small. It is generally assumed that the successive ionizations are independent events, and thus, the number of primary ionization electrons follows a Poisson distribution:

$$P_{\text{Poisson}}(n \mid \mu_{E_{ee}}) = \frac{\mu_{E_{ee}}^{n}}{n!} e^{-\mu_{E_{ee}}}, \tag{3.13}$$

However, U. Fano proposed that the primary ionization fluctuations from charged particles were sub-Poissonian [72]. The variance of the fluctuations, σ_N^2, is smaller than the variance expected for a Poisson process by a factor F, the “Fano factor”:

$$\sigma_N^2 = \frac{F}{\mu_{E_{ee}}} \tag{3.14}$$

In the case of a Poisson process F = 1, while for ionization fluctuations F < 1. However, it is important to point out that for higher energies, the effect of the Fano factor is obscured by the energy resolution.

In [73] a solution to include the Fano factor to the primary ionization is proposed, by using the COM-Poisson distribution.

The avalanche process is modelled so that the probability of ionization of a secondary electron is independent of its past interactions. Experimental measurements showed that the number of secondary electron/ion pairs follows the Polya distribution [74], [75], [76], [77]:

$$P_{Polya}(S) = \frac{1}{\langle G\rangle}\frac{(1+\theta)^{1+\theta}}{\Gamma(1+\theta)}\left(\frac{S}{\langle G\rangle}\right)^{\theta} \times \exp\Big(-(1+\theta)\frac{S}{G}\Big) \tag{3.15}$$

where S is the number of secondary electrons for 1 primary electron entering the avalanche region, G is the mean gain and θ controls the shape of the distribution. The impact of such parameter is shown in Figure 3.4. Each electron's avalanche is considered independent from the others, thus the probability of creating S secondary electrons given N primary electrons reaching the avalanche region is given by the Nth convolution of the Polya distribution:

$$\begin{aligned} P_{\text{Polya}}(S \mid N) = \frac{1}{G}&\left(\frac{(1+\theta)^{(1+\theta)}}{\Gamma(1+\theta)}\right)^{N}\left(\frac{S}{G}\right)^{N(1+\theta)-1} \\ &\times \exp\left(-(1+\theta)\Big(\frac{S}{G}\Big)\right) \\ &\times \prod_{j=1}^{N-1} B(j+j\theta, 1+\theta) \end{aligned}$$

For enough large values of N, the resulting convolution of Polya distributions tend to follow a Gaussian distribution.

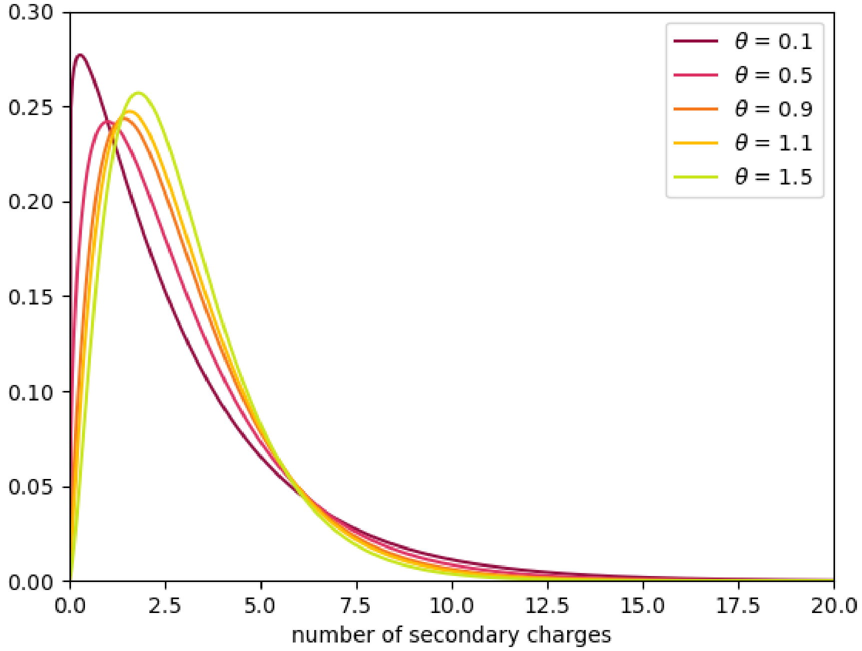

Figure 3.4: Examples of Polya distributions, which demonstrate the impact of theta on the overall shape distribution.

3.3 Events/pulses analysis

The automation of the pulse processing was performed by former Ph.D student F. Vazquez de Sola Fernandez. For more details the reader is encouraged to read [67].

The signal coming out of the preamplifier is proportional to the energy deposited in the detector. Thus, the amplitude of a pulse provides an estimate of the energy deposited in the gas. The second parameter that we want to extract is called the rise time: it is the time that it takes for a pulse to go from the baseline to the maximum of its height. We calculate it as the time difference between 90 % and 10 % of the pulse amplitude. The rise time is a measure of the dispersion of the arrival time of the primary electrons, which depends on the radial position of the event relative to the sensor and the energy deposited. For point-like events, the energy is deposited at a “single” location, the electrons diffuse as they drift towards the sensor; the further away from the electrode, the longer it will take all primary electrons to reach it, the larger the dispersion and thus the longer the rise time. As a result, the rise time is related to the drift distance, and thus, this quantity can be used

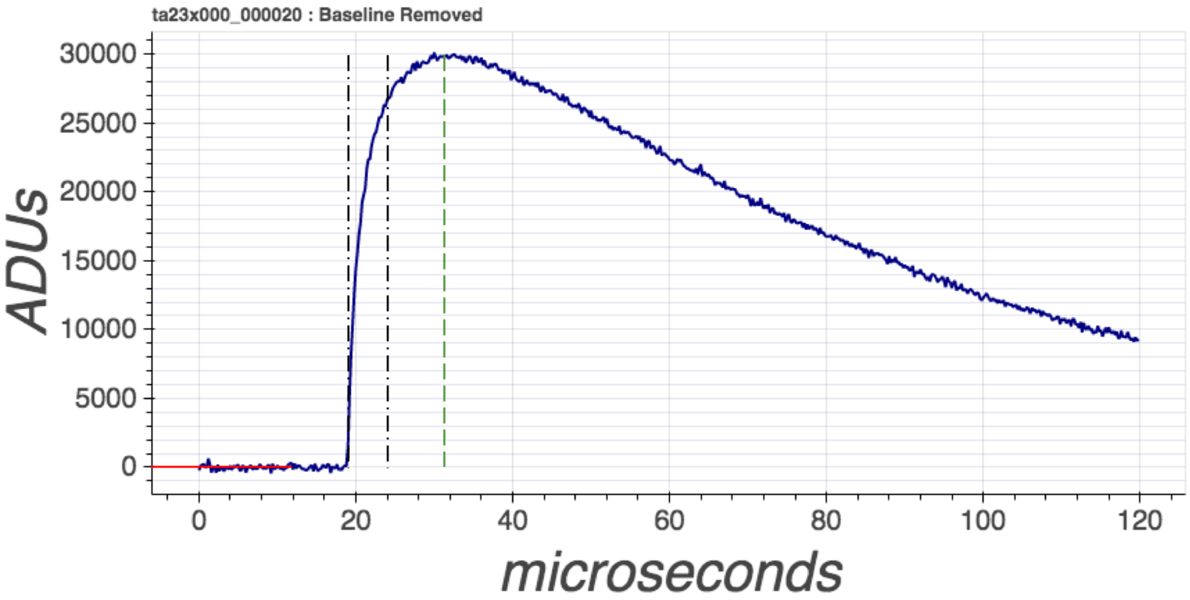

Figure 3.5: Example of raw pulse recorded with an SPC detector. The red line shows the averaged baseline, the two dashed black lines show the rise time: computed between the times at which the pulse reaches 10 and 90 % of its amplitude. The green dashed line shows the maximum of the pulse.

to identify surface from volume events. For track events, the particles deposit their energy along a trajectory in the gas. The rise time of such events is no longer dominated by the diffusion of the primary electrons, but rather depends on the different locations of the event trajectory. Indeed, for track events the rise time becomes the difference in drift time between the closest and furthest parts of the trajectory relative to the anode. This, leads to longer rise times than for point-like events, as a result we can discriminate track events from point-like events based on their rise times.

The method used to process the data is called the Double Deconvolution, as it deconvolves both the electronic response and secondary ions drift, it corrects for the ballistic deficit and increases our sensitivity to short rise times. The ballistic deficit is the impact of the preamplifier decay time on the amplitude of the signal, which depends on the rise time. The method consists in:

1. Raw pulses are smoothed by a running average to diminish the noise amplification before the deconvolution. Figure 3.5 shows an example of raw pulse.

2. Deconvolution of the preamplifier response function.

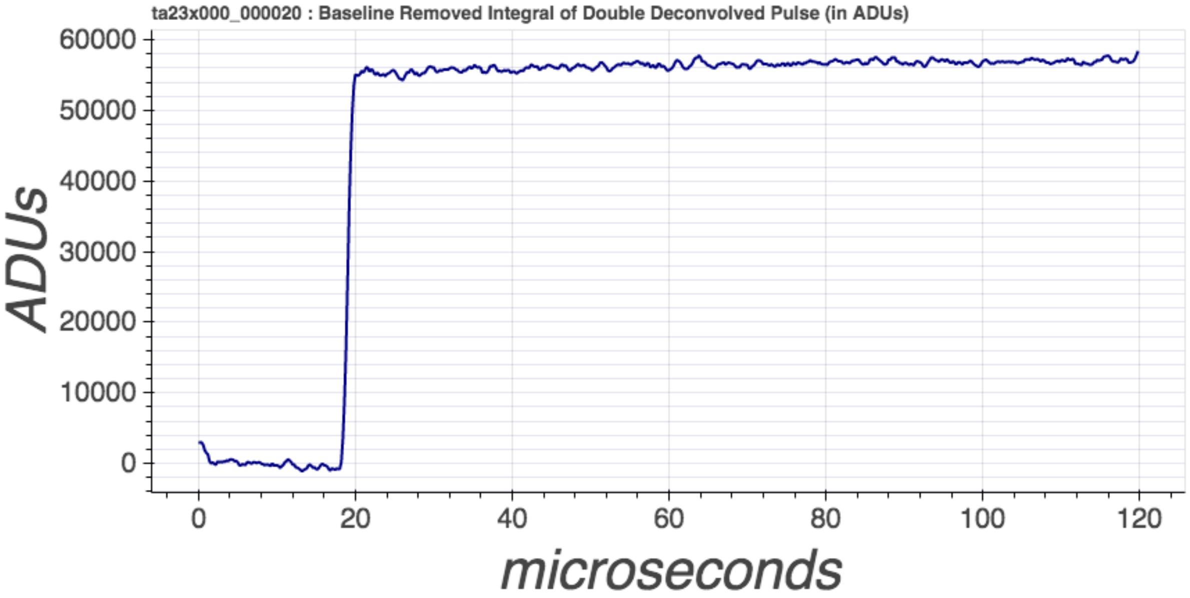

Figure 3.6: This pulse corresponds to the integrated and treated (double deconvolved) pulse from Figure 3.5.

3. Deconvolution of the ion-induced current, using division in Fourier space.
4. The resulting pulse is integrated and has an amplitude directly proportional to the energy deposited, see Figure 3.6.

From that method, the energy and the rise time can be extracted from the pulse, along with other parameters like:

- Width: Full-Width Half Maximum of the pulse.
- Time since last event.

Plotting these parameters against each other can make concentrations of events appear, and allow for easy background rejection. In particular, plotting the rise time as a function of the energy allows to identify volume events and surface events, and track events from point-like events. Figure 3.7 shows the rise time as a function of energy of data taken with a 15 cm diameter filled 700 mbar of neon, with HV on the sensor of 850 V and on the umbrella 0 V. A source of ^{55}Fe was placed at the south pole and ^{37}Ar was injected into the sphere. ^{55}Fe emits X-rays with mean energy of 5.9 keV

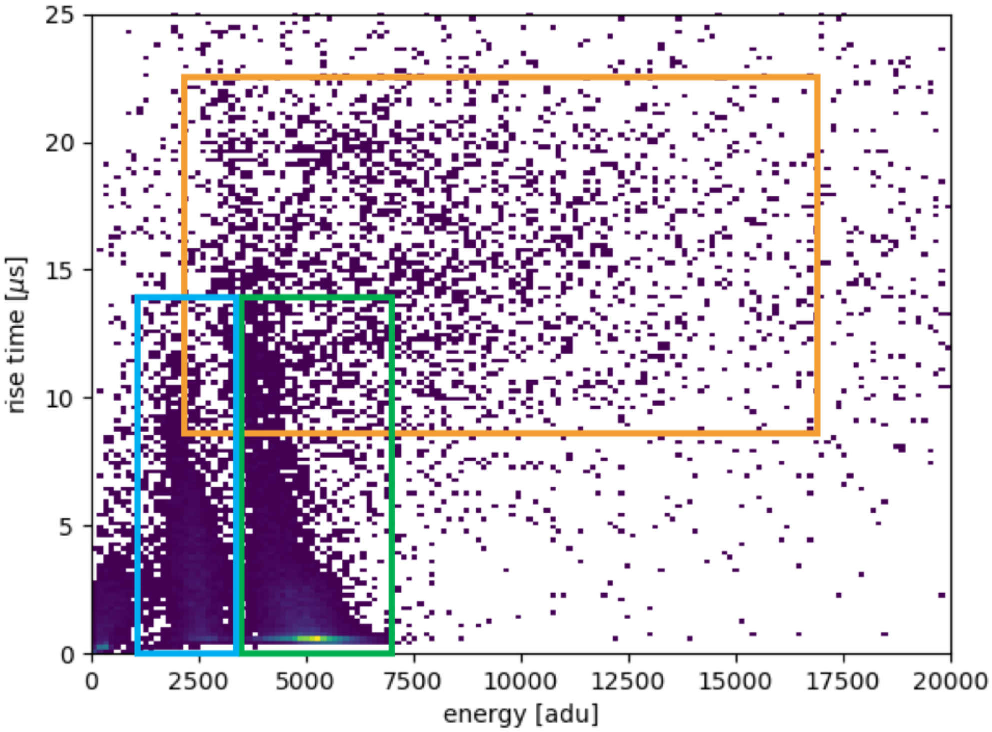

Figure 3.7: Data taken with a 15 cm diameter SPC filled with 700 mbar of neon. The voltage applied on the sensor was 850 V and on the umbrella 0 V. The orange box shows track events, with high rise time, which are muons crossing the detector; the green box shows the ^{55}Fe event (point-like events); the blue box shows the 2.82 keV peak of the ^{37}Ar.

and ^{37}Ar emits X-rays at two energies: 270 eV and 2.82 keV. Different populations of events are within colored boxes: the orange box shows the high rise time events corresponding to muon track events; the green box shows the ^{55}Fe events; the blue box shows the 2.82 keV peak of the ^{37}Ar. By applying a rise time cut we can extract the ^{55}Fe and ^{37}Ar energy spectrum from these data.

3.4 Detectors

Spherical proportional counters were mainly developed for Dark Matter searches, and in particular largely focused on a favored class of low-mass particle candidates Weakly Interacting Massive Particles (WIMPs). The direct detection of such particles relies on the detection of nuclear recoils of few keV generated by elastic scatterings on a target.

The NEWS-G collaboration developed two detectors for dark matter searches, this section is pro-

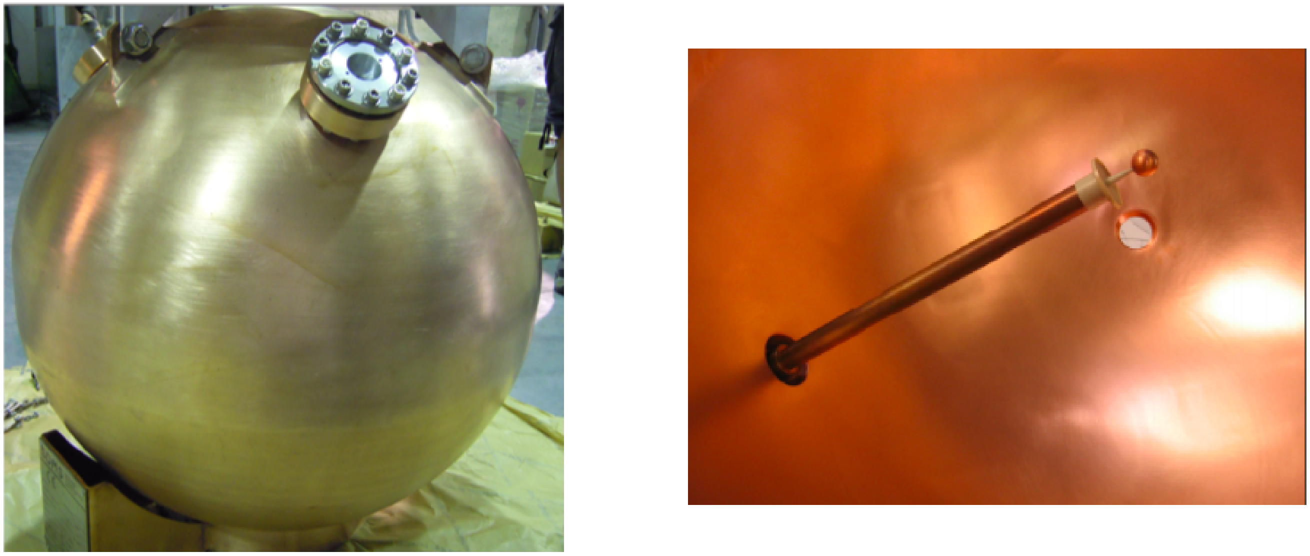

Figure 3.8: SEDINE detector and inside view of the detector.

viding a brief overview of both detectors.

3.4.1 SEDINE

In 2017, the SEDINE detector was installed at the Laboratoire Souterrain de Modane (LSM) in France, for a long-running dark matter data taking. The SPC outer shell, the rod and the sensor were made of pure copper. The detector was a 60 cm diameter SPC, connected to a copper tube to feed HV to the electrode and the handling gas system. The location of the laboratory, under the Fréjus Mountain, allowed to shield the detector from cosmic rays. At ground level, the secondary particles of cosmic rays are mainly high energetic muons, called "cosmic muons". Because of their energy, these particles can not be stopped by shielding, thus, the best protection is to install detectors underground. A compact shielding was developed in order to protect the detector against natural radioactivity.

- The first, or outer layer of the shielding is made of polyethylene bricks 30 cm thick. Its purpose was to thermalize neutrons induced by cosmic muons and stops part of the environmental γ background.
- The second, or middle layer is made of lead brick 10 cm thick. The purpose of this layer was

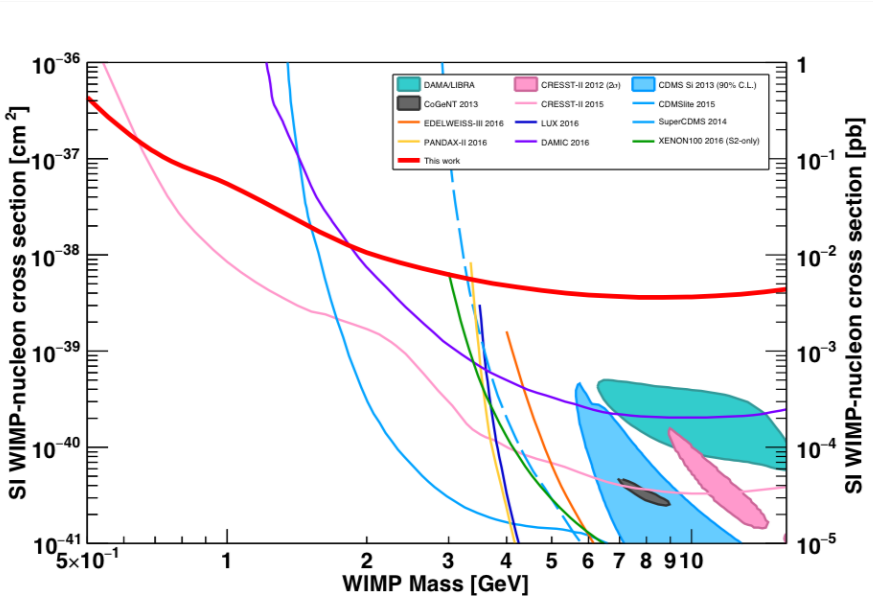

Figure 3.9: Constraints in the spin-dependent WIMP-nucleon cross section as a function of the WIMP mass. The results of the analysis of the data is shown in red [78].

to stop γ radiation from the rock walls: environmental background.

- The last, or inner layer is made of copper 5 cm thick. Its purpose was to stop γ radiations coming from the lead layer.

The collaboration released a new constraint in the spin-dependent WIMP-nucleon cross section [78] after taking data in 2017. Figure 3.9 shows the constraint set by the experiment in a new region below 0.6 GeV/c^2.

3.4.2 NEWS-G at SNOLAB

The next generation of detector for dark matter searches took into account areas of improvements from the SEDINE experience, and in particular optimize the background. For this, a new detector was developed, SNOGLOBE, and installed at SNOLAB, located at 2 km below the surface. This new location of the detector will help reduce the cosmic muon event rate compared to the LSM. A series of improvements were performed on the new detector:

- New SPC shell:

  - Made of low activity copper (C10100).
  - Larger detector: 140 cm of diameter and 10 mm thick in order to increase the target exposure.
  - 500 μm of pure copper was electroplated [79] onto the inner surface of the detector to remove contamination from the ^{210}Pb decay chain.

- A new sensor was developed, the achinos [80], in order to maintain the balance between charge amplification, high gain, and the strength of the electric field at high radial distances. This new sensor is made of a set of anode balls at equidistance from the center of the electrode, see Figure 3.11.

- New shielding, from outer layer to inner layer, see Figure 3.10:
  - A 40 cm thick polyethylene (PE) panels stops neutrons induced from entering the detector.
  - A layer of 25 cm of lead follows to protect against γ radiation.
  - A layer of 3 cm of Roman lead was used to shield the detector from ^{210}Pb contamination present in the previous layer of lead.

The development of the shielding was possible thanks to the work of former Ph.D. student A. Brossard who estimated the nature and distribution of the different backgrounds for the new experiment, using a Geant4 simulation [81]. For more details about the background estimation of SNOGLOBE the reader is encouraged to read [82].

The detector was commissioned during the summer 2019 at the LSM, without the PE shielding, using two gas mixtures, pure methane at 135 mbar and Ne+CH_4 at 1 bar. The analysis of the data in methane is on-going. The experiment was relocated at SNOLAB at the end of 2019. The installation was interrupted in 2020, due to the COVID-19 pandemic, and resumed in the spring 2021. The NEWS-G collaboration expects to take dark matter data at SNOLAB during this fall 2021.

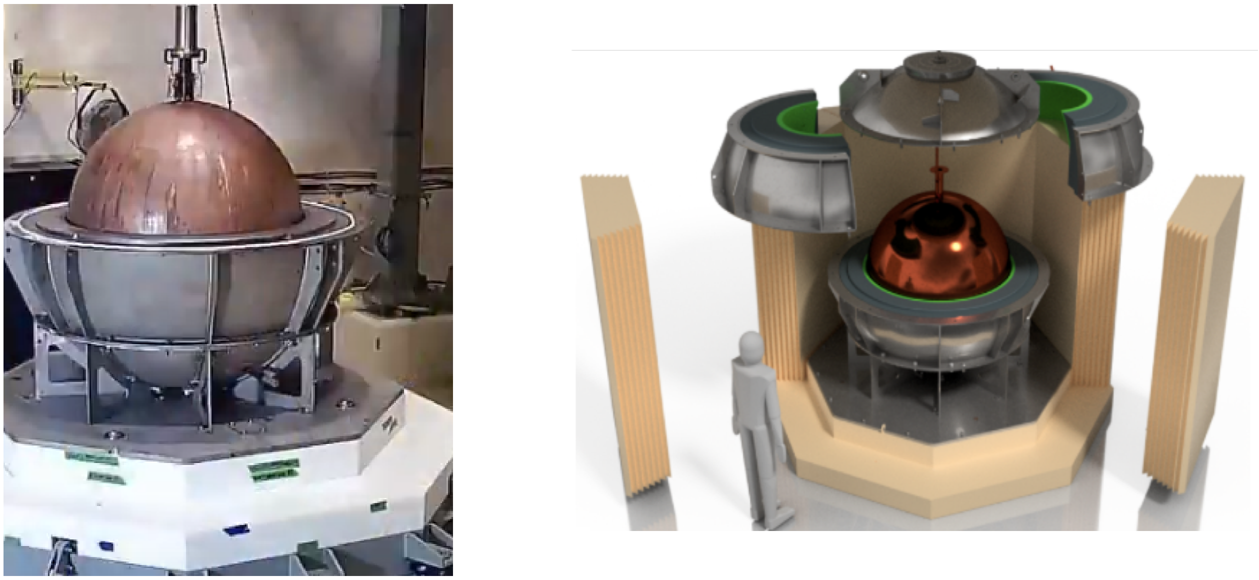

Figure 3.10: NEWS-G at SNOLAB. Left picture shows the installation of the detector inside of its let shielding. The right illustration shows the detector and the different layers of shielding, courtesy of K. Dering.

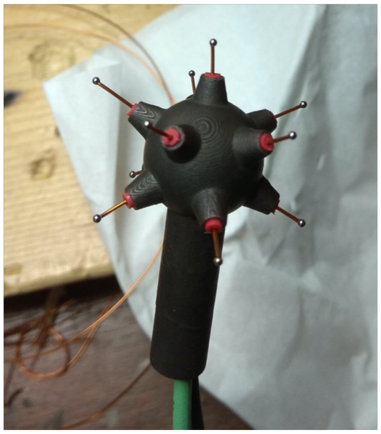

Figure 3.11: Picture of an achinos sensor. Courtesy of G. Savvidis, Ph.D. student.

Chapter 4

Quenching factor theory and experimental procedures

In this chapter, we will introduce two models that are widely used to describe energy loss from nuclear recoils in a medium: the Lindhard theory [83] and a Monte Carlo software called SRIM (Stopping and Range of Ions in Matter) [84].

As aforementioned, a WIMP or CEνNS neutrino interact in the gas producing nuclear recoils with small kinetic energy, of a few keV. The energy deposited in an ionization detector, such as a spherical proportional counter, can be calibrated with γ or X-ray sources of known energy. As mentioned in Section 3.1.2 these particles interact with electrons through Compton scattering or photoelectric effect, producing electrons depositing their energy in the gas. However, a nuclear recoil and an electronic recoil of the same energy do not produce the same amount of primary ionization. Hence, a nuclear recoil will appear "quenched" (less ionization energy deposited) than an electronic recoil of the same energy.

4.1 Model predictions for quenching factor

The observed ionization energy from a nuclear recoil does not represent the total kinetic energy of the recoil. Depending on the material, some of that energy will also be converted into heat or light. Certain detector technologies are sensitive to the energy deposited in the various channels, but spherical proportional counters are only sensitive to the ionization energy (since light and heat are not detected). We introduce the observed nuclear recoil energy, E_{ee}, in electron volts electron equivalent, eV_{ee}, as the nuclear recoil energy that is measured by ionization and is associated to the electronic recoil calibrations. The total kinetic nuclear recoil energy, E_{nr}, is expressed in electron volts nuclear recoil, eV_{nr}.

We introduce the nuclear quenching factor as the ratio of the observed energy, E_{ee}, to the total nuclear recoil energy, E_{nr}:

$$QF(E_{nr}) = \frac{E_{ee}}{E_{nr}} \tag{4.1}$$

We can note that the quenching factor depends on the nuclear recoil energy, and is expected to decrease with the energy.

The quenching factor allows the observed energy to be converted to the total nuclear recoil energy, which is the quantity of interest in detecting WIMPs or neutrino via CEνNS. Indeed, the limits set on dark matter cross sections depend on WIMP energy and thus on the total nuclear recoil energy deposited in the detector. As for detecting the CEνNS interaction, which is considered a counting experiment, the number of events observed above a given detection threshold is the important quantity. The rate depends on the quenching factor.

When it comes to describe the energy loss of nuclear recoils in a medium, the Lindhard theory developed in 1963, is often chosen as model [83]. A brief explanation of the model is provided following [83] [85] and [86]. After a particle interaction, a nuclear recoil dissipates energy by a series of atomic and electronic collisions before coming to a stop. In the Lindhard model, it is assumed that the incoming recoiling nucleus and the target atoms have the same atomic and mass numbers. A nuclear recoil dissipating energy involves a competition between energy transfer to atomic electrons, η, and energy transfer to atomic motion, ν, so that the total nuclear recoil energy: $E_{nr} = \eta + \nu$. A fraction of the energy is transferred to atomic motion as heat, while the remaining energy is transferred to atomic electrons and can be observed as ionization or scintillation. The nuclear stopping power includes a screened Coulomb potential to model the nuclear scattering, which uses a Thomas-Fermi screening function.

The fraction defined as ionization reduction factor, or nuclear quenching factor due to losses to the nuclear stopping power is:

$$f_n(E_{nr}) = \frac{\eta(E_{nr})}{E_{nr}} = \frac{\eta(E_{nr})}{\eta(E_{nr}) + \nu(E_{nr})}. \tag{4.2}$$

The average energy transfer to electron, $\bar{\eta}$, and atomic motion, $\bar{\nu}$, depends on the electronic and nuclear stopping powers respectively. They are obtained by integrating over all nuclear recoil energy possibilities. By writing the integral explicitly [86], we have:

$$f_n(E_{nr}) = \frac{\int_0^{E_{nr}} (dE/dx)_{el.}\, dE}{\int_0^{E_{nr}} (dE/dx)_{el.} + \int_0^{E_{nr}} (dE/dx)_{nucl.} dE} \tag{4.3}$$

In their paper, Lindhard *et al.* [83] described the stopping powers as a function of a scaling of the energy, ε, and stopping cross sections. Thus, if we re-write f_n, we have:

$$f_n(E_{nr}) = \frac{\bar{\eta}(\varepsilon)}{\varepsilon} \tag{4.4}$$

where $\bar{\eta} = \varepsilon$ - $\bar{\nu}$, and the average energy transfer to atomic motion, after integrating over all possible nuclear recoil energies, has a numerical solution parametrized by Lindhard *et al.* [83] as:

$$\bar{\nu}(\varepsilon) = \frac{\varepsilon}{1 + kg(\varepsilon)} \tag{4.5}$$

The ionization energy reduction factor, or quenching factor, f_n, as a function of nuclear recoil energy can then be expressed as:

$$f_n = \frac{kg(\varepsilon)}{1 + kg(\varepsilon)} \tag{4.6}$$

with Z the nucleus atomic number, A the mass number, $\mathrm{k} = 0.133\mathrm{Z}^{2/3}\mathrm{A}^{-1/2}$, $\varepsilon = 11.5E_r\mathrm{Z}^{-7/3}$ and $g(\varepsilon)$ was fitted by $g(\varepsilon) = 3\varepsilon^{0.15}+0.7\varepsilon^{0.6}+\varepsilon$, parametrization provided by [86].

In Lindhard's model, there are four approximations:

1. When ionized electrons scatter off of nuclei they are not energetic enough to produce nuclear recoils.
2. The atomic binding energy of electrons is negligible.
3. The energy transfer to electrons is much smaller than the energy transfer to atomic motion.
4. Electronic ($\bar{\eta}$) and atomic ($\bar{\nu}$) collisions are treated independently.

Lindhard's model is known to be quite successful at modelling the energy loss of nuclear recoils in solids, at the same time it is known that its validity at low energies is uncertain. In a second paper Lindhard, Scharff and Schiott [87] state that at low energies, $\varepsilon \lesssim 10^{-2}$, corresponding to nuclear recoil energies less than few keV_{nr}, the nuclear scattering and stopping becomes questionable. The reason behind this statement, is that the Thomas-Fermi treatment is a "crude approximation" [87] when the recoiling nucleus and atom do not come close to each other. Additionally, Lindhard's model does not take into account the density of the material investigated.

A numerical simulation package is also available to estimate quenching factors, the Transport of Ions in Matter (TRIM) from the Stopping and Range of Ions in Matter software package (SRIM) [84], introduced in 1985. SRIM approximates the travel of the nuclei with binary nuclear collisions, hence, assuming each collision to be independent and their trajectory to follow a straight path between each collision. The energy of the incoming nuclei is dissipated through nuclear and electronic energy losses. The stopping power to nuclear motion implements a universal screening potential, while a semi-empirical approach is considered for the electronic stopping power. One important assumption is that electrons are treated as a free electron gas in the electronic stopping power model. The nuclear and electronic stopping powers are assumed independent. The package was developed for solids, hence, a phase correction is applied when calculating the stopping powers in gases. For the case of compound targets SRIM uses Bragg's rule [88], which sums linearly the stopping powers of all atoms in the molecule, and uses the the Core and Bond (CAB) method to correct for the chemical bonds.

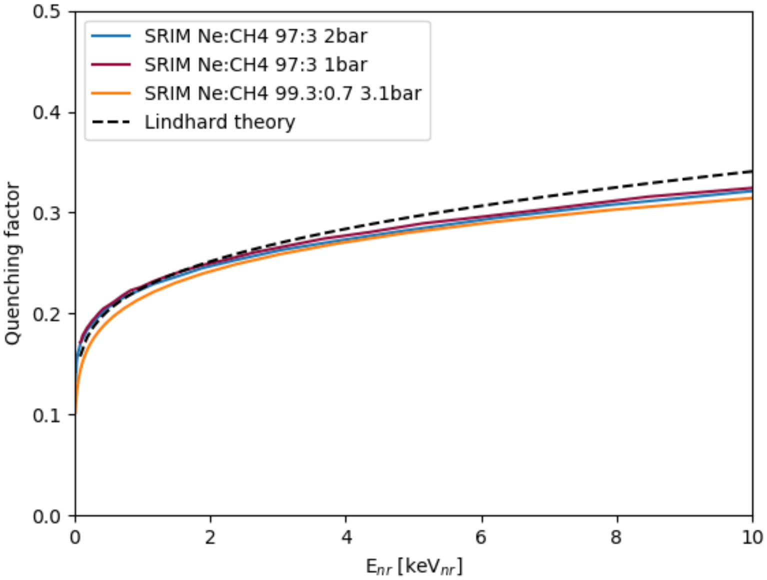

Figure 4.1: Comparison of the expected quenching factors from Lindhard and SRIM using different pressures. The Lindhard theory does not take into account the density of a medium. The model used by SRIM takes into account the density of the medium, we show that the quenching factor predictions are not impacted by the different pressures.

Figure 4.1 shows a comparison of the expected quenching factor in neon by Lindhard theory as well as for three SRIM simulations: Ne:CH_4 (3 %) at 1 and 2 bar and Ne:CH_4 (0.7 %) at 3.1 bar. From this figure, we can see that the pressure is not expected to have a significant impact on the QF returned by SRIM, of the order of 1 % along the energy range covered. Also, SRIM and Lindhard are in reasonable agreement at low energies (below 4 keV_{nr}) , after the discrepancy reaches about 6 % between Lindhard and SRIM (Ne:CH_4 (3 %) 2 bar).

4.2 Experimental methods

In this section, we review the present methods to extract the quenching factor, as well as proposed procedures for future quenching factor experiments.

4.2.1 Neutron scattering

A common method to extract the quenching factor is to use a neutral projectile, such as a neutron, to mimic the momentum transfer of a WIMP or neutrino. Neutron beams can be produced using an ion beam interacting with an appropriate target, based on the neutron energy of interest.

From kinematics we can calculate the total nuclear recoil energy from the neutron energy and the scattering angle. The scattered neutrons are detected by a "backing detector" that is installed after the target so that the scattering angle is known. The neutron energy is known from the beam and target parameters and can be measured precisely with time of flight. More precise measurement of the neutrons energy is possible, by directly probing the beam. The total nuclear recoil energy is thus:

$$E_{nr}(\theta_s, E_n) = 2E_n \frac{M_n^2}{(M_n + M_T)^2} \left(\frac{M_T}{M_n} + \sin^2\theta_s - \cos\theta_s \sqrt{\left(\frac{M_T}{M_n}\right)^2 - \sin^2\theta_s} \right), \tag{4.7}$$

where θ_s is the scattering angle of the neutron regarding its initial trajectory (beamline), E_n is the incident neutron energy, M_n is the neutron mass and M_T is the target mass (nucleus).
Figure 4.2 show the quenching factor measurements conducted with such an experiment set up.

4.2.2 Ion irradiation

It is possible to measure the quenching factor using an ion beam. In [10], the quenching factor of α particles in ^{4}He+C_4H_{10} (5 %) was investigated. The α particles were generated between 1 up to 50 keV using an Electron Resonance Ion Source. With this set up, the incident ions mimick the recoils induced by elastic scattering in the detector. The result of such experiment is shown in Figure 4.3.
In [11], the authors use the COMIMAC facility, which is a table-top ion and electron beam, com-

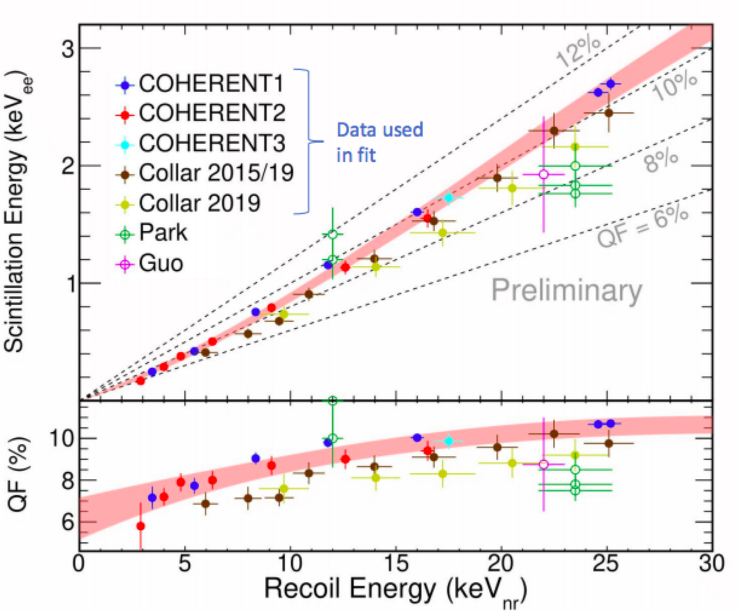

Figure 4.2: Preliminary results of the quenching factor measured by the COHERENT experiment on CsI [89]. Five measurements were performed using scattering neutrons, which show good agreement with each other.

posed of a COMIC ion source (Compact Microwave Coaxial) and a volume target. The beam is able to produce energies within tens of eV up to 50 keV. In the experiment, protons with kinetic energies ranging from 1.5 keV up to 25 keV were produced and aimed to a gas mixture composed of C_4H_{10} + CHF_3 (50 %).

4.2.3 Neutron capture

Neutron capture can be a tool to measure the quenching factor at some recoil energies. The reaction is inelastic and consists iof a nucleus absorbing a free neutron, which creates a heavier isotope in an excited state. The heavier isotope decays by emitting one or multiple γ-rays, which produces a nuclear recoil of the order of 1 keV$_{\mathrm{nr}}$ for γ-rays of $\sim$ MeV [90].

The nuclear recoil energy, E$_{nr}$, depends on the energy of the emitted γ-ray and the target mass nucleus, M, [91]:

$$E_{nr} = \frac{E_\gamma^2}{2M} \tag{4.8}$$

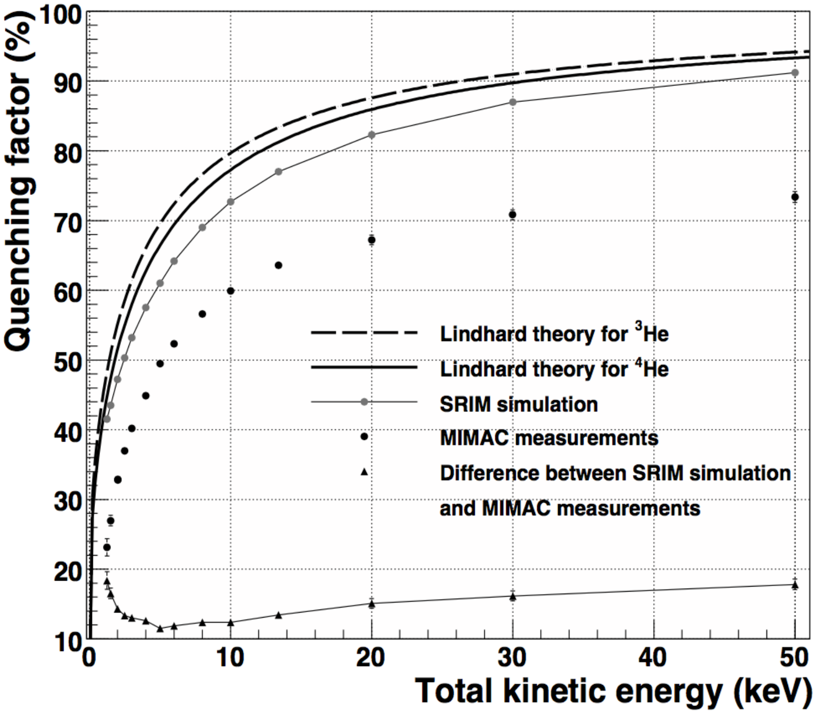

Figure 4.3: Quenching factor from [10] of helium ions in helium gas for different pressures. Here we can notice the disagreement between the simulation and the data.

A study of measuring the quenching factor in neon and argon gas mixtures using this technique was performed with an SPC, by D. Durnford [91]. The study investigated the nuclear recoil spectra of neutron capture in the two gas targets. The nuclear recoil energy produced were mostly below 2 keV$_{\mathrm{nr}}$. The conclusion of this work, was that using neutron capture as a method to extract the quenching factor for these two gases was not feasible due to the lack of features of the energy spectra of both neon and argon, and also the rather broad energy resolution of the SPC detector. In [91] is pointed out that this technique might be used for other targets and other detector technologies. For example, neutron capture with hydrogen was performed by NEWS-G collaborators at the Aristotle University of Thessaloniki using the reaction ^{1}H(n, γ)^{2}H. The experiment was conducted with an SPC filled with He + CH4 (10 %), the quenching factor of ^{2}H in the gas mixture is: QF = 0.82 at E_{nr} = 1.33 keV$_{\mathrm{nr}}$ [92] (unpublished results).

4.2.4 Estimation using electron and ion W-values

A new method to extract the quenching factor from the mean ionization energy, or W-value, was developed recently [93]. In the paper, the authors derive a quenching factor using the W-values from electrons and ions in the same medium:

$$QF(E) = \frac{E_{ee}}{E_{nr}} = \frac{N_i^i.W_e(E)}{n_i^i W_i(E_{nr})} = \frac{W_e(E)}{W_i(E_{nr})}, \tag{4.9}$$

where E_{nr} is the total kinetic nuclear recoil energy deposited in the detector and is equal to E the total kinetic energy of the electron, E_{ee} is the ionization energy observed in electron equivalent energy via ionization, N_i^i is the mean number of e-/ion pairs created by an ion, W_i is the mean ionization necessary to create an e-/ion pair for an ion and W_e is the mean ionization necessary to create an e-/ion pair for an electron. Thus, by measuring the W-value of different ionizing particles, electrons and ions, with same kinetic energy and in the same medium, the authors were able to estimate the quenching factor for several ion species: H^+, H_2^+, H_3^+, He^+, N^+, N_2^+, C^+, O^+, Ar^+, in several pure gas mixtures: H_2, CH_4, Ar, N_2, CO_2, C_3H_8. Figure 4.4 shows an example of the quenching factors estimated using this method in argon gas for different ion species.

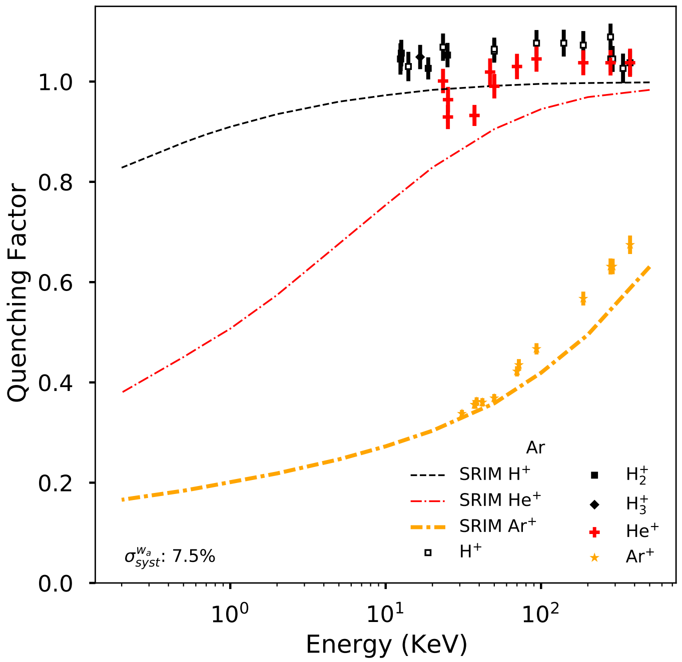

Figure 4.4: Quenching factors calculated for three ions in argon gas [93]. The QF data points were calculated using existing W-value measurements. They are compared to their SRIM expected values in dashed lines.

4.2.5 Nuclear resonance fluorescence

Nuclear resonance fluorescence (NRF) consists of the resonant excitation from an excited state atom, or nuclei, by absorption and emission of radiation, which results into a momentum transfer to the nucleus [94]. The process can be seen as elastic photo-nuclear scattering: with a photon scattering off of a nucleus and inducing a low-energy nuclear recoil. The nuclear recoil energy, E_{nr}, depends on the energy of the incident and emitted photons, which is approximated by the resonance energy, E_r, the angle of fluorescence, θ_f, and the target mass nucleus, M [95].

$$E_{nr} = \frac{2(E_r \sin\theta_f/2)^2}{M} \tag{4.10}$$

The description of the nuclear recoil energy by Equation 4.10 is valid for short lifetimes of the excited nuclear state, allowing no momentum transfer to the medium.

In [95] it is proposed to use NRF as a technique to estimate the nuclear quenching factor of targets, using a photon beam to induce known nuclear recoil energies. To the best of our knowledge, this technique has not been used yet for such purposes.

Chapter 5

Quenching factor Measurement at the Triangle Universities Nuclear Laboratory

In order to measure the quenching factor of the neon-based gas mixtures used by NEWS-G, it was chosen to use the neutron scattering method. In this section, we present our experiment to measure the quenching factor using the neutron scattering method. This method was readily available to us, through our collaborators at the Triangle Universities Nuclear Laboratory facility (TUNL) [96], and was of particular interest as the method directly mimicks the interaction of a WIMP/neutrino with a nucleus.

This section describes our measurement of the QF. First, we cover the neutron beam at TUNL, then we present the experimental set up, followed by aspects of the energy calibration and stability of the detector, and finally the data taking processing.

5.1 Neutron beam

5.1.1 Neutron production at TUNL

The neutron beam used for our measurements was produced using a tandem Van de Graaff accelerator at the TUNL facility. The facility can produce a variety of particles, including protons, deuterons or tritons, which are accelerated and aimed at a target to produce neutrons. The neutron energies can be controlled through their production mechanism. In order to produce a sub-keV neutron beam, a proton beam on a lithium target was used.

For our measurement a H^- beam was produced by a duoplasmatron of a direct extraction negative ion source [97]. Then the beam was directed towards a "chopper" and a "buncher" in order to create a pulsed beam. The chopping technique consists in applying a transverse electric field, which varies periodically. The bunching technique consists in modulating the beam energy as a function of time. The combination of the two methods results in compressed beam segments. The time separation between each beam segment was tuned so that the resulting neutron beam segments would not overlap. The period of the neutron beam is 400 ns.

Then, the H^- pulsed beam enters the Van de Graaff accelerator, which has a maximum terminal voltage of 10 MV. The negative ions are accelerated towards a positively-charged terminal at the center of the accelerator. There, they go through a stripping chamber which removes the electrons. The newly created positive ions are accelerated away from the positively charged terminal and exit the tandem accelerator with an energy of 2.296 MeV.

An analyzing magnetic spectrometer and a series of magnets follows the tandem accelerator, which measures the beam current and energy. The beam can then be sent to various target areas. In our case, a dedicated quenching factor measurement station developed by our colleagues at TUNL was used. Figure 5.1 shows the tandem accelerator of the TUNL facility and show where our measurement took place. The station was shielded from the rest of the beam line to eliminate accidental background, thus provides a collimated neutron beam into the experimental areas.

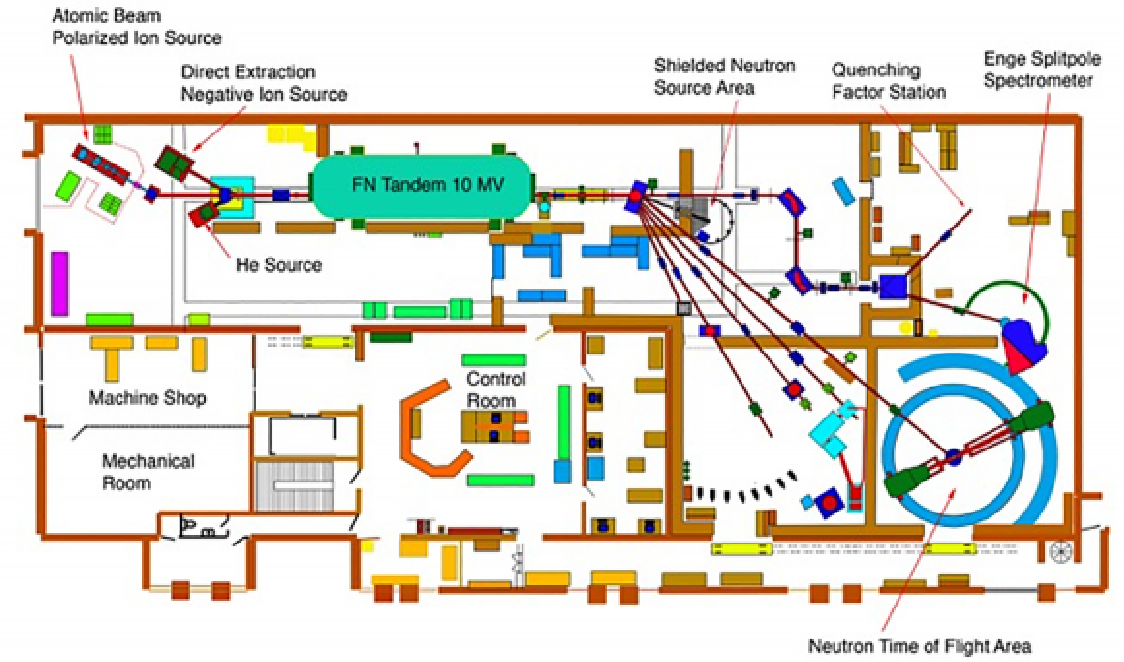

Figure 5.1: Scheme of the TUNL tandem accelerator facility [96]. Our measurement took place in the quenching factor station.

Once the proton beam enters the quenching factor station it scatters off a suitable target for neutron production. In our experimental set up the following reaction was used:

$$\mathrm{p} + {}^{7}\mathrm{Li} \longrightarrow \mathrm{n} + {}^{7}\mathrm{Be} + \gamma \tag{5.1}$$

The neutron beam was focused onto a target made of a 700 nm lithium fluoride (LiF) layer on a tantalum foil which produces a monochromatic neutron beam. The thickness of the target was chosen to minimize the energy loss of the protons in the target, and hence to avoid a large neutron energy spread. This reaction is endothermic with a negative Q-value, Q = −1.644 MeV and has an energy threshold [98]:

$$E_p^{th} \sim \frac{-Q(m_n + m_{Be})}{m_{Be}} = 1.881\,\mathrm{MeV}. \tag{5.2}$$

The energy range of the neutron beam produced can go from 40 keV to 700 keV. The neutron energy, E_n, can be calculated by kinematics [98]:

$$E_n = \left[\frac{\sqrt{m_p m_n E_p}}{m_n + m_{Be}} \cos\phi + \sqrt{\frac{m_p m_n E_p}{(m_n + m_{Be})^2} \cos^2\phi + \frac{E_p(m_{Be} - m_p) + m_{Be} Q}{m_n + m_{Be}}} \right]^2, \tag{5.3}$$

where m_p, m_n and m_{Li} are the proton mass, neutron mass and beryllium-nucleus mass, respectively, and ϕ is the angle of the neutrons' trajectory with the beam line. We looked at a neutron collimated beam at $\phi = 0$. The collimation was performed thanks to a shielding, made of layers of lead and polyethylene, installed at the LiF target, see Figure 5.3.

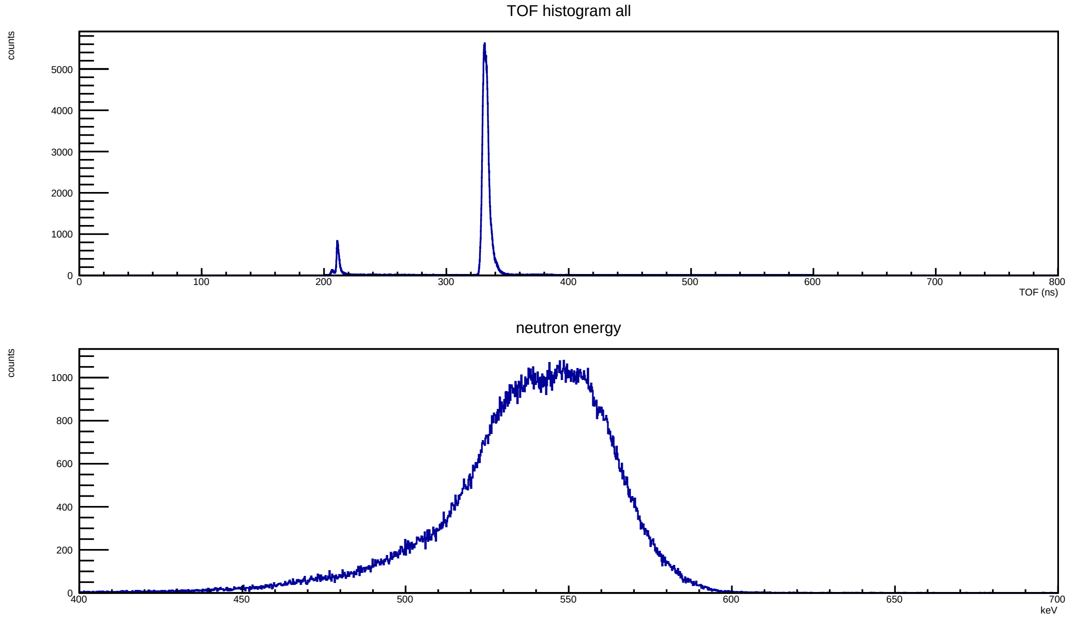

Figure 5.2: TOF measurement of the neutron energy. Courtesy of L. Li.

5.1.2 Monitoring of the neutron energy

The neutron energy was measured using the time-of-flight method (TOF) at the beginning of the experiment.

An important feature of the experiment was a Beam Pick-off Monitor, that triggered when the pulsed proton beam crossed the Li target, providing the time when the neutrons and gammas are produced in the target. A 0-degree backing detector was used to measure the neutron energy and its dispersion, using the time difference between the TOF of neutrons and gammas:

$$\Delta t_{n,\gamma} = \frac{L}{v_n} - \frac{L}{c}, \tag{5.4}$$

with $\Delta t_{n,\gamma}$ the arrival time difference between neutron and gamma events, L the traveling distance, v_n the neutrons' velocity and c the speed of light. Such measurements were performed by our collaborators at TUNL. The TOF was measured from two distances (BPM - 0-degree BD): 127.4 cm and 161.5 cm, resulting in neutron energy means of 544 keV and 546 keV, respectively. The neutron energy for our quenching factor measurement was averaged between the two TOF: with mean 545 keV and standard deviation 20 keV. The energy spread mainly comes from the target thickness. Figure 5.2 shows the time of flight measurement and the respective neutron energy distribution.

5.2 Experimental set up

In January 2019, and for a period of two weeks, we took data in the target room 4, or quenching factor station, at the TUNL facility.

A 15 cm diameter SPC, 3 mm thick, made of aluminum, filled with 2 bar of Ne + CH_4 (3 %), was used to perform the experiment. The sensor was a 2 mm diameter metallic ball, set to a positive HV of 1700 V, with no umbrella. Digitized pulses from a charge-sensitive RC feedback preamplifier, CANBERRA 2006 [99], were recorded using a Struck SIS3316 digitizer [100].
The SPC was exposed to the neutron beam: the southern hemisphere was aligned with the neutron beam line to avoid the anisotropies of the electric field lines in the northern hemisphere caused by the rod holding sensor. The neutron beam is contained in the south hemisphere, Figures 5.3 shows the size of the beam in the SPC, and 6.4 in the next chapter for a detailed view. Figure 5.3 shows the experimental set up. Backing detectors (BDs) consisting in a combination of Hamamatsu R7724 photomultiplier tube [101] and liquid scintillator, EJ-309, made by Eljen [102], recorded the scattered neutrons. The liquid scintillator allowed neutrons and gammas to be differentiated by pulse shape discrimination. This technique relies on different ionization density, which produces different signals characteristics. The target and beam line were shielded with lead and high density

polyethylene, in order to eliminate or reduce gamma and neutron background, respectively. The backing detectors were shielded from gammas with lead caps of 2mm of thickness. Figure 5.4 provides more details on the shielding and collimator dimensions.

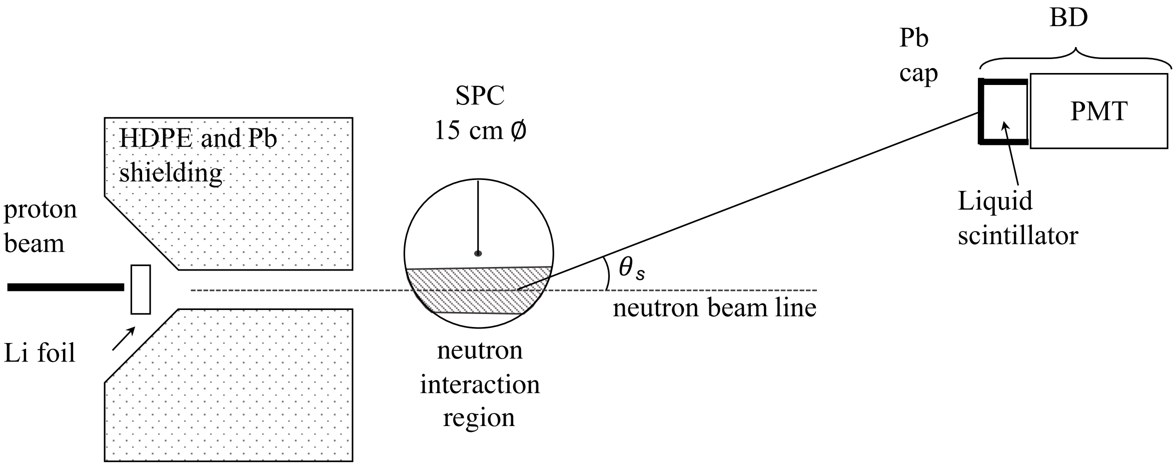

Figure 5.3: Diagram of the experiment not at scale. The protons interact with the Li target, generating a neutron beam. A neutron from the beam scatters off of a neon nucleus with an angle θ_s and is detected by a BD set at a given position. The diagram shows the experiment is shielded from residual particles (neutrons/gammas) by a shielding enclosing the LiF target. The diagram also shows the neutron interaction region in the SPC.

Two configurations for the backing detectors were used to record the data: the annulus structure and the multiple energy configurations.

The annulus structure consists of a metallic structure in the shape of a ring holding the backing detectors. This structure was designed and built by our collaborators at TUNL, with a radius of 29.4 cm (as measured from the center of one backing detector to the center of the annulus). Our colleagues at TUNL placed the annulus structure using accurately surveyed markings in the target hall. Figure 5.5 shows such a configuration, with the SPC's south hemisphere aligned with the beam line and the center of the annulus structure. The structure holds 8 backing detectors, set at the same scattering angle and thus, recording the same nuclear recoil energy. By changing the distance between the SPC and the annulus structure, different scattering angles, and thus different nuclear recoil energies, were recorded. Using this configuration, we recorded 5 nuclear recoil energies, or energy runs.

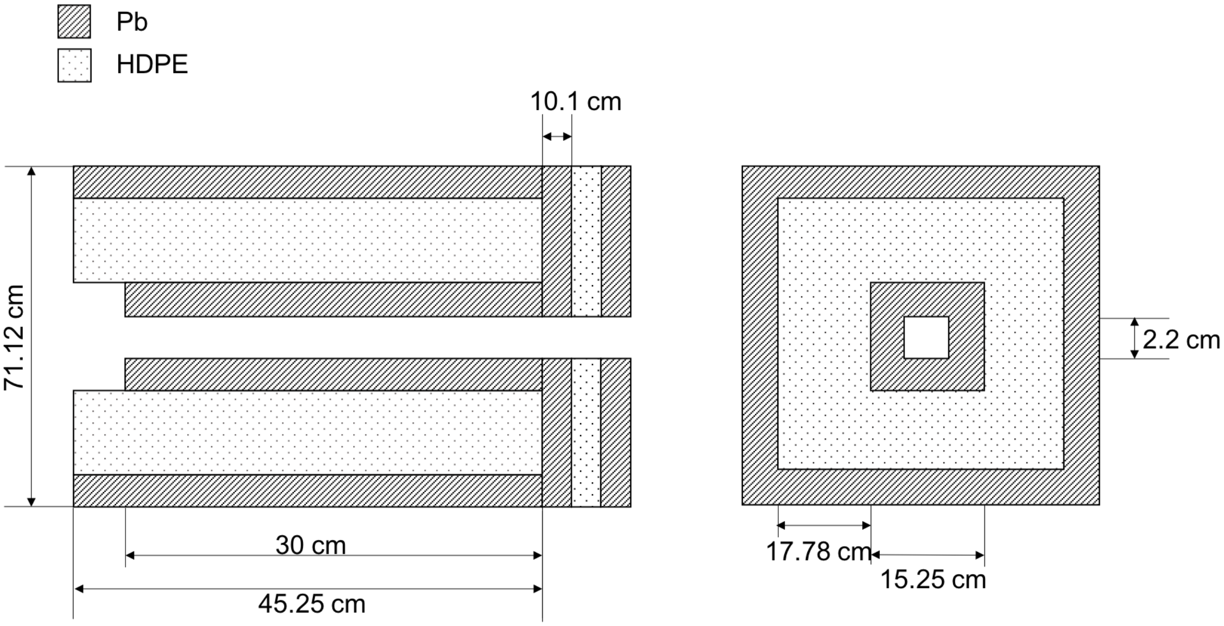

Figure 5.4: Diagram of the shielding/collimator around the neutron beam line. The diagram shows the different layers of lead and high density polyethylene (HDPE) that are shown in Figure 5.3.

In order to detect nuclear recoils with energies of $0.3\,\mathrm{keV_{nr}}$ with the annulus structure, the required distance to the SPC resulted in too low of an event rate to be practical. Instead, another option was adopted; a pair of BDs were placed at roughly 1 m from the SPC. We took the opportunity of this configuration to record two additional energies, overlapping higher energies taken with the annulus structure, see Figure 5.6. The two backing detectors recording the smallest energy were at a transverse distance of 12.5 ± 0.1 cm from the beam line, the second pair of BDs recording 1 keV was set at 22 ± 0.1 cm from the beam line and the last pair of BDs was set at 31.25 ± 0.1 cm. The eight nuclear recoil energies investigated during the experiment are shown in Table 5.1 along with other details specific to each energy run.

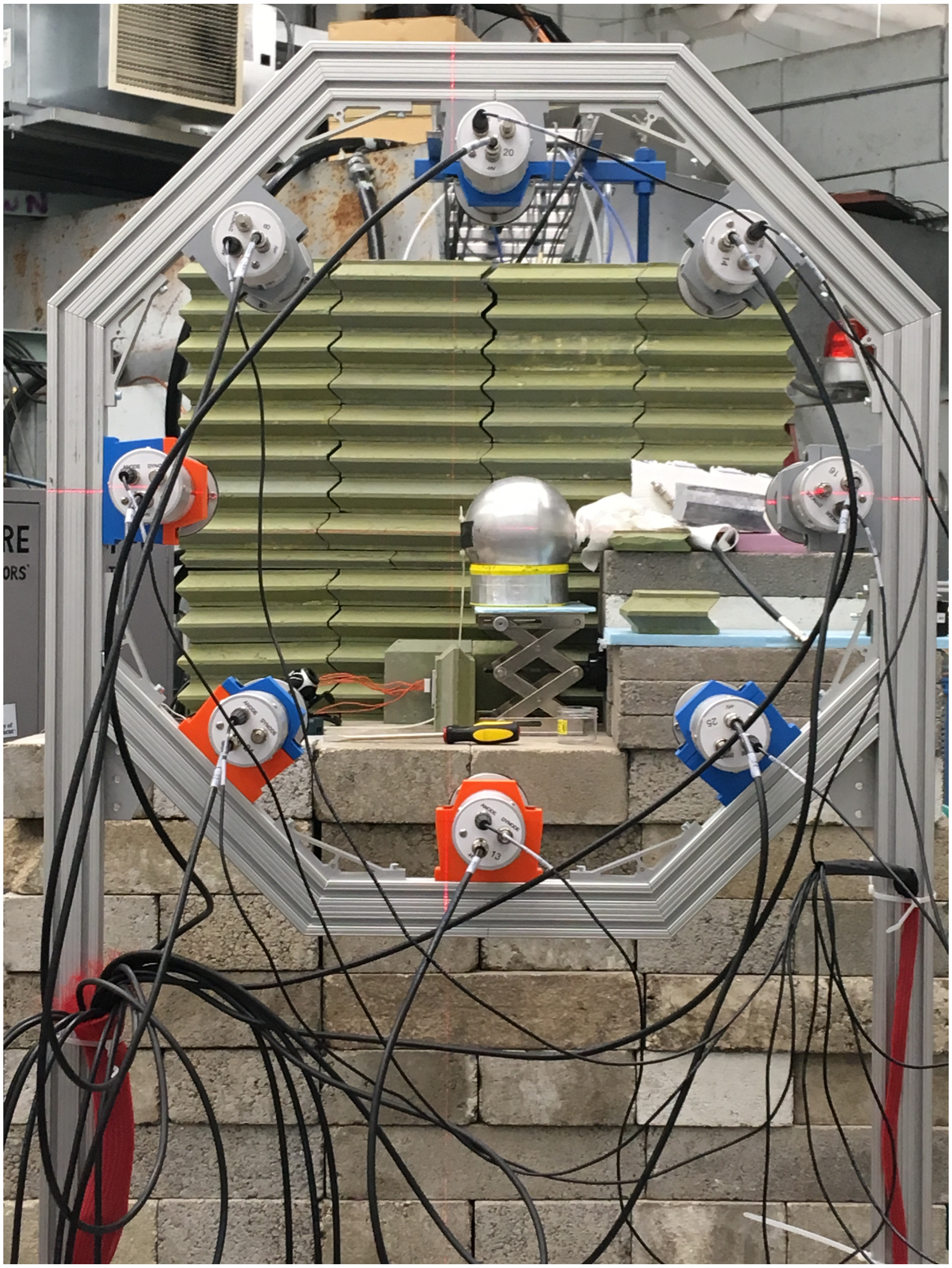

Figure 5.5: Experimental set up 1: annulus structure. The annulus configuration holding 8 BDs and used for 5 energy runs. We can see the SPC aligned with the center of the annulus structure. Behind the SPC we can see the a part of the shield protecting the experiment from the beam line background.

Run	$\mathrm{E_{nr}}$ [$\mathrm{keV_{nr}}$]	$\sigma_{E_{nr}}$ [$\mathrm{keV_{nr}}$]	θ_s [^{o}]	σ_{θ_s} [^{o}]	Distance [cm]	Exposure
8	6.8	1.15	29.02 ± 0.4	2.45	44.6 ± 0.4	4h
7	2.93	0.46	18.84 ± 0.1	1.47	77.9 ± 0.2	7h14
14	2.02	0.29	15.63 ± 0.3	1.12	103.4 ± 1.6	36h21
9	1.7	0.26	14.33 ± 0.06	1.1	106.8 ± 0.1	16h
10	1.3	0.2	12.48 ± 0.05	0.94	124.7 ± 0.1	23h
14	1.03	0.2	11.13 ± 0.3	1.1	103.7 ± 1.5	36h21
11	0.74	0.11	9.4 ± 0.03	0.69	169.3 ± 0.08	33h22
14	0.34	0.11	6.33 ± 0.26	1.1	104.4 ± 0.5	36h21

Table 5.1: Table with the chosen eight nuclear recoil energies, their corresponding scattering angles (from measurements taken on site), the distance from the SPC to the BDs, and time exposures.

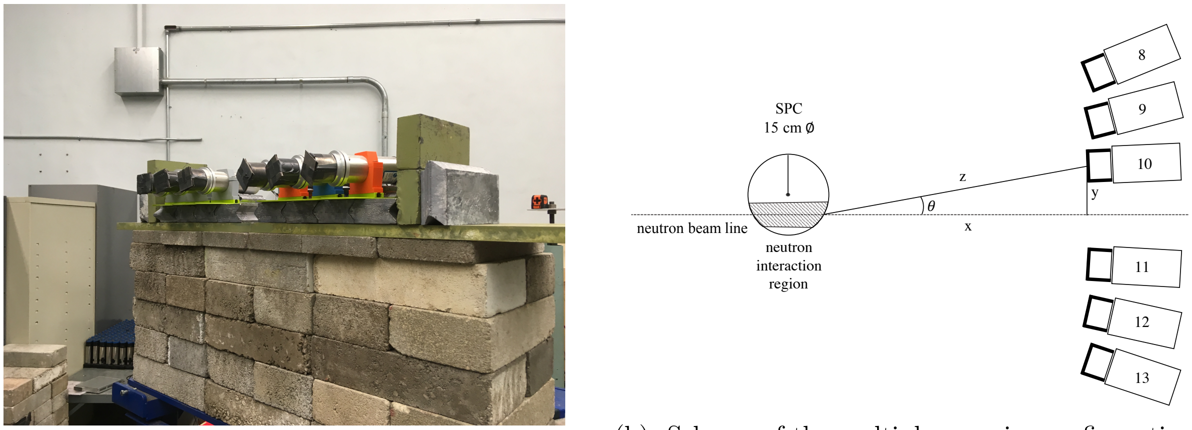

(a) Picture of the multiple energies configuration.

(b) Scheme of the multiple energies configuration.

Figure 5.6: Experimental set up 2: multiple energy configuration. Three pairs of BDs recording three nuclear recoil energies at the same time. The beamline goes through the two middle BDs. The two quantities measured were y and z, and x was calculated based on these two distances and reported in Table 5.1 for consistence. Each pair of x and y was averaged to calculate the scattering angle. The number on the BDs is for analysis purposes and correspond to the channel used.

5.3 Energy calibration

5.3.1 Energy scale

The electronic energy calibration of the SPC was performed primarily using an ^{55}Fe source that was placed at the south pole of the SPC. The ^{55}Fe emits X-rays at 5.9 keV, providing an electron ionization energy scale within the range of nuclear recoil energies that were investigated. We used the source to calibrate the electronic recoil energy scale and to monitor for gain drifts. Calibration data were thus taken for 5 min every hour to provide an energy scale and correct for time-variations in gain (with the neutron beam on). By adding the ^{55}Fe source, the event rate in the SPC with the beam ON increased from about 330 Hz to 340 Hz. To select ^{55}Fe events we use the rise time parameter of the pulses in order to select volume and point-like events. Figure 5.7a shows the rise time as a function of energy, the ^{55}Fe events are shown mostly in green and blue on the Figure at about 25 000 ADC. We can see a large number of track events at higher rise times. To select the ^{55}Fe events we apply a rise time cuts. From Figure 5.7a we observe that the rise times from ^{55}Fe are between about 1 and 2 μs. However, we applied an strong rise time cut from 1 to 1.51 μs in order to reject background events due to the beam (in particular Compton scatterings from gammas), and thus, extract with more accuracy the ^{55}Fe mean.

An example of the energy spectrum of the selected ^{55}Fe events is shown Figure 5.7b. To obtain the energy scale for each calibration run, we fitted the spectrum to a Gaussian for the peak and a combination of a complementary error function with a linear function for the background:

$$f(x) = \frac{N}{\sigma\sqrt{2\pi}} \exp\left(- \frac{(x\mu - 5.9(\text{keV}))^2}{2\sigma^2} \right) + p + qx + r * \text{erfc}\Big(xs - 5.9(\text{keV})\Big), \tag{5.5}$$

where N and σ are the height and the standard deviation of the ^{55}Fe peak, respectively, μ is the energy scale provided from the mean of the ^{55}Fe peak. p and q are the parameters of the linear function, r and s are the parameters of the complementary error functions. All these parameters were let free in the fit.

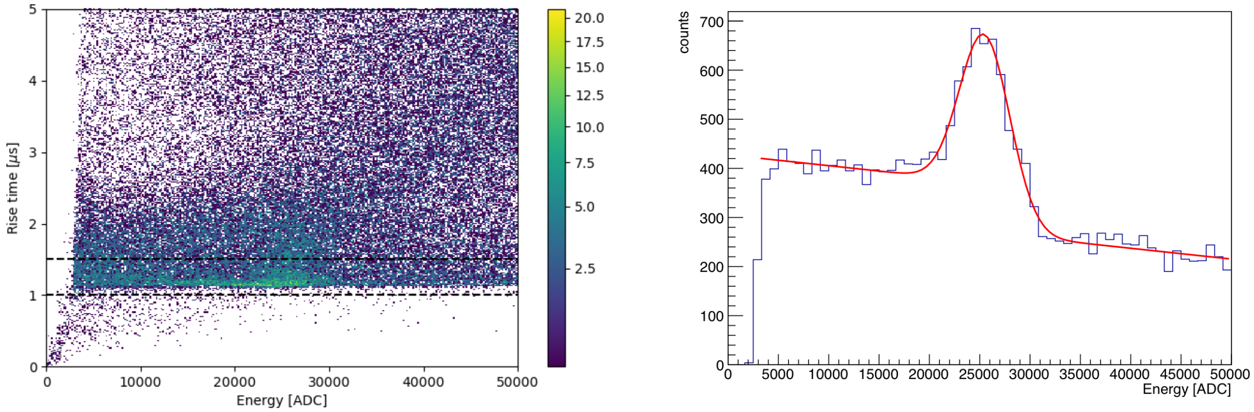

(a) Rise time as a function of the energy for a calibration data set. The ^{55}Fe events are the concentration of events at about 25 000 ADC. The black dashed lines show the rise time cuts performed to the data to select ^{55}Fe events.

(b) Energy spectrum of the ^{55}Fe obtained by applying rise time cuts shown on Figure 5.7a: between 1 and 1.51 μs. The red curve corresponds to the fit performed to the calibration data set using Equation 5.3.1.

Figure 5.7: Energy calibration of the 2019 campaign using an ^{55}Fe source.

Finally, the energy scale dependence as a function of time was determined, see Figure 5.8. As the gain was not stable for the first few hours of the experiment, we modelled the energy scale as a function of time with a partition of two linear functions: the first to describe the first few hours when the gain was not stable and the second linear function for the stable gain time period.

Looking at the evolution of the energy scale, or gain, is also a good way to assess the degradation of the gas quality in the detector. Hence, the monitoring of the energy scale was performed online as a way to assess the gas quality. From Figure 5.8 we observe a decrease of 2 % of the energy scale, in the stable region, over the entirety of the experiment, which shows no leaks in our detector. A tool to assess the oxygen contamination is to look at the rise time as a function of energy of the events. Indeed, the larger the concentration of oxygen in the gas the stronger is the correlation between the rise time and the energy of the events. The explanation of the phenomenon is that oxygen is an electro-negative atom that captures the primary electrons as they drift toward the anode. Surface events are more impacted by this effect than volume events as their primary electrons must travel further in the gas, hence, their probability to be captured is higher. Figure 5.9a shows no correlation between the rise time and the energy of the events, hence, there is no oxygen contamination susceptible to impact our data.

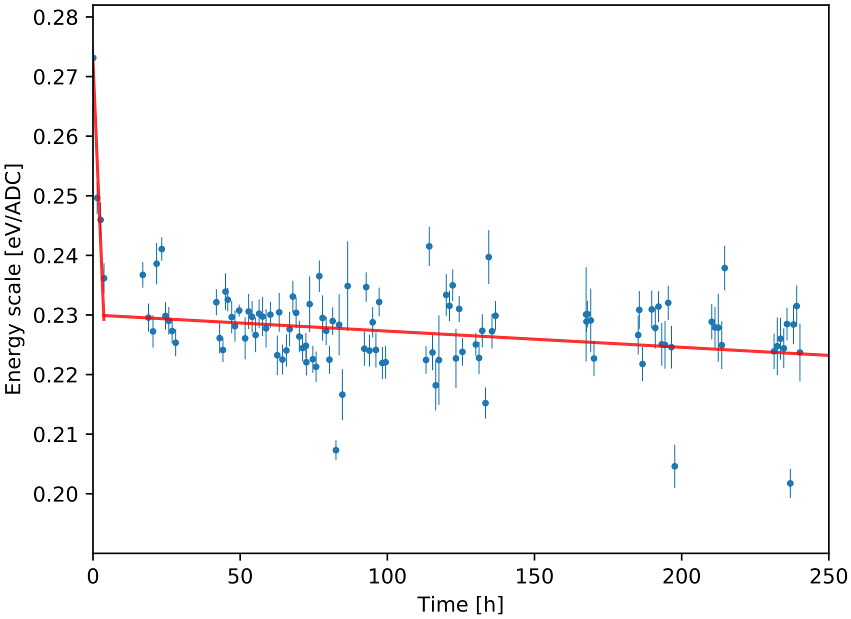

Figure 5.8: Evolution of the energy scale (mean of the ^{55}Fe peak) as a function of time. The blue data points represent the mean and errors of the energy scale returned by the fit shown Figure 5.7b. In red we show the fit of the calibration data with the partition of two linear functions.

5.3.2 Energy response: linearity

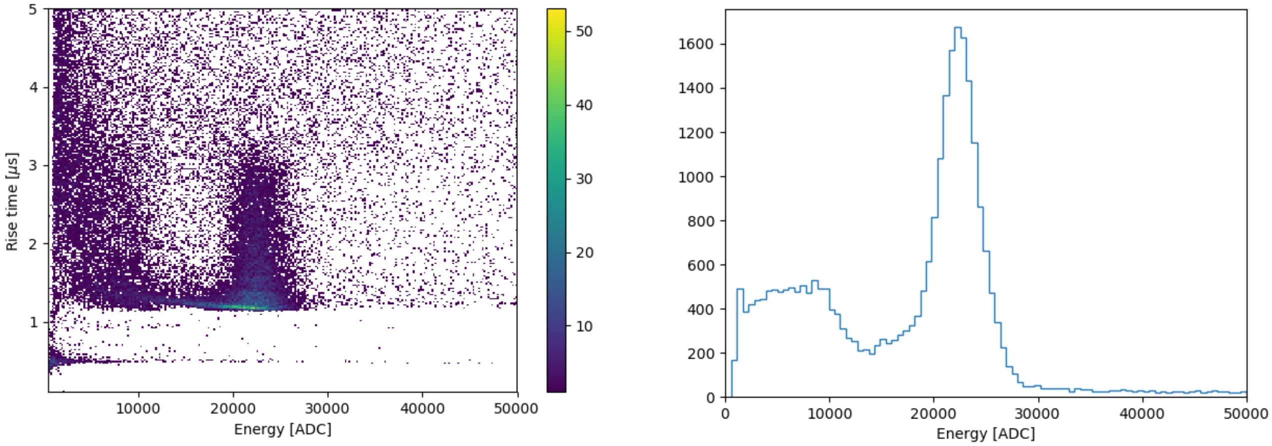

(a) Rise time as a function of the events energy for ^{55}Fe and ^{37}Ar calibration data.

(b) ^{55}Fe and ^{37}Ar energy spectrum, selected with rise time cut.

Figure 5.9: ^{55}Fe and ^{37}Ar calibration data taken at the TUNL facility: beam off, HV = 1650 V and P = 1.96 bar.

Prior to the experiment, we used an ^{37}Ar source to measure the linearity of the energy scale in the detector, on site. ^{37}Ar is a radioactive gas which decays by electron capture. This radioactive source was fabricated by the NEWS-G collaboration using a thermal neutron reactor flux [103], using the reaction $^{40}\mathrm{Ca}(n,\ \alpha)^{37}\mathrm{Ar}$. We added the ^{37}Ar to the neon mixture that we used for our experiment. Data were taken with ^{37}Ar and ^{55}Fe so that we could have calibration points at 2.82 keV and the 5.9 keV for ^{37}Ar and ^{55}Fe, respectively. Figure 5.9a and Figure 5.9b show the rise time as a function of energy of such data set, and the resulting energy spectrum after rise time cuts between. These data calibration were taken with the neutron beam off, the SPC filled with 1.96 bar of neon and let the ^{37}Ar spread in the volume over night and HV = 1650 V.

The energy of ^{55}Fe events follows a Gaussian distribution. However, those from the ^{37}Ar are scattered at lower energies. The extraction of the 2.82 keV peak was not possible with these data, as the location of the peak varied by 10 % depending on the rise time cuts chosen: 1 μs $\leqslant$ rise time $\leqslant$1.4 μs or 1.6 μs. A more in depth study showed that the energy spectrum per different slices of rise time of the ^{37}Ar led to a dispersion of the mean (when extractable) of 20 %, against 4.5 % for the ^{55}Fe for the same data set. Thus, we concluded that the anisotropy of the electric field in the north had too great impact on the ^{37}Ar events, and thus, these data could not provide a trustworthy calibration data point. Our sensor followed a very simple design and did not have an umbrella to correct for the anisotropy of the electric field in the north hemisphere. ^{37}Ar events sample the whole volume of the detector, whereas the ^{55}Fe events sample a small region of the volume in the southern hemisphere, where the neutron beam was directed. The linearity of other SPC detectors with neon was measured in a previous calibration experiment [66] and with a similar S15 detector used for the preliminary QF campaign in 2018, see Appendix A. These two measurements show possible deviation from the linear energy response by similar orders of magnitude: 0.5 and 0.7 % for the preliminary TUNL experiment and calibration experiment, respectively. Moreover, the recoil events were located in the southern part of the detector, which was calibrated by the ^{55}Fe source, precisely for the reason aforementioned. Section 7.2.5 shows a study of a possible non-linearity of the energy response and shows that the effect on the quenching factor is rather small. An uncertainty from a possible non-linearity is provided in the same section.

5.3.3 Gain stability from background events

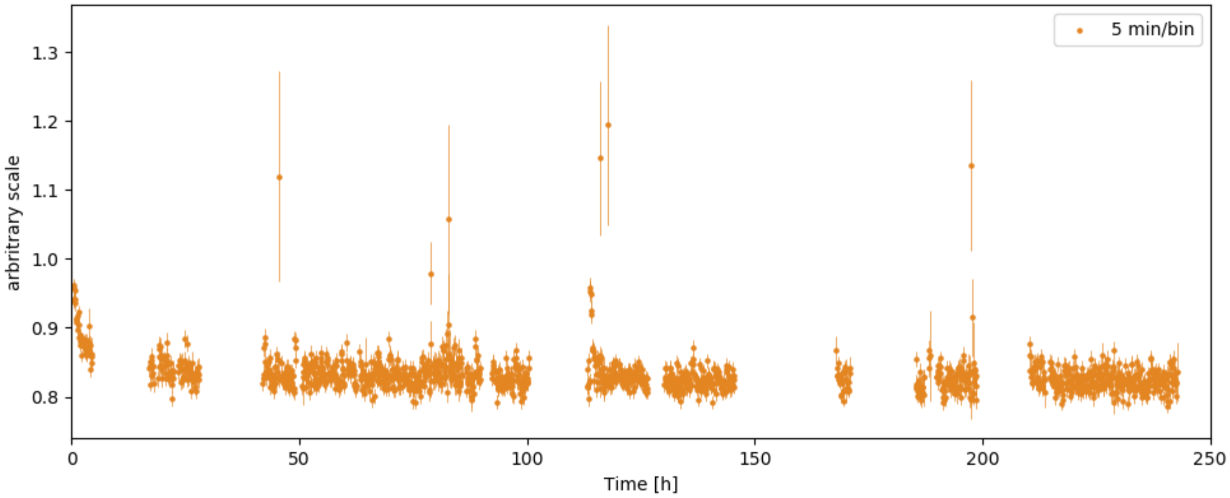

Figure 5.10: Energy scale provided from the background data, which correspond to cosmic muons and surface events, for time period of 5 minutes. The energy spectra are then fitted using a Gaussian, the point recorded are the energy scale provided by the mean of the Gaussian fit, along with the error bar provided by the fitter. Courtesy of P. Gros.

The gain stability of the detector was monitored by the calibration data. These data showed that the gain was stable throughout the experiment; the energy scale as a function of time is shown in Figure 5.8. This figure shows that three energy scale points are outliers. It is expected that the gain is subject to fluctuation and some of them can be larger than others, but these are quite punctual, thus not taking place for more than a few minutes. Figure 5.8 does not give us enough information about the time scale of such change in gain, as the calibration data were only taken every hour. Hence, as a check, we looked at the evolution of the gain of the data by looking at the background (no PSD cut). The events selected have a rise time above $3.8\,\mu$s and correspond to track and surface events. The track events mainly come from high energy gammas coming from the beam and interacting in the gas. The resulting mean of the energy spectra were used to monitor the evolution of the gain over time. Figure 5.10 shows the resulting gain from such background for the entirety of experiment every 5 minutes. The Figure shows the same trend as the energy scale extracted from the ^{55}Fe calibration data: gain stabilizing for the first few hours of the experiment and then global stability, see Figure 5.11. One can also observe sporadic gain surges, but they are rare in comparison to the stable periods of the gain: the outliers represent 0.83 % of all the data.

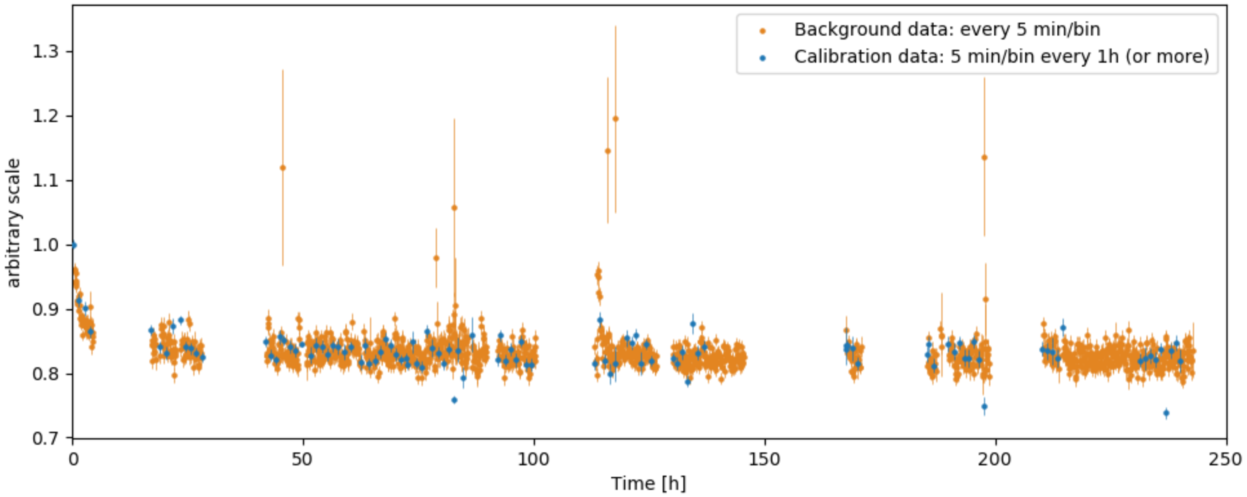

Figure 5.11: Comparison of the energy scale provided by the calibration data, in blue, and the background study, in orange. Each data point corresponds to 5 min of data taking. The calibratin data monitored the gain every hour, while the gain monitoring from the background data is continuous through the experiment. From this figure, we observe that the gain was getting stable the first 4 hours, and thus, the modelling of the energy scale as a function of time with a partition of two linear functions is representative of the gain behavior.

5.4 Data taking and processing

5.4.1 DAQ

The backing detectors (BD), the beam pulse monitor (BPM), and SPC output signals were all connected to a Struck Innovative SIS3316 16-bit 250MHz digitizer/ADC converter [100]. An upper energy threshold of 8000 ADC was applied to the BDs pulses in order to reduce the event rate. The digitizer readout was triggered by the BD signals. The SPC signal was readout at 250 MHz in a 120 μs window adjusted so that the BD trigger is located at approximately 40 μs on the SPC trace. Thus, based on the DAQ configuration we expect to see an excess of events at 40 μs resulting from neutron interactions in the SPC and BDs. Finally, the SPC signals were down-sampled to 5 MHz, as they do not require the same sampling needed to conduct pulse shape discrimination on the BDs signals.

5.4.2 Processing

The data were processed twice using two different methods. First, the data were processed using a simple trapezoidal filter to estimate the energy in the SPC and a pulse profile to estimate the energy in the BD to sort gamma events from neutron events. Thanks to the pulse shape discrimination allowed by the backing detectors, we were able to identify the gamma events and to only keep neutron like events for the rest of our analysis. The PMT of a BD produces a pulse when receiving the light from the scintillator, where the tail of the pulse corresponds to the last scintillator molecules to de-excite. The tail is sensitive to the incident particle, or the ionization density. The technique uses the difference in decay of the pulse to identify particles, by comparing the energy in the tail and the total energy. More precisely, in our analysis the PSD parameter corresponds to the ratio of the total integral of the pulse to the integrated charge in the tail of the pulse.

Thanks to this technique, we were able to significantly reduce our data files by rejecting events with a PSD < 1.35, about 90 % of the data were identified as gamma events by the BDs.

As aforementioned, the data are processed using a trapezoidal filter for the SPC related quantities and pulse profile for the BDs related quantities. Following this first step, the events having a PSD < 1.35 were then "skimmed" out of the data, which allowed to reduce the files by several orders of magnitudes. The events passing the PSD cut had their raw variables written in new data file.

Then, the reduced data were processed by a double deconvolution treatment, see Section 3.3, to account for the response of the preamplifier and the drift of the ions [67]. This method allows for a precise estimate of the rise time of the pulses, thus giving an estimation of the diffusion of the primary electrons along their drift toward the anode and thus about the radial distance of the event. This method also allows us to have a precise estimate of the energy of the event. Section 3.3 provides more details on the processing of the data. Figure 5.13a and 5.13b show a raw SPC

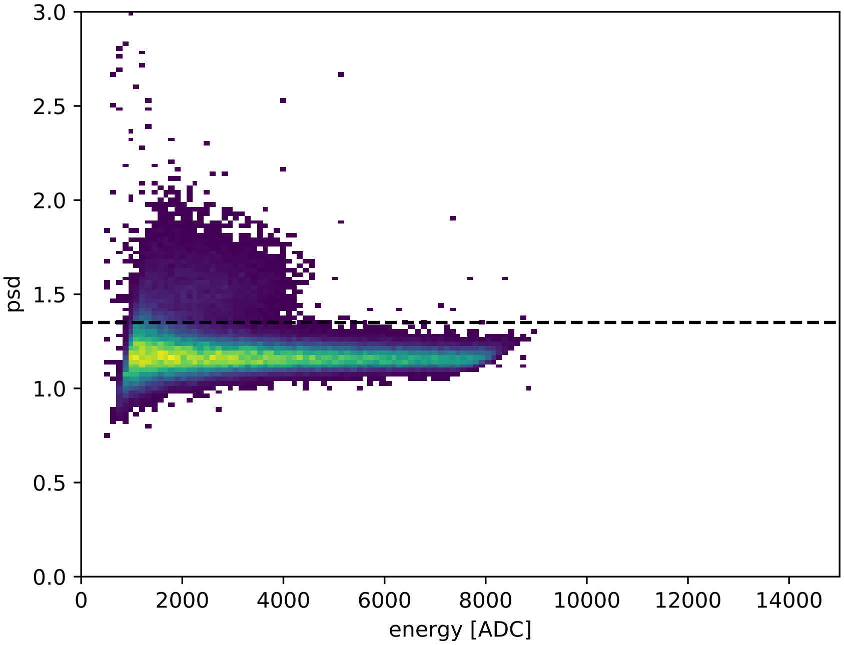

Figure 5.12: PSD as a function of the energy of the events in the backing detectors, corresponding to 1h data of run8. The plot shows two population of events: the population with a smaller psd corresponds to gamma events and the population of events with a larger psd are neutron like events. The psd cut was set such as most of the gamma events, which are below 1.35, would be rejected. The psd cut is shown with the dashed black line. The energy cut above 8000 ADC is visible.

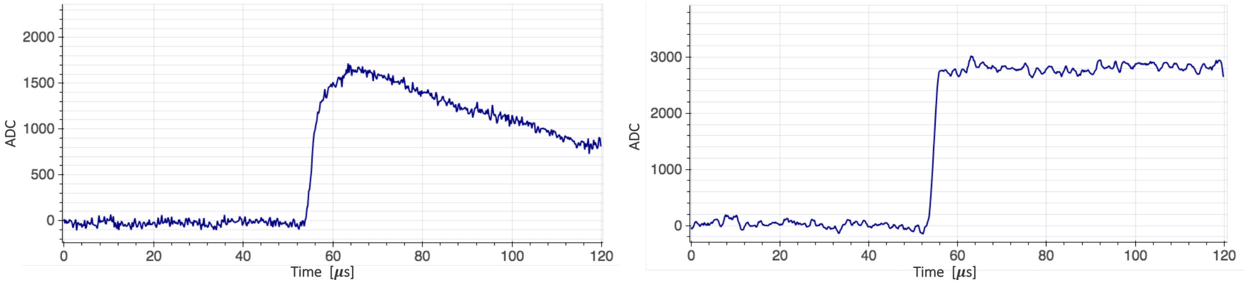

(a) SPC raw pulse.

(b) Integral of a SPC treated pulse.

Figure 5.13: Example of a low energy event ($\sim$ 700 eV) observed at TUNL. We show the raw and corresponding treated pulses from the SPC S15 at TUNL. The treated pulse follow the double deconvolution method introduced in Section 3.3.

pulse of energy 700 eV and a treated and integrated pulse showing what the amplitude and thus the energy corresponds to.

Input parameters	Values
Preamplifier decay time	50 000 ns
HV applied on anode	1700 V
Pressure	2 bar
Ion mibility	$7\,\mathrm{cm}^2\mathrm{bar/V/s}$
Radius of the anode	0.1 cm
Inner radius SPC	7.5 cm

Table 5.2: Table summarizing the input parameters of the processing. While some of these parameters are directly extracted from the experimental conditions: HV, pressure, radius of the anode, and inner radius of the SPC, other parameters were tuned to allow for a better energy reconstruction.

The inputs of the parameters used in the processing for the TUNL data, are shown in Table 5.2. The values of the HV applied on the anode, the pressure, the anode and SPC radii, were extracted from the experimental conditions. However, the preamplifier decay time and the ion mobility were tuned in order to better reconstruct the energy, and avoid any under or over deconvolution [67]. The preamplifier decay time was measured to be 47 000 ns, while the ion mobility in neon is $4.14\,\mathrm{cm}^2\mathrm{bar/V/s}$ [104]. The values of these parameters were changed by about 7 % and 80 % compared to theoretical values.

5.5 Rise time stability

The rise time stability was investigated, as a rise time cut is applied to select the recoil data, see Section 6.1, in particular we looked at the evolution of the quantity in the rise time region of interest. To do so, we looked at the data with a PSD cut, in order to look at neutron like events. Figure 5.16 shows an example of rise time spectrum for a period of 10 min. One can see an excess of events between 1 and 2 μs, this excess of events corresponds to nuclear recoils in the gas. Thus, we looked at this particular population of rise time to check any drift in the rise time as a function of time.

Figure 5.15 shows the rise time as a function of time throughout the experiment. We observe the same population of events below 2 μs, which corresponds to recoil events. We observe that the rise time of this population stays stable for the entirety of the experiment. The overall rate changes, which depends on several factors: the configuration of the annulus structure and the beam intensity; thus the rate is quite difficult to interpret. However, we see that indeed the rate changes throughout the experiment without impacting the recoil events' rise time distribution. Thus, the rise time does not depend on the rate. From this Figure, we can also observe some sudden drop in the rate, at about 13 000 min and 14 200 min, for example.

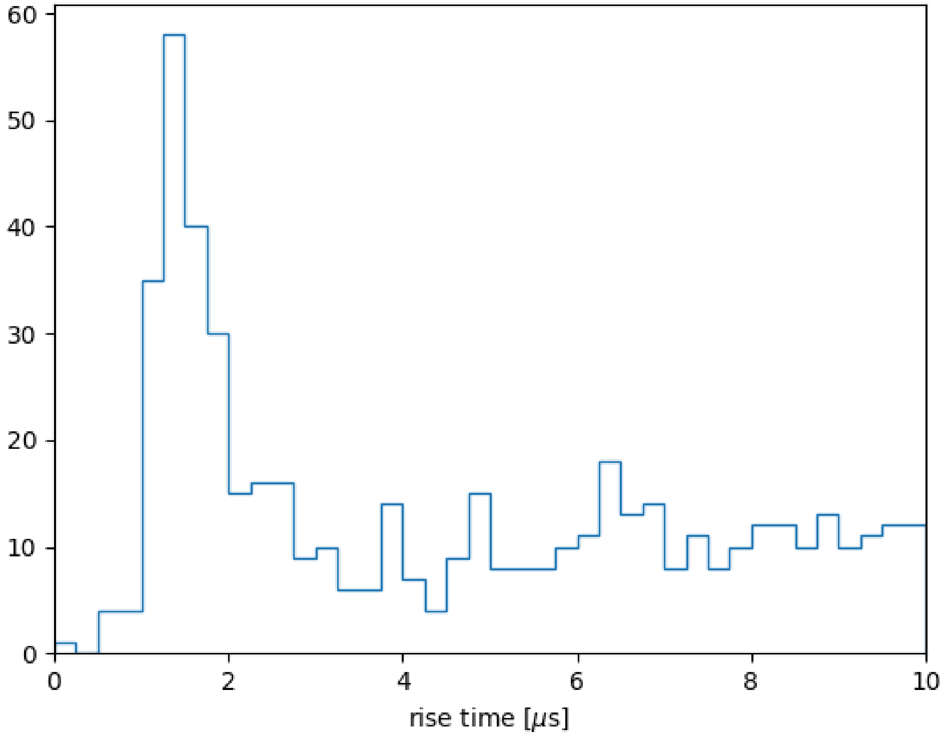

Figure 5.14: Example of rise time spectrum after PSD cut. This particular distribution corresponds to the first 10 min of run7. We see an excess of event between 1 μs and 2 μs, which are recoil events in the gas. We are using this population to probe any rise time drift, which is shown in Figure 5.16.

To complement Figure 5.15, we looked at the evolution of the mean of the population of events shown in Figure 5.14. For this, we fitted the distribution with a truncated Gaussian and we reported the mean and error on the mean (returned by the fit) on Figure 5.16. Figure 5.16 shows the evolution of the rise time mean as a function of time, every bin corresponds to 10 min. We can observe that the rise time is stable in time. The surges of the rise time values, or high uncertainties

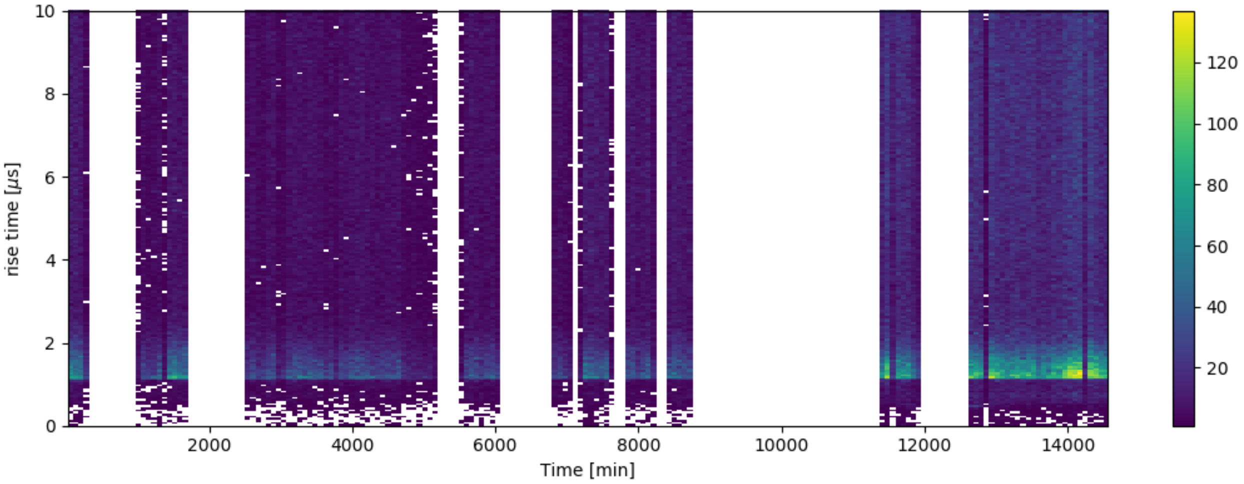

Figure 5.15: Rise time as a function of time. Only a PSD cut was performed on the data. The population of events below 2 μs (blue) is the recoil events, the other events represent background from cosmic muons or unphysical events (purple). This plot allows to see that the rise time distribution of the recoil events does not depend on the rate, which varies throughout the experiment. Thus, the rise time cut used to select the data do not need to be adjusted with time.

on the returned means, are consistent with significant event rate drops.

In addition to the gain monitoring, we also investigated the evolution of the rise time as a function of time and the impact of the event rate on the same quantity. The conclusion from this study is that the rise time was stable in time and that except for the large event rate drops, the event rate did not impact the rise time distribution.

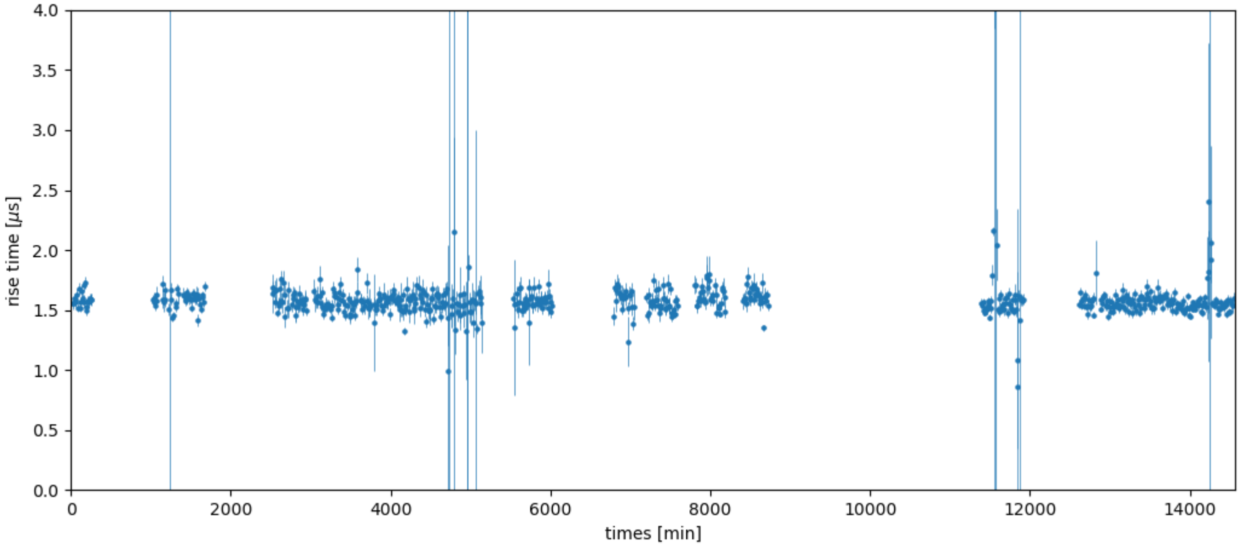

Figure 5.16: Rise time as a function of time. Each bin represents the Gaussian mean of the recoil population, shown in Figure 5.14, for 10 min with its respective error. This plot allows to see that the rise time is stable throughout the experiment.

Chapter 6

Quenching factor measurement analysis

In this chapter, we cover the analysis performed on the data taken at the TUNL facility. First, we present the sets of cuts performed to the data in order to select the neon nuclear recoils. Then, we describe the analysis approach to extract the quenching factor from our data. We propose a new method, to extract the quenching factor by performing an unbinned posterior fit to the data, and fitting all the data sets simultaneously.

6.1 Nuclear recoil event selection

In this section, we present the data cuts to select neon nuclear recoils.

As covered in Section 5.4.2, a first set of cuts was performed in order to select neutrons interacting in the BDs. This primary cut on the backing detectors is a pulse shape discrimination cut (PSD), designed to separate environmental and beam gammas from neutron events. Figure 6.1a shows the PSD parameter as a function of energy. There are two populations of events: one is centered at a PSD of 1.2 and another is centered at a PSD of 1.7. The first corresponds to gammas events and the second to neutron events. By setting a cut below a PSD of 1.35 we are able to cut gamma events. As mentioned in Section 5.4.2 90 % of the data were identified as gamma events

Run number	TOF cut [ns]
8	95 - 140
7	135 - 185
9	140 - 205
10	150 - 215
11	205 - 265
14	145 - 205

Table 6.1: Table summarizing the TOF cut for the different runs.

and thus rejected. Figure 6.1b shows the PSD parameter as a function of time of flight (TOF).

To select neutrons coming specifically from the beam, a second set of cuts was performed. Figures 6.1b and 6.1c show the PSD as a function of TOF and the TOF spectrum for run 8. Figure 6.1b clearly shows a population of neutrons coming from the beam clustered around a PSD of 1.5 and a time of flight of 350 ns. The TOF depends on the location of the annulus structure, thus TOF cuts varied from one run to another. The TOF cuts for all data sets are summarized in Table 6.1.

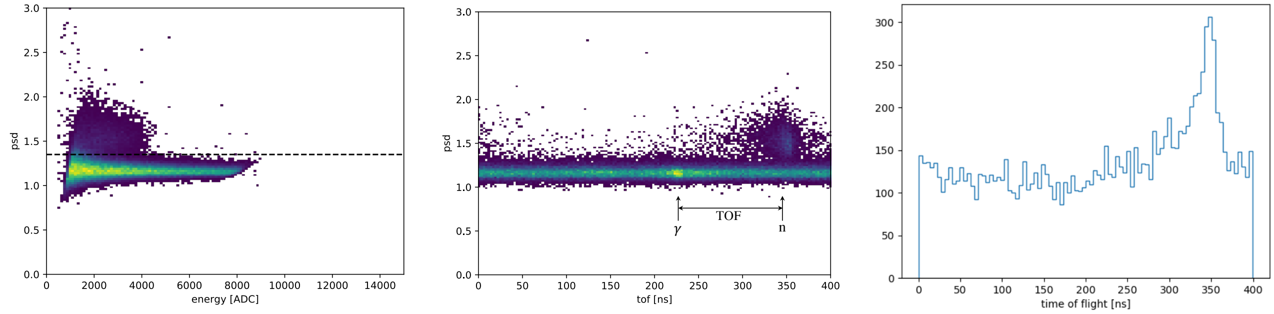

(a) PSD as a function of energy of the events in the BDs, corresponding to 1h data from run 8. The PSD cut was determined to reject most of the gamma events, which are below 1.35.

(b) PSD as a function of time of flight (TOF) for run 8. The TOF of the gammas and neutrons associated with the beam are found at 225 ns and 350 ns, respectively.

(c) Time of flight (TOF) spectrum of the neutrons for the run 8 between the Beam Pick Off Monitor and the triggering BD. The spectrum is obtained after the PSD cut.

Figure 6.1: Set of cuts to select events consistent with neutron beam interactions in the BDs: PSD and TOF.

A third set of cuts was performed on SPC related quantities.

The first quantity we cut on is the onset time, which represents the time difference between the

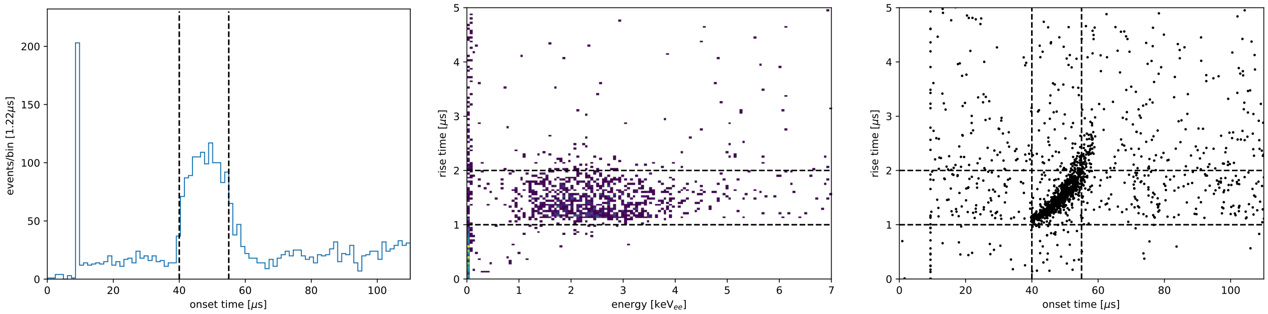

(a) Onset time spectrum for run 8 after PSD and TOF cuts. Observation of an excess of events between 40 and 55 μs, which represents the coincident events between the SPC and the BDs, and thus nuclear recoils.

(b) Rise time as a function of energy for run8 after PSD, TOF and onset time cuts. The concentration of events represents the neon nuclear recoils. Events between 1 and 2 μs are selected to build the energy spectra.

(c) Rise time as a function of the onset time (drift time of the events) for run8 after PSD and TOF cuts. The population with correlated rise time and onset time correspond to volume events in the SPC.

Figure 6.2: Set of cuts performed on SPC related quantities: the onset time and the rise time.

BD trigger and the start of the pulse in the SPC. This time difference is caused by the drift time of the primary electrons from the interaction point to the sensor minus the TOF between the interaction point in the SPC and the BD. Hence, by approximation the onset time is the drift time of the primary electrons in the SPC. The start of the pulse in the SPC is defined as the time the SPC signal reaches 10 % of its maximum amplitude. From the DAQ set up, which recorded every coincident event between the triggering BD and the SPC with a trace starting at 40 μs, we expect to see an excess of events with an onset time of 40 μs induced by neutrons. The onset time spectrum, shown in Figure 6.2a, shows a clear excess of events between 40 μs and roughly 60 μs. This peak corresponds to recoil events and the flat part corresponds to random background events. The onset time signal (recoils) window was defined between 40 and 55 μs.

Finally, we selected events occurring in the volume of the SPC to reject surface background events. These events are selected by placing a cut on the rise time of the pulses from the SPC. Figure 6.2b shows the rise time as a function of energy for SPC events passing the onset time and time of flight cuts (events from several energy runs). One can see that the data are clean and we can identify the recoil events in the rise time band between 1 and 2 μs. The recoil events were thus selected within this rise time range.

Figure 6.2c shows the rise time of SPC events as a function of the onset time. There's a well defined population of events between 40 and 55 μs in onset time and between about 1 and 2 μs in rise time, which is the recoil events. This plot shows a clear dependence in rise time and onset time (drift time of the primary electrons), which is expected, and that the interactions took place in the volume of the detector.

6.2 Energy spectra

The nuclear recoil energy spectra were obtained after applying the different cuts mentioned in the previous section. The energy spectra were converted to keV by using the energy scale presented in Section 5.3. Figure 6.3 shows the energy spectra obtained for the eight runs of the QF experiment. From these, we observe a noise peak present below 80 eV and a small, and seemingly, flat environmental background. Moreover, we can see that the peak shapes of the recoil events are not symmetric and cannot be modelled by a Gaussian. These asymmetric distributions preclude the traditional method used to extract the quenching factor, which consists in calculating the ratio of the mean of the observed distribution with the total kinetic nuclear recoil energy. Thus, we built a model to describe the peak shape, including its dependence on the quenching factor.

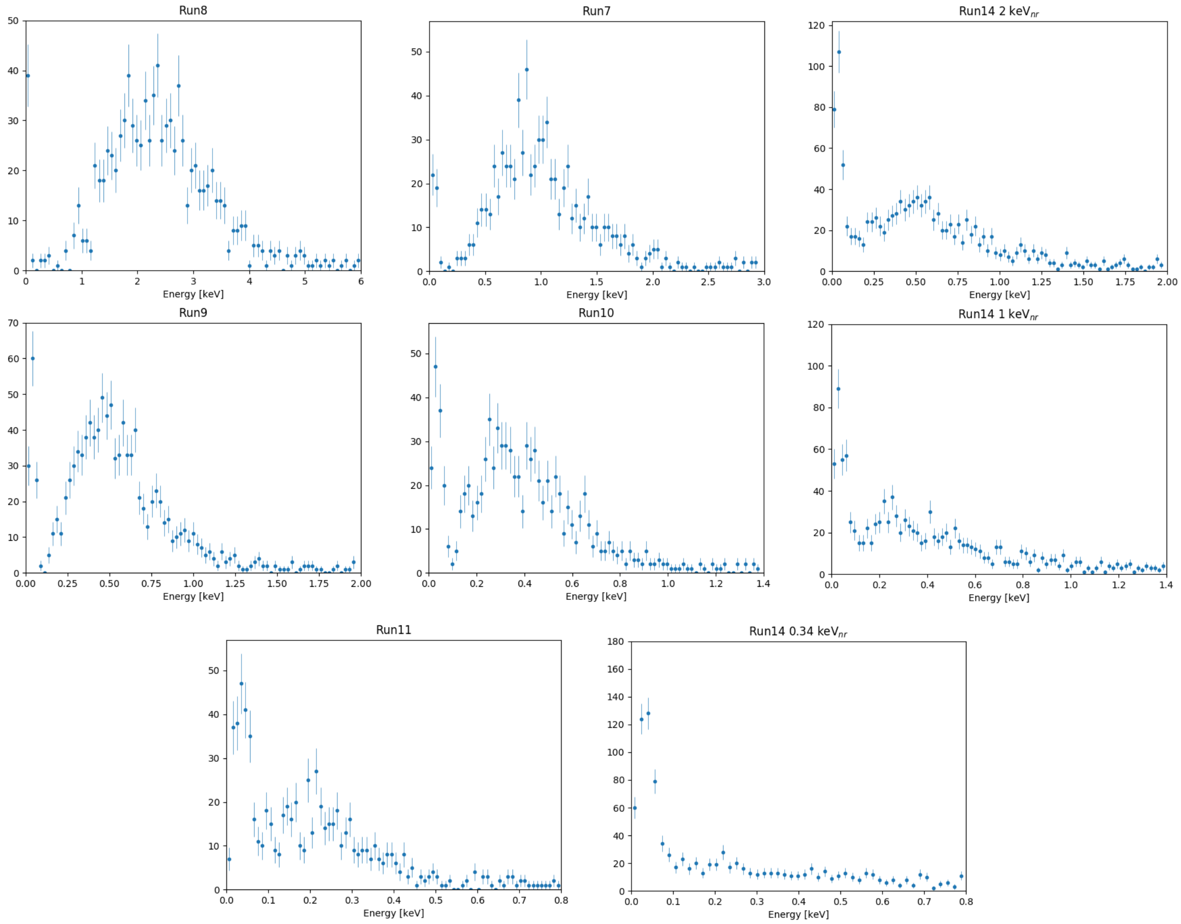

Figure 6.3: Nuclear recoils energy spectra for the respective energies investigated. The mean nuclear recoil energies are: 6.8 keV$_{\mathrm{nr}}$, 2.93 keV$_{\mathrm{nr}}$, 2 keV$_{\mathrm{nr}}$, 1.7 keV$_{\mathrm{nr}}$, 1.3 keV$_{\mathrm{nr}}$, 1 keV$_{\mathrm{nr}}$, 0.74 keV$_{\mathrm{nr}}$, and 0.34 keV$_{\mathrm{nr}}$ moving from left to right and top to bottom. We observe a clear nuclear recoil signal for seven out of 8 spectra.

6.3 Physics model for the nuclear recoil spectrum

The shape of the recoil peak is governed by several factors: the scattering angle, the neutron energy, the quenching factor, the resolution of the detector and the efficiency reconstruction of our processing. In this section, we explain the model derived and each input to describe the expected recoil distribution.

6.3.1 Geometry of the experiment: scattering angle distribution

Because of the finite size of the SPC and neutron beam, we probe a distribution of scattering angles and not a single value of scattering angle. Thus, each particular experimental configuration probes a scattering angle distribution and thus different nuclear recoil energies, which results in a widening of the peak. The scattering angle distribution depends on the size of the SPC and the BDs, the shape and cross section of the beam and other distances relevant to the experiment. A Monte Carlo simulation was developed, taking into account the geometry of the experiment, to estimate the scattering angle distributions for all energy runs.

Our collaborators at TUNL determined the cross section of the beam to be 5 cm × 5 cm at 2.54 cm from the exit of the collimator (without the last layer of lead bricks) and 6 cm × 6 cm at 27.94 cm, which places the last measurement 2 cm before the SPC. All these quantities have ± 1 cm of uncertainties. We assume its shape to be square based on the collimator hole having a square shape. The distribution of neutrons in a cross section profile of the beam is assumed to be uniform based on an analysis performed by our collaborators at TUNL. This was determined by looking at the beam profile in two locations along the beam line with a backing detector, and looked for differences in the rate of the neutron population along the orthogonal plane to the beam line. Figure 6.4 shows the geometry of the beam inside of the SPC resulting from these measurements. Listed in Table 6.2 are the key quantities and considerations for the study of the expected recoil peak distributions built through Monte Carlo simulation.

Figures 6.5a and 6.5b show the neutron interactions obtained through the Monte Carlo simulation in the SPC and in the BDs using the same configuration as for run 8 ($6.8\,\mathrm{keV_{nr}}$). Figure 6.6 shows the corresponding scattering angle distribution for this configuration. From the simulation, we estimated the scattering angle distributions for each energy run. These distributions were fit to a Gaussian and we were able to their means and standard deviations for each run. These quantities are reported in Table 5.1.

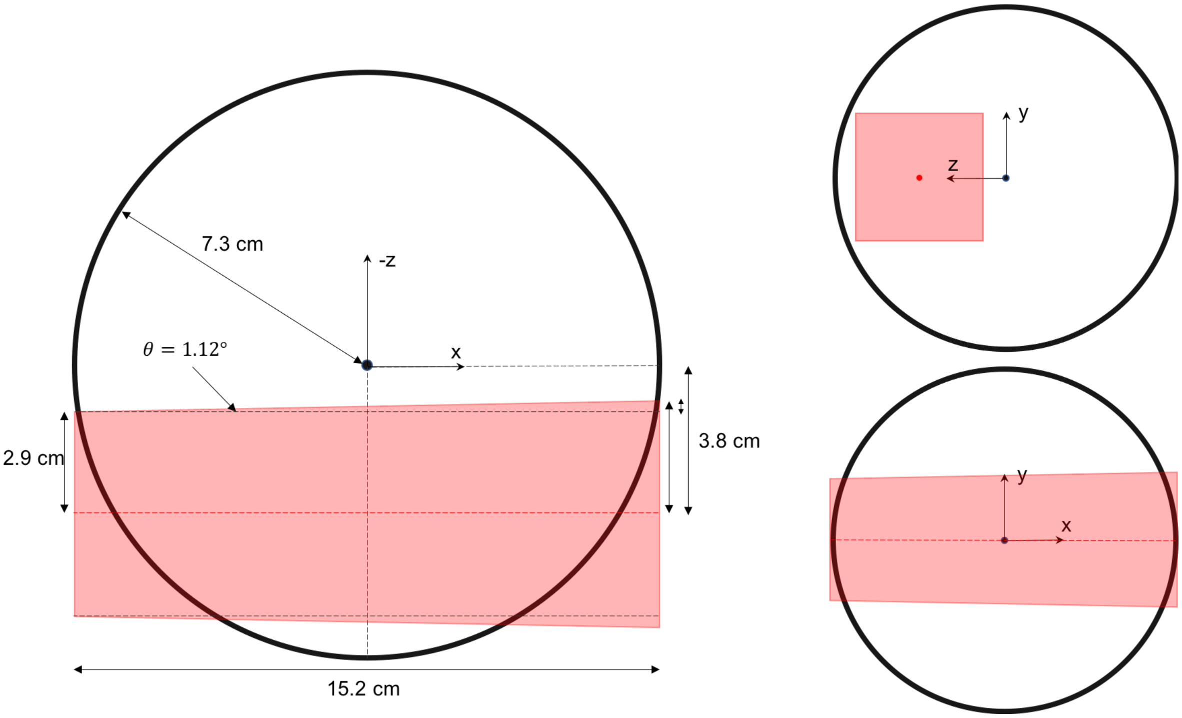

Figure 6.4: Geometry of the SPC and neutron beam to estimate the expected peak shape of the recoils events. The left view corresponds to the top view, with the neutron beam coming on the left and exiting the detector on the right. The top right view corresponds to the front view of the SPC with the beam coming out of the page and the bottom right view corresponds to the side view of the experiement.

6.3.2 Neutron energy distribution

The neutron energy distribution directly impacts the shape of the nuclear recoil distribution. The neutron energy was obtained by using the TOF of the neutrons recorded by a BD directly in line with the beam, or 0-degrees BD. The energy of the neutron beam was measured by our collaborators at TUNL, and estimated to be 545 ± 20 keV (mean ± standard deviation). The neutron energy distribution was modelled by a normal distribution.

By taking into account the scattering angle and neutron energy distributions we were able to obtain the expected nuclear recoil energy distributions. Figure 6.7 shows several of these energy distributions, which display a rather large width relative to their mean. The figure also shows that the energy distributions for different runs overlap.

Quantities	Values
Outer diameter of the SPC	15.2 cm
Thickness of the SPC shell	3 mm
Width BDs	5.08 cm
Diameter BDs	5.08 cm
Distance from the anode to the center of the beam	3.8 cm
Cross section of the beam at 2.54 cm of the exit of the beam line collimator	5x5 cm^2 ± 1 cm
Cross section of the beam at 27.94 cm of the exit of the beam line collimator	6x6 cm^2 ± 1 cm
Dispersion of the neutron beam	∼ 1.12 °
Beam profile	Uniform distribution of neutrons
Distance between SPC surface and exit of the collimator	21.4 cm ± 5 mm
Distance surface of the SPC (center of the south hemisphere) to center of annulus	Varies depending on the nuclear recoil energy investigated, see Table 5.1

Table 6.2: Table summarizing the key quantities and considerations for the Monte Carlo simulation building the scattering angle distributions.

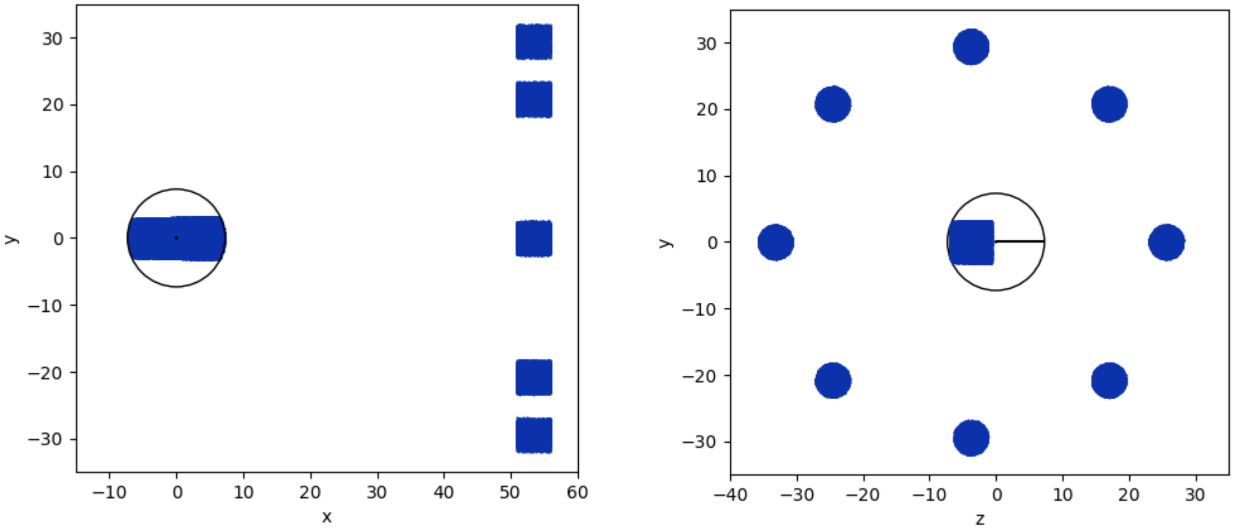

(a) Side view of the interactions taking place in the SPC and in the BDs.

(b) Front view of the interactions taking place in the SPC and in the BDs.

Figure 6.5: Monte Carlo interactions in the SPC and BDs providing the scattering angle distributions.

Now that we have a model for the expected nuclear recoil energy, the next sub-sections will describe the expected recoil energy distributions observed by our detector.

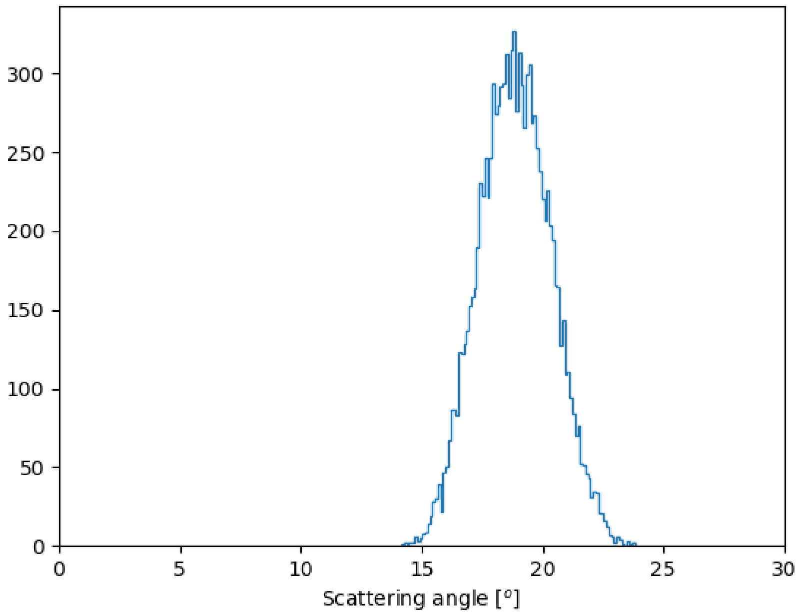

Figure 6.6: Example of scattering angle distribution provided by the Monte Carlo simulation. This distribution is associated with the run7 configuration.

6.3.3 Quenching factor parametrization

The energy observed in the detector from a nuclear recoil is quenched relative to an electronic recoil of the same energy. Knowing the energy of the recoils, we can quench their energies prior to get the number of primary electrons and applying the response of the detector.

To estimate the expected signal in our detector, the quenching factor needs to be included in the model. Based on the expected nuclear recoil energy distributions from the MC simulation and the energy spectra observed, the energy range covered by an energy run is quite large and the QF is expected to vary within that energy range. Thus, the quenching factor used in our model depends on the nuclear recoil energy.

As mentioned in Section 4.1, the Lindhard theory is one of the best predictions when it comes to describe energy loss of nuclear recoils which have same mass and atomic numbers as the target atoms. The Lindhard model includes 11 parameters as Equation 4.6 shows.

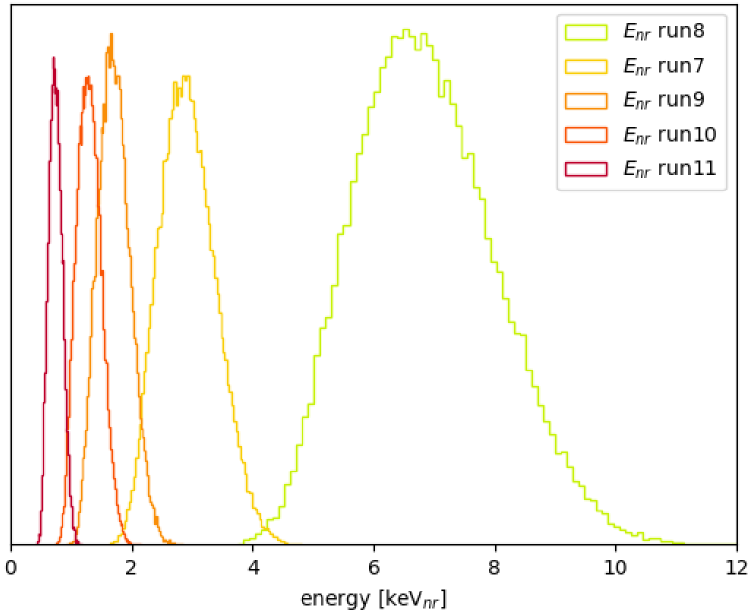

Figure 6.7: Simulation of the energy distributions of the nuclear recoils for the energies recorded with the annulus structure. The simulation takes into account the geometry of the experiment and the energy distribution of the neutrons energy.

To describe the QF in our model, we opted for a simple parametrization having two variables:

$$QF(E_{nr}) = \alpha E_{nr}^{\beta} \tag{6.1}$$

This parametrization was used by other dark matter experiments, like EDELWEISS [105], and can reproduce the Lindhard theory and SRIM simulations well [84].

Although this parametrization is much simpler than the Lindhard model, it is able to reproduce that theory over the energy range of interest. For example, with parameters α=0.23 and β=0.15, the Lindhard theory and our model agree to within less than 1 %. Figure 6.8a shows a plot that compares the two mathematical functions. Equation 6.1 is able to reproduce accurately Lindhard, that is based on physical models. Although our parametrization only has two variables, it is able to produce a wide range of different shapes depending on the values of α and β. Therefore, we expect that this parametrization is sufficient to parametrize the quenching factor. Figure 6.8 shows the wide range of shapes depending on the values of α and β. In our analysis, the parameters α and β are free and estimated by the chosen minimizer, Minuit.

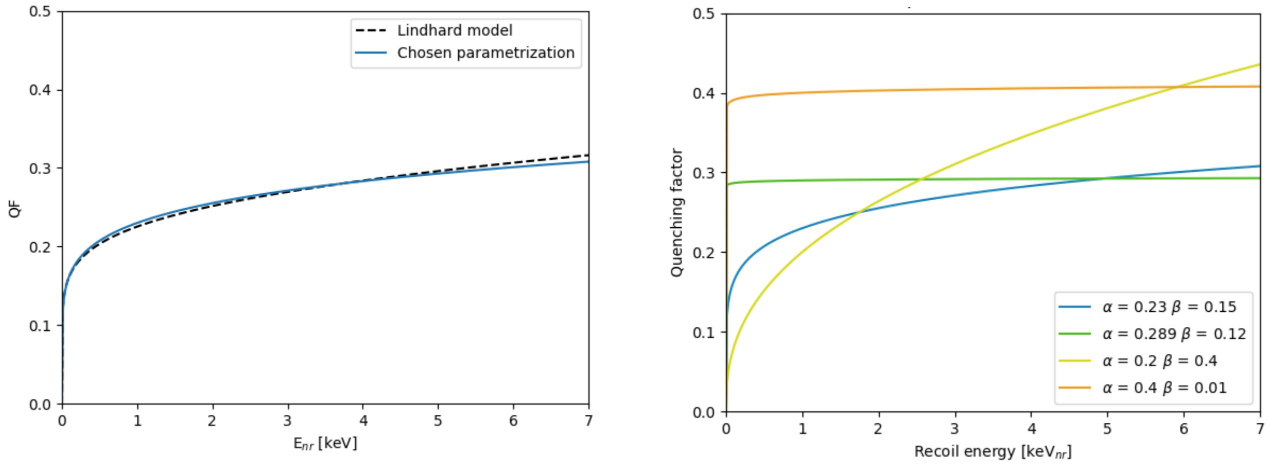

(a) Comparison between Lindhard in dashed black and the 2 variables parametrization discussed and chosen to model our data in blue. The blue curve matches well the Lindhard model.

(b) Example of the parametrization for different values of α and β. It illustrates the large range of shapes that the 2 variables parametrization covers.

Figure 6.8: Quenching factor parametrization compared with Lindhard theory and illustration of the flexibility that the chosen parametrization covers in terms of shape.

6.3.4 Response of the detector

So far, we have described the expected energy deposited in the SPC. The next step in our model is to describe the energy response of the SPC. This includes the primary and secondary ionization processes. The response of the detector as described in Section 3.2.3 is included in the peak shape.

The primary ionization was modelled by assuming that the number of primary ionized atoms follow a Poisson distribution, and include amongst other the scattering angle, the neutron energy and the quenching factor. Hence, the expected nuclear recoil energy depends on the neutron energy and the scattering angle. Then, the expected ionization recoil energy is calculated with the QF: $E_{ee} = E_{nr} \times QF(E_{nr})$. Which leads to calculate the mean number of primary electron/ion pairs created. This quantity is calculated using the W-value: $\mu_{pe} = E_{ee}$ / W. Finally, we calculate the probability of observing j_{pe} primary electrons given the mean number of primary electron/ion pairs created: $P_{Poisson}$ (j_{pe} | μ_{pe}).

Although the number of primary electron/ion pairs created does not exactly follow a Poisson distribution, see Section 3.2.3, we still choose to model it using this simpler shape. Our choice is motivated by the rather wide recoil distributions, which shows a greater dispersion than anticipated from modelling primary ionization in neon, with an expected Fano factor of about 0.2 [73]. The energies investigated are also high enough that the Fano factor's effect should be folded in the energy resolution.

The secondary ionization is modelled using a convolution of Polya distributions. First, we convert the energies E_{ee} in number of secondary electrons. Thus, the two following probabilities are equivalent:

$$P_{Polya}^{Nth}(E_{ee} \mid j_{pe}) \Leftrightarrow P_{Polya}^{Nth}(n_{se} \mid j_{pe}) \tag{6.2}$$

6.3.5 Energy reconstruction efficiency

A study of the energy reconstruction efficiency related to our processing, taking into account rise time cuts, was performed so that it could be included in the model. To achieve this, empty traces (or noise events) were selected randomly from the TUNL data. The empty traces were used to simulate uniformly distributed energies up to 1 keV with representative noise from the TUNL data. F. Vazquez de Sola Fernandez provided such events, recreating the conditions of the TUNL experiments, in a data file which gave access to the **true** energy of the events. Then, these events were processed using the same inputs as for the TUNL data, providing the **reconstructed** energy of the events. Figure 6.10 show an example of simulated pulses using the empty traces from the TUNL experiment.

The simulated events were compared to the TUNL data as shown in Figures 6.9a and 6.9b. One can see that the rise time and energy are correlated at low energies, which is well reproduced by the simulation. The events in the correlated region are mostly events with a slope in the baseline where the energy was not extracted properly by the processing (about 70 %). It is important to note that at low energies (below 200 eV), approximately 10 % of events have this slope in the baseline.

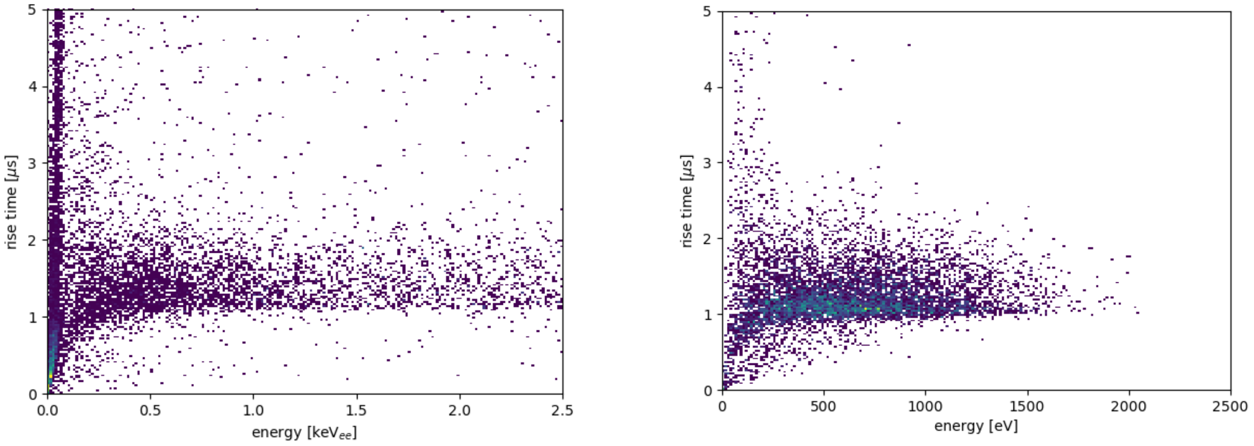

(a) Recoil data: all runs (onset cut).

(b) Simulated recoil events.

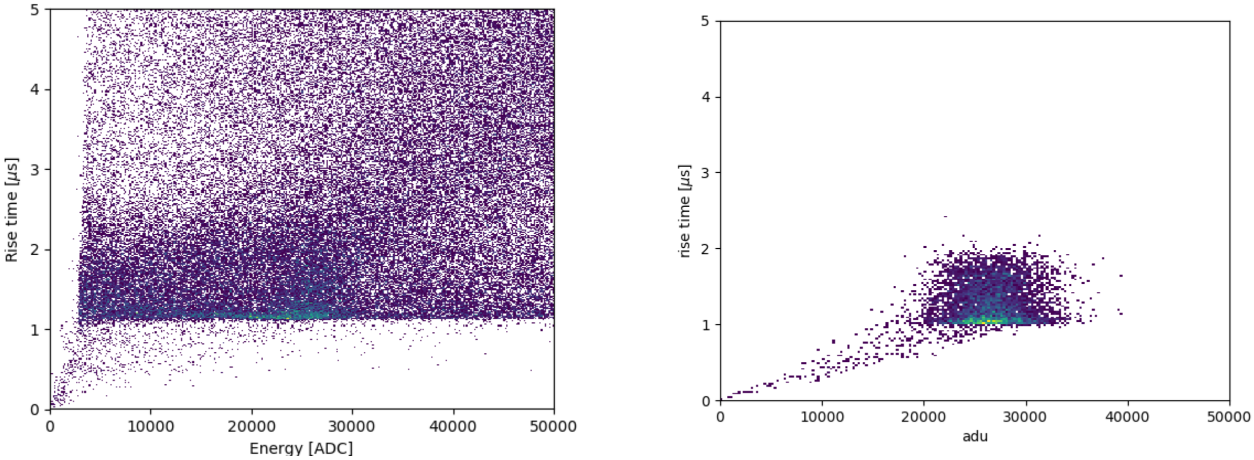

(c) Calibration data with ^{55}Fe.

(d) Simulated ^{55}Fe events.

Figure 6.9: Comparison of the rise time as a function of energy for the TUNL data (left) and the simulation (right). We can observe that the simulation reproduces well the data for both the recoils and the ^{55}Fe events (ignoring the background that is not modelled). The rise time distributions are comprised between 1 and 2 μs. Also, the two top plots show that the rise time decreases as a function of energy, thus the simulation was also able to capture such behavior.

From Figure 6.9, one can see that the lower end of the rise time distribution for the TUNL data is above 1 μs for energies above 500 eV, whereas the simulated events' rise time ends at about 0.8 μs for energies above 500 eV. Figures 6.9c and 6.9d show the ^{55}Fe from the simulation and the calibration data taken for the experiment. Once again, the lower rise time end is lower for the simulation than for the data. Thus, the lower rise time cut to select the simulated events had to be adjusted to 0.85 μs, by using the ^{55}Fe events from the simulation as it provided more events than

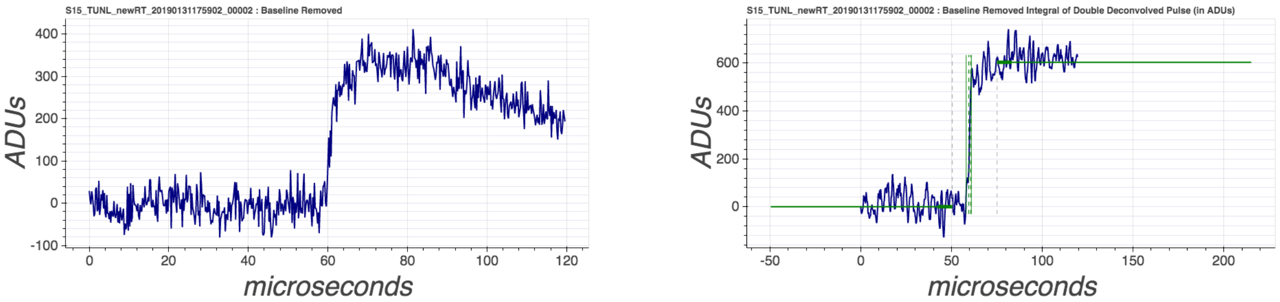

Figure 6.10: Example of simulated pulses used to build the energy reconstruction efficiency. The Figure on the left shows the raw pulse and the Figure on the right the integral of the treated pulse, using the same parameters input as the TUNL data. The **true** energy of the event is 225 eV while the reconstructed energy is 150 eV. The two green horizontal lines show where the average baseline before the beginning of the pulse and the maximum of the pulse. The two vertical dashed lines show where the pulse reaches 10 and 90 % of its amplitude, where the rise time is the difference of the two.

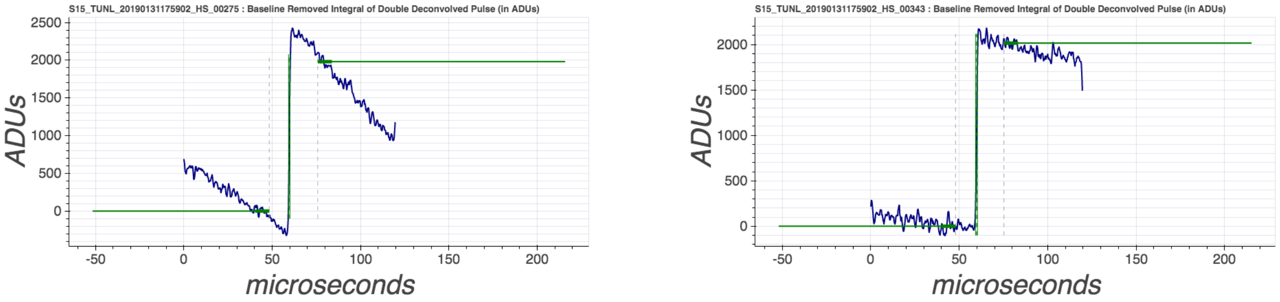

Figure 6.11: Example of the integral of treated pulses from the correlated rise time energy region. We can see that the baseline is inclined. The two green horizontal lines show where the average baseline before the beginning of the pulse and the maximum of the pulse. The two vertical dashed lines show where the pulse reaches 10 and 90 % of its amplitude, where the rise time is the difference of the two. The left plot, with the quite inclined baseline, shows that both the rise time and energy are underestimated by the processing.

the simulated recoil events, and thus the ^{55}Fe allowed an easier estimation of the low rise time end.

To build the efficiency curve, a histogram is filled with the true energies of the events. Then, the events with positive reconstructed energies and rise time between 0.85 and 2 μs are selected and a second histogram is filled with their true energy. The second row of plots in Figure 6.12 show such histograms: the left plot corresponds to the true energy spectrum and the right plot corresponds to the events that passed the reconstructed energy cut (positive energy) and rise time cuts. To obtain the efficiency curve, one can divide the latter by the former spectrum. The efficiency curves

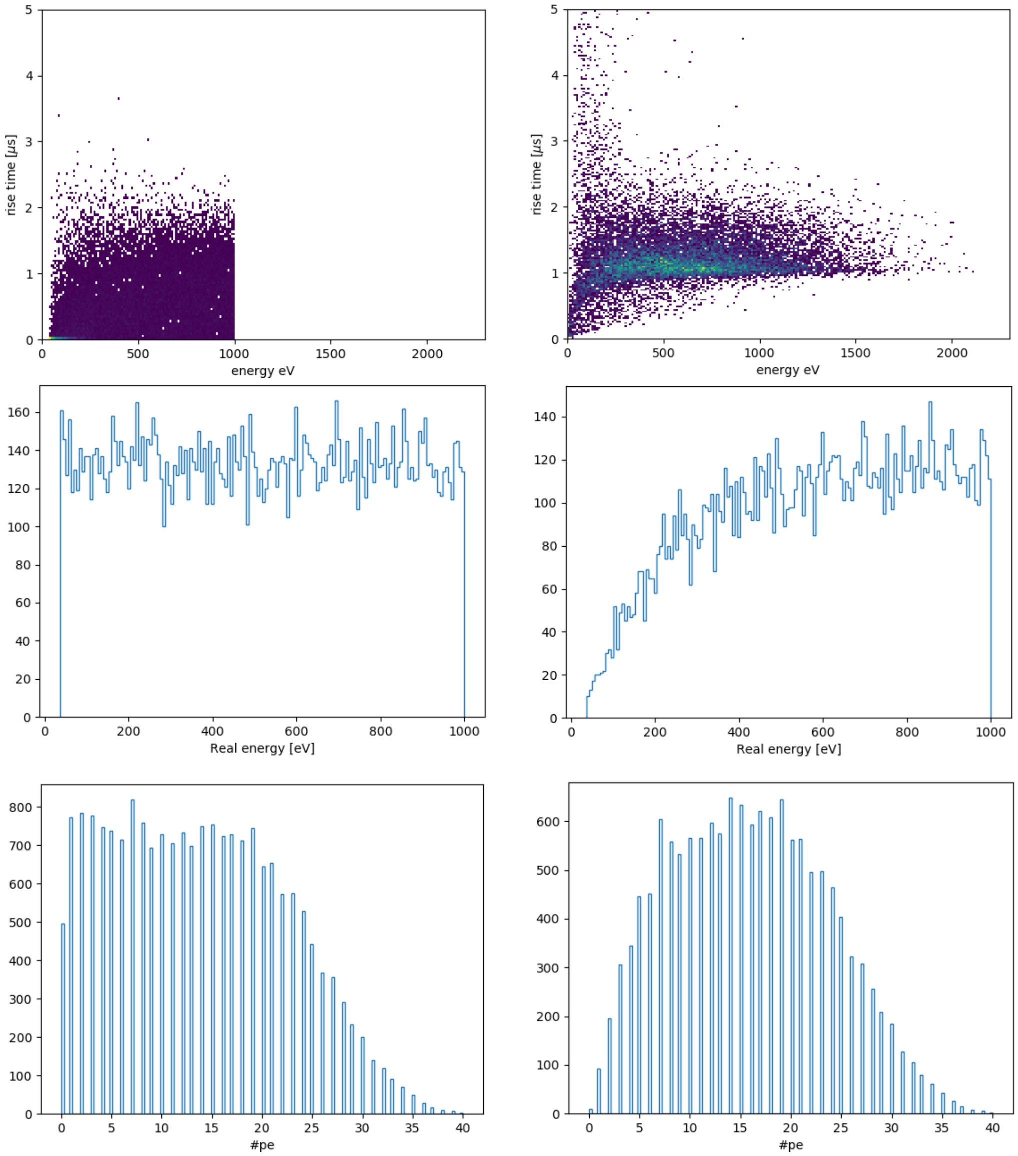

Figure 6.12: Efficiency curve construction obtained from simulated data. First row: the left plot corresponds to the rise time (reconstructed) as a function of the true energy and the right plot corresponds to the rise time as a function of the reconstructed energy. Second row: the left plot corresponds to the true energy histogram (eV) and the right plot corresponds to the true energies of the events having a positive reconstructed energy. Third row: the plots are essentially the same plots as the second row but the energies are in number of primary electrons.

as a function of the energy in eV and as a number of primary electrons are displayed Figure 6.13. Based on the simulation, the efficiency of our reconstruction reaches about 80 % at roughly 400 eV. Thus, the analysis for runs 10, 11 and 14 (1 keV and 0.34 keV), which have events mostly below

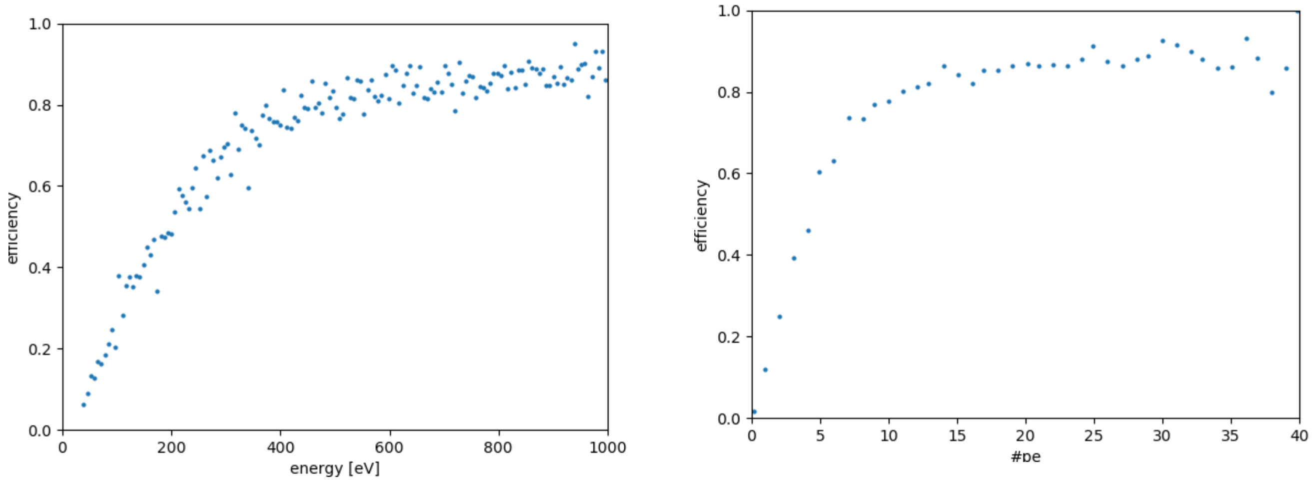

(a) Efficiency as a function of the energy in eV.

(b) Efficiency as a function of the energy in primary electrons.

Figure 6.13: Efficiency curves of the reconstructed energy by our processing (pulse treatment), which takes into account rise time cuts and positive energy cut.

400 eV is impacted by the efficiency curve.

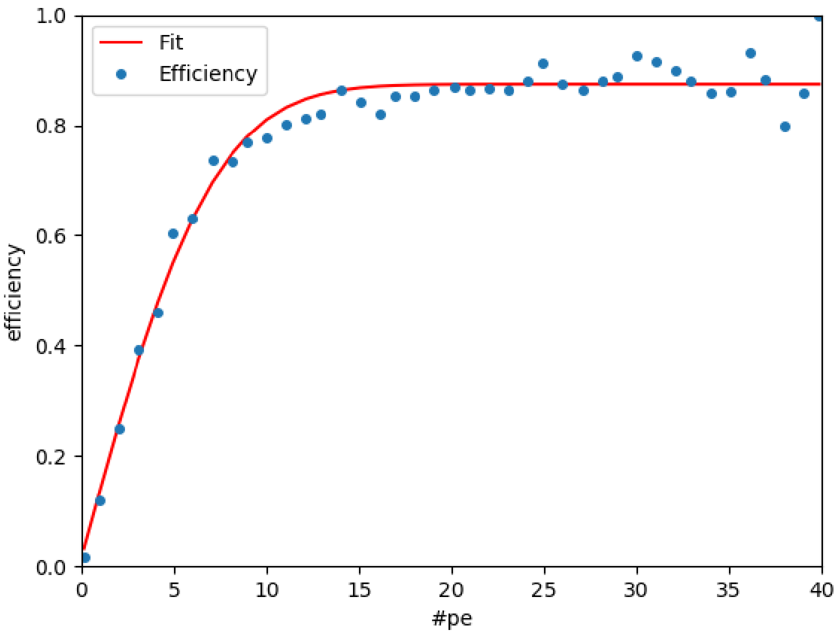

Figure 6.14: Efficiency curve as a function of the number of primary electrons, in blue. A fit was performed using equation 6.3, represented by the red curve.

The efficiency curve is fitted with an error function of the form:

$$\varepsilon(j_{pe}) = a_e \times \mathrm{erf}\left(\frac{j_{pe} - b_e}{c_e}\right) \tag{6.3}$$

where a_e, b_e and c_e are fitted coefficients, and j_{pe} the number of primary electrons. Figure 6.14 shows a fit performed to the efficiency curve, the returned values of the parameters are: a_e = 0.874 ± 0.0067, b_e = -0.12 ± 0.19 and c_e = 8.01 ± 0.43. The uncertainty on b seems quite large, but the actual impact on the resulting efficiency curve is small. Figure 6.15 shows the impact of the parameter b's error on the curve.

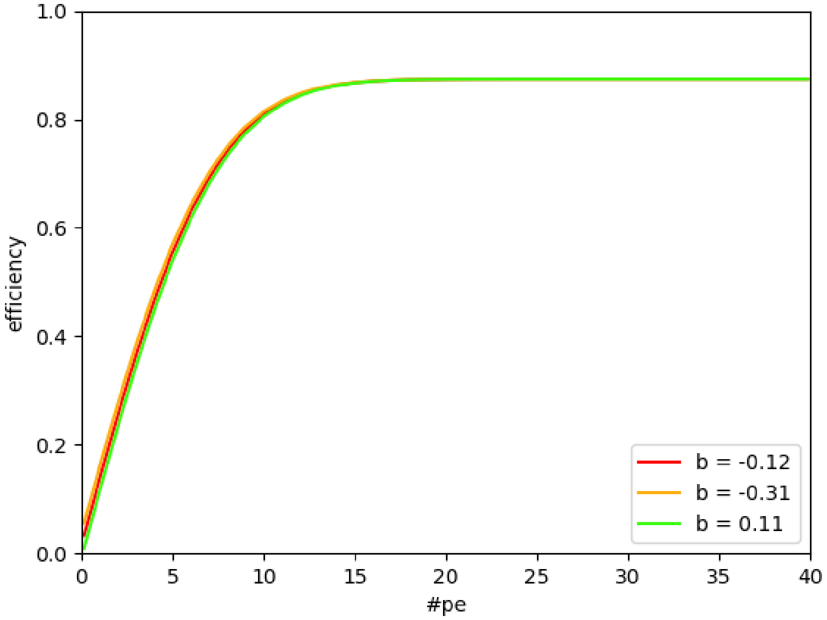

Figure 6.15: Demonstration of the small impact that the error on the parameter b has on the efficiency curve. The red curve takes into account the mean returned by the fit, and the orange and green curve represent the efficiency curve with b± 0.19.

6.3.6 Energy scale distribution

In order to account for the variations of the gain throughout the volume of this detector due to the anisotropy of the electric field lines, the energy scale is allowed to fluctuate to reproduce the phenomenon. The energy scale follows a distribution within the volume of the detector. The energy scale used to convert the data from ADC to keV units was extracted from the ^{55}Fe calibration data that sampled a small region of the detector volume in comparison to the recoil events. To support the idea that the energy scale extracted from the ^{55}Fe is sampling a smaller region than the volume sampled by the recoil events a Geant4 simulation was created using the specifications of the detector that were used for the experiment. Table 6.3 summarizes the values and conditions used in the simulation.

Parameters	Value
SPC material	Aluminum
SPC inner radius	7.3 cm
SPC thickness	3 mm
Calibration window (drilled)	1 mm
^{55}Fe location	South pole - 7.6 cm from center
Gas mixture	Ne + CH_4 (3 %)
Pressure	2 bar
Number of events simulated	1.0×10^6

Table 6.3: Table summarizing the parameters values used to simulate the ^{55}Fe events in the SPC, with the same working conditions as in TUNL.

From this simulation we estimated that about 70 % of ^{55}Fe events interacted in the southern hemisphere, while 30 % are taking place in the north. In our experiment we saw that the ^{55}Fe events taking place in the northern hemisphere do not impact the overall resolution of the calibration peak, as they are in a low energy tail. By comparing the regions of interactions between the ^{55}Fe events and the recoil events, we observed that the volume sampled, or electric field lines sampled, by these two types of events were significantly different. The ^{55}Fe events sampled a small fraction of the electric field lines in the southern hemisphere compared to the volume sampled by the recoils, happening uniformly throughout the beam line (Figures 6.16 and 6.17). Three views of the SPC in the beam line are shown Figure 6.16: side view, top view and front view. Each of them is providing a sense of where the neutrons scattered in the SPC solely based on the geometry of the experiment. For a better visualization of the SPC, the sensor as well as the rod, were drawn for a better distinction between the southern and northern hemispheres. Thus, events interacting in the

^{55}Fe sampled volume might be subject to a different electric field line density than events interacting close to the equator plan, resulting in a different gain. To account for the different possible gain in the different regions of the detector, we assume that the gain sampled by the neutron beam fluctuates with a Gaussian distribution whose mean is that measured by the ^{55}Fe spectrum and a width which is left floating in the fit. The energy points are then multiplied by the values of the energy scale chosen.

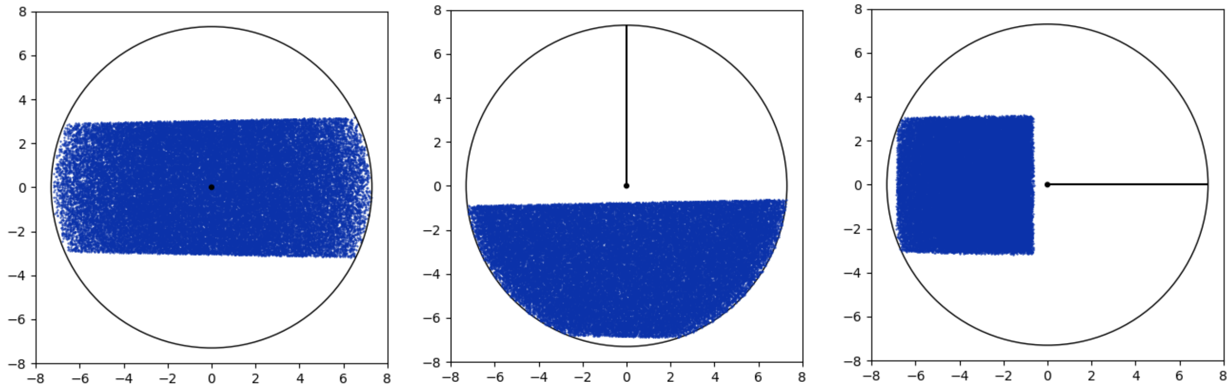

Figure 6.16: Monte Carlo simulation displaying the neutrons interaction in the southern hemisphere of the SPC. The left plot represents the side view of the experiment, the middle plot represents the top view of the experiment and the right plot corresponds to the front view of the experiment.

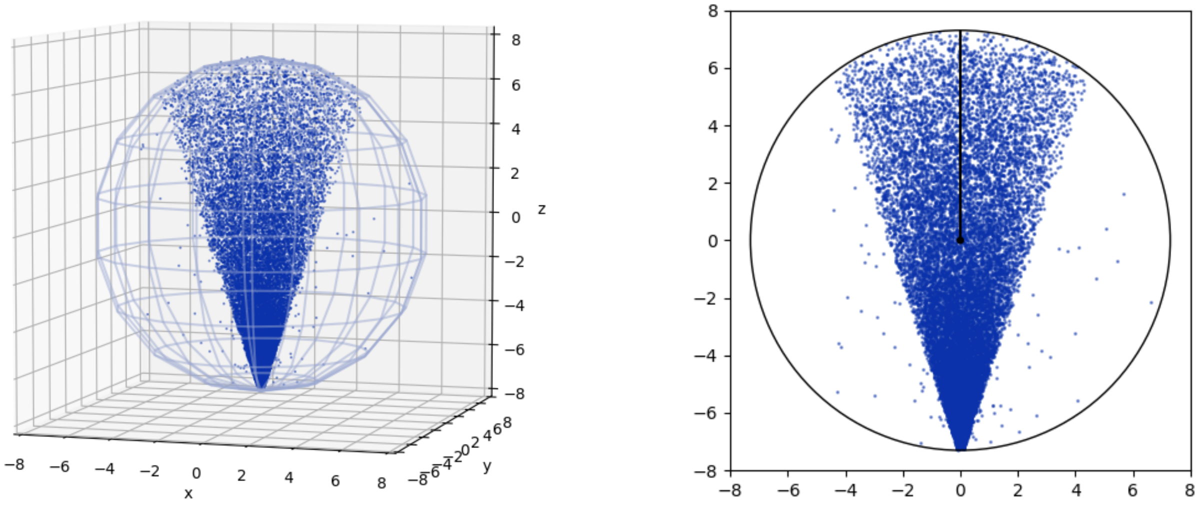

Figure 6.17: Interaction points of the ^{55}Fe calibration source in the detector a spredicted by Geant4 simulation. The distribution of these points is not identical to the region sampled by the neutron beam.

6.3.7 Tests of the model

Two tests were performed to check the accuracy of our model. The results provided by the Monte Carlo simulation generating the scattering angle distributions were compared to a Geant4 simulation. We also compared the peak shape returned by the model to calibration data.

Comparison of the scattering angle distributions from a Geant4 simulation

A Geant4 simulation recreating the conditions of the experiment and generating scattering angle distributions was developed by A. Brossard. The scattering angle distributions were compared to the scattering angle distributions generated with the Monte Carlo simulation developed in this scope, and which only took into account the geometry. Figure 6.18 shows a comparison of such scattering angle distributions. The means and standard deviations of such Geant4 simulation are given in Table 6.4 and compared with the scattering angle distributions' values from the Monte Carlo simulation. Both simulations agree quite well, within $1\,\sigma$ of the estimated errors from the Monte Carlo simulation. Thus, we are confident in using these values to characterize the scattering angle distribution in our model. The values reported by the MC simulation are thus used to estimate the quenching factor.

Run	Geant4 θ_s [^{o}]	Geant4 σ_{θ_s} [^{o}]	MC $\theta_s \pm \delta_{\theta_s}$ [^{o}]	MC σ_{θ_s} [^{o}]	Distance (cm)
8	29.23	2.7	29.02 ± 0.4	2.45	44.6 ± 0.4
7	18.9	1.53	18.84 ± 0.1	1.47	77.9 ± 0.2
14	15.68	1.17	15.63 ± 0.3	1.12	103.4 ± 1.6
9	14.38	1.1	14.33 ± 0.06	1.1	106.8 ± 0.1
10	12.5	0.93	12.48 ± 0.05	0.94	124.7 ± 0.1
14	11.19	1.07	11.13 ± 0.3	1.1	103.7 ± 1.5
11	9.43	0.65	9.4 ± 0.03	0.69	169.3 ± 0.08
14	6.38	0.98	6.33 ± 0.26	1.1	104.4 ± 0.5

Table 6.4: Comparison of the scattering angle distributions between my Monte Carlo simulation and the Geant4 simulation.

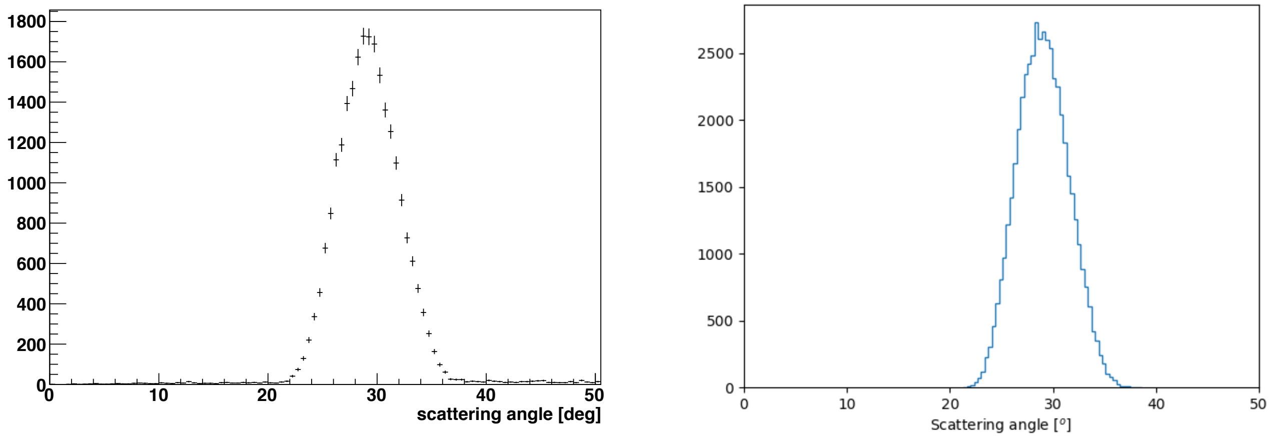

Figure 6.18: Comparison of the scattering angle distribution obtained through Geant4 simulation and simple Monte Carlo simulation. We can observe that the distributions are in good agreement with each other: they both display a Gaussian like shape, their means are 29.23^{o} and 29.02^{o} for the Geant4 and Monte Carlo simulations, respectively, and their standard deviations are2.7^{o} and 2.45^{o} for the Geant4 and Monte Carlo simulations, respectively.

Comparison of the peak shape with calibration data

The detector response component of the model was validated by using a simple Monte Carlo simulation using the model developed in the scope of the TUNL data, to reproduce the ^{55}Fe calibration data. The Monte Carlo simulation took as input the mean energy emitted by an ^{55}Fe source, 5.9 keV, the characteristics of the gas used and the response of the detector. The simulation produced an expected observed peak shape for ^{55}Fe events. Figures 6.19a and 6.19b show the expected peak shape of the ^{55}Fe generated by the MC simulation and the ^{55}Fe data. We used data taken in the Queen's Lab with the same detector we used at TUNL within few days of the experiment, and the data taken on site with beam OFF. We did not use the TUNL calibration data for the comparison with the simulation because the extraction of a clean ^{55}Fe peak was challenging, for reasons listed in Section 5.3. Table 6.5 shows the results of a Gaussian fit to the three ^{55}Fe peaks: data and simulation. The means are in agreement within 1 σ error, which represents about 0.1 % of the returned value. The standard deviations do not agree within error, which is 1.1 % of the returned value by ROOT. The value of the standard deviation for the simulation is within 1 σ with one of the ^{55}Fe peaks and within 4.3 % away from the standard deviation of the other ^{55}Fe data. The simulation and the data are in good agreement, showing similar resolution, and thus, it allows us to conclude that our model for the ^{55}Fe is a successful at describing the calibration data beam OFF. The ^{55}Fe events are expected to follow the same behavior with beam ON, as the resolution is not expected to be dependent on the beam activity, as observe during the 2018 preliminary campaign, see Appendix A.

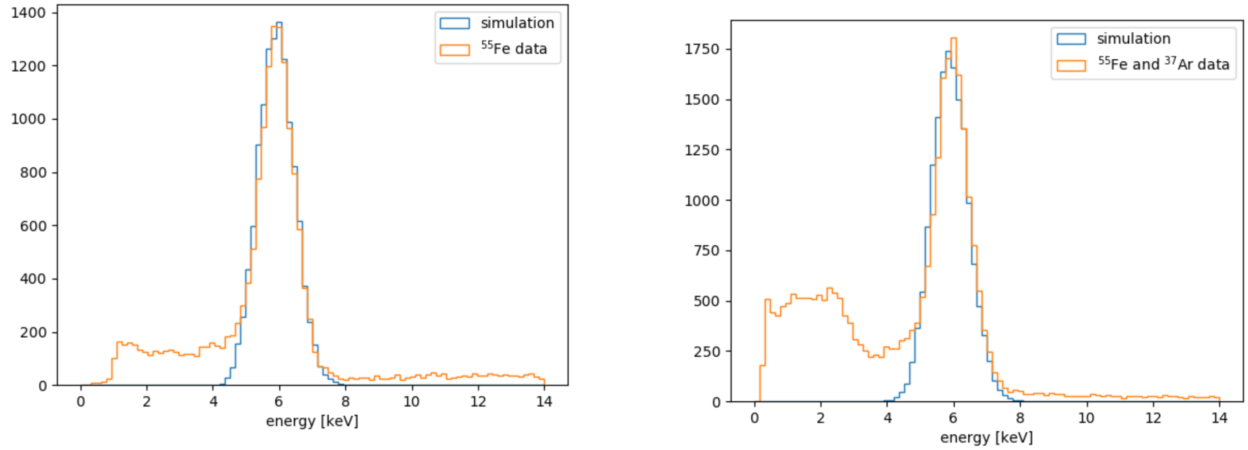

(a) Comparison of the ^{55}Fe data taken at Queen's a few days before the TUNL experiment (ta23x000_DD2_q00.root) and the expected peak shape of the ^{55}Fe.

(b) Comparison of the ^{55}Fe data taken at TUNL with ^{37}Ar (SIS3316_20190129211525.root) and the expected peak shape of the ^{55}Fe.

Figure 6.19: Comparison of the ^{55}Fe peak simulation and data at TUNL and at Queen's University. The two comparisons show good agreement between the data and the model, showing similar width, and thus resolution, of the ^{55}Fe peak.

	Mean	Standard deviation
^{55}Fe data taken at Queen's	$5.89 \pm 6.38 \times 10^{-3}$ keV	$0.58 \pm 7.52 \times 10^{-3}$ keV
^{55}Fe (^{37}Ar) data taken at TUNL	$5.90 \pm 5.8 \times 10^{-3}$ keV	$0.557 \pm 6.22 \times 10^{-3}$ keV
Monte Carlo ^{55}Fe	$5.90 \pm 7.21 \times 10^{-3}$ keV	$0.555 \pm 5.20 \times 10^{-3}$ keV

Table 6.5: Comparison of the ^{55}Fe peak simulation and data at TUNL and at Queen's University. The peaks were fitted with a Gaussian, we are reporting the means and standard deviation as returned by ROOT. The means reported by the fit show agreement within error, which represents about 0.1 % of the returned value. The standard deviations reported by the fit show reasonable agreement, the standard deviation reported for the simulation agrees within error with the ^{55}Fe peak from TUNL, but do not agree within error with the standard deviation of the ^{55}Fe peak from Queen's.

6.4 Background and noise peak model

In order to model the background in the SPC energy spectrum, we selected events outside of the "signal onset time window", which is between 40 and 55 μs. Except for the onset time cut selection, all the other cuts are the same as for the recoil events. Figure 6.20a shows the background spectrum obtained for run 8 by selecting events in the background onset time window: 60 to 75 μs. It shows at low energy a noise peak below 80 eV and a flat event distribution up to 10 keV. The background spectra that we built with this method displayed some discrepancies with observations from the signal energy spectra: the mean of the noise peak is at higher energies shifted by 5.26 eV and the amplitude of the flat background is smaller than the flat background observed in the signal energy spectra. Figure 6.20b shows the signal and background energy spectra, which shows that the flat background contribution from the signal spectrum (red) is less than expected. By looking at the number of events of a background only region, we found that there were 2.6 times more events from the signal onset time window than events coming from the outside onset time window, 57 against 22 events, respectively. The reason for such discrepancies between the signal and background windows is unknown.

Figure 6.21 shows the noise peaks of all energy runs normalized by their time exposure. We can see that after normalization, most of the runs have comparable noise peak's integral. Table 6.6 shows the integrals of the noise peaks. Runs 8, 7, and 14 at 0.34 keV_{nr} have the largest integrals. The noise peak for run 14 at 0.34 keV_{nr} was expected to have comparable integrals with the two other energies taken during run14. We think that the discrepancy between this particular energy and the two others are coming from the very low nuclear recoils contamination in the noise peak.

In order to avoid difficulties associated with modelling a fluctuating noise peak, we imposed an energy cut on the data and only implemented a flat background, modelled as a uniform distribution in energy.

In order to determine a robust lower energy threshold for the analysis, we looked at the location

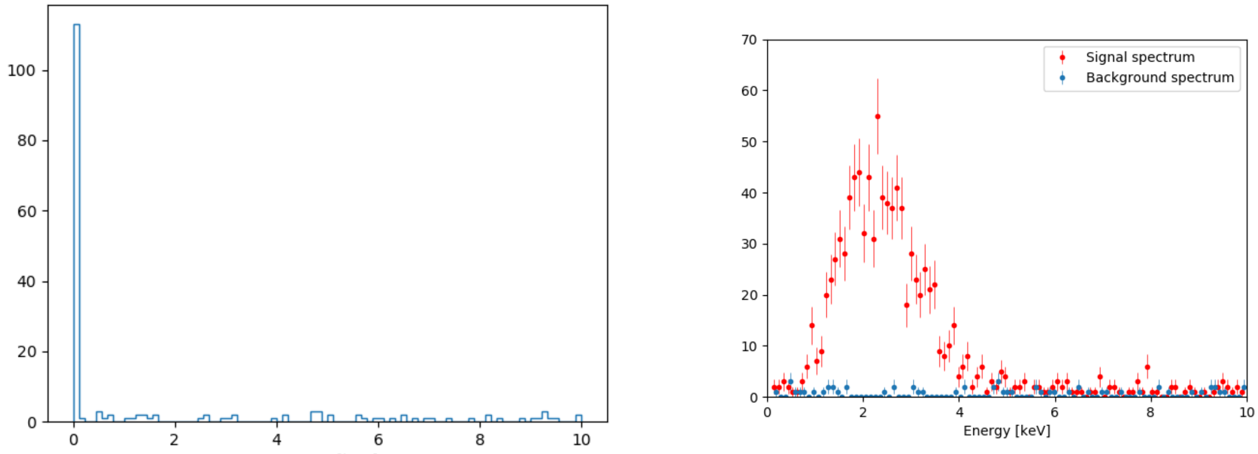

(a) Background spectrum from run8.

(b) Overlap of the signal and background spectra.

Figure 6.20: Study of the background energy spectru

of the noise peak relative to the recoil data in the runs. A study of the noise peak was performed in order to assess at which energy the noise peak is no longer a contamination to the signal or the flat background. Figure 6.22 shows the eight signal energy spectra zoomed in to the noise peak. The noise peaks were modelled with a gaussian, and their means and standard deviations are reported in Table 6.6. An observation from Figure 6.22 and Table 6.6 is that the width of the noise peak depends on the time exposure. Thus, the longer the time exposure is, the wider the noise peak is. Thus, our energy cut will be set from run 14. Thus, a rather conservative low energy analysis threshold of 100 eV was chosen.

	run 8	run 7	run 9	run 10	run 11	run 14 2 $\mathrm{keV_{nr}}$	run 14 1 $\mathrm{keV_{nr}}$	run 14 0.34 $\mathrm{keV_{nr}}$
μ [$\mathrm{eV_{ee}}$]	39.8	44.20	39.73	37.45	40.02	35.03	38.01	35.50
σ [$\mathrm{eV_{ee}}$]	17.05	17.41	16.14	19.38	17.55	20.84	23.31	22.08
Integral	0.416	0.416	0.28	0. 22	0.29	0.26	0.30	0.46

Table 6.6: Mean, standard deviation and integral of the eight noise peaks. Note how the noise peak becomes wider with the time exposure.

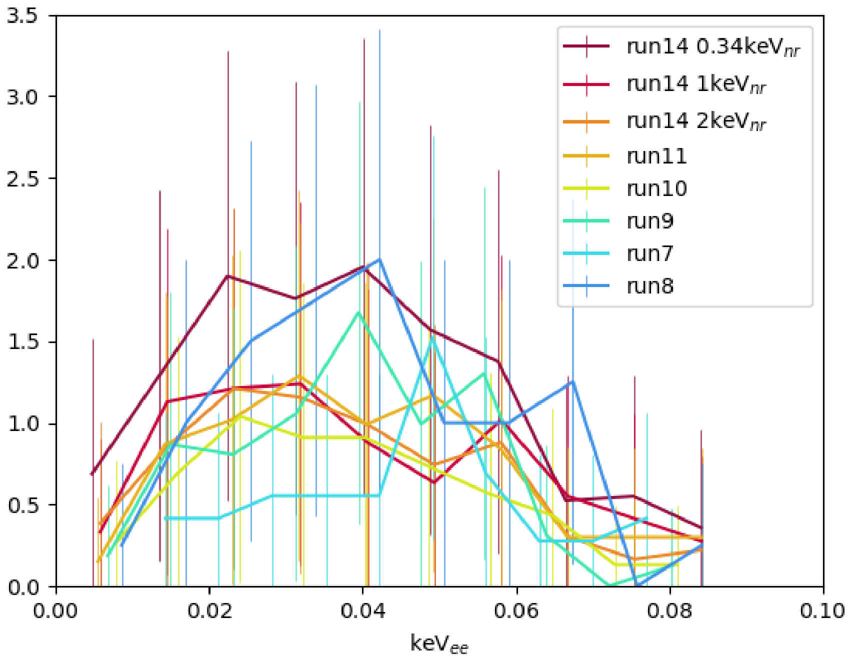

Figure 6.21: Normalized in time noise peaks from the eight energy runs from the signal energy spectra.

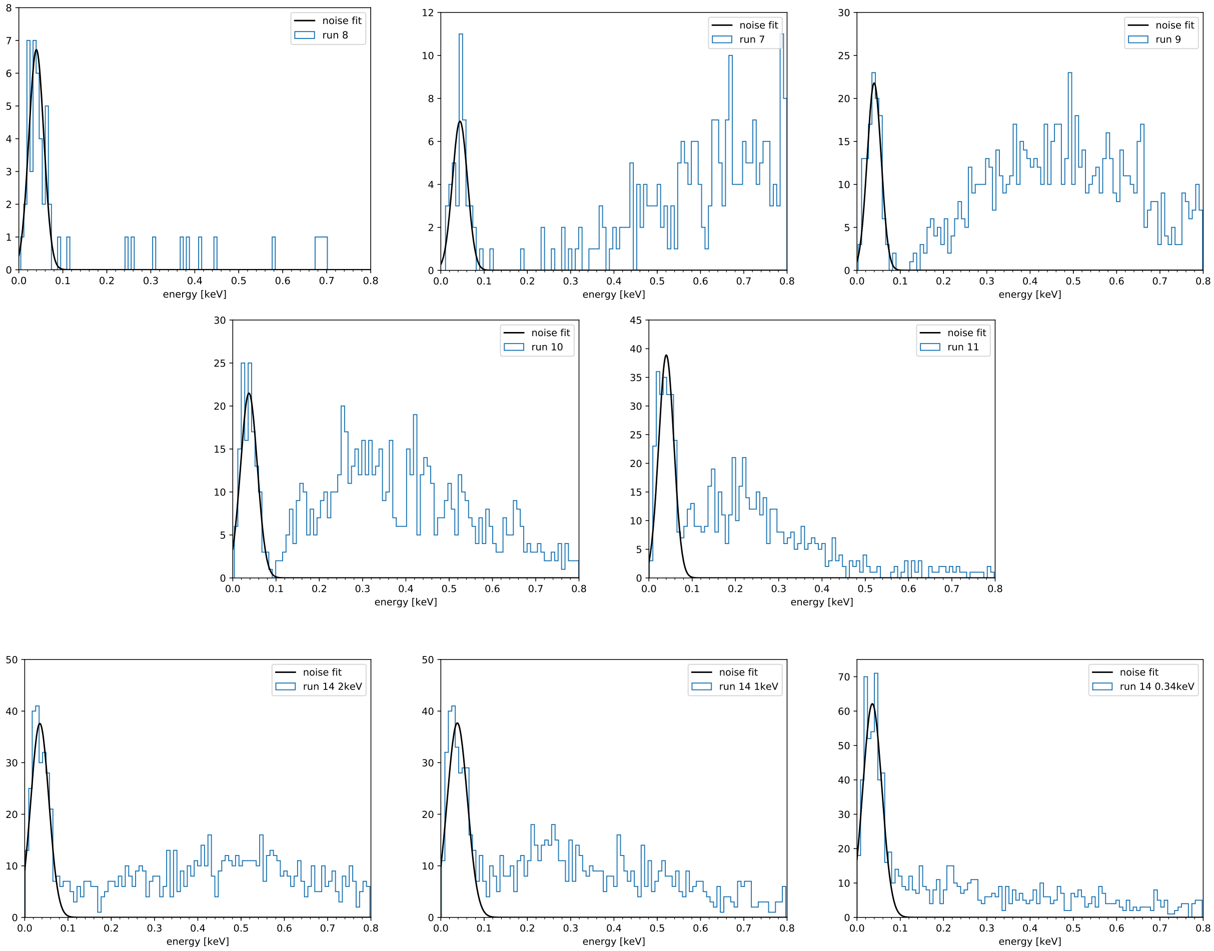

Figure 6.22: Zoom of the energy spectra with a focus on the noise peak.The black line shows a fit to the noise peak. The energy spectra are organized by experimental configuration: the energies taken with the annulus structure are on the first two rows, then multiple energy configuration on the last row. These fits were used to estimate the energy where the contamination from the noise peak would be much less than the flat background and/or the recoil events, and thus to estimate the energy threshold of the analysis.

6.5 Bayesian analysis

This Section focuses on the analysis methodology used to extract the quenching factor. A Bayesian analysis was performed using the model discussed in Section 6.3.

A joint unbinned fit over the data sets from the different run configurations was performed. The energy ranges shared by multiple runs provided an increased statistical accuracy on the quenching factor.

The minimizer chosen for this analysis is iminuit [106] a python package based on the Minuit minimization library [107] [108].

6.5.1 Bayesian framework

Bayes' theorem can be derived from conditional probability:

$$P(A|B) = \frac{P(A \cap B)}{P(B)} \tag{6.4}$$

where P(A $\cap$ B) is the joint probability of having both A and B true. The joint probability can be written as:

$$P(A \cap B) = P(A|B)P(B) = P(B|A)P(A) \tag{6.5}$$

and finally we get Bayes' theorem:

$$P(A|B) = \frac{P(B|A)P(A)}{P(B)} \tag{6.6}$$

Bayes' theorem gives the probability of observing the model parameters given the data. The posterior probability function is given by:

$$P(\vec{\theta}|\vec{x}) = \frac{L(\vec{x}|\vec{\theta})P(\vec{\theta})}{P(\vec{x})}. \tag{6.7}$$

where $\vec{\theta}$ are the N observations of x, and θ are the parameters of the experiment.
The likelihood $L(\vec{x}|\vec{\theta})$ represents the probability to observe the data given the parameters. $P(\vec{\theta})$ represents the prior probability distribution for the model parameters, which describes the prior knowledge of the parameters and is often provided by experimental measurements. In the case where no knowledge on the parameters is available, the prior is called non-informative and it is common to use a constant distribution, known as flat prior. $P(\vec{x})$ is called the evidence and is the probability of observing the data $\vec{x}$ and is independent of the values of the parameters, θ, of interest. Since $P(x)$ does not depend on the model parameters being fit, it appears as a scaling factor which is not relevant when fitting a model to the data.

To extract the quenching factor, a Bayesian fit of the model to the recoil energy spectra using the posterior probability was performed. One can use the maximum of the posterior to find the central values of the parameters that are the most likely to reproduce the data. The posterior probability was built using the likelihoods from each energy run as well as (informative) prior distributions on neutron scattering angles obtained from the known geometry. The next section, we derive the likelihood functions that were used in the analysis.

6.5.2 Likelihood

The extended likelihood for a single energy run, j, is:

$$L_j(\vec{x}|\vec{\theta}) = \frac{\mu_j^{N_j}}{N_j!} e^{-\mu_j} \prod_i^{N_j} P(x_i), \tag{6.8}$$

where $\vec{x}$ represents the set of data of the energy run, $\vec{\theta}$ represents the parameters of the experiment we use in our model, μ_j represents the expected number of events in run j, and N_j represents the observed number of events in run j. The first term represents the Poisson probability of observing N_j events from an expected number of events μ_j. $P(x_i)$ represents the probability of observing the energy x_i. In our case we consider 2 types of events, the recoil events that constitute our signal and background events. The total probability of observing an event of energy x_i can be written as:

$$P_{tot}(x_i) = P(x_i \mid \mathrm{s})P(\mathrm{s}) + P(x_i \mid \mathrm{BG})P(\mathrm{BG}). \tag{6.9}$$

Where s represents the signal, or recoil events, and BG represents the background. We can rewrite this as:

$$P_{tot}(x_i) = P_s(x_i)f_s + P_{BG}(x_i)f_{BG} = P_s(x_i)\frac{\mu_s}{\mu_s + \mu_{BG}} + P_{BG}(x_i)\frac{\mu_{BG}}{\mu_s + \mu_{BG}}, \tag{6.10}$$

where P_s represents the probability density function of observing the energy x_i from a signal event, f_s represents the expected fraction of signal events, P_{BG} represents the probability density function of observing the energy x_i from a background event, f_{BG} the fraction of expected background events, μ_s and μ_{BG} being the expected number of signal and background events, respectively.

For computational reasons the natural logarithm of the likelihood is used when computing the maximum (or minimum) of the likelihood function. The logarithm is a monotonically increasing function, this characteristic is important because it ensures that the maximum value of the log likelihood is at the same point as the likelihood function.

The negative log-likelihood of Equation 6.8 is:

$$\begin{aligned}
-\ln(L) &= \mu - N\ln(\mu) + \ln(N!) - \sum_i^N \ln\Big(P(x_i)\Big) \\
&= \mu - N\ln(\mu) + \ln(N!) - \sum_i^N \ln\Big(P_s(x_i)f_S + P_{BG}(x_i)f_{BG}\Big) \\
&\sim -\sum_i^N \ln\Big(P_s(x_i)f_s + P_{BG}(x_i)f_{BG}\Big)
\end{aligned} \tag{6.11}$$

where in the last expression, we removed the first three terms with μ and N since they are irrelevant for the fit, as they do not depend on the investigated parameters. Thus, the likelihood function only depends on the expected fraction of signal event (indeed f_{BG} = (1-f_s)), the probability density function of getting the energy x_i from a signal event, $P_s(x_i)$, and the probability density function of getting the energy x_i from a background event, $P_{BG}(x_i)$.

To describe the background events we used the background model described in Section 6.4 and to describe the signal events we used the model described in Section 6.3. The energy distribution for the background is uniform in energy, while the model describing the recoil events takes into account the scattering angle and neutron energy distributions, the quenching factor, the response and resolution of the detector, and the energy reconstruction efficiency of the processing used on the data.

We want to write $P_s(x_i|\vec{\theta}, I)$ as a function of the parameters of our model. For this, we condition the probability $P_s(x_i|\vec{\theta}, I)$ relative to the number of primary electrons, j_{pe}, created in the gas, and express P_s in terms of the response of the detector subject to Poisson and Polya fluctutations:

$$\begin{aligned} P_s(x_i|\vec{\theta}, I) &= \sum_{j_{pe}=1}^{N_{pe,max}} P(x_i, j_{pe}|\vec{\theta}, I) \\ &= \sum_{j_{pe}=1}^{N_{pe,max}} P(x_i|j_{pe}, \vec{\theta}, I) P(j_{pe}|\vec{\theta}, I) \end{aligned} \tag{6.12}$$

Where $N_{pe,max}$ is the maximum number of primary electrons, which is determined by the upper limit of the fitting energy range.

This operation allows to derive $P_s(x_i|\vec{\theta}, I)$ as a function of the number of primary electrons. $\vec{\theta}$ represents the free parameters of our model, amongst others the quenching factor's parameters, α and β, while I represents the other parameters of our model which are fixed in the fit, like the W-value. The expected number of primary electrons depends on the quenching factor, the W-value, the neutron energy, the scattering angle and the gain.

As aforementioned, this step also allows to derive $P_s(x_i|\vec{\theta}, I)$ as a function of other probabilities: $P(x_i|j_{pe}, \vec{\theta}, I)$, which represents the probability of observing the energy x_i given a number of primary electrons, and $P(j_{pe}|\vec{\theta}, I)$, which represents the probability of observing j_{pe} primary electrons given the parameters of the model. From Section 3.2.3, we know that the probability of observing S secondary electrons given a number N of primary electrons describes the avalanche process (or secondary ionization), which is modelled by the convolution of Polya distributions. We also know that the probability of observing N number of primary electrons given an expected number of primary electrons, set by the model's parameters, describes the primary ionization and is modelled following a Poisson distribution.

We assume the number of primary electrons is given by a Poisson distribution and the number of secondary electrons is given by a convolution of Polya distributions, and so we can write Equation 6.12 as:

$$P_s(x_i|\vec{\theta}, I) = \sum_{j_{pe}=1}^{N_{pe,max}} P^{N^{th}}_{\text{Polya}}(x_i|j_{pe}, \vec{\theta}, I) P_{\text{Poisson}}(j_{pe}|\vec{\theta}, I), \tag{6.13}$$

the negative log-likelihood becomes:

$$-\ln(L) = -\sum_{i}^{N} \ln\Big(f_s \sum_{j_{pe}=1}^{N_{pe,max}} P^{N^{th}}_{\text{Polya}}(x_i|j_{pe}, \vec{\theta}, I) P_{\text{Poisson}}(j_{pe}|\vec{\theta}, I) + f_{BG} P_{BG}(x_i)\Big). \tag{6.14}$$

As explained in Section 6.3 the recoil peak depends on the neutron energy and scattering angle distributions, thus they need to be included in the likelihood. For this, we integrate over all possible neutron energy, E_n, and scattering angle, θ_s, values that are within $\mu_{E_n} \pm 4\sigma_{En}$ and $\mu_{\theta_s} \pm 4\sigma_{\theta_s}$ ranges, respectively. Then, the probability of each neutron energy (scattering angle) sample is calculated following a normal distribution of mean μ_{E_n} (μ_{θ_s}) and standard deviation σ_{E_n} (σ_{θ_s}).

For more clarity, let's write explicitly the quenching factor parameters, α and β, the neutron energy and the scattering angle distributions in the negative log-likelihood:

$$\begin{aligned}
-\ln(L) = -\sum_{i}^{N} \ln\Bigg(f_s \Big(\sum_{j_{pe}=1}^{N_{pe,max}} P^{N^{th}}_{\text{Polya}}(x_i \mid j_{pe}, I) \int_{\theta_s} \int_{E_n} P_{\text{Poisson}}(j_{pe} \mid \theta_s, E_n, \alpha, \beta, I) \\
\times P_{\theta_s}(\theta_s \mid \mu_{\theta_s}, \sigma_{\theta_s}, E_n, I) P_{E_n}(E_n \mid \mu_{E_n}, \sigma_{E_n}, I)\Big) + (1 - f_s) P_{\text{BG}}(x_i)\Bigg)
\end{aligned} \tag{6.15}$$

where P_{θ_s} represents the probability for a particular scattering angle, θ_s, and P_{E_n} represents the incident neutron energy probability. P_{θ_s} only depends on μ_{θ_s} and σ_{θ_s}, and P_{E_n} only depends on

μ_{E_n} and σ_{E_n}. Thus, we can remove the other variables from these probabilities:

$$
\begin{aligned}
-\ln(L) = -\sum_{i}^{N} \ln \Bigg(f_s \Big(\sum_{j_{pe}=1}^{N_{pe,max}} P^{N^{th}}_{\text{Polya}}(x_i \mid j_{pe}, I) \int_{\theta_s} \int_{E_n} P_{\text{Poisson}}(j_{pe} \mid \theta_s, E_n, \alpha, \beta, I) \\
\times P_{\theta_s}(\theta_s \mid \mu_{\theta_s}, \sigma_{\theta_s}) P_{E_n}(E_n \mid \mu_{E_n}, \sigma_{E_n}) \Big) + (1 - f_s) P_{\text{BG}}(x_i) \Bigg)
\end{aligned}
\tag{6.16}
$$

Now, we include the energy scale fluctuation. The energy scale distribution was modelled by a normal distribution of mean 1, normalized to the ADC/eV conversion factor from the ^{55}Fe, and standard deviation σ_a, which is a free parameter of the fit. We note, that we allow the energy scale to fluctuate by an arbitrary standard deviation in order to account for possible gain fluctuation in the volume sampled by the recoil events. In the likelihood, this fluctuation is included by multiplying the energy x_i by a percentage of the energy scale, following the distribution aforementioned, and summing over all possible values of the energy scale.

$$
\begin{aligned}
-\ln(L) = -\sum_{i}^{N} \ln \Bigg(f_s \Big(\sum_{j_{pe}=1}^{N_{pe,max}} \int_a P_{\text{Polya}}(x_i \mid a, j_{pe}, I) P_a(a \mid \mu_a, \sigma_a) \times \\
\int_{\theta_s} \int_{E_n} P_{\text{Poisson}}(j_{pe} \mid \theta_s, E_n, \alpha, \beta, I) \times P_{\theta_s}(\theta_s \mid \mu_{\theta_s}, \sigma_{\theta_s}) P_{E_n}(E_n \mid \mu_{E_n}, \sigma_{E_n}) \Big) \\
+ (1 - f_s) P_{\text{bg}}(x_i) \Bigg)
\end{aligned}
\tag{6.17}
$$

The reconstruction efficiency curve developed in Section 6.3.5 is included:

$$
\begin{aligned}
-\ln(L) = -\sum_{i}^{N} \ln \Bigg(f_s \Big(\sum_{j_{pe}=1}^{N_{pe,max}} \varepsilon(j_{pe}) \int_a P_{\text{Polya}}(x_i \mid a, j_{pe}, I) P_a(a \mid \mu_a, \sigma_a) \times \\
\int_{\theta_s} \int_{E_n} P_{\text{Poisson}}(j_{pe} \mid \theta_s, E_n, \alpha, \beta, I) \times P_{\theta_s}(\theta_s \mid \mu_{\theta_s}, \sigma_{\theta_s}) P_{E_n}(E_n \mid \mu_{E_n}, \sigma_{E_n}) \Big) \\
+ (1 - f_s) P_{\text{bg}}(x_i) \Bigg)
\end{aligned}
\tag{6.18}
$$

We remind that I denotes fixed parameters of the model that are not specified: the mean gain: $\langle G \rangle$=1000, the W-value and θ_p: 27.6 eV and 0.12 respectively [66]. P_a, P_θ and P_{E_n} are the distributions of the energy scale, the scattering angle and the neutron energy respectively. They are modelled as normal distributions with means: μ_a, μ_{θ_s} and μ_{E_n} and standard deviations: σ_a, σ_{θ_s} and σ_{E_n}. a is the energy scale, E_n is the neutron energy, θ_s is the scattering angle, $N_{pe,max}$ is the maximum number of primary electrons, α and β the parameters of the quenching factor function.

Isotopes	^{20}Ne	^{22}Ne	^{27}Al	^{12}C	^{13}C	H
Number of interactions in the gas	25600	1887	7	541	8	3787

Table 6.7: Summary of the number of elastic neutron-nucleus scattering for different target isotopes. These results were generated from a Geant4 simulations of 10^7 neutrons toward the SPC (A. Brossard).

The gas mixture used for the experiment was Ne+CH$_4$ (3 %). The two most common isotopes of neon present are ^{22}Ne and ^{20}Ne with abundances: 9.25 % and 90.48 %, respectively. The abundance of ^{21}Ne being of 0.27 % we assumed for the analysis that the neutron interactions with this isotope is negligible. For more details on the interaction rates on other isotopes present in the gas mixture a Geant4 simulation was developed by A. Brossard. Table 6.7 summarizes the different interaction rates. The interaction rate of ^{12}C recoils represents 1.7 % of all interactions. The contribution on hydrogen is significant, but the recoil energy observed are above 20 keV$_{\mathrm{ee}}$ and thus above our fitting range (see Section 6.5.3). Thus, our model does not take into account interactions on such isotopes. The contamination from aluminum recoils in the gas was estimated to be 0.02 %, which is negligible compared to the other interaction rates.

The interaction fractions for the two neon isotopes were calculated by A. Brossard using Geant4. The calculations took into account: the density of the gas, the composition of the gas, and the cross section for neutrons of energy 545 keV with the different isotopes. The interaction fractions for ^{22}Ne and ^{20}Ne were included in the likelihood:

$$-\ln(L) = \sum_{i}^{N} \left[\ln \left(f_S\Big(0.924 P_s^{^{20}Ne}(x_i) + 0.076 P_s^{^{22}Ne}(x_i)\Big) + (1 - f_S) P_{BG}(x_i) \right) \right], \tag{6.19}$$

In our model, we assume the ^{22}Ne and ^{20}Ne have the same quenching factor and the same

W-value. The only difference between the two isotopes is the nuclear recoil energy, which depends on the mass of the target.

6.5.3 Posterior

The final function that we want to minimize includes Gaussian priors on the scattering angle means, coming from measurements and simulations. The posterior for one energy run is:

$$\begin{aligned} -\ln(P) = -\sum_{i}^{N} \Bigg[\ln \Bigg(& f_S \Big(0.924 P_s^{^{20}Ne}(x_i) + 0.076 P_s^{^{22}Ne}(x_i) \Big) + \\ & (1 - f_S) P_{BG}(x_i) \Bigg) - \ln(p_{\theta_s}(\theta_i)) \Bigg], \end{aligned} \tag{6.20}$$

where p_{θ_s} the Gaussian prior on the scattering angle.
By including Equation 6.18, which was the likelihood contribution for one isotope, in Equation 6.20, we get:

$$\begin{aligned} -\ln(P) = -\sum_{i}^{N} \Bigg[\ln \Bigg(& f_s \Big(f_{^{20}Ne} \sum_{j_{pe}=1}^{N_{pe,max}} \varepsilon(j_{pe}) \times \int_a P_{\text{Polya}}(x_i \mid a, j_{pe}, I) P_a(a \mid \mu_a, \sigma) \times \\ & \int_{\theta_s} \int_{E_n} P_{\text{Poisson}}(j_{pe} \mid \alpha, \beta, \theta_s, E_n, I) \times P_{\theta_s}(\theta \mid \mu_{\theta_s}, \sigma_{\theta_s}) P_{E_n}(E_n \mid \mu_{E_n}, \sigma_{E_n})) + \\ & f_{^{22}Ne} \sum_{j_{pe}=1}^{N_{pe,max}} \varepsilon(j_{pe}) \times \int_a P_{\text{Polya}}(x_i \mid a, j_{pe}, I) P_a(a \mid \mu_a, \sigma) \times \\ & \int_{\theta_s} \int_{E_n} P_{\text{Poisson}}(j_{pe} \mid \alpha, \beta, \theta_s, E_n, I) \times P_{\theta_s}(\theta_s \mid \mu_{\theta_s}, \sigma_{\theta_s}) P_{E_n}(E_n \mid \mu_{E_n}, \sigma_{E_n}) \Big) + \\ & (1 - f_s) P_{\text{bg}}(x_i) \Bigg) - \ln(p_{\theta_s}(\theta_i)) \Bigg] \end{aligned} \tag{6.21}$$

Finally, the sum of the 8 negative log-posteriors (8 runs) is minimized, thus constraining the common values of the parameters, α, β and σ_a:

$$\ln \Big(P(I, \vec{\theta} | x_i) \Big) = \sum_{j}^{runs} \ln \Big(P_j(I, \vec{\theta} | x_i) \Big) \tag{6.22}$$

The fraction of expected signal events for each run, the parameters of the quenching factor, α

and β, the scattering angle mean for each run, θ_s, and the standard deviation of the energy scale distribution, σ_a, are free parameters of the fit. The quenching factor parameters and the standard deviation of the energy scale are common to all energy runs. Overall, the fit has 19 free parameters (f_s and θ_s for each energy run, α, β and σ_a) and 6 fixed parameters (E_n, σ_{E_n}, σ_{θ_s}, θ_p, the W-value and the mean gain). f_s and σ_a were bounded by limits between 0 and 1.

Parameters	Status in fit	Values
Expected fractions of signal events: f_{sj}	Free	-
Scattering angle means: θ_{sj}	Free	Prior
Quenching factor parameter: α	Free	-
Quenching factor parameter: β	Free	-
Standard deviation of the energy scale: σ_a	Free	-
Neutron energy mean: μ_{E_n}	Fixed	545 keV [*]
Neutron energy standard deviation: σ_{E_n}	Fixed	20 keV [*]
Scattering angle standard deviations: $\sigma_{\theta_{sj}}$	Fixed	Table 5.1
Mean ionization energy: W-value	Fixed	27.6 eV [66]
Mean gain: $\langle G \rangle$	Fixed	1000
Shape Polya: θ_P	Fixed	0.12 [66]

Table 6.8: Table summarizing the parameters in the analysis, their status in the fit and their values if fixed. Their are 19 free parameters and 6 (more exactly 13) fixed parameters. [*] Values communicated by our collaborators at TUNL, see Section 5.1.2.

6.6 Test: bias and pull plots

The first step before checking any bias is to generate fake data sets with the model we are using in the analysis. We generate a fake data set, corresponding to an energy run, as follows:

1. We set a value for the quenching factor parameters: α and β
2. We set a value for the fraction of expected signal events: f_s
3. We set an expected number of total events, n_{exp}: for both signal and background contributions.

4. We randomly draw the number of signal events on ^{22}Ne and ^{20}Ne isotopes following a Poisson distribution with means $f_{^{22}Ne} f_s n_{exp}$ and $f_{^{20}Ne} f_s n_{exp}$, respectively.
5. We randomly draw the number of background events following a Poisson distribution of mean $f_{BG} n_{exp}$
6. We calculate the total number of events of the fake data set: $n_{tot} = n_{^{20}Ne} + n_{^{22}Ne} + n_{BG}$
7. We randomly draw the scattering angle for the i_{th} data set following a normal distribution of mean μ_{θ_s} and standard deviation $\sigma_{e-\theta_s}$, which represents the error on the mean of the scattering angle.
8. We randomly draw $n_{^{20}Ne}$ events following $P_s^{^{20}Ne}$.
9. We randomly draw $n_{^{22}Ne}$ events following $P_s^{^{22}Ne}$.
10. We randomly draw n_{BG} events following P_{BG}.

By generating fake data sets with the model and then fitting them, we can determine if the posterior is biased or contains programming errors. Table 6.9 lists the parameters and their values that are used in generating such fake data sets. The values chosen are realistic values in the sense that they are the same or close values for our experiment. Therefore, the fake data are generated as close as possible to our experimental conditions and thus probe similar nuclear recoil energies.

As in the real analysis, the parameters in bold are free parameters of the fit (for a single energy run). An example of such a data set is shown Figure 6.23. The histogram represents the fake data set generated from the model with the parameters shown above. The black curve represents the model with the original parameters and the red curve the model with the parameters returned by the fit.

In order to ensure that the posterior is unbiased and is reporting the correct errors, pull plots were created for each of the free parameters: α, β and σ_a, f_s and θ_s. If a variable X is generated

Parameters	Value in fake data set
Maximum number of primary electrons: $N_{max,pe}$	360
θ_p	0.12
W-value	27.6 eV
Mean gain: $\langle G \rangle$	1000
Neutron energy mean: μ_{E_n}	545 keV
Neutron energy standard deviation: σ_{E_n}	20 keV
Interaction fraction for ^{22}Ne: $f_{^{22}Ne}$	0.1
Interaction fractions for ^{20}Ne: $f_{^{20}Ne}$	0.9
Total number of expected events: n_{exp}	1000
Fraction of signal events: f_s	**0.9**
Quenching factor parameter: α	**0.29**
Quenching factor parameter: β	**0.08**
Energy scale conversion standard deviation: σ_a	**0.23**
The scattering angle mean: θ_s	29 °
The scattering angle standard deviation: σ_{θ_s}	2.45 °
The error on the scattering angle mean: $\sigma_{\mu_{\theta_s}}$	0.4 °

Table 6.9: Table summarizing the parameters values used to generate a fake data set. The values shown are similar values to those found in our experiment. The parameters in bold are free parameters of the fit.

randomly following a Gaussian distribution of mean μ and standard deviation σ, then it is expected that the following quantity:

$$p = \frac{X - \mu}{\sigma}, \tag{6.23}$$

should also be a Gaussian distribution centered at 0 with width 1. To produce the pull plots, X is the value returned by Minuit, μ is the true value of the fake data set generated and σ is the error returned by the fitter. We discuss briefly in Section 6.7 how Minuit calculates the errors.

In order to generate pull plots, hundreds of data sets are created following the aforementioned algorithm. Then, the fake data sets are fitted using the analysis model we developed, returning the most likely values of the free parameters and their errors. Then, we use Equation 6.23 to look for any bias for a given parameter.

Figure 6.24 shows an example of pull plot for the scattering angle variable. In black is shown a Gaussian centered at 0 and of standard deviation of 1. The red curve shows the Gaussian fit of the pull plot, it shows a very slight bias in comparison to the Gaussian with mean 0.

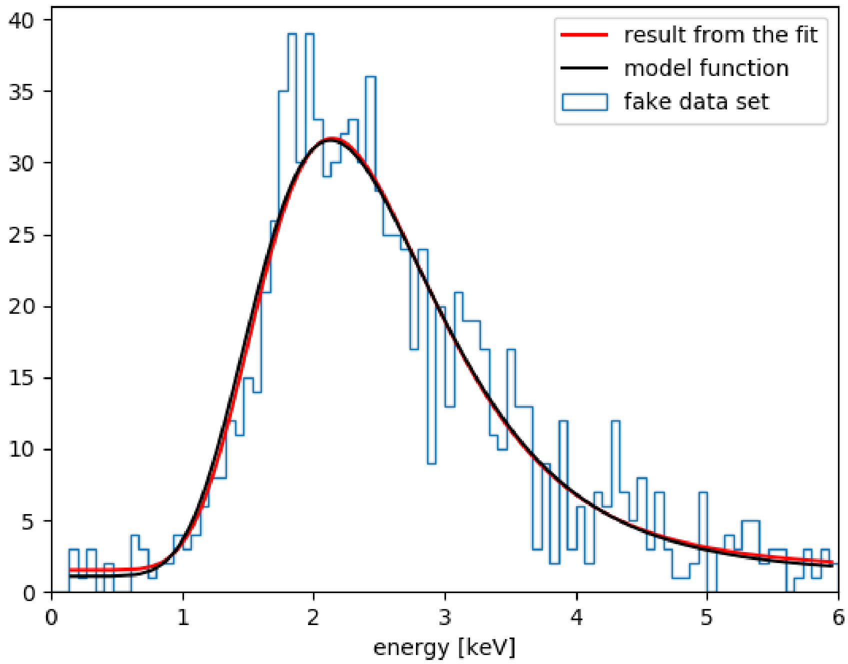

Figure 6.23: The blue histogram corresponds to a fake data generated using the model, in black is the corresponding function used to randomly generate the data and the red curve corresponds to the best model resulting from the fitting data.

A test to check potential biases in the analysis was performed, for this test 400 data sets were generated. Five different energies were generated simultaneously, reproducing the energy runs recorded during our experiment, and fitted simultaneously. The general variables are the same as mentioned above, the specific quantities to each run are mentioned below in Table 6.10. There are 13 free parameters of the fit: the fractions of expected signal events, f_{sj}, the scattering angle, θ_{sj}, the quenching factor parameters, α and β, and the standard deviation of the energy scale distribution, or resolution, σ_a.

Figure 6.25 shows the pull plots for the 13 parameters of the model. In general the shapes of the pull plot distributions are Gaussian like. The Freedman-Diaconis rule [109] was applied to the pull plots, in order to have the optimal number of bins in each histogram. Gaussian fits were performed to the pull plots to extract the means and standard deviations. The results of such fits

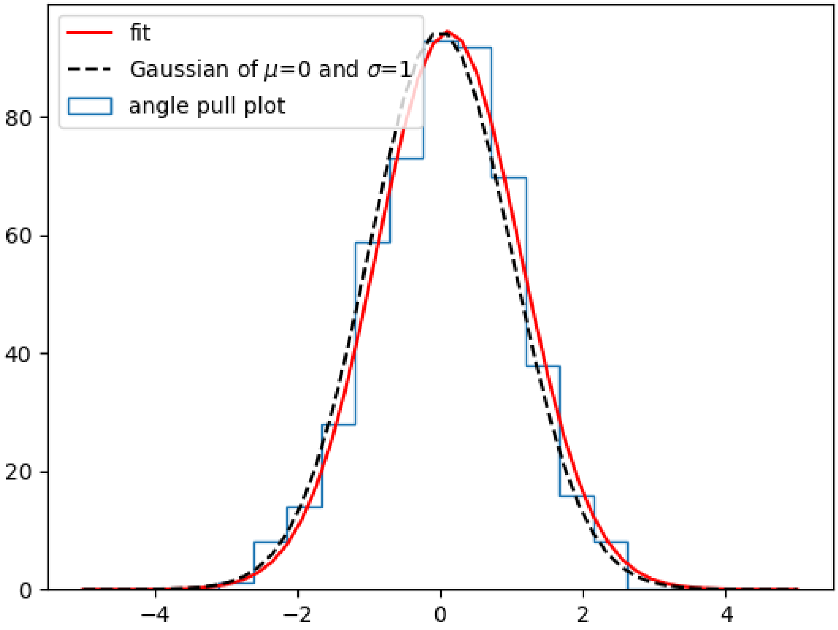

Figure 6.24: Pull plot of the free parameter scattering angle, for a given energy, in blue. The black curve corresponds to a Gaussian centered at 0 with a standard deviation of 1, which is the expected distribution for the pull plots generated for the free parameters of the fit. And in red is the corresponding Gaussian distribution function of the pull plot returned after fit.

E_{nr} [keV$_{nr}$]	μ_{θ_s}	σ_{θ_s}	$\sigma_{\mu_{\theta_s}}$
6.8	$29^{\,o}$	$3^{\,o}$	$0.5^{\,o}$
2.7	$18^{\,o}$	$1.5^{\,o}$	$0.3^{\,o}$
1.6	$14^{\,o}$	$1.1^{\,o}$	$0.3^{\,o}$
1.3	$12.5^{\,o}$	$1.0^{\,o}$	$0.1^{\,o}$
0.74	$9.5^{\,o}$	$0.7^{\,o}$	$0.1^{\,o}$

Table 6.10: Table summarizing the parameters and the values, used to generate the five fake data sets. The values are the mean scattering angle, μ_{θ_s}, the standard deviation of the scattering angle distribution, σ_{θ_s}, and the error on the mean of the scattering angle distribution, $\sigma_{\mu_{\theta_s}}$. The values used to generate the fake data sets were chosen to produce nuclear recoil energies similar to runs 8, 7, 9, 10, and 11.

are shown in Figure 6.25. Figure 6.26 shows a summary of the means and the standard deviations of the pull plots' parameters along with the errors reported by the fit. Some parameters show a slight bias, as well as an overestimation of the errors. The parameters of interest, α and β, show a small bias consistent with the errors returned by the fit. It was suggested to investigate the results of the fit with different binning conditions, twice as many and twice as less as indicated by the Freedman-Diaconis rule. We also looked at the mean and standard deviations of the pull plots without histogramming these quantities from the NumPy package [110]. Figure 6.26 shows such comparisons. The four method show the same trends for both the means and the standard deviations, however, when some disparities exist, the calculation is generally off the values reported by the fits with the three different binning.

Figure 6.27 shows the distributions of returned α and β. We fitted the distributions of α and β, while these were following the Freedman-Diaconis rule. This choice was motivated by the good agreement between the result of the fit with the fits resulting from larger or smaller binning. Moreover, the values reported by the fit are more conservative than the values calculated by NumPy. Both α and β show a consistent bias. The mean of the α distribution returned by the fit is 0.289, when the true α value to generate the data was 0.29, thus there's a bias of 0.001 or 0.34 %. We used The mean of the β distribution returned by the fit is 0.0813, when the true value used to generate the data was 0.08. Thus, there's a bias of 0.013 or 1.6 %. The biases for α and β are smaller than the errors returned by Minuit: by a factor 5.2 and 16.15 for α and β respectively. The maximum impact on the QF is 0.47 % at low energy and 0.07 % at high energy. Because the biases are small, we report them as systematic uncertainties.

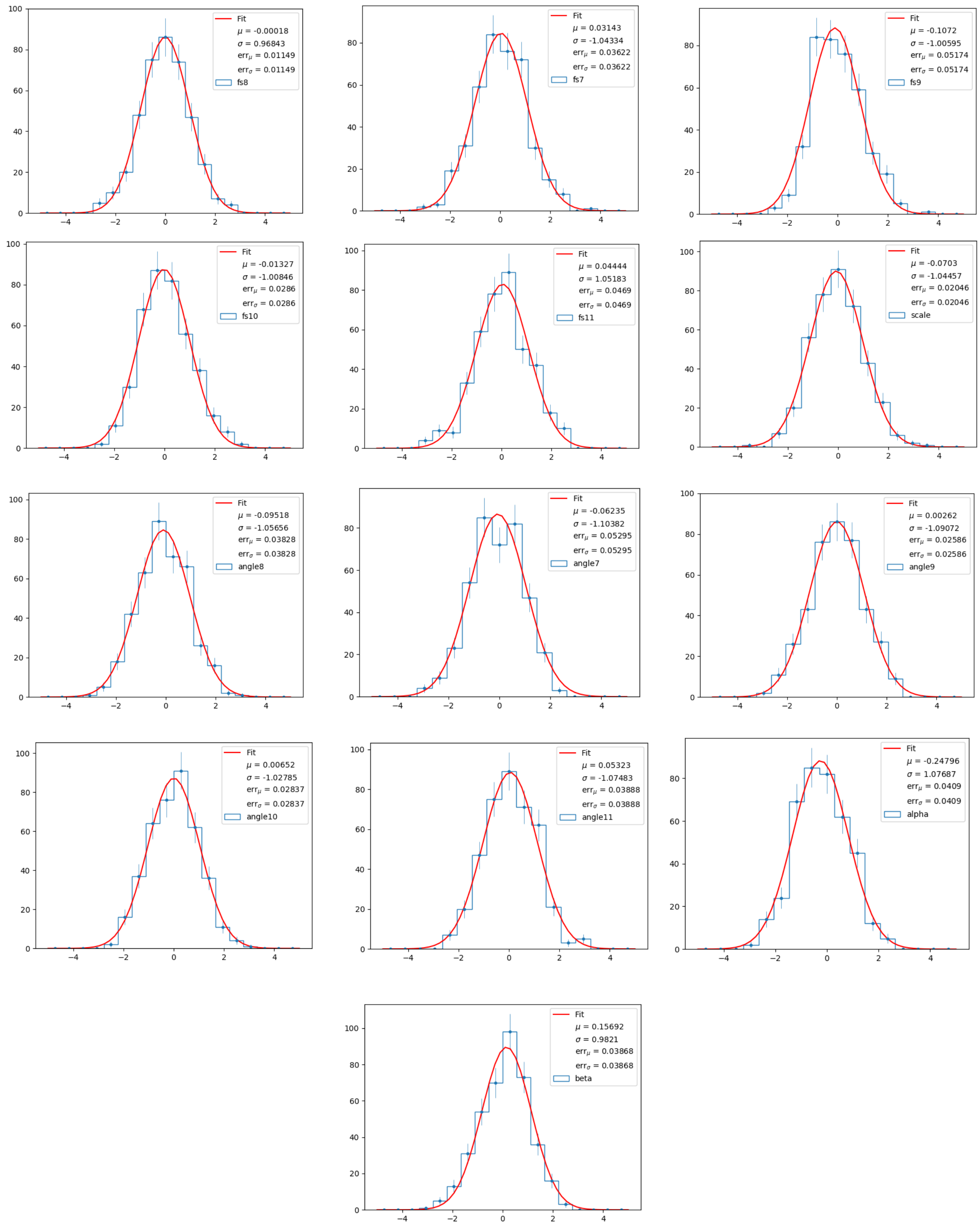

Figure 6.25: Pull plots for 5 sets of data generated simultaneously and fitted simultaneously. We display the errors for each bin of the pull plots' histograms, as well as the Gaussian fit that was performed. The values of the fit, the mean and the standard deviation, and their respective errors, are shown on each plot. We can note, that the errors on both the mean and standard deviation are similar when rounded at 5 digits.

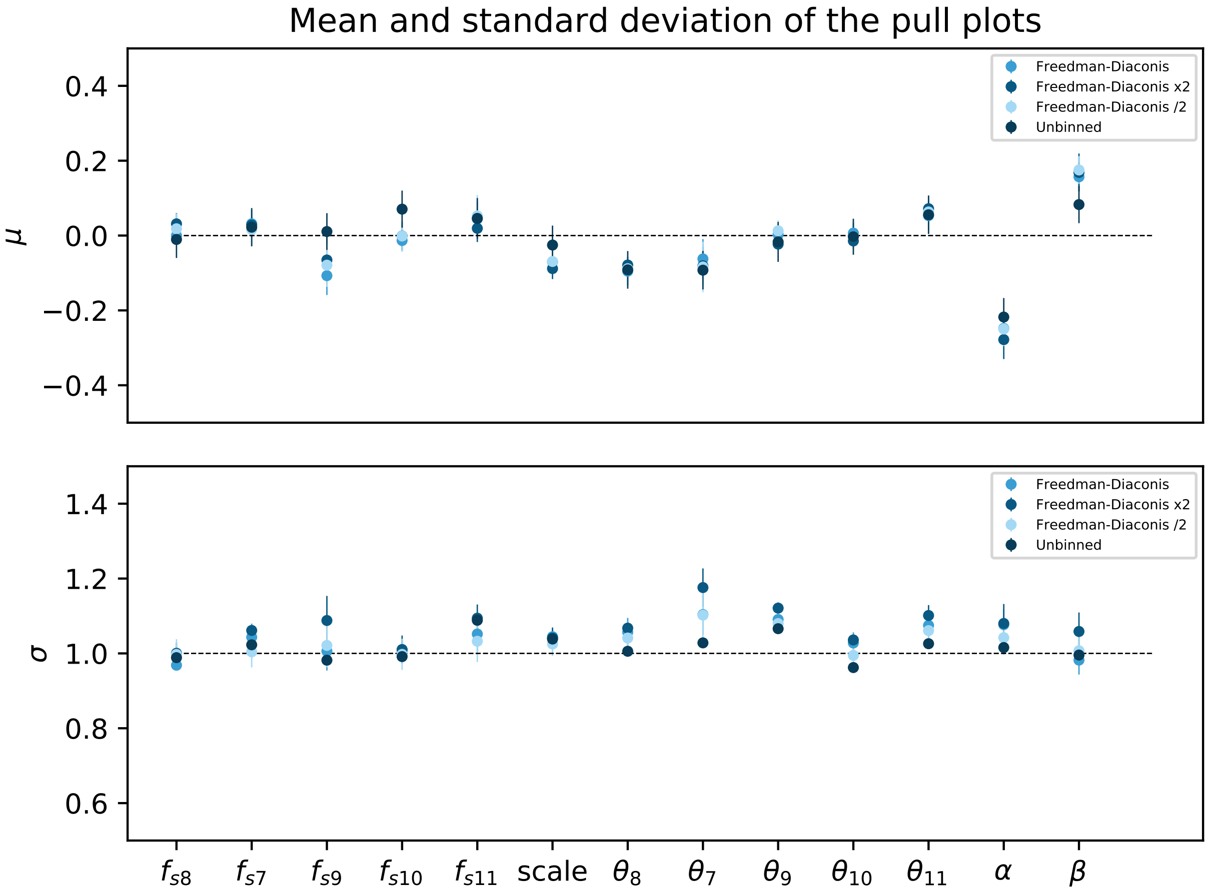

Figure 6.26: Summary of the mean and standard deviation of the pull plots for the parameters: $f_{s8}, f_{s7}, f_{s9}, f_{s10}, f_{s10}, f_{s11}, \sigma_a$, α, β and the five scattering angles tested. The upper plot shows significant biases for α and β, the different means are distributed around 0. The small biases on α and β are discussed in the text. As for the standard deviation, most of the parameters are consistent with 1. We compare the means and standard deviations from fitting the pulls plots with different binning: Freedman-Diaconis binning, Freedman-Diaconis binning times 2 and Freedman-Diaconis divided by 2. We can observe that for the majority of the cases, the values of the fits are in good agreement, within error. We also investigated the means and standard deviations of the pull plots as returned by the NumPy package. The values seem in general in good agreement with the three fitting conditions, however, the unbinned means and standard deviations, tend to show more "optimistic" values of the mean and standard deviation, pulling the values closer to 0 and 1, respectively.

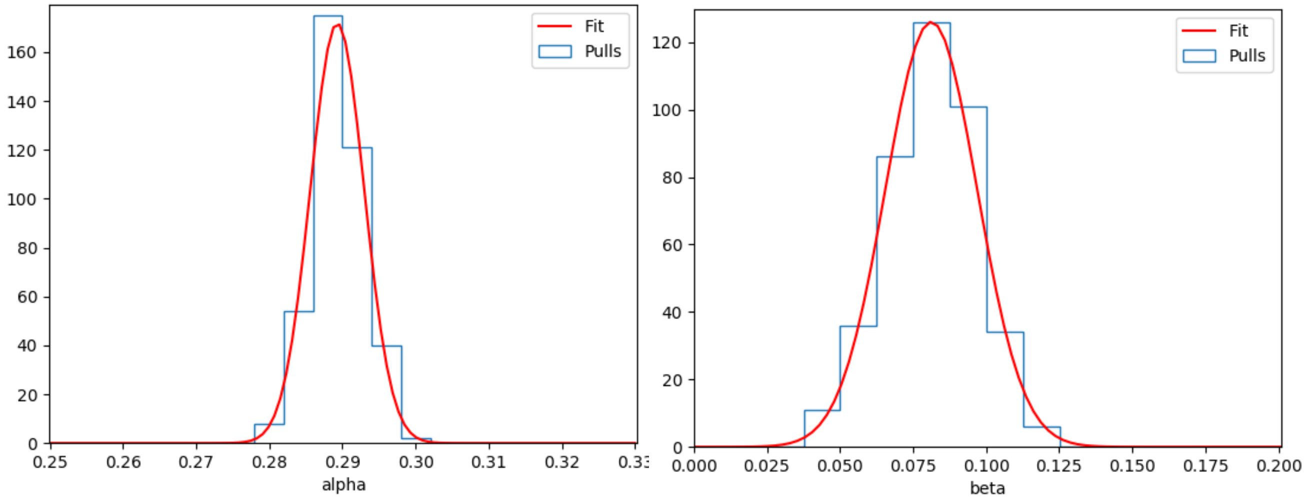

Figure 6.27: Distributions of α and β. The values were returned after each fit of the fake data set. The means of the two distributions are close to the values used to generate all the data sets. The shift with the true value represents the bias of the analysis for these two variables. The red curve represents the Gaussian fits performed on the distributions to extract such values.

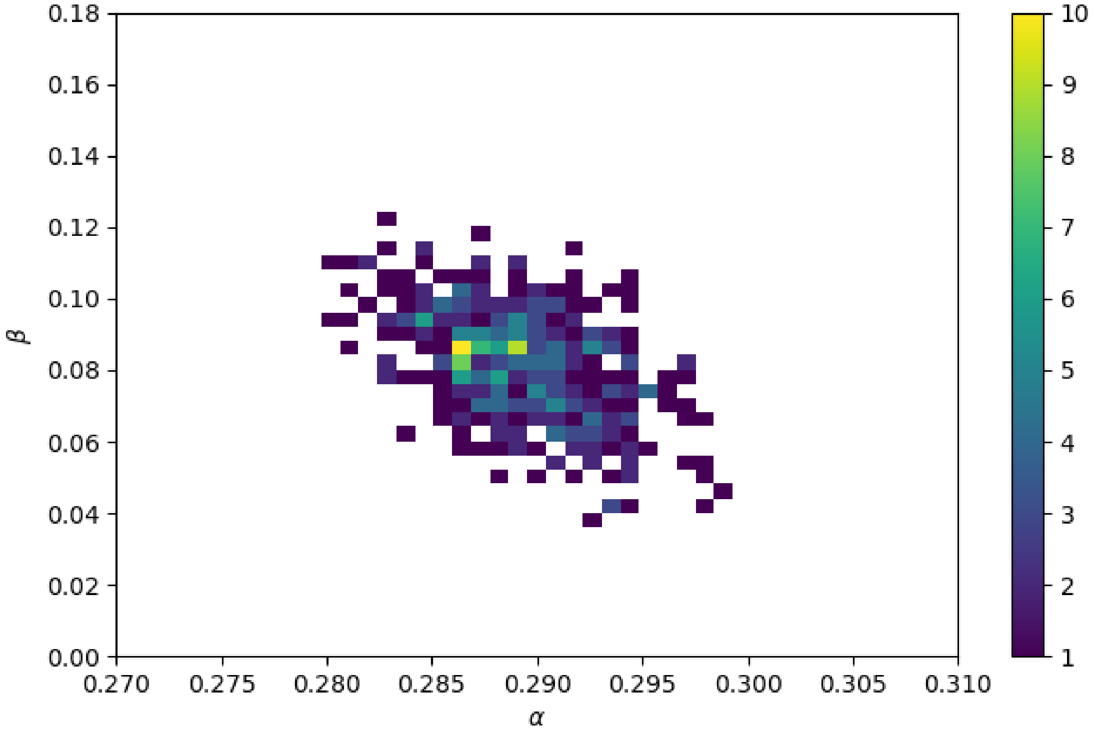

Figure 6.28: 2D histogram of α and β. The values were returned after each fit of the fake data set. The means of the two distributions are close to the values used to generate all the data sets. This figure shows an anti-correlation between α and β.

6.7 Errors returned by Minuit

Minuit can compute the errors using three different methods: MIGRAD, HESSE and MINOS. In our analysis, we use the MIGRAD method, which assumes that the function to be maximized is Gaussian:

$$P(x) = \frac{1}{\sqrt{2\pi\sigma}} e^{-\dfrac{(x-\mu)^2}{2\sigma^2}} \tag{6.24}$$

Minuit minimizes functions, thus, we take the negative log-function, which is a parabola:

$$-\ln\Big[P(x)\Big] = \ln\Big[\frac{1}{\sqrt{2\pi\sigma}}\Big]\frac{(x-\mu)^2}{2\sigma^2} \tag{6.25}$$

and the second derivative is:

$$\frac{d^2}{dx^2}\Big[-\ln P(x)\Big] = \frac{1}{\sigma^2} \tag{6.26}$$

MIGRAD calculates the 1$^{\text{st}}$ derivative of the function to minimize. When it finds the minimum it approximates the second derivative matrix by assuming that the minimized function is a Gaussian and returns the corresponding errors. The diagonal elements of the 2$^{\text{nd}}$ derivative matrix gives the second derivatives with respect to one parameter at a time. When this matrix is inverted, to give the error matrix, the diagonal elements include contributions from all of the other elements of the 2$^{\text{nd}}$ derivative matrix (correlation). The error on each free parameter of the function is provided by the diagonal elements of the error matrix, see equation 6.26.

A common approach of obtaining parameter estimates and errors for a posterior is to use a Markov Chain Monte Carlo (MCMC) to sample the distribution. These samples can then be used to create marginal distributions for all the parameters. However, this method is often time consuming and prone to errors if the chain does not properly sample the whole space. If the posterior is Gaussian, the errors and covariance matrix returned by Minuit completely specify the distribution and the results obtained are identical to the results from a MCMC. In this analysis we assume that the posterior distribution is Gaussian, or Gaussian like, and thus, we directly use the errors and covariance Matrix returned by Minuit.

A common technique to visualize the posterior function is to plot a "profile distribution". A profile distribution is created by plotting the posterior as a function of one of the parameters, where all other parameters are at their minimum. When the posterior function is Gaussian-like, both the profile posterior and the posterior distribution obtained through sampling, are in good agreement [111]. If the posterior function is not Gaussian-like, then the posterior distributions have to be sampled from the posterior with a Monte Carlo method. Figure 6.29 shows three profile log-posteriors out of the 19 free parameters of the fit: the fraction of expected events for run8, f_{s8}, and the quenching factor parameters, α and β. While we acknowledge that a profile posterior is not equivalent to a posterior distribution, it shows the behavior of the posterior near the minimum for a given parameter. Hence, by showing that the profile posterior is Gaussian or Gaussian-like near the minimum of the profile function, we show that the approximation chosen for our analysis, Gaussian-like posterior, is supported.

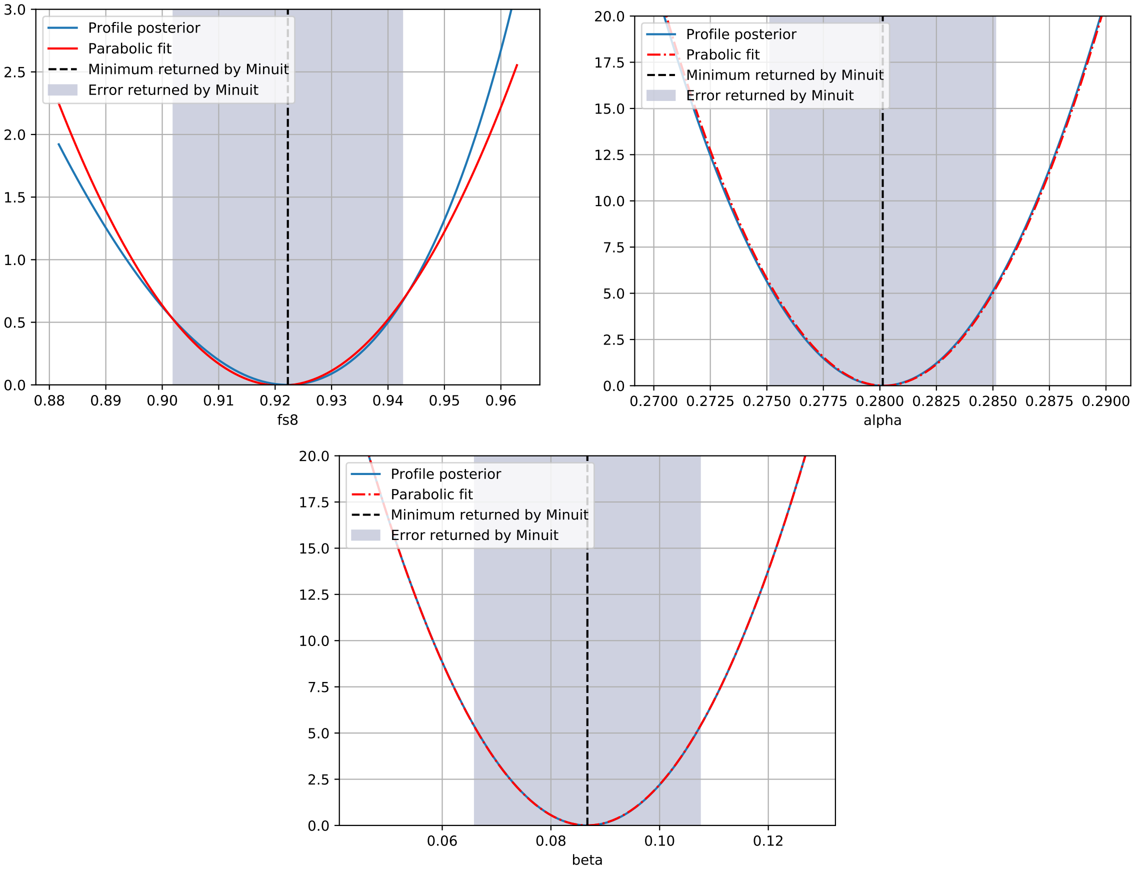

Figure 6.29: Profile (log)posterior for three variables out of the 19 free parameters of the fit: the fraction of expected events for run8, f_{s8} and the quenching factor parameters, α and β. Here, we show that the profile of the log-posteriors have a parabola shape, which is expected from a posterior that is Gaussian-like. In red we show a fit to the profiles with a parabolic function. Although the fit performed on the profile of f_{s8} shows some discrepancies with the fit, however the fit is reasonable near the minimum. The parabolic fits for the quenching factor parameters match their respective profiles really well. The black dashed line shows the minimum returned by Minuit, and the shaded grey region shows the error returned by Minuit. A change in the (log)posterior probability function of 0.5 relative to 0, shows the corresponding $1\,\sigma$ error of the distribution. We can see for the profile of f_{s8}, that the change of 0.5 in the profile corresponds with the error returned by Minuit. However, we can see for α and β that the change of 0.5 in the profile posterior does not correspond to the errors returned by Minuit. The reason is that the profile method does not take into account the correlations between the parameters, and hence, a change in 0.5 of the profile posterior gives a smaller "error" than the one returned by Minuit. We acknowledge that the profile posterior is not equivalent to the posterior distributions. However, it is a good indication of the posterior shape, and thus validates our approximation of considering the posterior Gaussian in our analysis.

Chapter 7

Quenching factor measurement results

In this chapter, we present the results of the nuclear recoil response in 2 bar of Ne + CH_4 (3 %) in an SPC. We fitted the data simultaneously using the minimizer Minuit and the model described in the previous chapter. We first present the results of the fit and the different sources of systematic uncertainties impacting our results. Then, we discuss the parametrization impact on the QF results by fitting individually the energy runs.

7.1 Results from the Bayesian fit

The fit to the data was performed for a different energy range depending on the energy run. The noise peak was cut off of the data at the same energy for all the runs; 100 eV, as explained in Section 6.4. The upper energy limit of the fit varied, Table 7.1 provides such values.

	run 8	run 7	run 9	run 10	run 11	run 14 0.34 keV	run14 1 keV	run14 2 keV
E_{max} [keV]	6	3	2	1.4	0.8	0.8	1.4	2

Table 7.1: Table summarizing the upper energy limit of the fit in the analysis.

The values of α and β and their errors (stat + sys θ_s) returned by the joint fit are:

$$\alpha = 0.2801 \pm 0.005 \quad \text{and} \quad \beta = 0.0867 \pm 0.020$$

Figure 7.1 shows the resulting quenching curve using the α,β parametrization. The results of the fit will be further discussed in Section 7.3. We provide the covariance and correlation matrices in Appendix B. First, we will provide details on uncertainties and tests performed on the analysis and model.

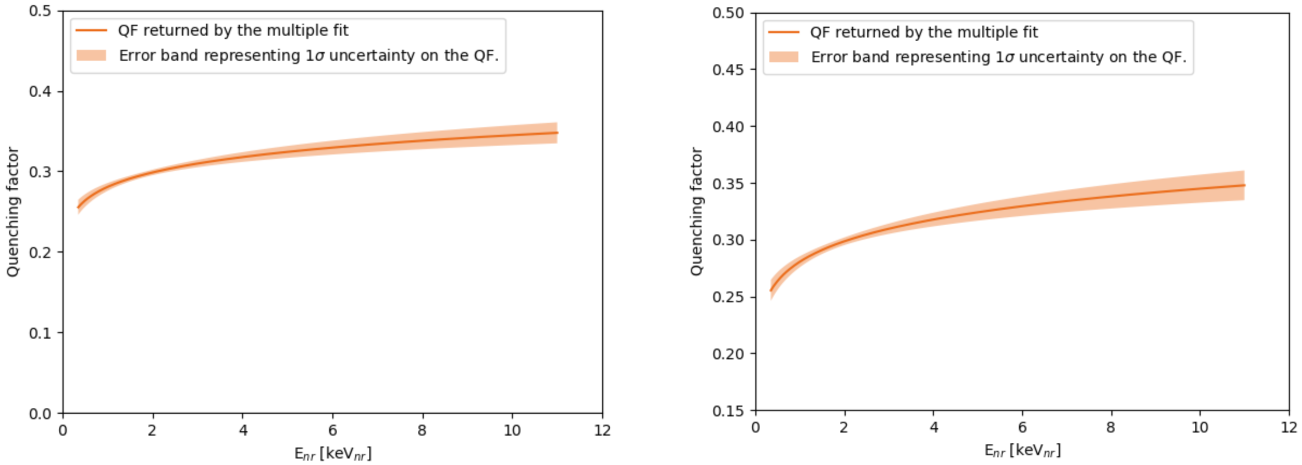

Figure 7.1: Quenching factor as a function the nuclear recoil energy. The orange curve corresponds to the QF mean and the error band corresponds to $1\,\sigma$ error. The right plot shows a zoom of the left plot.

7.2 Systematic uncertainties

7.2.1 Scattering angles

In this analysis one of the non negligible sources of uncertainties comes from uncertainty on the scattering angles, and in particular for run14. Indeed, the distance between the backing detectors' plane and the surface of the SPC was measured for each new angle configuration 3 times.

To calculate the error on the scattering angle values, the uncertainties were propagated from the measured distances (adjacent: distance from BDs' plane to SPC and opposite: annulus radius) through Monte Carlo simulations. All other sources of uncertainties that could impact the mean of the scattering angle, as well as the spread, were included to a Monte Carlo simulation and showed that they were negligible. This includes: the distances from the exit of the collimator to the surface of the SPC, the size of the beam in the SPC (from cross section uncertainty), SPC's size, and BDs' size. For each configuration the mean and uncertainties are given in Table 5.1.

As a result, it was chosen that the error on the scattering angle mean would be included in the analysis by including a prior to the function to minimize.

7.2.2 Neutron energy uncertainty

The uncertainty on the neutron energy was determined from errors in measuring distances between the 0-degree backing detector and the exit of the collimator and fitting errors. Our collaborators at TUNL estimated the error on the neutron mean energy to be 2 keV, which has a 0.36 % impact on the nuclear recoil energy. As this systematic has a negligible impact on the nuclear recoil spectrum, it was not included as a source of uncertainty in the analysis.

7.2.3 Noise contribution

The fluctuation of the electronic baseline noise was also investigated. We looked at the noise peak of each energy run and found that in average the mean of the noise peak is at 38.7 eV and the standard deviation of the peak is 19.22 eV. By convoluting the energy response of the detector with a Gaussian of mean 0 and standard deviation of 0.02 keV we estimated the impact on the quenching factor parameters to be of 0.2 %, thus being negligible.

7.2.4 Efficiency curve uncertainty

We consider the uncertainty in how we determined the efficiency to reconstruct events as a function of energy. Indeed, as explained in Section 6.3.5, to build the efficiency curve we had to adapt the lower rise time cut to select the reconstructed events. Thus, the lower rise time cut was set at 0.85 μs instead of 1 μs as in the selection of the data. To study the impact of the efficiency curve on the values returned by Minuit, we generated two other efficiency curves but with a different lower rise time cut. It was decided to investigate the impact of a stricter and a looser rise time

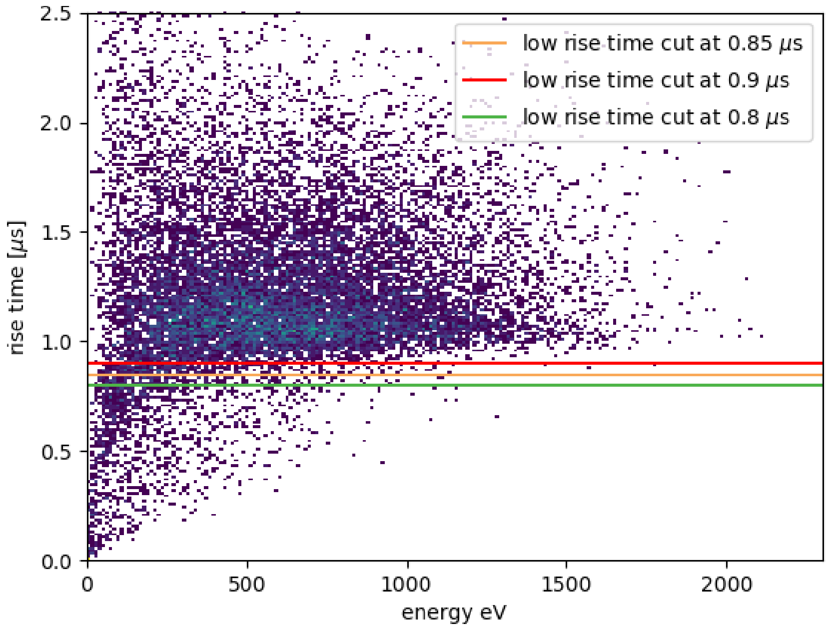

Figure 7.2: Rise time as a function of the energy of simulated events to construct the efficiency curve (already shown in Section 6.3.5). The three different lines represent the different values of the low rise time cut to select the reconstructed events.

cut. Figure 7.2 shows the corresponding low rise time cuts chosen to build new efficiency curves: $0.9\,\mu$s and $0.8\,\mu$s, called condition 2 and 3 respectively (condition 1 being the original rise time cut chosen in Section 6.3.5).

Figure 7.3 shows the resulting efficiency curves for the low rise time cuts' test compared with the nominal energy efficiency. As expected, the stronger cut ($0.9\,\mu$s) results in a higher energy threshold for reconstruction of the events, while the looser cut results in a lower energy threshold for reconstruction. Fits were performed to these efficiency curves using an error function, see Equation 6.3. The resulting parameters' values for condition 2 and 3 are shown in Table 7.2.

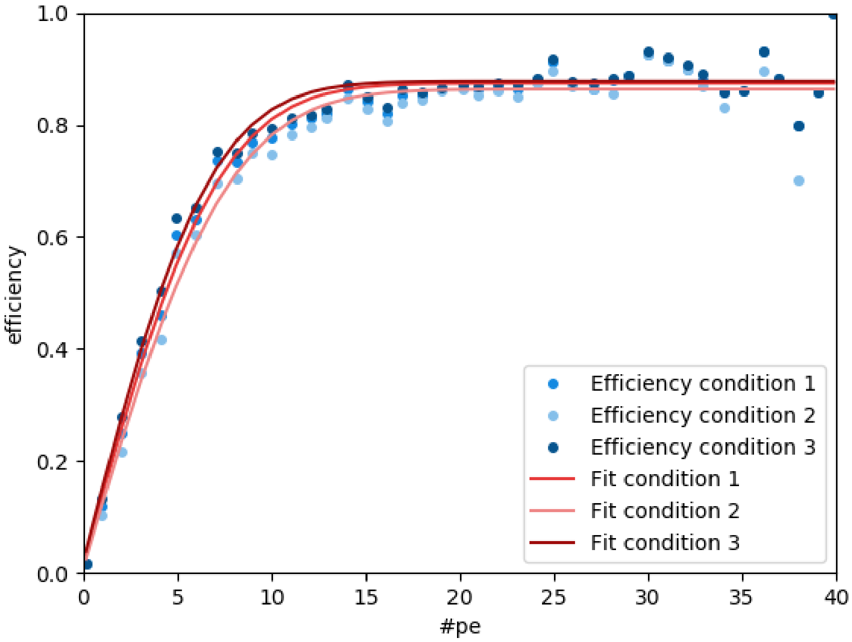

Figure 7.3: Efficiencies to reconstruct the events' energies obtained from the nominal rise time cut (condition 1), and additional rise time cuts tested: condition 2 and 3, are shown in different shade of blues. As expected, the energy efficiency resulting from the stronger rise time cut (condition 2: 0.9 μs) display a lower successful reconstruction rate than the other efficiencies built with lower rise time cuts. The efficiencies were fitted with an error function, Equation 6.3. The resulting fit functions of the energy efficiencies are shown in shade of red.

	Condition 1	Condition 2	Condition 3
a_e	0.874 ± 0.0067	0.863± 0.0084	0.877± 0.0066
b_e	-0.12 ± 0.19	-0.08 ±0.25	-0.167 ± 0.19
c_e	8.01 ± 0.43	8.54± 0.56	7.57 ± 0.415

Table 7.2: Values of a_e, b_e, and c_e returned by the fit for the nominal efficiency and the two efficiencies resulting from higher and lower rise time cuts. We also report the errors returned by the fit on each parameter. The differences between condition 1 and condition 2, and 3 are called systematic uncertainties. Except for the parameter b_e, the systematic uncertainties are larger than the errors returned by the fit (minimum of times 2).

	Condition 1	Condition 2	Condition 3
α	0.2801	0.2789	0.2811
β	0.0867	0.0899	0.0839
σ_α	0.0050	0.0050	0.0050
σ_β	0.02	0.02	0.02

Table 7.3: Values of α and β returned by the fit with the different efficiency curves, as well as the errors returned by the fit.

The analysis was then run with the three different efficiency curves. Table 7.3 lists the values of the quenching factor parameters, α and β and their errors, for the different conditions of the efficiency curve. Figure 7.5 shows a comparison of the two quenching factor curves obtained from condition 2 and 3 with the original quenching factor curve, or condition 1. The differences between the means of α and β for condition 1 with the mean values of α and β for condition 2 and 3 represent potential systematic errors: α is impacted by 0.35-0.4 % and β is impacted by 3.2-3.7 %. There is an asymmetry between the two systematic errors reported, we chose to report the maximum error between the two.

Thus, the systematic uncertainty from the efficiency curve is (mean ± error from fit ± systematic):

$$\alpha = 0.2801 \pm 0.005 \pm 0.0012 \qquad \beta = 0.0867 \pm 0.02 \pm 0.003$$

The efficiency curve systematic error can change the quenching factor by 0.8 % at low energy (0.43 $\mathrm{keV_{nr}}$) and 0.3 % at high energy (10 $\mathrm{keV_{nr}}$), which is small compared to the error returned by the fit.

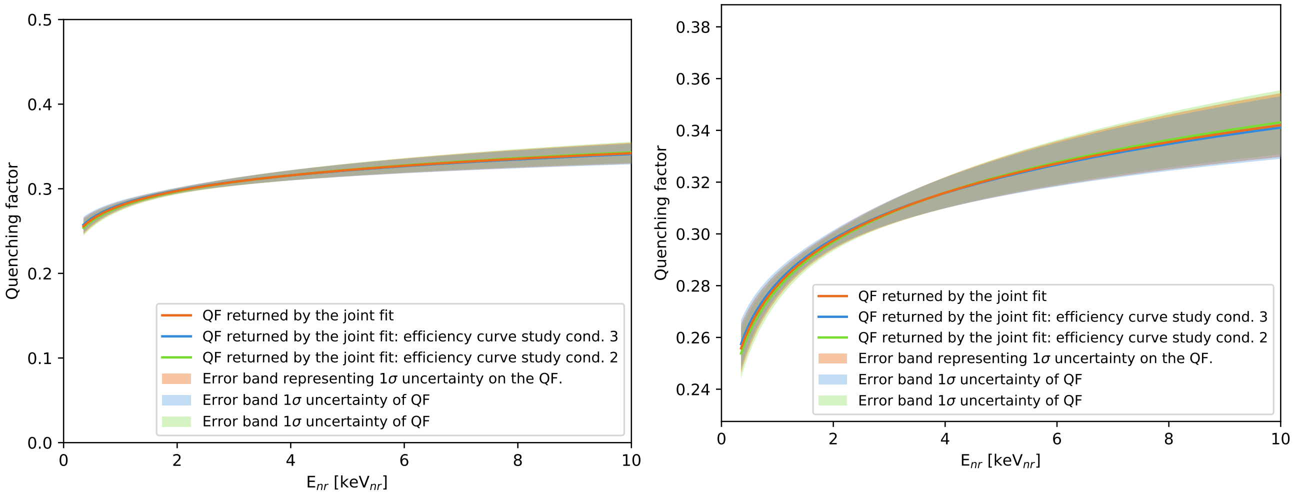

Figure 7.4: Quenching factors as a function of the nuclear recoil energy, for the two different conditions, in green and blue, studying the efficiency curve and original efficiency curve in orange. The plot on the right is a zoom of the left plot.

7.2.5 Non-linearity in energy response

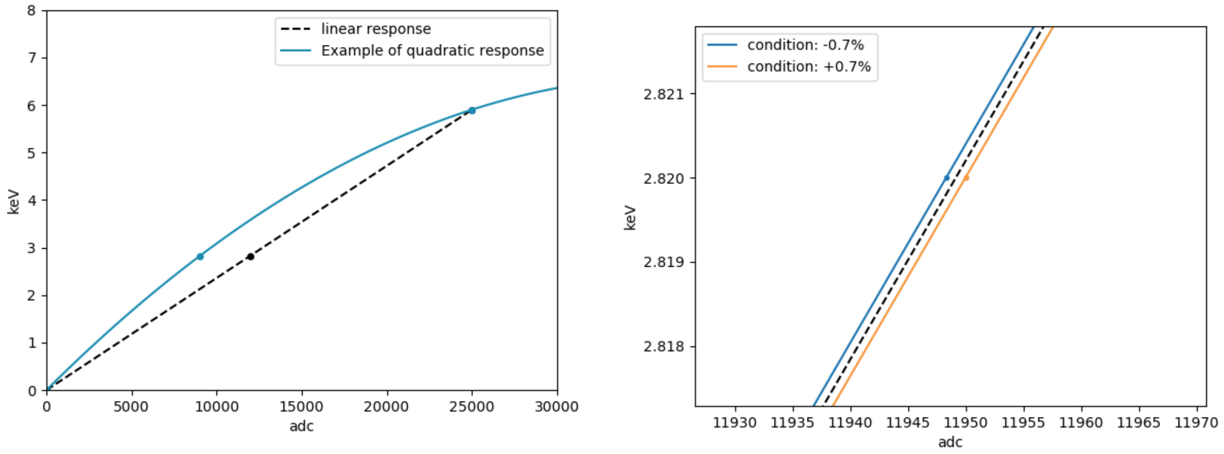

(a) Example of quadratic energy response in blue and linear energy response black. The blue (shifted) and black (linear) dots at 2.82 keV show the positions of the hypothetical ^{37}Ar peak, while the blue dot at 5.9 keV shows the ^{55}Fe.

(b) Shows the two quadratic energy responses that were investigated: shifting the position of the hypothetical ^{37}Ar peak by 0.7 % in blue and in orange. The black dashed line is the linear response.

Figure 7.5: Building the alternative energy responses.

We investigated the possible effect of non-linearity in energy response of the detector. For this, we implemented quadratic energy responses, that we used to correct the data and then looked at the results of the fit. The choice to study quadratic responses over other forms was arbitrary. Figure 7.5a shows how such quadratic responses were built: the positions of the ^{55}Fe (5.9 keV) from experimental data and a hypothetical ^{37}Ar peak (2.82 keV) were reported in ADC and in keV. The dashed black curve is the linear energy response, the black dot shows where the hypothetical ^{37}Ar peak should be for the response to be linear. If the hypothetical ^{37}Ar peak is shifted by some percentage from its linear position, one obtains the blue dot on Figure 7.5a and the new energy response can be estimated using a quadratic form.

From [66] it was shown that the energy response was linear in our detectors using an ^{37}Ar source in 1.5 bar of Ne+CH$_4$ (98:2). Figure 7.6 shows the energy spectrum of the 270 eV and 2.82 keV lines along with the fit to the data. The W-value was determined by fitting both peaks, and the same value was returned within 0.7 %. The 0.7 % difference in W-values between the two calibration energies necessarily incorporates expectation variation in W as a function of energy, statistical uncertainty on W, as well as any potential non-linearity in the detector response. Therefore, 0.7 % represents an upper limit on the non-linearity measured in this SPC set-up. Furthermore, other data using ^{37}Ar were collected in the NEWS-G laboratory at Queen's University for neon based gas mixture and lead to the same observation. An ^{37}Ar and ^{55}Fe data set was taken for the 2018 preliminary QF campaign and is discussed in Appendix A.2. Thus, we used the 0.7 % uncertainty from this analysis in the study of the non-linearity response. Figure 7.5b shows the resulting quadratic responses for a shift of the ^{37}Ar peak by ±0.7 %, corresponding to a shift of 84 ADC from its linear position. Thus, we expect the impact from this uncertainty on the quenching factor to be small or negligible.

The data were corrected with the two non-linear responses, then the fit was performed to the data. Table 7.4 shows the values of α and β returned by the fit for such responses. For condition 2, α and β are impacted by 0.21 % and 4.6 % respectively. For condition 3, α and β are impacted by 0.03 % and 3.5 % respectively. Once again, the systematic uncertainty from this source is asymmetric. We will report the larger one on the QF.

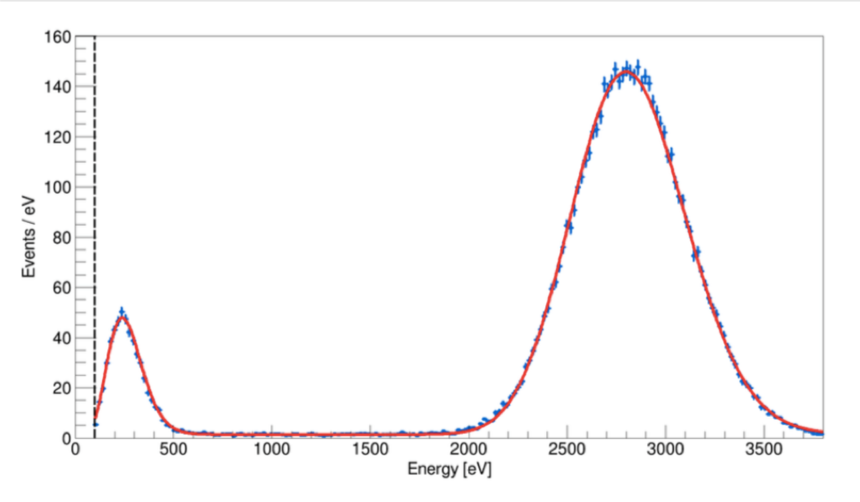

Figure 7.6: Energy spectrum of the ^{37}Ar taken with a 30 cm diameter SPC filled with 1.5 bar of Ne+CH$_4$ (98:2). The 270 eV and 2.82 keV lines of X-rays are visible. The red curve shows the fit to the data performed. Figure 4 of paper [66]. For more details, the reader is encouraged to review [66].

	Condition 1	Condition 2	Condition 3
α	0.2801	0.2795	0.2802
β	0.0867	0.0907	0.0837
σ_α	0.0050	0.0050	0.0050
σ_β	0.02	0.02	0.02

Table 7.4: Table summarizing the values of α and β returned by the fit with the different energy responses, as well as the errors returned by the fit. Condition 1 corresponds to the nominal linear energy response, while condition 2 and 3 correspond to a -0.7 % and +0.7 % shifts, respectively, in the position of a 2.82 keV and following a quadratic response.

Figure 7.7 shows a comparison of the quenching factor as a function of the nuclear recoil energy for the linear and quadratic responses, built from a ± 0.7 % shift in the position of the hypothetical ^{37}Ar peak. The orange quenching factor curve corresponds to the linear energy response, and the orange error band corresponds to 1 σ error for a given energy. The purple and red quenching factor curves correspond to the ± 0.7 % shift in the the hypothetical ^{37}Ar position, quadratic responses, along with their respective error bands. In this work, the errors are calculated from the covariance matrix provided by Minuit and thus takes into account the correlations between the parameters of the fit.

The maximum difference between the linear QF and the quadratic QFs is 0.6 % at low and 0.7 % at high energy. We report the systematic uncertainty from the possible non-linear response (mean ± error from fit ± systematic):

$$\alpha = 0.2801 \pm 0.005 \pm 0.0006 \qquad \beta = 0.0867 \pm 0.02 \pm 0.004$$

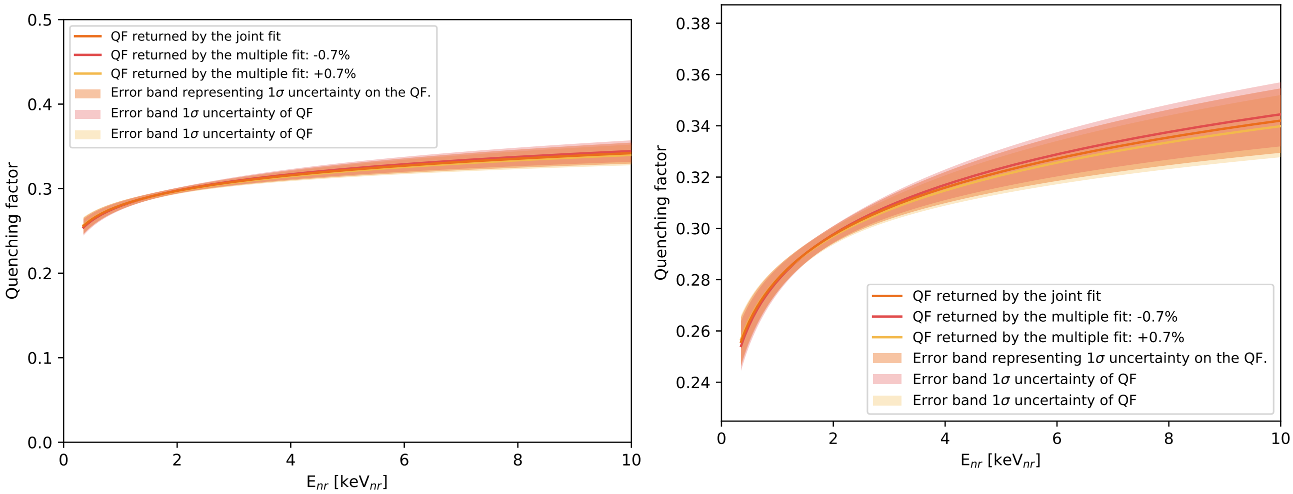

Figure 7.7: Quenching factors as a function of the nuclear recoil energy, for ± 0.7 % shift (yellow and red, respectively) and linear response in orange. The plot on the right is a zoom of the left plot.

Finally, we allowed the quadratic term, or position of the ^{37}Ar peak, to vary in the fit with a prior on its position based on [66] with ± 0.7 %. The returned parameters are within less than $1\,\sigma$ with the linear response. The values of α and β are within $0.08\,\sigma$, or 0.14 %, and $0.33\,\sigma$, or 7.7 %, respectively from the linear response. The value of the shift of the ^{37}Ar position is 1.6 %, which is $2.2\,\sigma$ from the linear position and corresponds in a shift of about 190 ADC from the linear position. The values of α and β and their errors returned by the fitter are:

$$\alpha = 0.2805 \pm 0.005 \qquad \beta = 0.08 \pm 0.021$$

The quenching factor as a function of the nuclear recoil energy for the floating quadratic response is shown Figure 7.8 along with the linear QF. From the shift of 1.6 % of the ^{37}Ar position, which shows that the fitter prefers a small non-linearity of the energy response, the impact on the

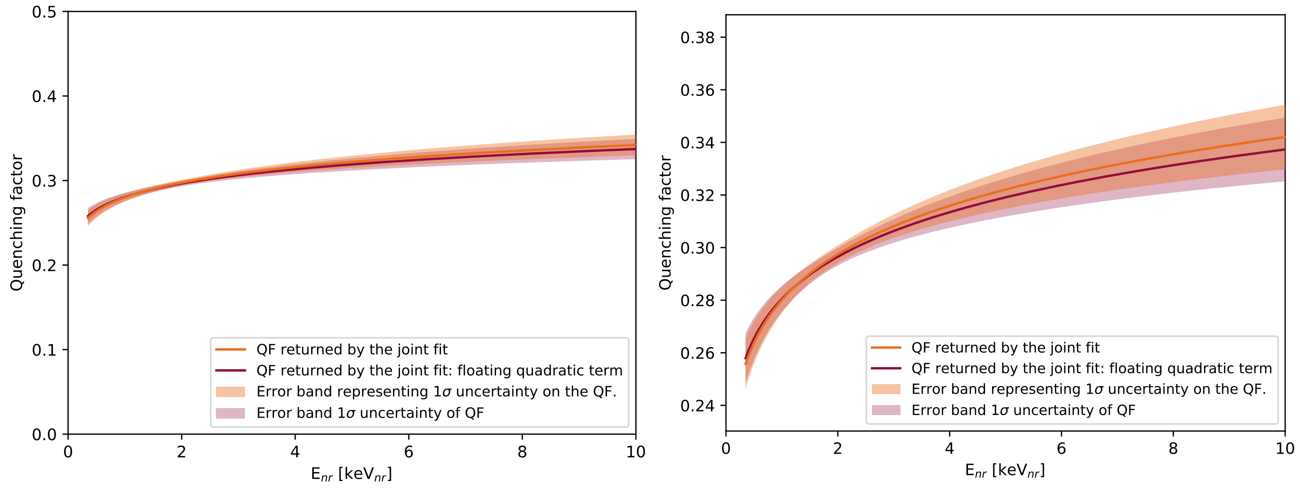

Figure 7.8: Comparison of the quenching factor for the linear response and a quenching factor with floating energy response (floating shift of the ^{37}Ar position): floating quadratic term. The right plot is a zoom of the left plot.

QF is 0.95 % at low energy and 1.3 % at high energy. For future studies, a Bayesian posterior ratio for the two models: linear and floating quadratic energy responses, could be performed in order to estimate if the floating quadratic energy response model is over-fitting the data, and thus, if the small non-linearity is a real effect.

7.2.6 Offset in the energy response

We looked at a possible offset of the energy response. For this, we looked at the noise peak of the SPC without any cuts, and looked where the mean of such peak was lying. By fitting the noise peak with a Gaussian, the mean of the noise peak was found to be shifted from zero by -13.7 ADU. We re-ran the analysis with an offset applied to the energy response, which was then applied to the data. The impact of such energy response on the quenching factor parameters was defined as the systematic uncertainty coming from such offset.

The values returned for α and β are:

$$\alpha = 0.2823 \pm 0.005 \qquad\qquad \beta = 0.0836 \pm 0.021$$

The impact on the mean values of α and β are 0.78 % and 3.6 %, respectively. This possible electronic offset leads to an impact on the mean of the QF of 1 % at low energy (430 $\mathrm{eV_{nr}}$) and 0.06 % at high energy (10 $\mathrm{keV_{nr}}$). We report the systematic uncertainty from the electronic offset on the quenching factor parameters (mean ± error from fit ± systematic):

$$\alpha = 0.2801 \pm 0.005 \pm 0.0022 \qquad \beta = 0.0867 \pm 0.02 \pm 0.0031$$

7.2.7 Energy scale

Finally, a study of the energy scale uncertainty was performed in order to assess its impact on the QF. For this, we used the uncertainty on the mean of the energy scale, returned by the fit, see Section 5.3 for more details. We remind that the energy scale mean was extracted from the mean of the ^{55}Fe peak by performing a Gaussian fit. By taking into account the hundreds of calibration data taken through the experiment, the average uncertainty on the energy scale mean, was estimated to be 1.35 %.

The energy scale of the experiment was then shifted by ± 1.35 %, and the analysis was rerun in order to determine the impact on the QF. Table 7.5 gives the values of α and β after shift of the energy scale.

	Condition 1	Condition 2	Condition 3
α	0.2801	0.2765	0.2836
β	0.0867	0.0868	0.0865
σ_α	0.0050	0.0050	0.0050
σ_β	0.02	0.02	0.02

Table 7.5: Table summarizing the values of α and β returned by the fit with the shift in the energy scale, as well as the errors returned by the fit. Condition 1 corresponds to the nominal mean energy scale, while condition 2 and 3 correspond to a -1.35 % and +1.35 % shifts, respectively, in the energy scale.

For condition 2, the impact on α and β are 1.23 % and 0.11 %, respectively, while for condition 3, the impact on α and β are 1.25 % and 0.23 %. We chose to report the largest of these uncertainties as systematic uncertainty of the quenching factor.

Figure 7.9 shows the impact of the energy scale shift by +1.35 % on the QF. The orange curve represent the quenching factor with the nominal energy scale, with corresponding error band in orange. The blue curve corresponds to the quenching factor after shift of the energy scale by + 1.35 %, with associated error band in blue.

The maximum impact on the QF from the energy scale systematic uncertainty is 1.3 % at low energy (0.43 $\mathrm{keV_{nr}}$) and 1.24 % at high energy (10 $\mathrm{keV_{nr}}$). We report the systematic uncertainty from the uncertainty on the energy scale mean (mean ± error from fit ± systematic):

$$\alpha = 0.2801 \pm 0.005 \pm 0.0036 \qquad \beta = 0.0867 \pm 0.02 \pm 0.00015$$

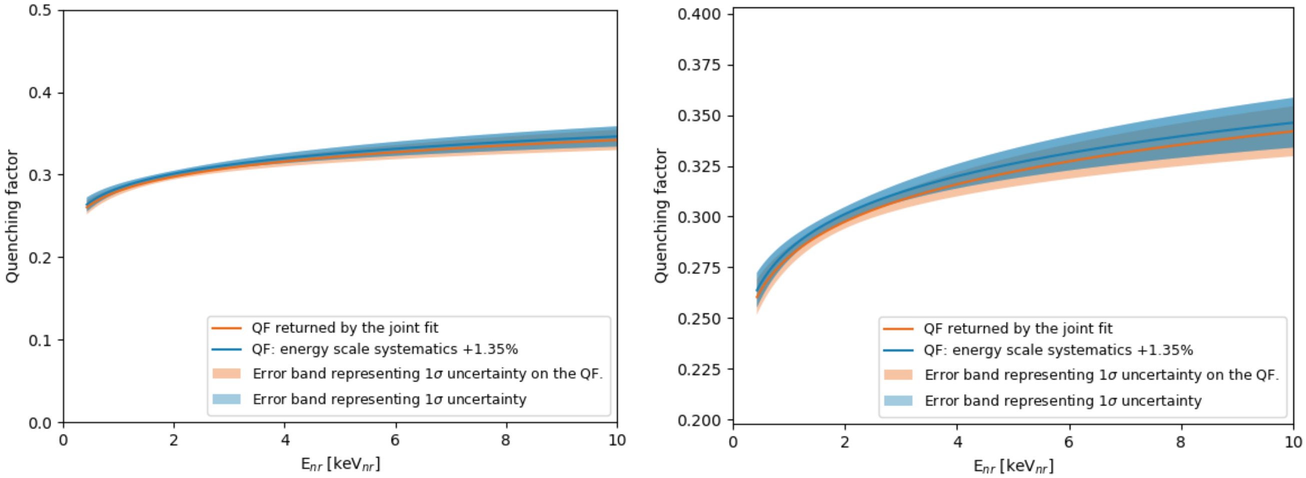

Figure 7.9: Comparison of the quenching factor for the nominal energy scale, in orange, with associated error band, in orange, with the resulting QF from an energy scale shifted by 1.35 % from its central value, in blue, with associated error band. The right plot is a zoom of the left plot.

After investigating all the sources of uncertainties in our experiment and model as described above, the uncertainty on the scattering angle has a significant impact on the nuclear recoil distribution and thus on the quenching factor. To account for this source of systematic uncertainty a gaussian prior on the scattering angle was implemented in our model. We report the systematic uncertainties from the energy response, the reconstruction efficiency, the possible electronic offset, and the energy scale decoupled from the error returned by the fit in Section 7.3.

7.2.8 Discussion: individual fits

A final test was performed to check if the parametrization adopted to model the quenching factor would affect the estimate of QF. For this, an independent fit to each of the data set was performed using the same model as described in 6.3 and the same fitting procedure using iminuit. However, the energy scale's standard deviation was fixed as it is a common parameter of all the runs, which depends on the detector and not on the experimental configuration. The value used for the width of the energy scale distribution was the value returned by the joint fit.

Figure 7.10 shows the energy spectra and the comparison between the joint fit results, solid line and orange error band, and the independent fit results, dashed line and blue error band, for the energy runs. The energy runs taken with the annulus structure (run 7, 8, 9, 10 and 11) show a good agreement between the joint fit's and the single fit's results, within error of the independent fits errors.

However, the three energy runs not recorded with the annulus structure (run 14) show quite a discrepancy between the single and the joint fits. Moreover, the error bands of the independent fits for each energy of run 14 is larger than the error bands from comparable energies taken with the annulus structure. Both behaviors can be explained by the accuracy with which the distances were recorded for run 14. Indeed, as previously mentioned the backing detectors were not installed on a pre-designed structure. Despite our care, the distances measured could have been off by a few mm (2 mm), thus shifting the position of the recoil peak. Another possibility is the orientation of the backing detectors which might not have been perfectly parallel to the beam line, which was not the case for the annulus structure, and assumed for all configurations to calculate the scattering angle distributions. This issue in particular would impact the width of the nuclear peak, as the solid angle angle of the BDs would be larger. With all these uncertainties linked to run 14, it is not surprising that the single and joint fits differ. Hence, we recommend for future quenching factor measurements to use pre-designed structures in order to control those uncertainties.

A common observation between the energy spectra is the error band for the multi fit is narrower

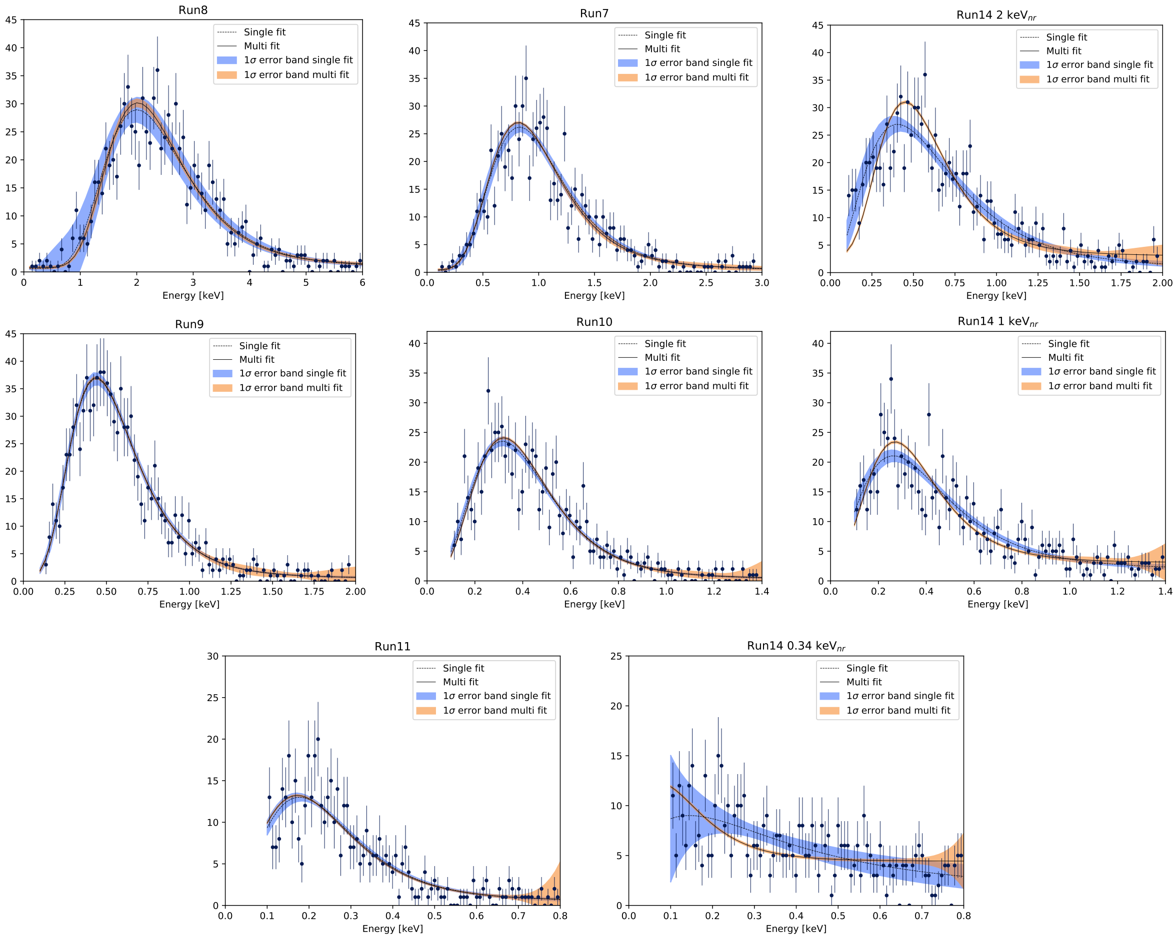

Figure 7.10: Comparison of the single fit (dashed line and blue error band) to multi fit (solid line and orange error band) for the 8 energy spectra.

for the recoil distribution than the error band of the single fit. This behavior is expected as the joint fit has access to more statistics and imposes more constrains on the values of the parameters, in particular the values for α and β that are constrained over the energy range covered by all the runs. One can observe a feature in the multi fit error band (orange), the errors become larger for some energy spectra (lower in energy) at the upper end of the energy range covered (background).

In order to test the quenching factor parametrization that we used in our model, we report one point from each of the five energy runs taken with the annulus structure. We chose not to report the QF from run14 as the errors were quite large and thus did not provide meaningful informations.

The energy point reported for each energy run is the mode (roughly) of the recoil distributions, see Table 7.6. Figure 7.11 shows the independent QFs (determined from the modes), along with their error bars. The five points were fitted with the $\alpha \mathrm{E}_{nr}^{\beta}$ parametrization, the resulting curve of such fit is given by the solid blue curve along with its error band. Figure 7.11 shows that the independent QFs are consistent with the $\alpha\beta$ parametrization. The same figure shows a comparison of the independent QFs and their fit with the QF curve from the joint fit to the data in orange along with its error band. Again, the independent QFs are in reasonable agreement with the joint fit, less than $1\,\sigma$.

	run8	run7	run9	run10	run11
Mode [$\mathrm{keV_{nr}}$]	6.5	2.9	1.7	1.3	0.74
Range [$\mathrm{keV_{ee}}$]	3.8-9.0	1.7-4.4	0.88-2.48	0.6-2.0	0.4-1.0

Table 7.6: Table summarizing the modes of the energy distributions and the energy ranges used to report the independent QFs.

Finally, we looked at the behavior of the independent QFs for an energy range and not only for the mode of the distribution. Typically, the energy ranges investigated correspond to $\pm\,1\,\sigma$ of the modes, they can be found in Table 7.6. Figure 7.12 reports the independent QF curves along with the joint fit in black. This figure is another illustration of the energy overlap between the different energy runs, in particular at about $2\,\mathrm{keV_{nr}}$, where three energy runs overlap. Runs 10, 9 and 7 display an error band feature already observed in the joint fit error band: larger at the edge of the energy range and narrower at the center. However, the feature for the three independent QFs is stronger than that of the joint fit. The reason being that the correlation between α and β is quite high for these three runs: > 0.98. Moreover, the feature is explained by the statistics available in the energy distributions. Indeed, at the mode the error bands are the narrowest due to the high statistics constraining α and β. Thus, the narrow region of the error band of the joint fit is caused by the higher statistics available in that region.

In conclusion, the independent fits confirms that the α,β parametrization adequately describes the behavior of the QF in the energy range investigated. The independent fits also display the same error band feature as the joint fit's error band, which is caused by a high correlation between the quenching factor parameters and statistics of the energy runs.

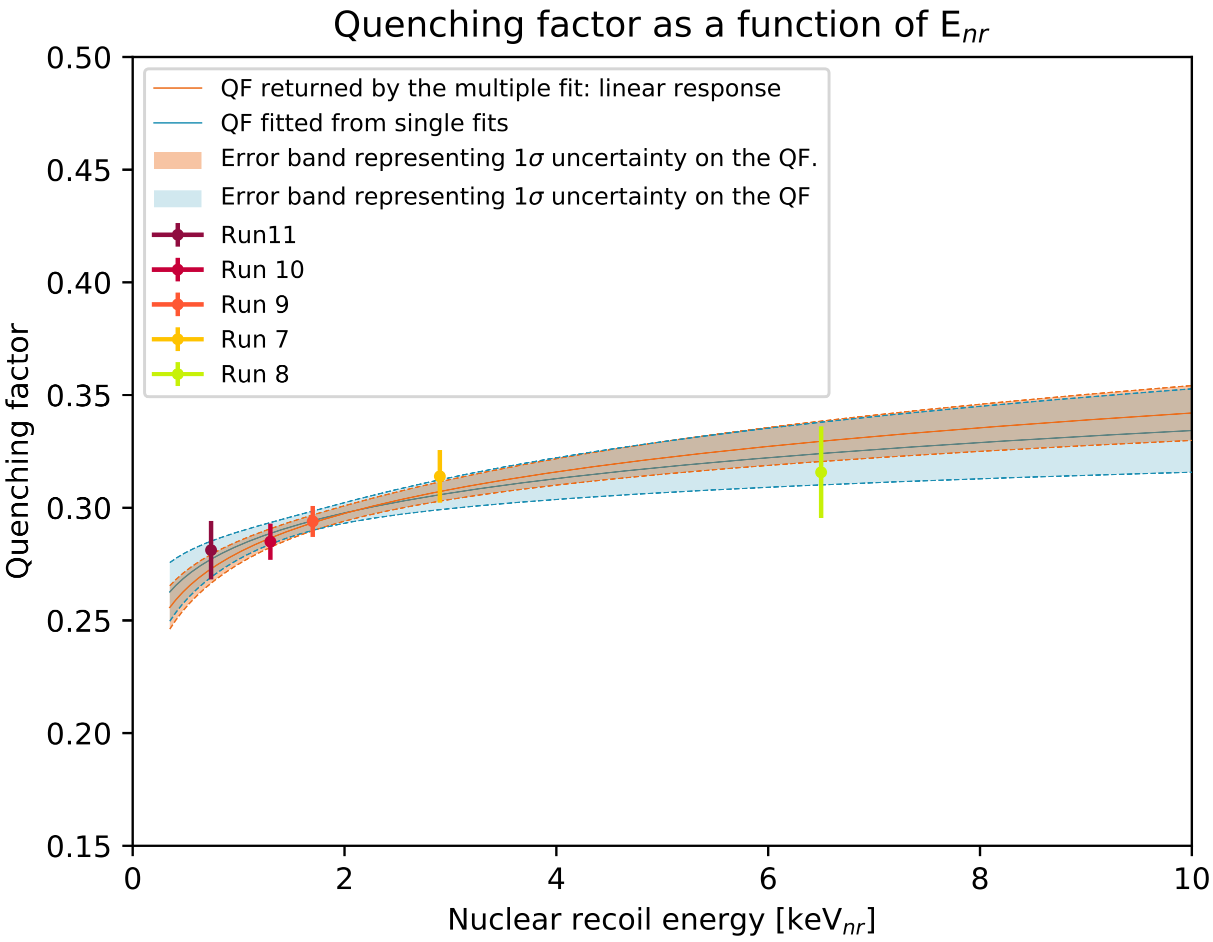

Figure 7.11: Shows the QF for the modes of 5 of the energy runs (annulus structure): 5 points in maroon, red, orange, yellow and green, along with the error bar for the energy. Fit in blue, performed by ROOT, of the 5 independent quenching factor points with the quenching factor parametrization: αE_{nr}^{β}, along with the $1\,\sigma$ error band returned by the fit. Comparison with the joint fit to the data and $1\,\sigma$ error band in orange.

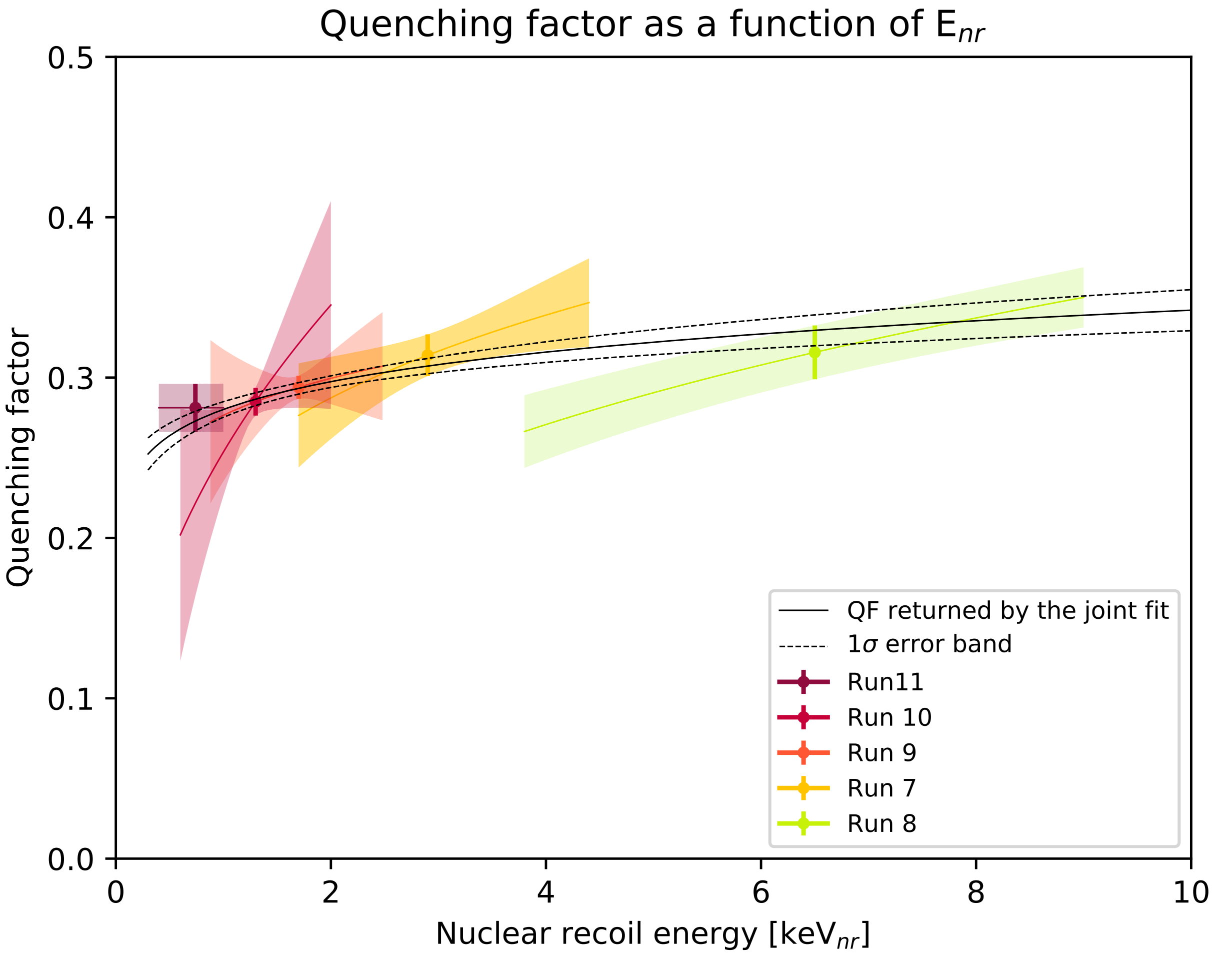

Figure 7.12: Shows the QF for the modes $\pm 1\,\sigma$ of five of the energy runs (annulus structure), along with the multi fit result, solid black line, and $1\,\sigma$ error band, black dashed line. The right plot is a zoom of the left plot.

7.3 Conclusion

Figure 7.13 shows the eight energy spectra, in blue, with the resulting unbinned joint fit, in red. The values returned for each free parameter are given in table 7.7. The expected fractions of signal events are consistent with each other for the runs taken with the annulus structure. Indeed, the exposure time was adjusted so that we would record similar statistics for each run. For run 14, the fraction of expected signal events decreases with the energy (or scattering angle), which is observed in other experiment [112] and expected from calculation.

Parameters	Values	Errors	Expected (angles)
f_{s8}	0.922	0.020	-
f_{s7}	0.947	0.022	-
f_{s9}	0.954	0.018	-
f_{s10}	0.958	0.023	-
f_{s11}	0.898	0.035	-
$\mathrm{f}_{s14,0.34\,\mathrm{keV}}$	0.234	0.039	-
$\mathrm{f}_{s14,1\,\mathrm{keV}}$	0.668	0.033	-
$\mathrm{f}_{s14,2\,\mathrm{keV}}$	0.733	0.029	-
α	0.2801	0.0050	-
β	0.0867	0.020	-
θ_8	28.55	0.34	29.02 ± 0.4
θ_7	18.89	0.09	18.84 ± 0.1
θ_9	14.33	0.06	14.33 ± 0.06
θ_{10}	12.47	0.048	12.48 ± 0.05
θ_{11}	9.41	0.033	9.4 ± 0.03
$\theta_{14,0.34keV}$	6.57	0.26	6.33 ± 0.26
$\theta_{14,1keV}$	11.55	0.18	11.13 ± 0.3
$\theta_{14,2keV}$	14.51	0.15	15.63 ± 0.3
σ_a	0.238	0.01	-

Table 7.7: Table summarizing the most probable values of the free parameters returned by the fit, their errors, as well as the expected values and errors for the scattering angles.

The scattering angle means returned by Minuit are consistent within 1σ error with the measurements, except for run 14 at 2 keV and 1 keV and run 8, which are at $3.7\,\sigma$, $1.4\,\sigma$ and $1.17\,\sigma$ from their measured scattering angle respectively. From this, the only strong discrepancy from the measurements is run 14 at 2 keV, which means that 7/8 scattering angles are in agreement or reasonable agreement with their measured value. This result is important to both validate our measurements but also our model.

The standard deviation of the energy scale distribution is 23.8 % in our model. Which indicates non negligible fluctuation of the energy scale (or gain) throughout the volume of the detector we used: simple sensor with no umbrella to correct the anisotropy of the electric field lines in the north hemisphere.

As presented at the beginning of Chapter 7, the returned values of the quenching factor parameters α and β, from the fit, are constrained by all the energy runs:

$$\alpha = 0.2801 \pm 0.005 \quad \text{and} \quad \beta = 0.0867 \pm 0.020$$

The systematic errors from the possible non-linearity of the detector response, the efficiency curve, the possible offset, the energy scale, and the bias described in Section 7.2 were added in quadrature. The values of the quenching factor parameters α and β with the errors from the fit and the systematic uncertainties are:

$$\alpha = 0.2801 \pm 0.005\,(\text{fit}) \pm 0.0045\,(\text{sys}) \quad \text{and} \quad \beta = 0.0867 \pm 0.020\,(\text{fit}) \pm 0.0069\,(\text{sys})$$

The systematic uncertainties are reviewed and listed in Table 7.8. We show the impact of each systematic on α and β, as well as on the quenching factor at low and high energies.

	α	β	QF(HE)	QF(LE)
Noise	0.04 %	0.4 %	Negligible	Negligible
Efficiency curve	0.4 %	3.7 %	$\leqslant$0.80 %	$\leqslant$0.29 %
Non-linearity	0.21 %	4.6 %	$\leqslant$0.60 %	$\leqslant$0.70 %
Offset	0.21 %	4.6 %	$\leqslant$0.06 %	$\leqslant$1 %
Energy scale	0.21 %	4.6 %	$\leqslant$1.24 %	$\leqslant$1.3 %
Analysis bias	-0.34 %	+1.6 %	$\leqslant$0.07 %	$\leqslant$0.47 %
Total	1.6 %	6.9 %	$\leqslant$2.9 %	$\leqslant$1.1 %

Table 7.8: Table summarizing the uncertainties investigated for the analysis and their impact on α, β, and impact on the quenching factor. The fluctuation of the baseline noise has a negligible impact on the QF. The total systematic uncertainty counts the uncertainties from the efficiency curve, the possible non-linearity, the electronic offset, the energy scale and the analysis bias. The last two columns evaluate the maximum impact on the quenching factor at high and low energies (HE: 10 keV_{nr} and LE: 0.43 keV_{nr}) from these sources of uncertainties considering the αs and βs returned from the different studies. The last raw corresponds to the total uncertainties on α, β and QF by adding in quadrature the different systematic contributions from the efficiency curve, the possible non-linearity, the electronic offset, the energy scale and the analysis bias.

The quenching factor reported in this work applies to an energy range between 0.43 and 11 keV_{nr},

Runs	χ^2	ndf	χ^2/ndf	p-values
run 8	89.55	82	1.09	0.26
run 7	67.46	80	0.84	0.84
run 9	59.75	78	0.77	0.93
run 10	74.74	77	0.97	0.55
run 11	65.79	81	0.81	0.89
run 14: 2 keV	140.4	87	1.69	2.5e-4
run 14: 1 keV	92.75	89	1.04	0.37
run 14: 0.34 keV	88.75	87	1.02	0.43

Table 7.9: Table summarizing the χ^2, the number of degrees of freedom (ndf), χ^2/ndf and p-values for each run. The χ^2/ndf and p-values are satisfactory except for run 14 at 2 keV$_{\mathrm{nr}}$, where the χ^2/ndf is close to 2 and the p-value smaller than 5 %. This values are indicative, we remind that the fit performed in this analysis was unbinned.

that was estimated by converting the results of the fitting curves in Figure 7.14a into Figure 7.14b using the results of the quenching factor.

The fit shows good agreement for the most part of the energy runs except for run14 at 2 keV. A Pearson's χ^2/ndf test was performed as well as calculating the p-value for each run, they are summarized in table 7.9. It is still unclear why the model seems to be unsatisfactory for run14 at 2 keV$_{\mathrm{nr}}$. However, the accuracy with which the scattering angles were determined for run14, is known to be less precise than for the runs recorded with the annulus structure. Thus, when giving the prior on the scattering angles for run14, the error on the mean might have been underestimated and thus over-constrained the fit.

The quenching factor as a function of the nuclear recoil energy is plotted Figure 7.15, between 0.4 and 10 keV$_{\mathrm{nr}}$. The orange curve represents the quenching factor mean returned by the fit. The error band represents 1σ error for a given energy and was calculated using the covariance matrix returned by Minuit, thus takes into account all statistical errors and the systematic error from the scattering angles. The systematic errors coming from the non-linearity of the detector response, the efficiency curve, the possible offset, the energy scale, and the bias are provided separately from the errors returned by the fitter, and are shown by the orange dashed region on Figure 7.15.

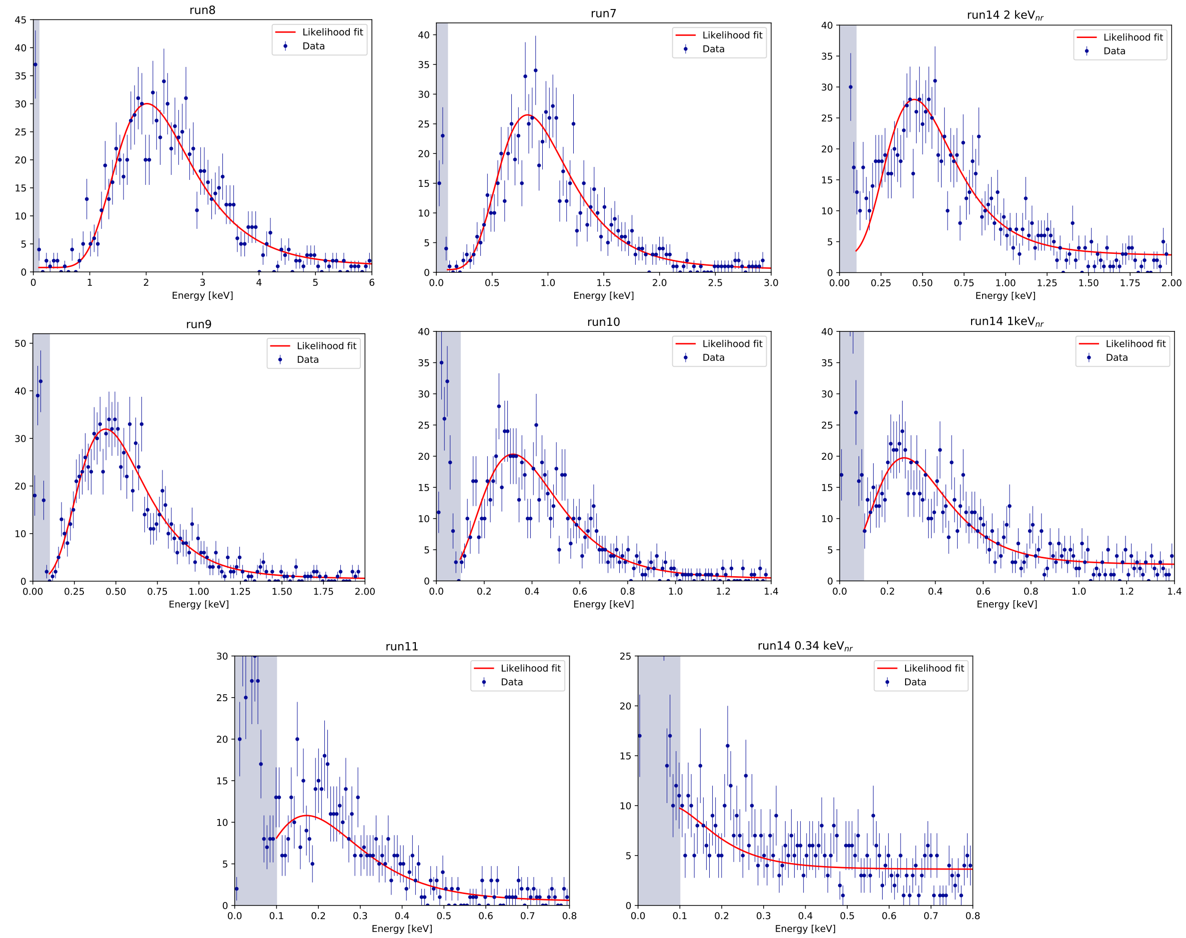
run8

run7

run14 2 keV$_{nr}$

run9

run10

run14 1keV$_{nr}$

run11

run14 0.34 keV$_{nr}$

Figure 7.13: Results of the unbinned joint fit on the quenching factor data. The spectra are ordered by decreasing values of the recoil energies. Recall that the mean gain, the W-value, θ_p, the neutron energy, neutron energy's standard deviation and scattering angles' standard deviations are fixed, and that the fraction of expected signal events for each run, as well as the scattering angles, the standard deviation of the gain fluctuation (or energy scale), α and β are free parameters of the joint fit.

The Lindhard theory is often used to compare with experimental results, it shows reasonable agreement in silicon and germanium but also in LXe and LAr [113], [114]. Two measurements in gases were performed in ^{4}He and isobutane, [10] [11]. They showed some discrepancy between Lindhard and their experimental results as well as with the SRIM simulation. To stay consistent with other reports on QF measurements, we compared our results with the quenching factor of the

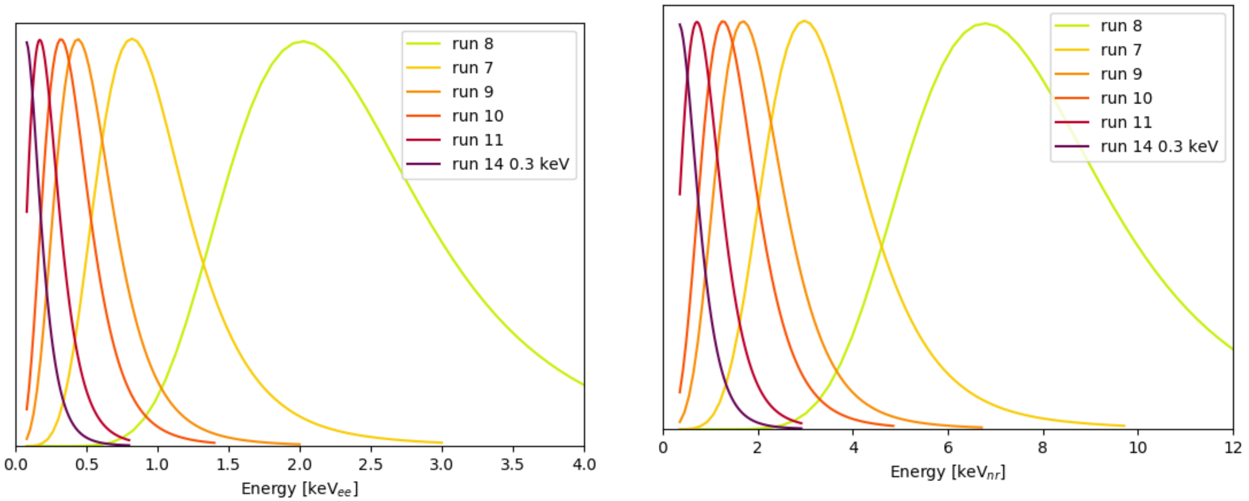

(a) Overlap of the resulting fitting curves in eV$_{ee}$.

(b) Overlap of the resulting fitting curves converted in eV$_{nr}$ by using the quenching factor result.

Figure 7.14: Overlap of the different energy runs using the fitting curves to the energy spectra, in eV$_{ee}$ and in eV$_{nr}$. Each curve corresponds to the energy range covered by a single run. These figures allow to illustrate the overlap in energy between the different runs, thus we have several energy runs constraining the same energy for the quenching factor. These figures also illustrate the motivation behind fitting all the energy runs simultaneously.

Lindhard theory, black dashed line, and the SRIM simulation, blue dots, in neon. The Lindhard theory and the SRIM simulation show good agreement for neon. The quenching factor that we extracted from our data is larger than the Lindhard theory and SRIM at energies below roughly 9 keV$_{\mathrm{nr}}$. The maximum discrepancy between our quenching factor and Lindhard/SRIM is 24 % at low energy. Our results show that the quenching factor in neon is more optimistic than expected, which will allow us to reach lower nuclear recoil energies. Figure 7.12 shows the QF curve obtained from the multi fit along with the single fits. We were able to show that the multi fit and single fits were consistent with each other, and in particular confirmed the shape of the final error band for the multi fit.

With this experiment we demonstrated the feasibility of measuring the quenching factor of gas mixtures using a Spherical Proportional Counter in a neutron beam below 1 keV. To our best knowledge, it is the first time that a quenching factor is extracted using a joint fit and report values for a quenching factor parametrization (αE_{nr}^{β}), so that the quenching factor is known for each energy

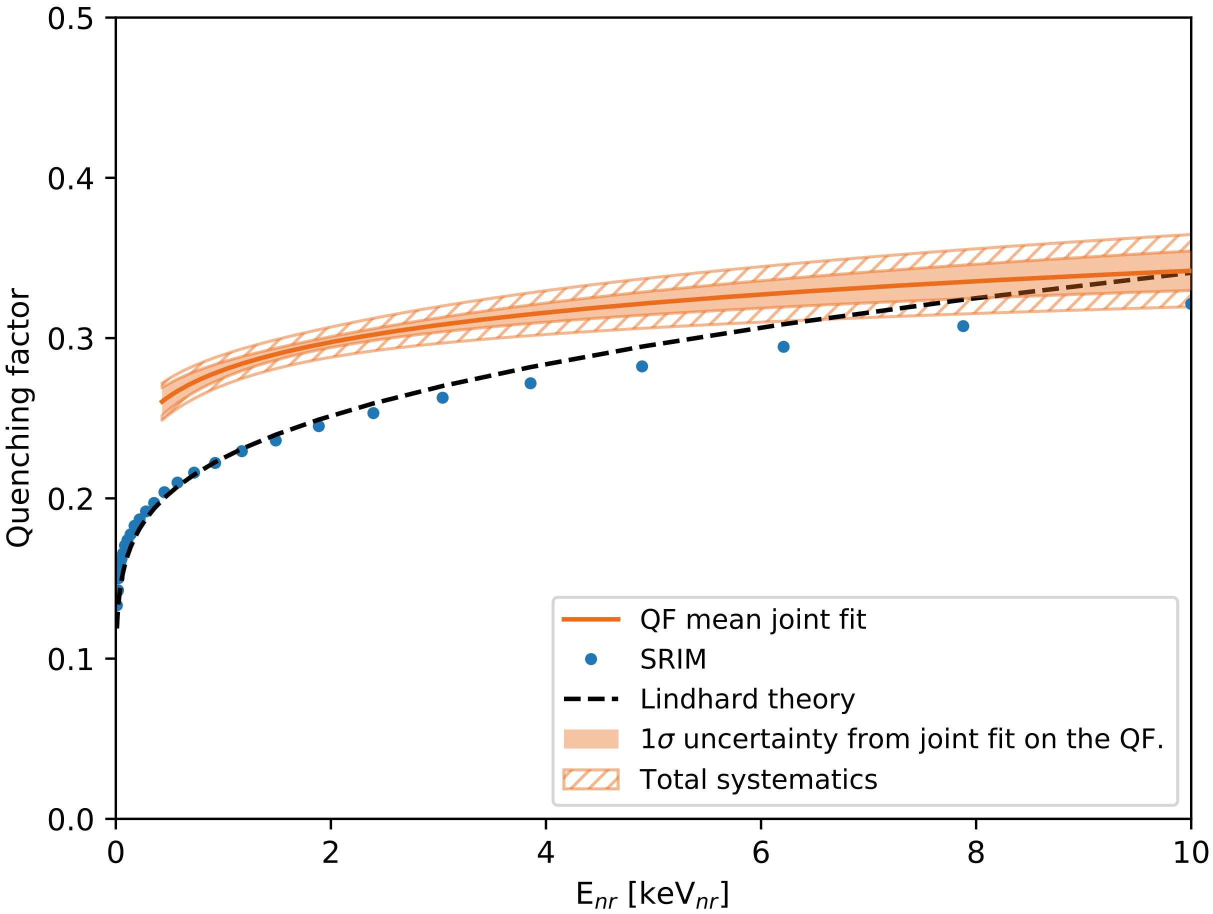

Figure 7.15: Quenching factor as a function of the nuclear recoil energy, using the values of α and β returned by the fit. The orange curve corresponds to the quenching factor mean for a given nuclear recoil energy. The orange error band corresponds to 1σ error on the quenching factor for a given nuclear recoil energy, as returned by the fit. The orange dashed region correspond to the total systematic uncertainties resulting from non-linearity of the detector response, energy efficiency, electronic offset, and energy scale uncertainties, as well as systematic from the analysis' bias. In dashed black is the Lindhard theory curve and the blue dots correspond to the quenching factor calculated by SRIM with the same gas conditions.

across the range covered: 0.43 and 11 $\mathrm{keV_{nr}}$. This is also the first time such measurements were performed in neon gas, which allow the NEWS-G collaboration to have a nuclear recoil calibration for the neon gas mixture used for WIMP searches.

Chapter 8

Expected Coherent elastic neutrino-nucleus scattering signal in a SPC detector from a nuclear reactor source

The NEWS-G collaboration is interested in detecting CEνNS at a nuclear reactor using an SPC. The main motivation comes from understanding the neutrino flux at a nuclear reactor and also to search for sterile neutrinos. The high neutrinos flux at a nuclear reactor is a compelling advantage compared to spallation sources despite the technical challenges induced by lower neutrino energies. In this section, we briefly cover the nuclear fission principles before describing our calculations to evaluates the CEνNS detection rates for different conditions. We consider four different targets, to estimate the best candidate to detect CEνNS. This section is the first step in our study to assess the feasibility of an experiment using a NEWS-G SPC at a nuclear reactor to detect CEνNS.

8.1 Nuclear reactor physics

8.1.1 Fission principles

Nuclear reactors provide a strong source of pure $\bar{\nu}_e$: up to 10 MeV. In the nuclear core, nuclear fissions take place continuously using the principles of nuclear chain reaction to produce energy. The nuclear fission takes place when a heavy nucleus ($Z \geqslant 90$) splits into two lighter nuclei. Fissions can be spontaneous if the nucleus is very heavy ($Z > 95$), or induced by an incident particle like a neutron. The two fission fragments are rich in neutrons and in an excited state, thus are highly unstable. They emit energy in the form of gamma rays and several neutrons to become more stable. On average, a fission reaction release about 200 MeV [115] [116], depending on the fissioning isotope, see Table 8.1. This energy is mainly contained in the reactor, while a small fraction is lost with escaping neutrinos. The neutrinos are emitted by the β^- decays from the fission products, see the scheme in Figure 8.1.

In nature, only ^{235}U is fissionable, i.e. it undergoes fission when hit by an incident thermal neutron (~ 10 MeV), it is said to be fissile. However, typically nuclear fuels do not only contain ^{235}U as the isotope is quite rare on Earth: 0.7 % of the total uranium present on the planet. An other isotope, ^{238}U, accounts for over 99 % of the uranium on Earth, but is not fissile. However, ^{238}U can undergo radiative capture, which leads indirectly to produce ^{239}Pu that is fissile. ^{238}U is said to be fertile.

$$^{238}_{92}\mathrm{U} + \,^{1}_{0}\mathrm{n} \longrightarrow \,^{239}_{92}\mathrm{U} \longrightarrow \,^{239}_{93}\mathrm{Np} \longrightarrow \,^{239}_{94}\mathrm{Pu} \tag{8.1}$$

Increasing the nuclear fuel concentration of ^{235}U to about 5 % is used for most of commercial nuclear reactors. This is known as enrichment. This process can reach up to 20 % concentration in research nuclear reactors.

The principle behind nuclear reactors is the chain fission reaction, where the fission-induced neutrons' flux is stable and where this newly created neutrons will result in subsequent fissions. The reaction can be described by Figure 8.2. A system's ability to maintain such a flux of neutrons is defined as criticality. Nuclear reactor are said to operate in a critical state, a typical fission

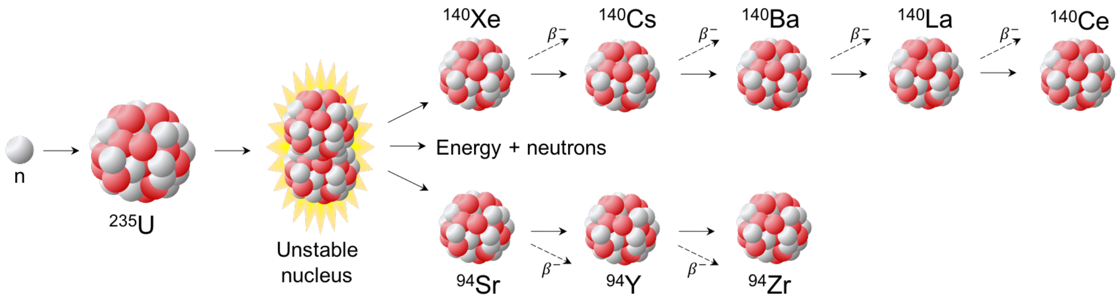

Figure 8.1: Example of fission reaction and beta decay of the fission fragments until stability.

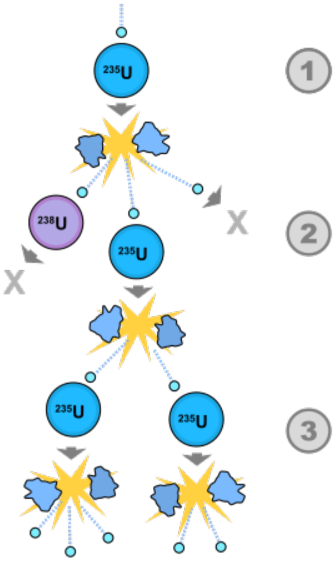

Figure 8.2: Chain reaction principle [117].

reaction of ^{235}U is as follow:

$$^{235}\mathrm{U} + {}^{1}_{0}\mathrm{n} \longrightarrow {}^{A_1}\mathrm{FP}_1 + {}^{A_2}\mathrm{FP}_2 + k\,{}^{1}_{0}\mathrm{n} + \gamma, \tag{8.2}$$

where $^{A_{1,2}}$FP are the fission products and k is the mean number of emitted neutrons per fission.

8.1.2 Nuclear reactors

A nuclear reactor is composed of three main components: the fuel, the coolant and the moderator. The second is used to recover the heat produced and the third thermalizes fast neutrons.

The choices of these components define the class of nuclear reactor. There are two main types of reactor:

- **Thermal reactors**: the fission-induced neutrons are thermalized in order to use the large cross section of thermal energies (n-isotope). Thus, the neutrons need to collide with light nuclei, located as close as possible to the fuel in order to decrease neutron losses and maximize the number of fissions. Hence, often the moderator is also used as coolant, like water (H_2O) and heavy water (D_2O), which are widely used in thermal reactors. The choice of moderator often drives the choice of fuel. Indeed, the cross section of thermal energies with ^{235}U allows to use lowly enriched uranium (up to 5 %) or even to use natural uranium in the case of heavy water. Thermal reactors are the most common class of nuclear reactor, and themselves are subcategorized in two classes. Nuclear reactors using water as moderator and coolant, and thus having an enriched core to ^{235}U, include Pressurized Water Reactors (PWRs) and Boiling Water Reactors (BWRs). The nuclear reactors using heavy water as moderator and coolant, and thus, not requiring enrichment are called Pressurized Heavy Water Reactors (PHWRs).

- **Fast neutrons reactors**: it is chosen to keep fast neutrons to generate more fissions. The cross section of fast neutrons with ^{235}U is low (in comparison to thermal neutrons), thus, one needs to keep the flux of neutrons constant in order to maximize the interactions with the fuel as well as having a compact core. Because of the lower cross section of fast neutrons with the available isotopes, it is necessary to have a higher enrichment of the fuel, which is of the order of 20 %. The high neutron flux allows to create more fissile isotopes from the fertile ones: this is called fuel regeneration. The coolant needs to use heavy atoms in order to avoid any moderation of the neutrons, thus, molten metals (sodium, lead) or gases (helium, CO_2) are chosen. Fast neutron reactors are for the most part research reactors.

In this work, we will consider thermal reactors as they represent the majority of the reactors in the world.

In Canada, the choice was made to use heavy water as a moderator and a coolant. This design is call the CANDU reactor (Canada Deuterium Uranium), they are classified as Pressurized Heavy Water Reactors. CANDU reactors were developed after the Second World War. Because the access to enrichment facilities was difficult (expensive to build and operate), heavy water was chosen as moderator to reduce the absorption of the neutrons by the moderator (like in light water). Heavy water is also more efficient at slowing down neutrons, thus it makes it more likely for a neutron to induce a fission. Hence, CANDU reactors can use natural instead of enriched uranium.

8.2 Reactor neutrinos

As mentioned previously, the $\bar{\nu}_e$ produced by a nuclear reactor are not directly a result of the fission reaction, but produced by the radioactive decay of the fission fragments. In general the fission fragments have different masses and can cover a wide range of isotopes, thus the radioactive decay period and energy can vary quite significantly. As a result, the estimation of the reactor antineutrino flux is a complex task, combining data from electron reactors spectra and distribution of beta branches provided by nuclear databases.

Since 99.9 % of reactor $\bar{\nu}_e$ are from ^{235}U, ^{238}U, ^{239}Pu, and ^{241}Pu [118], we consider only these four isotopes for the neutrino energy spectrum. The number of neutrinos emitted is proportional to the thermal power of the reactor. For example, a 1 GW reactor generates about $2 \times 10^{20}\,\bar{\nu}_e$/s. Table 8.1 summarizes the impact of the different isotopes on the neutrinos and energy released.

In order to estimate the reactor antineutrinos flux, models were developed combined with data using inverse beta decay as detection channel. There are not many models in the literature: Vogel

	^{235}U	^{238}U	^{239}Pu	^{241}Pu
Q_i, E (MeV)/fission	202.36 ± 0.26	205.99 ± 0.52	211.12± 0.34	214.26 ± 0.33
$\bar{E}_{\bar{\nu}_e}$ (MeV)	1.46	1.56	1.32	1.44
$\bar{\nu}_e$ / fission	5.58	6.69	5.09	5.89
p_i PWR	0.560	0.080	0.300	0.060
p_i PHWR	0.543	0.411	0.022	0.024

Table 8.1: Table summarizing the impact of each isotope to the reactor antineutrino flux: average energy released by fission [115], average neutrino energy, number of neutrinos released by fission [116] and the fraction of total thermal power produced by the isotope [119].

and Engel's [120], which is the "classic model" used for neutrino reactor, Kopeikei's [121], Mueller's [122], Huber's [123]. We decided to use the work proposed by M. Baldoncini [124], which uses the neutrino flux parametrization from Huber-Mueller [122]. The neutrino flux is defined as:

$$S(E_{\bar{\nu}}) = P_{th} LF \sum_{i=1}^{4} \frac{p_i}{Q_i} \lambda(E_{\bar{\nu}}) \tag{8.3}$$

with P_{th} the thermal power, considered to be 1 GW here, Q_i the average energy released per fission for the i^{th} isotopes, see Table 8.1, p_i is the power fraction for the i^{th} isotope, which is the fraction of the total thermal power emitted by fission by the i^{th} isotope, and:

$$\lambda(E_{\bar{\nu}}) = exp\Big(\sum_{p=1}^{6} a_p^i E_{\bar{\nu}}^{p-1}\Big) \tag{8.4}$$

a_p^i are the coefficients of the polynomial, their values can be found in Table 8.2. These coefficients were estimated from a fit to the data (energy spectra of each isotope) performed by [122]. LF is the load factor, or capacity factor, that is the percentage of the effective working condition of a nuclear core. LF is the ratio:

$$LF = 100 \frac{E_{real}}{E_{ideal}} \tag{8.5}$$

E_{real} is the net electrical energy output over a given period of time and E_{ideal} is the maximum net electrical energy output possible over the same period. Load factor data are provided by the IAEA [125].

The neutrino spectrum, 10 m from the core, is shown in Figure 8.3, with a load factor of 100 %. The change in LF only affects the overall amplitude of the neutrino flux. We note that the Huber-Mueller parametrization gives an unrealistic neutrino flux below 1.8 MeV, although this is a negligible effect for our purpose.

Figure 8.4 shows a comparison of neutrino spectra from a PWR and PHWR reactor. The difference between the two types of reactors comes from the power fraction of the i^{th} isotope. The energy spectrum from the PHWR reactor is shifted at higher energies by 0.7 %. This is expected, as

Isotope	a_1	a_2	a_3	a_4	a_5	a_6
^{235}U	3.217	-3.111	1.395	-0.369	$4.445.10^{-2}$	$-2.053.10^{-3}$
^{238}U	$4.833.10^{-1}$	$1.927.10^{-1}$	$-1.283.10^{-1}$	$-6.762.10^{-3}$	$2.233.10^{-3}$	$-1.536.10^{-4}$
^{239}Pu	6.413	-7.432	3.535	-0.882	$1.025.10^{-1}$	$-4.55.10^{-3}$
^{241}Pu	3.251	-3.204	1.428	$-3.675.10^{-1}$	$4.254.10^{-2}$	$-1.896.10^{-3}$

Table 8.2: Table summarizing the coefficients of the polynomial of order 5 used in equation 8.4 [122].

PHWR reactors are not using enriched uranium and that the mean energy released per fission is higher from ^{238}U, ^{239}Pu and ^{241} than from ^{235}U.

The Darlington power plant station, in Ontario, comprises four nuclear reactors with a total output of 3.512 GW when the four units are online. The typical thermal power of the unit 1 is 878 MW.

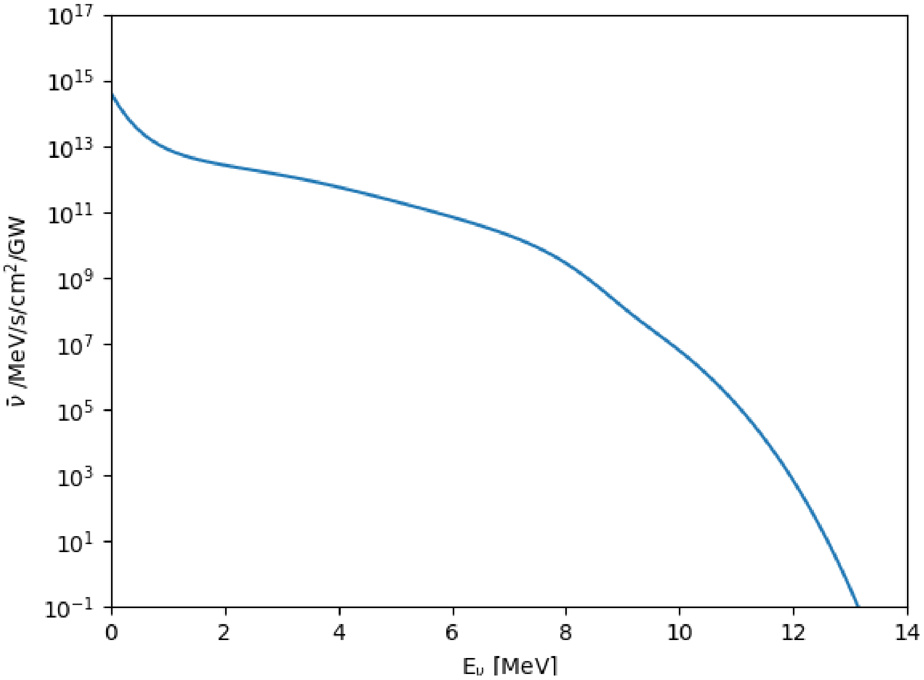

Figure 8.3: Neutrino spectrum for a PWR reactor, using Huber-Mueller parametrization. We consider the detector to be 10 m the source, a load factor of 100 %, and a thermal power of 1 GW.

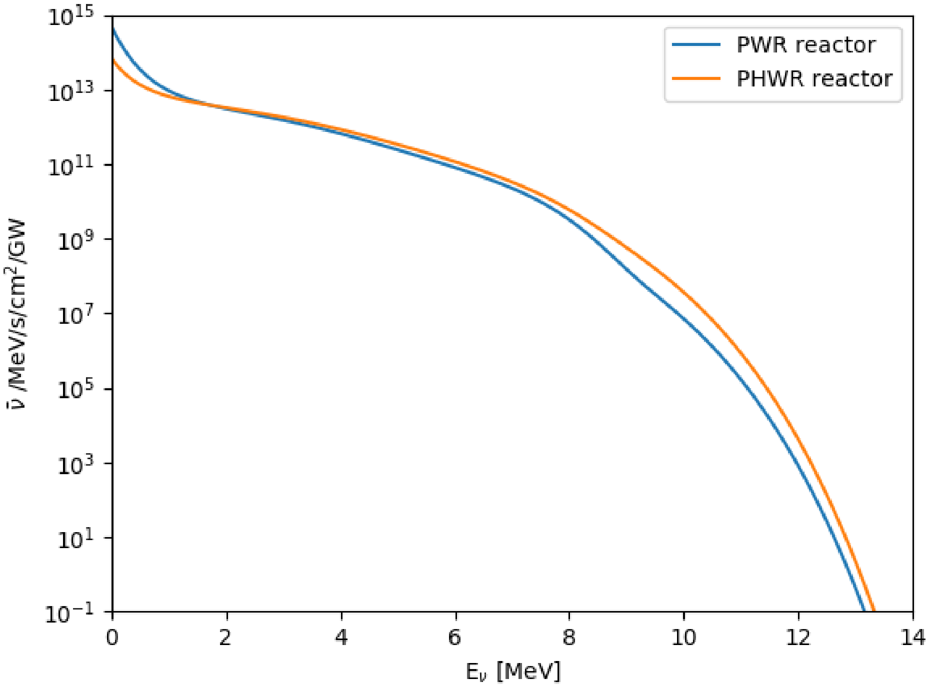

Figure 8.4: Comparison of neutrino spectra for a PWR and PHWR reactors with a load factor of 100 % and thermal power of 1 GW. The spectrum from PHWR goes to energies that are slightly higher than the one found in a PWR reactor.

8.3 Differential event rates

In this section, we estimate the CEνNS signal in a SPC detector placed 10 m away from the nuclear core. We will first estimate the differential event rate as a function of the total nuclear recoil energy, E_{nr}, then, we will calculate the differential event rate as a function of the nuclear recoil energy in electron equivalent, E_{ee}.

8.3.1 Differential event rates as a function of the nuclear recoil energy

To calculate the neutrino event rate from CEνNS in a detector, one must first obtain the differential event rate as a function of the nuclear recoil energy:

$$\frac{dR}{dE_{nr}} = \mathcal{N} \int_{E_\nu^{min}} \frac{d\phi}{dE_\nu} \times \frac{d\sigma(E_\nu, E_{nr})}{dE_{nr}} dE_\nu, \tag{8.6}$$

where $d\phi/dE_\nu$ is the neutrino flux and $\mathcal{N}$ is the number of target nuclei per unit mass (kg). In the case of CEνNS the target mass nucleus m_N is greater than the neutrino energy, $m_n \gg E_\nu$, thus the miminum neutrino energy necessary to generate a nuclear recoil is:

$$E_\nu^{min} = \sqrt{\frac{m_N E_{nr}}{2}} \tag{8.7}$$

$d\sigma(E_\nu, E_{nr})/dE_{nr}$ is the CEνNS differential cross section as a function of the nuclear recoil energy shown in Section **??**:

$$\frac{d\sigma}{dE_{nr}}(E_\nu, E_n) = \frac{G_F^2}{2\pi} M \left(2 - \frac{2E_{nr}}{E_\nu} + \left(\frac{E_{nr}}{E_\nu}\right)^2 - \frac{ME_{nr}}{E_\nu^2} \right) \frac{Q_W^2}{4} F^2(Q^2), \tag{8.8}$$

The differential event rates reported are expressed in /day/kg/GW/keV. Table 8.3 shows the different pressures depending on the target, for a 60 cm diameter SPC placed 10 m from the source and 1 kg of target material exposed. The pressures were calculated using the perfect gas law. The size of the SPC was chosen to match the dimension of the future surface experiment NEWS-G3 shield's detector, which goal is to assess surface backgrounds, and in particular cosmic muons and cosmogenic activation, in view of a CEνNS experiment. More will be presented about the NEWS-G3 shield experiment in Section 9. The size of the detector will be constrained by the space available on site, at the nuclear power plant station. Indeed, one must also take into account the size of the shielding which will be a cube of minimum 1.6 m of edge (based on the NEW-G3 shield design). From this table, we can see that the pressures needed to be achieved for xenon, argon and neon are feasible. In the other hand, the pressure for detecting CEνNS in helium might be challenging considering the high pressure required: 53.8 bar at 293 K. The pressure feasibility comes from several aspects: the safety, where the SPC vessel has to be certified for pressures above 2 bar and can not go above 11 bar (specifications for the NEWS-G3 SPC), and the gain, as when the pressure increases so does the HV applied on the anode in order to have a gain that allows to reach a low enough energy threshold. Sparks are created when the HV is too high, thus preventing us from reaching the ideal gain for such high pressures.

	Pressure (bar)			
Temperature	Xenon	Argon	Neon	Helium
273 K	1.5	5	9.9	50
293 K	1.64	5.38	10.68	53.8

Table 8.3: Table summarizing the different pressures depending on the gas mixture in a 60 cm diameter SPC.

For our purpose, we will be looking at both PWR and PHWR reactors. For the PHWR reactor, in addition to looking at the event rate with a LF of 100 %, we use the load factor of the Darlington 1 nuclear power plant (out of the four present on site), located on Lake Ontario in Canada, with an average load factor of 84.6 % [126]. In 2018, the load factor of the Darlington nuclear power plant facility reached 97.2 % [126]. We look at the impact of such changes of the load factor on the event rate of neutrinos.

Using Equation 8.6 the differential event rate of CEνNS events was calculated for the four different target nuclei: xenon, argon, neon and helium, in a SPC of 60 cm in diameter. The targets which seem to be the most advantageous are xenon, argon and neon, due to their highest event rates and achievable running conditions. By applying an energy detection threshold of 100 $\mathrm{eV_{nr}}$, which is the standard energy threshold in the literature [17] [127] and reachable by an SPC detector, by integrating the differential event rate above that threshold, we expect the event rates listed in Table 8.4. We also present the rates for the two load factors mentioned previously as well as the type of reactor. The impact of the load factor is non-negligible for the heaviest isotopes, with a difference in rate of 12.7 % in xenon. The impact of the reactor type (PWR/PHWR) is important, up to 21 % on the rate of xenon, and goes down with the target mass, with a difference of 16.3 %, 9.5 % and below 1 % for argon, neon and helium, respectively.

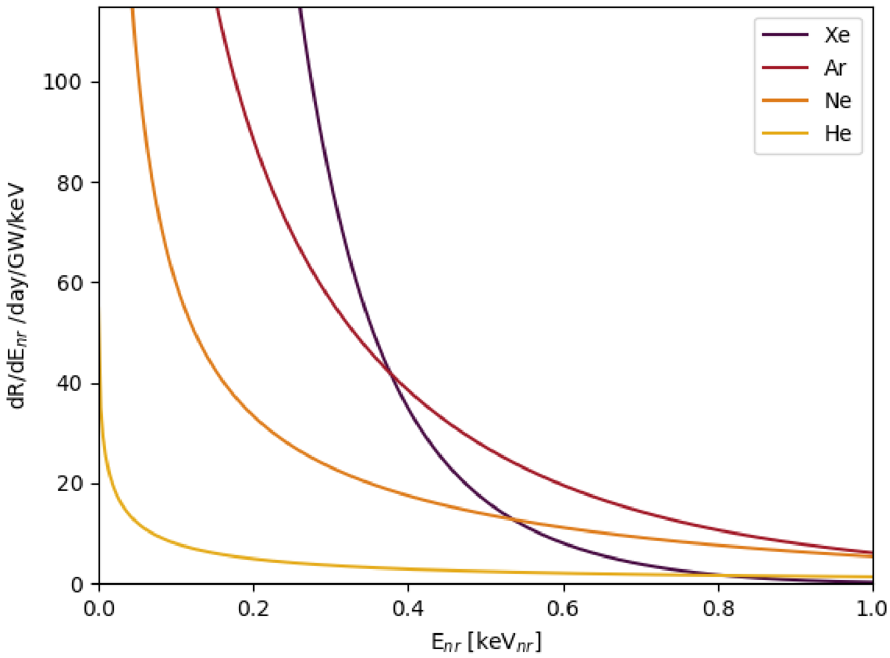

Figure 8.5: Differential event rate as a function of the nuclear recoil energy for different targets: Xe, Ar, Ne and He. We consider the SPC detector be 10 m away from the source and LF = 100 %. The differential event rate shown is for a PWR reactor.

			Xenon	Argon	Neon	Helium
PWR	LF = 100 %	Event rate	364	90	35	7
		Event rate > 100 $\mathrm{eV_{nr}}$	60	36	19	5
	LF = 97.2 %	Event rate	354	86	34	7
		Event rate > 100 $\mathrm{eV_{nr}}$	58	35	18	5
	LF = 84.6 %	Event rate	308	75	29	6
		Event rate > 100 $\mathrm{eV_{nr}}$	50	30	16	4.5
PHWR	LF = 100 %	Event rate	308	79	31	6
		Event rate > 100 $\mathrm{eV_{nr}}$	76	43	21	5
	LF = 97.2 %	Event rate	300	77	30	6
		Event rate > 100 $\mathrm{eV_{nr}}$	73	41	18	5
	LF = 84.6 %	Event rate	261	66	26	5
		Event rate > 100 $\mathrm{eV_{nr}}$	64	36	18	4.6

Table 8.4: Table summarizing the CEνNS rates for different gas targets in a SPC detector placed 10 m from the nuclear core. We consider 1 kg of target material and several LF. The event rates are in kg/day/GW.

8.3.2 Expected CEνNS signal in a SPC detector

Including the quenching factor and the energy response of the detector allows for the expected detectable signal of CEνNS to be estimated in our target materials.

For the quenching factor, we used Lindhard theory, which was introduced in Section 4.1, as:

$$f_n = \frac{kg(\varepsilon)}{1 + kg(\varepsilon)}, \tag{8.9}$$

where Z is the nuclei atomic number, A the mass number, k = $0.133\mathrm{Z}^{2/3}\mathrm{A}^{-1/2}$, $\varepsilon = 11.5 E_r \mathrm{Z}^{7/3}$ and g(ε) = $3\varepsilon^{0.15}$+$0.7\varepsilon^{0.6}$+ε.
The impact of the quenching factor on the event rate will be studied in Section 8.3.3.

For the response of the detector, we saw in Section 3.2.3 that for spherical proportional counters the primary and secondary ionization can be modelled following a Poisson and convolution of Polya distributions, respectively.

The analytical differential event rate of CEνNS in a detector is:

$$\frac{dR}{dE_{ee}}(E_{ee}) = \int^{E_{nr,max}} \frac{dR}{dE_{nr}}(E_{nr}) \mathcal{R}(E_{ee}|E_{nr}) \tag{8.10}$$

with $\mathcal{R}(E_{ee}|E_{nr})$ the response of the detector. By replacing the response with the response of an SPC detector, we have the differential event rate of CEνNS in our detector:

$$\frac{dR}{dE_{ee}}(E_{ee}) = \int^{E_{nr,max}} \frac{dR}{dE_{nr}}(E_{nr}) \sum_{j_{pe}=1}^{N_{pe,max}} P^{N^{th}}_{Polya}(E_{ee}|j_{pe}) P_{Poisson}(j_{pe}|E_{nr}) \tag{8.11}$$

To calculate the differential event rate of the CEνNS process including the response of the detector and the QF, we chose to develop a Monte Carlo simulation. Here is the algorithm to produce such differential event rate:

1. Pick randomly a nuclear recoil energy, E_{nr}, following the differential event rate: $\frac{dR}{dE_{nr}}$.

	Xenon	Argon	Neon	Helium
W-value (eV/ion pair)	22.6	26.4	27.6	41.3

Table 8.5: Table summarizing the W-values for the different nuclei targets investigated. The W-values for argon and helium were found in [128], the W-value for neon in [66] and for xenon in [129].

	Xenon	Argon	Neon	Helium
Upper energy bound (eV$_{ee}$)	250	800	1000	$\gg 1000$
Observable range (eV$_{ee}$)	200	550	950	$\gg 1000$

Table 8.6: Table summarizing the upper and observable energy range for each target investigated.

2. Apply Lindhard quenching factor to the energy: $E_{ee,qf} = \mathrm{QF}(E_{nr}) \times E_{nr}$.
3. Using the W-value for the respective target, calculate the mean number of primary electron for the given $E_{ee,qf}$: $\mu_{pe} = \dfrac{E_{ee,qf}}{\text{W-value}}$.
4. Pick randomly a number of primary electron(s) following Poisson: $\mathrm{n}_{pe} = \mathrm{Poisson}(\mu_{pe})$.
5. Pick randomly a number of secondary electrons following Polya: $\mathrm{n}_{se} = \mathrm{Polya}(\mathrm{n}_{pe})$.
6. Normalization.

The W-values for the different targets were obtained from [128] for argon and helium. The W-value in neon used in this calculations was estimated in [66], using a SPC and Ne:CH$_4$ (98:2). The W-value for xenon was obtained by averaging the values from [129], which gave a review of different measurements. The W-values are listed in Table 8.5. It is important to point out that in our model, the W-value does not depend on the energy, but has a fixed value.

Figure 8.6 shows the differential event rates as a function of the nuclear recoil energy in electron equivalent energy, E_{ee}, for xenon, argon, neon and helium. From these, we can see that the upper observable threshold varies with the target. We consider a detection threshold achievable by the NEWS-G detectors, $50\,\mathrm{eV_{ee}}$, the rates for the different targets are using this limit. The upper energy bound and the observable energy ranges are listed in Table 8.6.

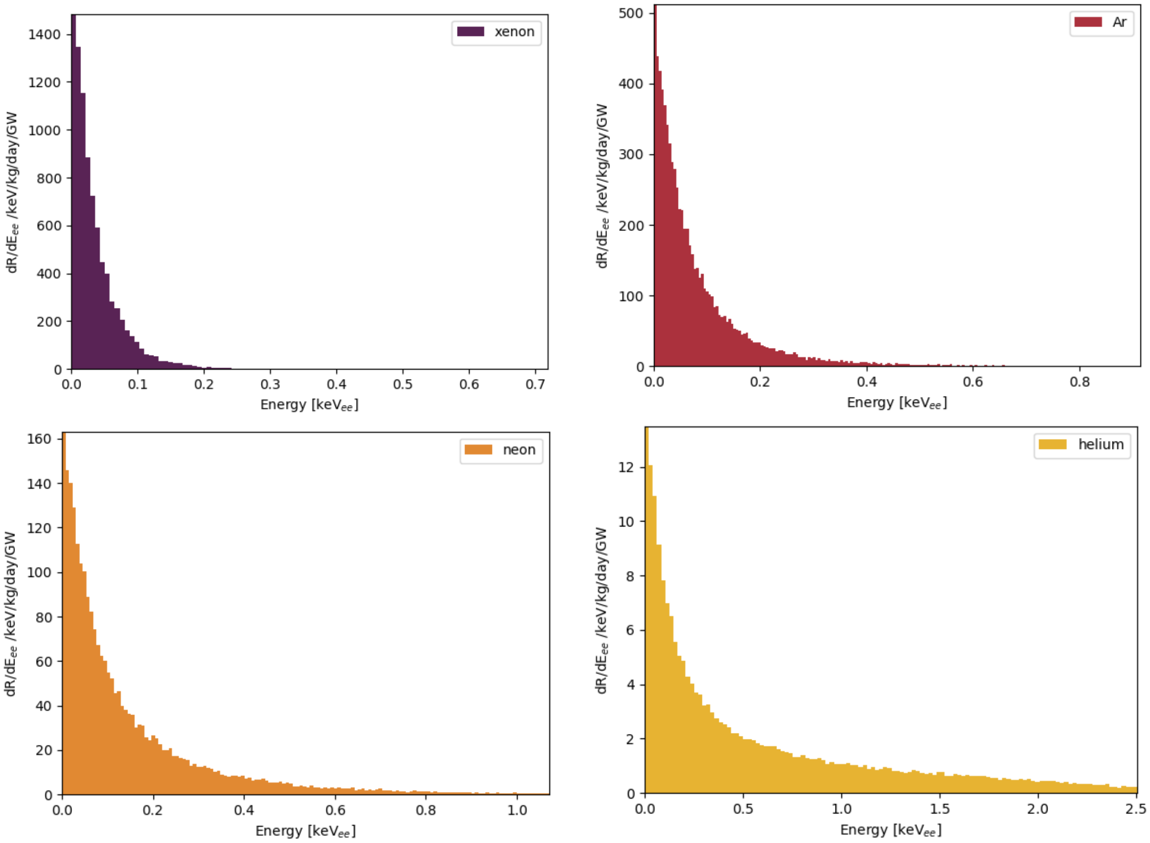

Figure 8.6: Differential event rates as a function of the nuclear recoil energy in eV$_{ee}$ obtained through Monte Carlo. The SPC detector is placed 10 m away from the source. The calculations take into account the response of the detector and the quenching factor, and were calculated for 1 kg for four targets: xenon, argon, neon and helium. We consider a PWR reactor with a LF = 100 % and 1 GW thermal power.

			Xenon	Argon	Neon	Helium
PWR	LF = 100 %	Event rate	192	60	25.6	5
		Event rate > 50 $\mathrm{eV_{ee}}$	13.5	16.4	11.2	3.6
	LF = 97.2 %	Event rate	186.6	57.8	25.0	4.8
		Event rate > 50 $\mathrm{eV_{ee}}$	13.0	15.9	10.9	3.5
	LF = 84.6 %	Event rate	162.3	50.2	21.8	4.5
		Event rate > 50 $\mathrm{eV_{ee}}$	11.2	13.8	9.5	3.0
PHWR	LF = 100 %	Event rate	181.8	58	25	4.4
		Event rate > 50 $\mathrm{eV_{ee}}$	17	20	13.2	3.6
	LF = 97.2 %	Event rate	176.6	56.3	24.3	4.3
		Event rate > 50 $\mathrm{eV_{ee}}$	16.4	19.6	13	3.5
	LF = 84.6 %	Event rate	154	49	21	3.7
		Event rate > 50 $\mathrm{eV_{ee}}$	14.3	17	11.2	3

Table 8.7: Table summarizing the event rates for the 1 kg of target material, we considered four targets: xenon, argon, neon and helium. The SPC detector is placed 10 m away from the source. The calculations take into account the response of the detector and the quenching factor. We show the event rates for different LF. The event rates are in /kg/day/GW.

The resulting rates from the Monte Carlo simulation are listed in Table 8.7. It appears that the best candidate for CEνNS detection with NEWS-G detectors is argon gas, regardless of the kind of nuclear reactor and load factor. Xenon and neon are also interesting targets that could be used in order to probe more targets and investigate any deviation in the Standard Model's cross sections. On the other hand, helium with its low rate and high pressure necessary to reach 1 kg of target material, seems to be an unlikely target choice for detecting CEνNS with an SPC.

These rates, despite giving us an order of magnitude of the expected signals in our detectors, have to be taken cautiously. Indeed, there's an important unknown in these calculations: the nuclear quenching factors of the investigated targets. As aforementioned, there are quenching factor measurements of liquid xenon and argon but not in gas. First measurements of quenching factor of neon nuclei in neon were presented in this work, and quenching factor measurement of helium ion in helium gas were performed in [10]. Moreover, the role that the pressure of the gas plays in the nuclear quenching factor is not well understood, it is expected to have a negligible impact from the prediction provided by SRIM, but the data shown by [10] in helium could imply a pressure dependence. More experiments have to be conducted in order to establish the impact of the pressure on the nuclear quenching factor.

8.3.3 Impact of quenching factor on the CEνNS event rate

One should measure the quenching factor of the proposed targets, at the desired conditions, prior to performing the CEνNS experiment, since the QF can significantly impact the event rate. In the mean time, in response to the uncertainty linked to the quenching factor for the targets investigated, we establish the impact of the quenching factor on the event rates presented in the previous section.

Impact of SRIM quenching factors on the CEνNS event rate in a SPC

			Xenon	Argon	Neon	Helium
QF SRIM	PWR	Event rate	192.7	60	25.7	5
		Event rate $> 50\,\mathrm{eV_{ee}}$	12.7	18.6	11.5	3.4
	PHWR	Event rate	183	59.3	25.2	4.4
		Event rate $> 50\,\mathrm{eV_{ee}}$	16.1	22.7	13.6	3.5
QF data	PWR	Event rate	-	-	26.4	-
		Event rate $> 50\,\mathrm{eV_{ee}}$	-	-	13	-
	PHWR	Event rate	-	-	25.7	-
		Event rate $> 50\,\mathrm{eV_{ee}}$	-	-	15.2	-

Table 8.8: Event rate using the quenching factor from SRIM for the two kind of nuclear reactors, as well as the impact from the quenching factor of neon nuclei in neon gas from the TUNL data. The event rates are expressed in /kg/day/GW

In this section, we look at the impact of the quenching factor on the rate of signal events. First, we looked at the quenching factors predicted by SRIM for the four different targets at their specific pressures to get 1 kg of target material in the detector.

Figure 8.7 shows a comparison between the quenching factors predicted by SRIM and by Lindhard. One can see that the two predictions (Lindhard/SRIM) are quite close, thus it is expected to have a small impact on the event rate. Table 8.8 shows the total and above threshold event rates for the two kind of reactors we are looking at (PWR/PHWR). The impact of the SRIM quenching factors on the event rates above threshold are:

	Xenon	Argon	Neon	Helium
PWR	−6 %	12 %	3 %	−5 %
PHWR	5.3 %	13.5 %	−3 %	−2.7 %

Table 8.9: Impact of the quenching factor on the CEνNS event rate, with 50 $\mathrm{eV_{ee}}$ threshold, in a SPC detector for the four targets investigated. We compare the event rate between two predictions: Lindhard and SRIM, Lindhard is considered the nominal condition. Depending on the target, the impact can range from 2.7 % for helium up to 13.5 % for argon.

The impact in argon is the greatest as the quenching factors' discrepancy takes place at low energies, where it is expected to have the most events. Despite these changes, argon remains the most promising target.

We investigated the impact of the quenching factor extracted from the TUNL data for the neon gas mixture on the CEνNS event rate. The event rate for the neon target is listed in Table 8.8 and shows an increase of the event rate (above threshold) of 16 % and 15 % for PWR and PHWR reactors, respectively, relative to an event rate derived using Lindhard. Despite this more optimistic quenching factor in neon, argon remains the best target for a CEνNS experiment if it has a quenching factor within the Lindhard and SRIM models, or above.

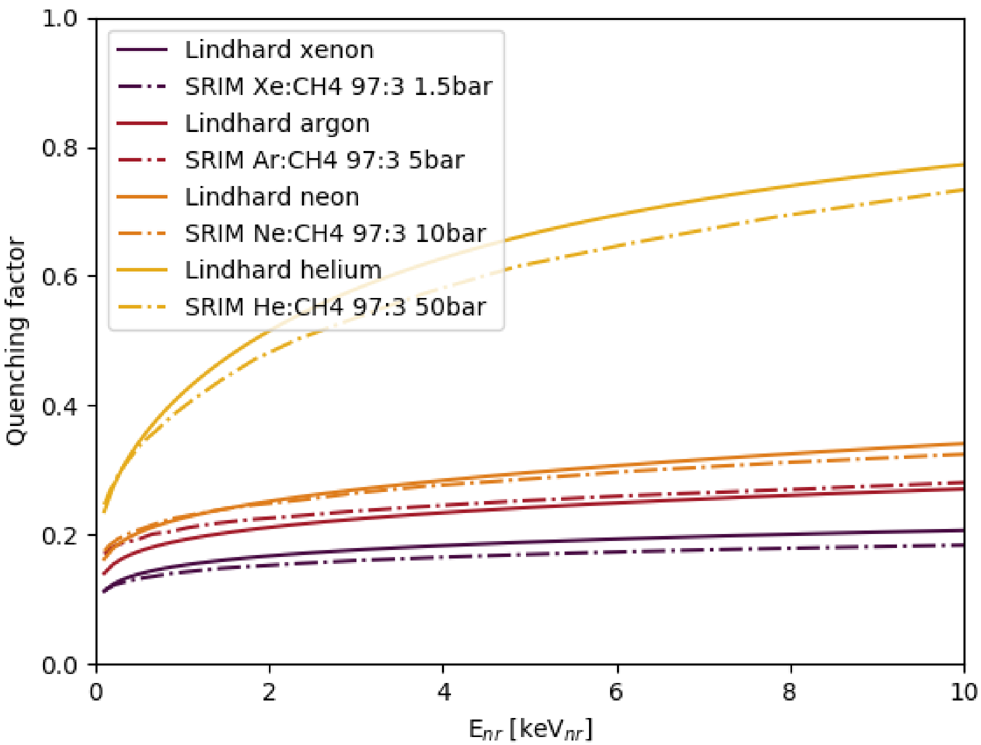

Figure 8.7: Illustration of the differences in quenching factor between different models: Lindhard and SRIM.

Impact of the uncertainties linked to quenching factor measurements on the CEνNS event rates in a SPC

In this section, we show a preliminary study of the quenching factor (relative) uncertainty's impact on the expected CEνNS event rate in an SPC. The motivation for this study, is to estimate with which uncertainty we will need to measure the quenching factor in the region of interest: $\leqslant 5\,\mathrm{keV_{nr}}$, for the targets under investigation in order to have an uncertainty of 10 % or less on the estimation of the event rate.

Table 8.10 shows the estimated required uncertainty on the quenching factor in order to have an uncertainty of about 10 %, or less, on the event rate of CEνNS. From this preliminary study, we estimated that the uncertainty on the quenching factor of argon, which is the favored candidate for a CEνNS experiment with an SPC, had to be of 10 %. The uncertainty on the quenching factor in xenon should be 5 % in order for the event rate uncertainty to stay below 10 %. As for neon and helium, these two targets allow more flexibility in the quenching factor uncertainty, as an uncertainty of 20 % would lead to uncertainties below 10 % on the event rate. The uncertainties reported in quenching factor measurement experiments in the region of interest: $\leqslant 5\,\mathrm{keV_{nr}}$, are of the order of 15-20 % in scintillation crystals [130], [131], between 10-20 % in liquid xenon [132], [133], [113]. To the best of our knowledge, as of today, there are no existing quenching factor measurements in argon (liquid nor gas) below $5\,\mathrm{keV_{nr}}$.

While an uncertainty of 10 % on the CEνNS event rate might not impact the detection of the interaction, we remind the 33 % total uncertainty in the 2017 COHERENT results. However, such precision will be required when aiming for precision measurements such as: any deviation of the observed CEνNS spectrum relative to expected spectrum, deviation in the cross section, sterile neutrino searches, monitoring reactor neutrino flux, and others. Hence, minimizing the uncertainties will be necessary. We conclude that the method developed to extract the quenching factor and presented in Section 6, could be a tool of interest in the CEνNS community in order to reach 5 % order uncertainty in the region of interest.

		Uncertainty on QF required	Uncertainties on R with QF uncertainty $\leqslant$ 10 %
PWR	Xenon	$\sim$ 5 %	10-20 %$\leqslant$ $\rightarrow$ 12.7-25 %
	Argon	$\sim$ 10 %	15-20 %$\leqslant$ $\rightarrow$ 11.8-14.2 %
	Neon	$\leqslant$ 20 %	20-25 %$\leqslant$ $\rightarrow$ 7.3-16.3 %
	Helium	$\leqslant$ 20 %	20-25 %$\leqslant$ $\rightarrow$ 7.06-8.2 %
PHWR	Xenon	$\sim$ 5 %	10-20 %$\leqslant$ $\rightarrow$ 12.-25 %
	Argon	$\sim$ 10 %	15-20 %$\leqslant$ $\rightarrow$ 11.2-14 %
	Neon	$\leqslant$ 20 %	20-25 %$\leqslant$ $\rightarrow$ 7-13.5 %
	Helium	$\leqslant$ 20 %	20-25 %$\leqslant$ $\rightarrow$ 5.5-6 %

Table 8.10: Impact of the quenching factor on the CEνNS event rate in a SPC detector for the four targets investigated. We estimate the impact of the quenching factor (relative) uncertainty on the event rate. By targeting 10 % uncertainty on the CEνNS event rate, we can estimate the required uncertainties on the quenching factor.

8.4 Conclusion on the event rate

We calculated the event rate of the CEνNS interaction in a 60 cm diameter SPC detector located 10 m away from a nuclear reactor of 1 GW. We considered three load factors: 100 %, 97.2 %, and 84.6 %. To model the neutrino flux we used the parametrization developed by Huber and Mueller [116] [122] and complemented by Baldoncini [124]. The neutrino spectrum model takes into account the four main isotopes contributing to the neutrino spectrum: ^{235}U, ^{238}U, ^{239}Pu, and ^{241}Pu. We investigated four targets as to estimate the best candidate for a successful CEνNS experiment. The investigated targets were: argon, helium, neon, and xenon. In our calculations we consider 1 kg of target material, which corresponds to different pressures depending on the target. We developed a Monte Carlo simulation, which takes into account the response of our detectors and the quenching factor to estimate the observed CEνNS signal in our detector. To calculate the event rate in our detector, we considered an energy threshold of 50 $\mathrm{eV_{ee}}$, which corresponds to about 2 electrons for argon, neon, and xenon, and 1 electron for helium. Argon has the highest event rate, closely followed by xenon, then neon, and finally helium. The relatively high pressure required to have 1 kg of helium in a 60 cm diameter SPC, and its low event rate makes helium an unlikely candidate for a CEνNS experiment.

We investigated the impact of the quenching factor on the CEνNS event rate in an SPC. We tested two models of quenching factors: Lindhard and SRIM, on the four targets investigated. The impacts on the different targets varied from about 3 % up to 13 %. However, it did not change the ranking of targets in terms of detectable event rate. We estimated the quenching factor uncertainty required to impact the CEνNS event rate by 10 % or less. A relative quenching factor uncertainty impacted differently each target. Hence, an uncertainty of 5 % of the quenching factor in xenon was estimated necessary to impact the CEνNS event rate by 10 % or less, while an uncertainty of 10 % of the quenching factor in argon would have the same effect on the CEνNS event rate. Neon is a more flexible target, where an uncertainty on the quenching factor of 20 % or less, impacts the quenching factor by 10 % or less. In Section 8.3.3, we discussed that the impact of the quenching factor uncertainty might not prevent from detecting CEνNS, as we have seen with the successful detection of the interaction by the COHERENT experiment [25]. But the knowledge of the quenching factor within 5 % (or less) will be required for precision measurements, where some of them were listed in Section 2.3. We propose the method developed in this work to extract the quenching factor with a 5 % uncertainty in the sub-keV region, as a tool for future quenching factor measurement as to optimize the statistics provided and thus minimize the uncertainty on the quenching factor.

We also looked at the impact of the type of nuclear reactor on the event rate: Pressurized Water Reactors and Pressurized Heavy Water Reactors. PHWR reactors provide a higher detectable event rate for all targets. For the three heavier targets: xenon, argon, and neon, the impact is of about 20 %, which is not negligible. Thus, when choosing a site, a CANDU reactor might be the best choice, as it provides a higher event rate of CEνNS events in our SPC detector. However, CANDU reactors do not require to be shut down when changing the fuel of the core. Hence, the background estimation on site might be challenging. Finally, the load factor also plays a role in the CEνNS event rate. Thus, a study of the recent load factors (per year) of candidate sites must be performed, and discussions needs to take place with different candidates in order to estimate the most reliable nuclear power station while the experiment is running.

Chapter 9

Preliminary estimation of background for a CEνNS experiment using an SPC detector at a nuclear reactor

The NEWS-G collaboration mainly focuses on dark matter searches, hence, the collaboration has limited experience with the backgrounds on surface. In response to this, the NEWS-G3 experiment was launched as a first step to assess surface backgrounds.

We are considering the NEWS-G3 detector and shielding as our experimental condition for a CEνNS experiment. First, we will present the NEWS-G3 detector and shielding, then, we will present the various backgrounds taking place in the SPC shell and shielding. Then, we will show the result of background contamination of a preliminary Geant4 simulation for the targets that were qualified as feasible for a CEνNS experiment with an SPC: argon, neon and xenon. Finally, we will briefly discuss other background contaminations, such as background coming from the nuclear reactor and cosmic muons.

9.1 Detector and shielding description

The NEWS-G3 experiment will take place in the laboratory of the NEWS-G group at Queen's University. The main goal of the experiment is to assess the background at sea-leavel in our detector in view to a CEνNS experiment. In particular, we want to estimate the backgrounds from the cosmogenic activation of the materials (copper) and the cosmic muon flux.

The detector is an SPC made of C10100 copper of 60 cm in diameter and 10 mm thick. The SPC is enclosed in a compact shielding, which follows a design similar to the GIOVE experiment [134]. The shielding has one layer of C10100 copper, two layers of PE, four layers of commercial lead, by MarShield [135], and a muon veto. The muon veto will be a combination of plastic scintillator made by Eljen, EJ-200 [136], with Hamamatsu R8520-406 PMTs [137]. The SPC is held by a structure made of C10100 copper. Finally, a steel structure allows to move the wall of the shielding holding the SPC.

Figure 9.1 shows an illustration of the NEWS-G3 detector and shield. Table 9.1 shows the dimensions of the NEWS-G3 shield and detector.

	Dimensions [cm]
SPC inner radius	30
SPC thickness	1
Copper shielding layer	10
Polyethylene shielding layers (each)	5
Lead shielding layers (each)	5
Plastic veto muon layer	5

Table 9.1: Detailed dimensions of the NEWS-G3 detector and shielding. The compact shielding comprises one layer of copper, two layers of polyethylene, four layers of lead, and a layer of muon veto between two lead layers

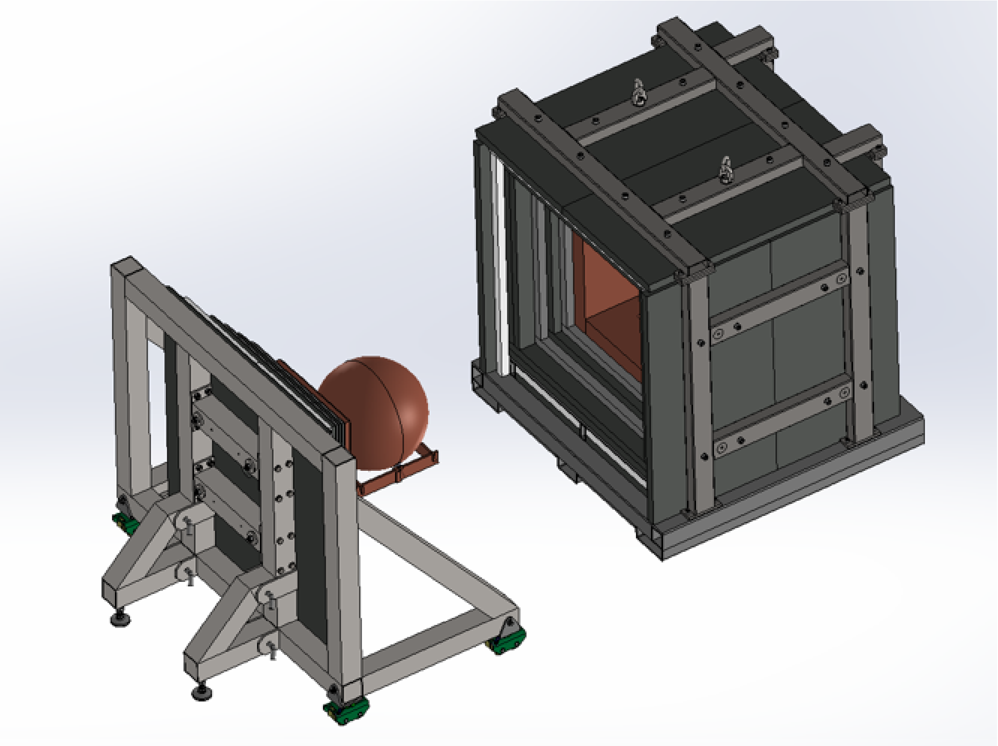

Figure 9.1: Illustration of the NEWS-G3 experiment. One of wall is movable and holds the 60 cm SPC. The shielding has successive layers of copper, lead, polyethylene, and a muon veto. Courtesy of S. Crawford.

9.2 Background from material

In this section, we will estimate the background coming from the SPC shell and the shielding. First, we will investigate the background coming from first layer of the lead, and then we will investigate the background from the copper SPC and shield. In our estimations, when looking at decay chains, like ^{232}Th decay chain, we assume secular equilibrium. Secular equilibrium exists when the production and decay rates are equal, which can take place when the half-life of the parent nucleus is much longer than the daughter nucleus.

9.2.1 Background contamination from the first layer of lead shield

The purpose of the lead layers is to stop the high energetic gammas ($\sim$ MeV) coming from the nuclear core and environmental radiations, before interacting in the SPC. Hence, the shielding is made of four 5 cm thick layers of lead. However, the lead itself is contaminated by radionuclides: ^{238}U, ^{232}Th, and ^{210}Pb, which can be problematic for rare events experiments. When manufactured, ^{238}U and ^{232}Th are substantially removed, however, the lead isotopes remain in the material. We do not know the exact contaminations of the lead chosen for the NEWS-G3 shield for these different radionuclides. Hence, we used upper limits from SuperCDMS and Edelweiss [138].

^{238}U and ^{232}Th decay chains

The ^{238}U and ^{232}Th isotopes are created in the core of supernovae and scattered around following the explosions. Their long half-lives of 14.1 Gyr and 4.5 Gyr for ^{238}U and ^{232}Th, respectively, explain the presence of such isotopes in the Earth's crust 4.5 Gyr after the formation of the solar system.

Figure 9.2 show the decay chains of both isotopes ^{238}U and ^{232}Th. Both decay by α-emission, followed by long decay chains of α and β-emissions. Because the half-lives of the daughter radionuclides of both chains are much shorter than the half-lives of the two parent radionuclides, then secular equilibrium of the chain is assumed. Following the work done in [82], we use the equilibrium assumption for the ^{232}Th decay chain. However, the equilibrium is broken in the ^{238}U chain, at the level of ^{210}Pb. Thus, in our study we consider the whole decay chain for the thorium, and the decay chain up to ^{210}Pb for ^{238}U, to be in equilibrium.

The activities of ^{238}U and ^{232}Th used in our study are listed in Table 9.2.

Isotopes	Activity [mBq/kg]
^{238}U	16.44
^{232}Th	2.16±0.2

Table 9.2: Upper limit activities of the ^{238}U and ^{232}Th from the SuperCDMS experiment [138]. No error was communicated on the upper limit of the ^{238}U.

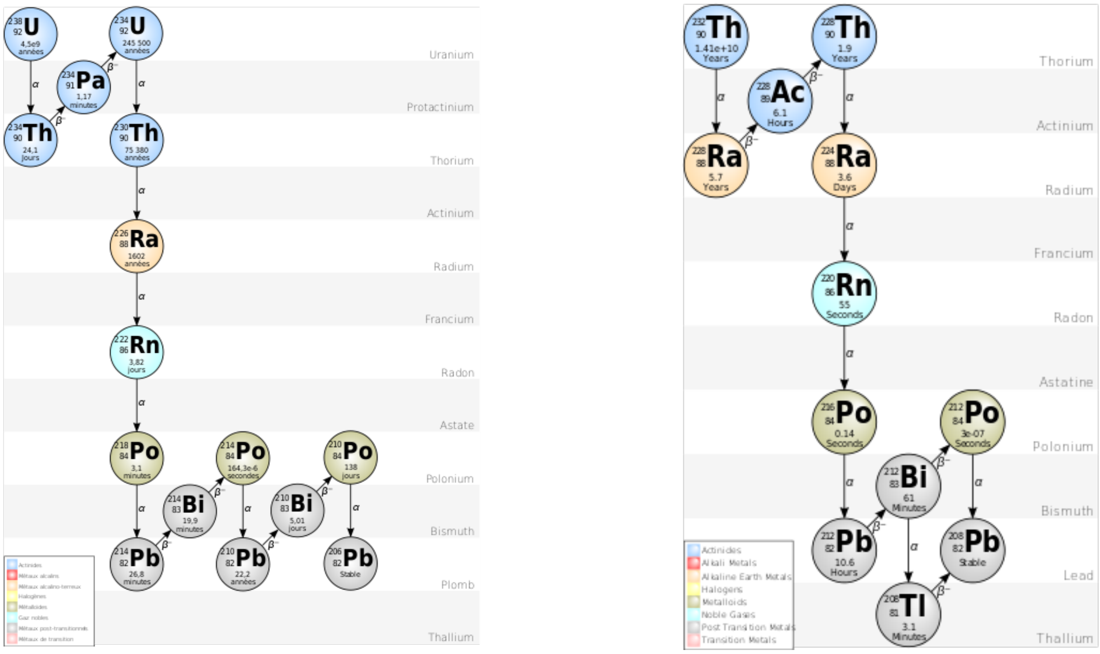

Figure 9.2: Decay chains of ^{238}U [144], on the left panel, and ^{232}Th [145], on the right pannel.

^{210}Pb decay chain

As aforementioned, ^{210}Pb is part of the ^{238}U decay chain, it decays with β-emission to ^{210}Bi. The decay of ^{210}Pb is followed by the emission of one or several gammas up to 46.5 keV. Then, ^{210}Bi decays by beta with energies up to 1.3 MeV and produce bremsstrahlung radiations. As for ^{238}U and ^{232}Th, we used an upper limit contaminations from another rare events experiment, Edelweiss [138]. Two measurements were available, hence we used the mean of these measurements. The contamination from the ^{210}Pb isotopes was estimated at 18 Bq/kg.

9.2.2 Background contamination from the copper SPC shell and shielding

The choice to use copper over different materials for the SPC shell and the last shielding layer is motivated by its rather low intrinsic radioactivity. The purpose of the 10 cm thick copper layer in the shielding is to protect the detector from the 30 mBq/kg of the ^{210}Pb.

In this section, we cover the contaminations from the copper SPC shell and the layer shielding.

Cosmogenic activation of the copper

The cosmogenic activation of copper is the production of radioactive isotopes induced by cosmic rays. Indeed, at the Earth's surface cosmic neutrons create spallation of nuclei, hence the event rate of isotope production depends on the neutron flux. The neutron flux has been estimated by several measurements at sea level [139] and several altitudes above sea level [140].

The main isotopes produced by cosmogenic activation in copper are: ^{60}Co, ^{58}Co, ^{57}Co, ^{56}Co, ^{54}Mn, ^{59}Fe, and ^{46}Sc. Figure 9.3 shows the activity as a function of time of these isotopes (courtesy of A. Brossard). More than half of the isotopes are in equilibrium after one year of exposure and after two years all isotopes but ^{60}Co are in equilibrium. Table 9.3 summarizes the activities for all isotopes after 1 and 2 years. Both activities will be used in order to assess the contamination from cosmogenic activation, as the time exposure of the copper will most likely surpass 2 years.

In our calculations, we chose to report only the contaminations from the main contaminants: ^{60}Co, ^{58}Co, ^{57}Co, and ^{56}Co, ^{54}Mn. This choice was motivated by the small activity that ^{59}Fe and ^{46}Sc have, and thus have an small expected contribution to the background.

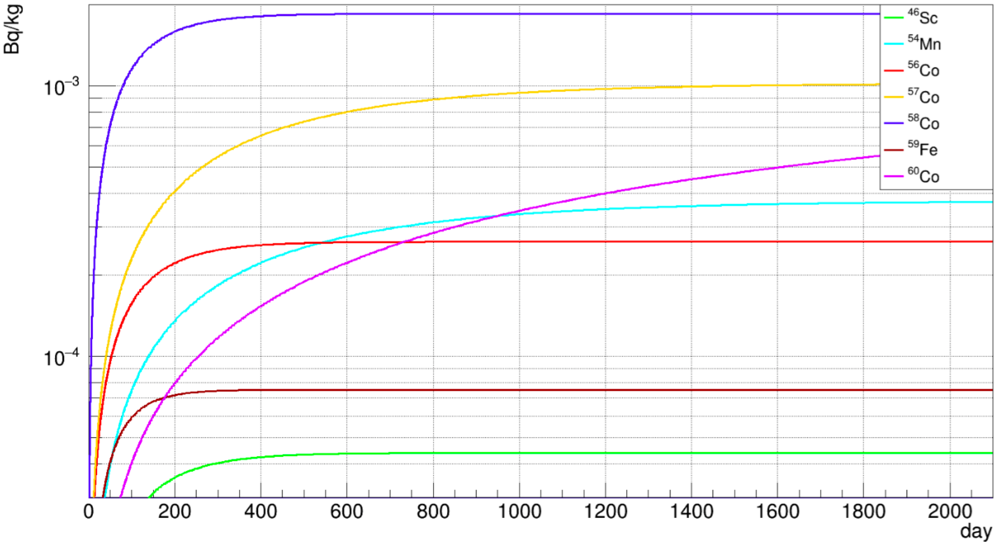

Figure 9.3: Activity of isotopes produced cosmogenically in copper. After one year of exposure, the largest contaminations are coming from the following isotopes: ^{60}Co, ^{58}Co, ^{57}Co, ^{56}Co, and ^{54}Mn. Courtesy of A. Brossard: using [141].

Isotopes	Activity after 1 year [Bq/kg]	Activity after 2 years [Bq/kg]
^{60}Co	1.5×10^{-4}	2.6×10^{-4}
^{58}Co	1.8×10^{-3}	1.8×10^{-3}
^{57}Co	6.5×10^{-4}	8.6×10^{-4}
^{56}Co	2.6×10^{-4}	2.6×10^{-4}
^{54}Mn	2.25×10^{-4}	3.0×10^{-4}
^{59}Fe	7.5×10^{-5}	7.5×10^{-5}
^{46}Sc	4.3×10^{-5}	4.5×10^{-5}

Table 9.3: Activities of the cosmogenic isotopes after 1 and 2 years. Values extracted from Figure 9.3.

^{238}U and ^{232}Th decay chains

The copper grade used in the NEWS-G3 detector and shielding is C10100. The activities of the ^{238}U and ^{232}Th chains are assumed to be the same as the copper used for SNOGLOBE [82]. The activities were measured by the Pacific Northwest National Laboratory (PNNL), eleven samples were extracted from the copper C10100 SPC to accurately estimate the contaminations from ^{238}U and ^{232}Th. Table 9.4 gives the activities for the two isotopes.

Isotopes	Activity [μBq/kg]
^{238}U	3 ± 0.1
^{232}Th	13 ± 0.2

Table 9.4: Mean activities of the ^{238}U and ^{232}Th from the SNOGLOBE 11 samples.

^{210}Pb decay chain

The ^{210}Pb contamination was estimated by the XMASS collaboration to be between 17 and 40 mBq/kg. They used a low-background alpha particle counter to measure the activity of their samples [142]. A sample of the copper used to make the SNOGLOBE shell was measured with this method and showed an activity of 28.5 ± 8.1 mBq/kg [82].

9.3 Background estimation through Geant4 simulation

In order to estimate the background coming from the shielding and the SPC shell and contaminating the gas, we developed a simple Geant4 simulation [81]. We investigated the background coming from the first lead layer, the copper layer and the SPC shell. The copper structure holding the detector was not simulated. Figure 9.4 shows the parts of the NEWS-G3 shielding that were simulated. The layers of lead, polyethylene and copper were simulated by extruding cubes, and not by simulating 6 panels as will be the case with the NEWS-G3 shield. Hence, no fasteners were simulated.

	Dimensions [cm]
SPC inner radius	60
SPC thickness	0.6
Copper shielding layer	10
Polyethylene shielding layer	5
Lead shielding layer	5
Gases	Pressure [bar]
Argon ($2\,\%CH_4$)	5.3
Xenon ($2\,\%CH_4$)	1.6
Neon ($2\,\%CH_4$)	10.6

Table 9.5: Summary of the quantities used in the Geant4 simulations: for the geometry and the gas conditions. Note: the thickness of the SPC simulated is smaller than the NEWS-G3 detector.

The Geant4 simulation package simulated the decays of the various radionuclides mentioned in the previous sections, and resulting energy deposition in the gas. We recorded their energy, position, momentum, mother particle etc. Then, using a simulation developed by the collaboration, a number of primary electrons corresponding to the interactions are generated. Then, this simulation uses Magboltz, which is a Monte Carlo software developed to solve transport equations for electrons in a gas and subject to an electric and magnetic fields [146]. Hence, the primary electrons created are drifted in the SPC, and their diffusion is used to generate a pulse. For more details about this simulation, the reader is encouraged to read [82] and [67] theses of former Ph.D. students A. Brossard and F. Vazquez de Sola Fernandez. Figure 9.5a shows an example of simulated pulse in argon gas. Finally, the pulses generated are processed with the double deconvolution method.

Three independent simulations were performed in order to estimate the background contaminations in three different gases: argon, neon and xenon. The contaminations are reported in differential rate unit (dru), which is equivalent to events/kg/day. The following sections present the parameters used to generate the primary electrons, and subsequent pulse formations, as well as the parameters used to process the data. Finally, we provide preliminary background event rates from the different radioisotopes contaminations in the three gas mixtures.

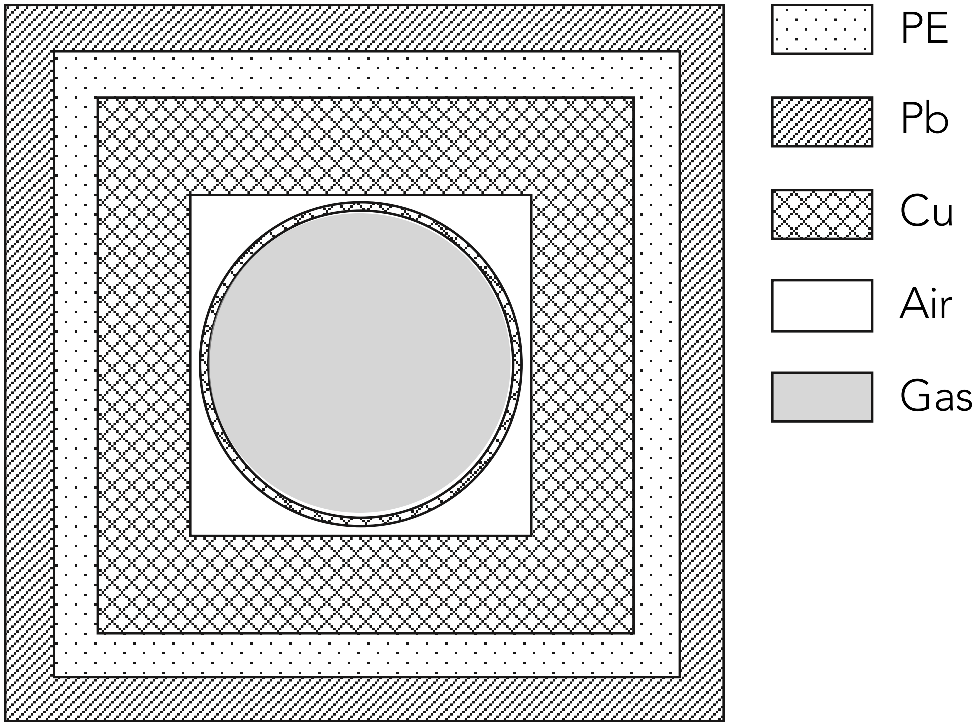

Figure 9.4: Scheme, not at scale, of the first three layers of the shielding and copper SPC, simulated in the Geant4 simulation.

9.3.1 Background in argon based gas mixture

First, we simulated the contamination from the radionuclides in an argon based mixture. All the details about the parameters used in the drift-pulse formation simulation are shown in Table 9.6. For this simulation, we assumed an ideal electric field condition. The choice of the parameters were chosen to match working conditions in view of a CEνNS experiment. As aforementioned, the pressure corresponds to 1 kg of target material in a 60 cm diameter SPC. The W-value and minimum ionization energy were found in [128], and the mobility of the argon ions in argon in [104]. The SEDINE geometry was referenced after the 60 cm diameter SEDINE detector from Section 3.4, with no electric field corrector. Hence, an ideal electric field is chosen in such geometry. The HV was chosen to have a gain allowing to access the sub-keV region. The preamplifier decay time is the decay time in a Canberra preamplifier [99]. The number of samples per events and the sampling period of the digitizer produce traces which are 1600 μs long.

Parameters	Values
Gas and fraction	Ar - 0.98
Gas and fraction	CH_4 - 0.02
Pressure	5.3 bar
W-value	26.4 eV
Minimum ionization energy	15.7 eV
Mobility	1.5 $(cm^2/V/\mu s)$bar
Detector Geometry	SEDINE
Electrode radius	0.315 cm
SPC radius	30 cm
Voltage sensor	3500 V
Voltage umbrella	0 V - Ideal
Mean gain	6800
Preamplifier decay time	47 000 ns
Sampling period of digitizer	480 ns
Samples per event	3333

Table 9.6: Table summarizing the parameters used to simulate the drift and pulses in argon with our simulation. Note: the HV on the umbrella was set to 0 V as we assumed an ideal electric field in the SPC.

The simulation, with these parameters, produced pulses as shown in Figure 9.5a. The corresponding treated pulse is shown in Figure 9.5b. The processing used the same inputs as in Table 9.6. From the simulation, we estimated that the maximum drift time of the primary electrons in the detector with such conditions was about 2.5 μs.

Figures 9.6a, 9.6b, and 9.6c show examples of energy spectra of γ events obtained with the Geant4 simulation. We can observe that the energy spectra of the different isotopes shown do not have the same behavior as the energy spectrum from nuclear recoils induced by a neutrino interaction.

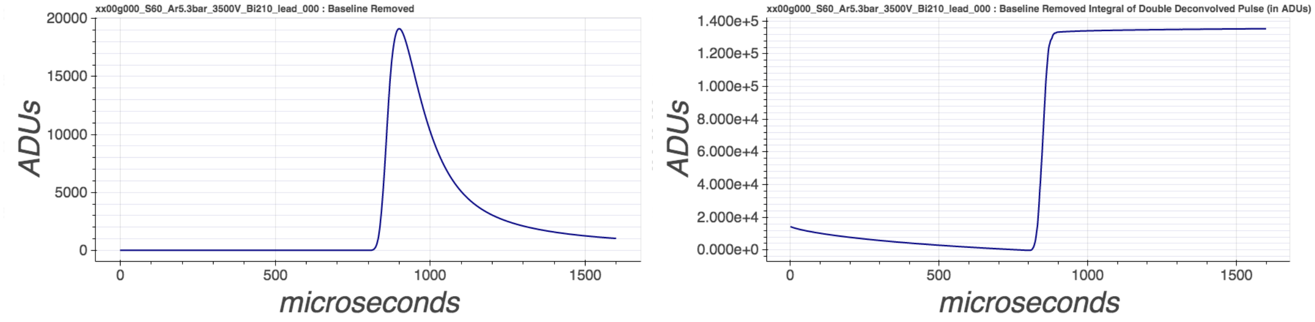

(a) Example of raw pulse.

(b) Example of treated pulse.

Figure 9.5: Example of pulse generated with our simulation, integrating the energy and position provided from Geant4, and the diffusion of the primary electrons in our detectors. These pulses corresponds to a 528 keV gamma depositing 63.9 keV through Compton scattering.

Table 9.7 shows the resulting γ contamination in the gas from the copper C10100 SPC shell and layer of the shielding, and the first lead layer. The rate contamination was calculated below 1 keV as to match the CEνNS energy region. The SPC produces 5.24±0.84 dru below 1 keV after 1 year and 5.53±0.87 dru after 2 years. The copper layer produces 9.61±1.27 dru below 1 keV after 1 year and 10.25±1.33 dru after 2 years. Finally, the first lead layer creates 1.01±0.35 dru below 1 keV in the gas. The total gamma contamination reaches 15.85±2.46 dru below 1 keV after 1 year and 16.79±2.55 dru after 2 years.

We also calculated the contamination below 0.8 keV, as we have shown in Section 8.3.2, that is the upper threshold for CEνNS events in argon. Considering this upper threshold, the number of γ background is 12.40±2.21 dru and 13.36±2.31 dru after 1 ad 2 years of exposition on surface, respectively.

From this study, we can state that the contamination of the gas is strongly dominated by the cosmogenic activation of the copper vessel and copper layer of the shielding.

We remind that the number of CEνNS events in argon at both a PWR and PHWR predict 16.4 and 20 dru, respectively. The CEνNS signal is 1.3 and 1.5 times larger than the background for PWR and PHWR, respectively. Hence, the contamination from this preliminary study is encouraging in view to a CEνNS experiment with argon.

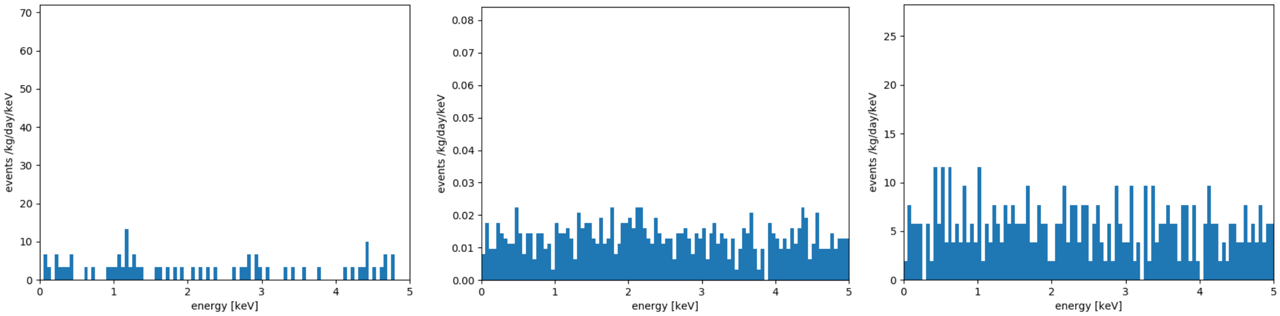

(a) γ energy spectrum in the gas from ^{210}Pb present in the SPC shell.

(b) γ energy spectrum in the gas from ^{238}U present in the copper layer.

(c) γ energy spectrum in the gas from ^{58}Co present in the copper layer.

Figure 9.6: Example of energy spectrum produced with the Geant4 simulation: γ contamination in the region of interest for CEνNS detection, in argon.

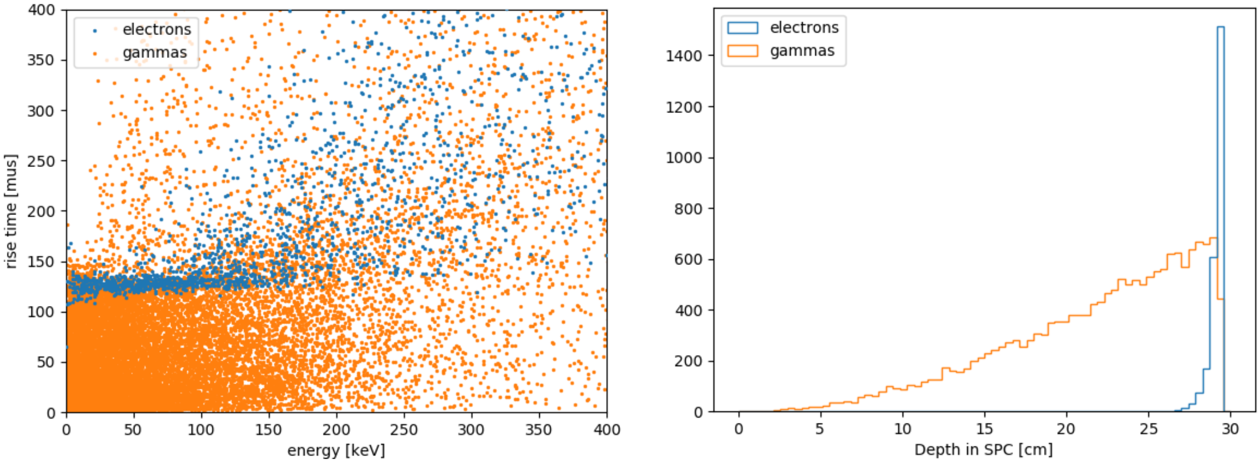

(a) Rise time as a function of the *true* energy deposited of the events (from Geant4). The blue data dots are the electron events and the orange dots are the gammas events. The rise times of the electrons are above 100 μs, and constitute what we call surface background. While the γ have rise times consistent with volume events. The rise times larger that 150 μs correspond to track-like events.

(b) Histogram showing the relative distance to the center of the SPC at which the interaction of the particle took place. The interactions of the electrons in the SPC take place in the first few cm after entering the gas. On the other hand, the γ are interacting in the whole volume of the gas. This histogram of the location of the interactions is consistent with our interpretation of the rise times of the events.

Figure 9.7: Repartition of electron and gamma events in 5.3 bar of argon from ^{238}U in the copper shielding layer.

Figure 9.7a shows the rise time as a function of the energy of the events from ^{238}U. We show the betas events and gammas events in two different colors. This figure illustrates why we reported only the contaminations from the gamma events and not from electrons. The electrons are what we call *surface events*. Thus they have high rise times of about 120 μs, while the CEνNS interactions take place in the whole volume of the detector, like the gamma events. Figure 9.7b shows the depth of gas travelled by a particle, gamma or electron, before interacting in the gas. The electrons interact within the first 2 cm of the gas. Hence, it is possible to remove the beta background by applying a rise time cut. This cut will however, impact the fiducial volume, and thus the fiducial mass. Figures 9.8 and 9.9 allow nice illustrations of the rise time cut's impact on the spacial distribution of the events. The most part of the electrons interacted within the first 3 cm of the gas. Hence, the volume loss and mass loss are impacted by 27 %, as well as the CEνNS event rate. Going forward, an important study will be to characterize the best rise time cut as to optimize the signal to background ratio.

	Isotopes	dru $\gamma \leqslant 1$ keV 1 year	dru $\gamma \leqslant 1$ keV 2 years	dru $\gamma \leqslant 0.8$ keV 1 year	dru $\gamma \leqslant 0.8$ keV 2 years
Copper SPC	^{60}Co	0.14 ± 0.010	0.24 ± 0.018	0.10 ± 0.0092	0.18 ± 0.016
	^{57}Co	0.94 ± 0.058	1.13 ± 0.076	0.79 ± 0.052	1.05 ± 0.069
	^{58}Co	1.30 ± 0.11	1.30 ± 0.11	1.05 ± 0.10	1.05 ± 0.10
	^{56}Co	0.38 ± 0.024	0.38 ± 0.024	0.29 ± 0.021	0.29 ± 0.021
	^{54}Mn	0.096 ± 0.015	0.13 ± 0.020	0.077 ± 0.013	0.10 ± 0.018
	^{210}Pb	2.31 ± 0.62	2.31 ± 0.62	1.98 ± 0.57	1.98 ± 0.57
	^{238}U	0.0059 ± 0.00014	0.0059 ± 0.00014	0.0047 ± 0.00012	0.0047 ± 0.00012
	^{232}Th	0.035 ± 0.0013	0.035 ± 0.0013	0.028 ± 0.0011	0.028 ± 0.0011
Total: Copper SPC		5.24 ± 0.84	5.53 ± 0.87	4.31±0.76	4.68 ± 0.79
Copper layer	^{60}Co	0.68±0.074	1.18 ± 0.13	0.53 ± 0.065	0.91 ± 0.11
	^{57}Co	0.20 ±0.026	0.26 ± 0.035	0.14 ± 0.022	0.19 ± 0.030
	^{58}Co	5.77 ± 0.74	5.77 ± 0.74	4.61 ± 0.66	4.61 ± 0.66
	^{56}Co	1.86 ± 0.16	1.86 ± 0.16	1.45 ± 0.14	1.45 ± 0.14
	^{54}Mn	0.53 ± 0.079	0.70 ± 0.11	0.46 ± 0.075	0.61 ± 0.10
	^{210}Pb	0.40 ±0.18	0.40 ± 0.18	0.40 ± 0.17	0.40 ± 0.17
	^{238}U	0.012 ± 0.001	0.012 ± 0.001	0.010 ± 0.0011	0.00091 ± 0.00091
	^{232}Th	0.076 ± 0.0081	0.076 ± 0.0081	0.060 ± 0.0072	0.060 ± 0.0072
Total: Copper layer		9.61±1.27	10.25 ± 1.33	7.65 ± 1.14	8.24 ± 1.21
1st lead layer	^{210}Pb	0.0064 ± 0.0046	0.0064 ± 0.0046	0.0032 ± 0.0032	0.0032 ±0.0032
	^{238}U	0.88 ± 0.29	0.88 ± 0.29	0.64 ± 0.26	0.64 ± 0.26
	^{232}Th	0.13 ± 0.058	0.13 ± 0.058	0.10 ± 0.051	0.10± 0.051
Total: 1st lead layer		1.01±0.35	1.01± 0.35	0.44±0.31	0.44 ± 0.31
Total		15.85±2.46	16.79±2.55	12.40±2.21	13.36±2.31

Table 9.7: Gammas background event rates from the different radioactive isotopes in the SPC copper shell, first layer of copper, and first layer of lead shielding in 5.3 bar of argon. We provide the contaminations of the different isotopes mentioned in the previous sections below 1 keV and 0.8 keV energy threshold. For the cosmogenic background, we consider both 1 and 2 years of the copper shell and shielding exposure at the surface.

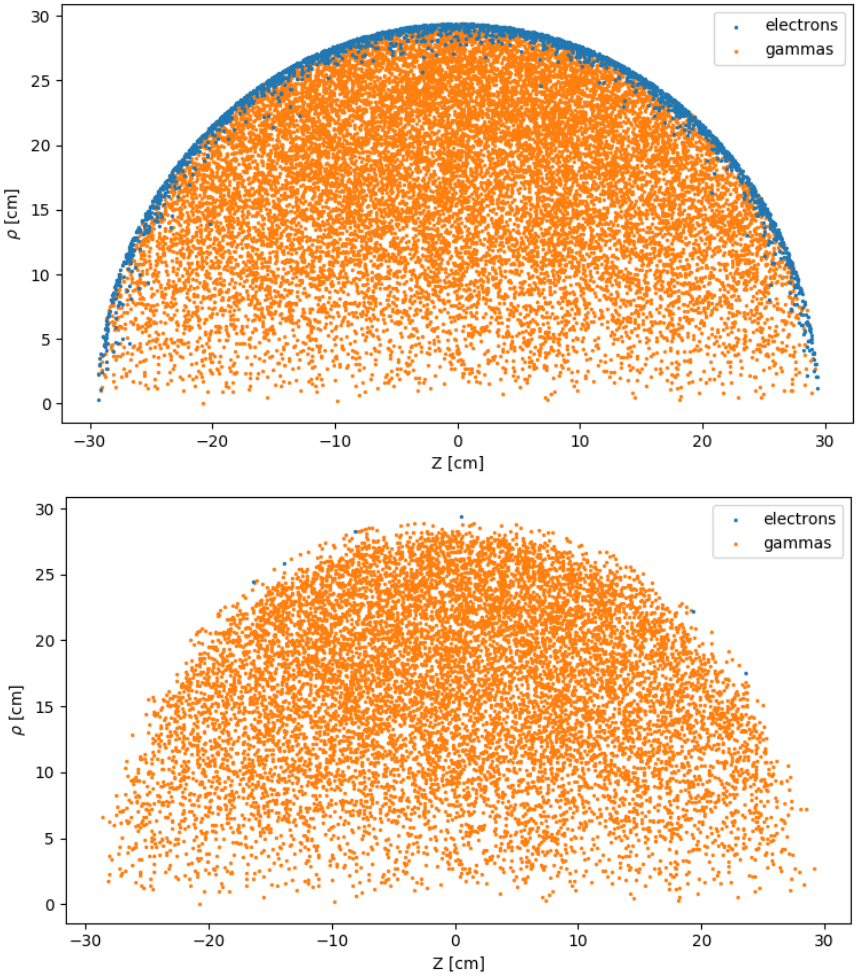

Figure 9.8: Spacial distribution of the events in cylindrical coordinates. The top plot shows the distribution of the electrons and the gammas events from ^{238}U in the copper layer of the shielding. The bottom plot shows the events passing a rise time cut of 110 μs. The electrons being mostly on the surface were cut out, while the gammas interacting in the volume remains. We also can see how much of an impact such a cut would have on the fiducial volume.

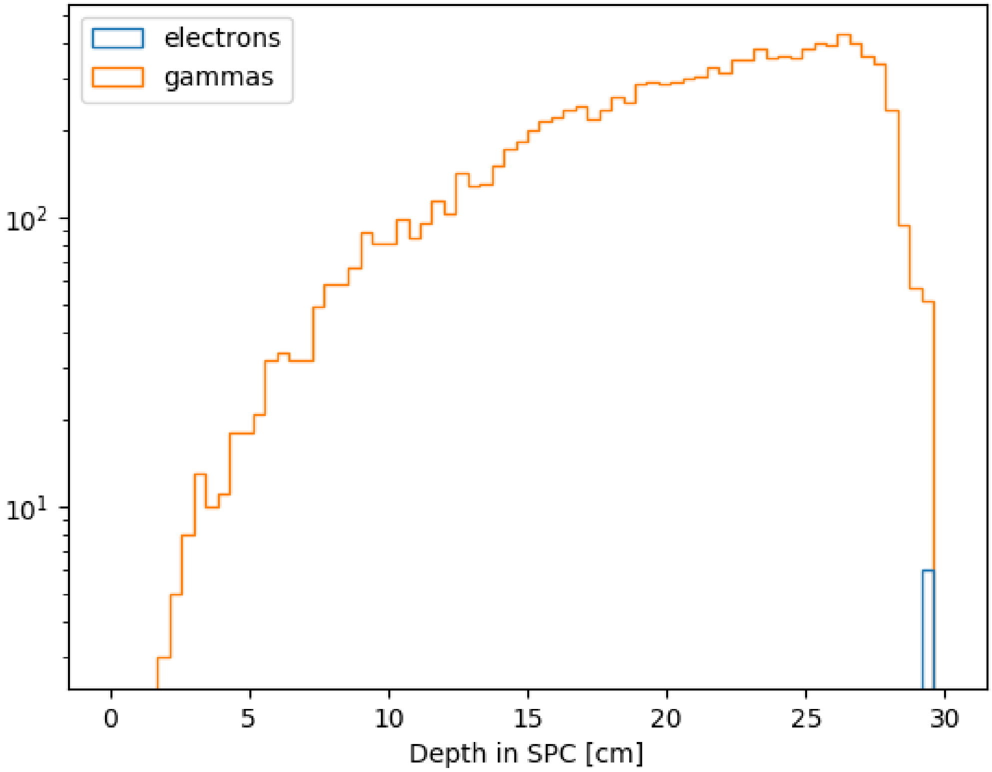

Figure 9.9: Histogram showing the relative distance to the center of the SPC at which the interaction of the particle took place, after a rise time cut of 110 μs. In comparison with Figure 9.7b, we can see that the electrons were removed.

9.3.2 Background in neon based gas mixture

A second simulation estimated the γ background from the radionuclides in a neon based gas mixture. The parameters used to simulate primary electrons and subsequent pulse formations from the Geant4 interactions in the gas, are found in Table 9.8. As mentioned previously, the choice of some parameters were motivated to match the conditions of a CEνNS experiment. Hence, the pressure chosen for the simulation was 10.6 bar, which corresponds to 1 kg of neon in a 60 cm diameter SPC. The W-value was found in [66], the minimum ionization energy in [64], and the mobility of neon ions in neon in [104]. The HV chosen allows to reach the sub-keV region.

Figure 9.10a shows an example of simulated pulse in neon. We also show the corresponding treated pulse in Figure 9.10b. From the simulation, we estimated that the maximum drift time of the primary electrons in the detector with such conditions was about 2.5 μs.

Parameters	Values
Gas and fraction	Ne - 0.98
Gas and fraction	CH_4 - 0.02
Pressure	10.6 bar
W-value	27.6 eV
Minimum ionization energy	21.6 eV
Mobility	4.14 $(cm^2/V/\mu s)$bar
Detector Geometry	SEDINE
Electrode radius	0.315 cm
SPC radius	30 cm
Voltage sensor	5000 V
Voltage umbrella	0 V - Ideal
Preamplifier decay time	47 000 ns
Sampling period of digitizer	480 ns
Samples per event	3333

Table 9.8: Table summarizing the parameters used to simulate pulses in neon with our simulation. Note: the HV on the umbrella was set to 0 V as we assumed an ideal electric field in the SPC.

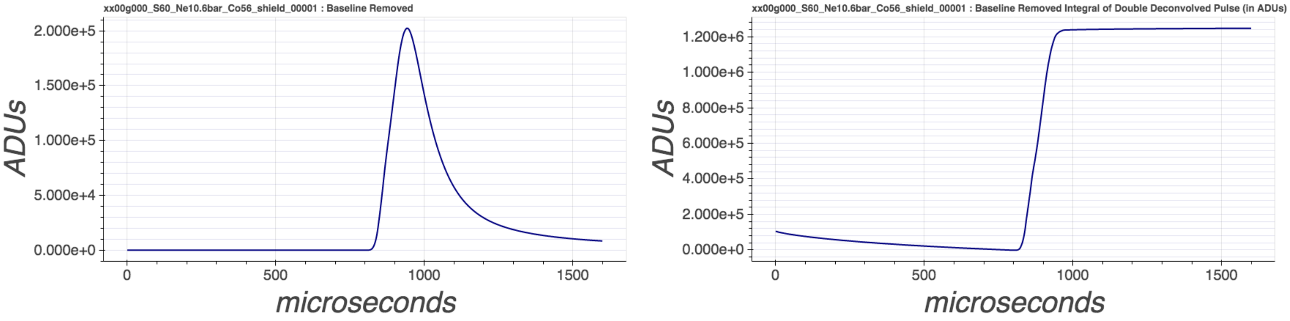

(a) Example of raw pulse.

(b) Example of treated pulse.

Figure 9.10: Example of pulse generated with our simulation, integrating the energy and position provided from Geant4, and the diffusion of the primary electrons in our detectors. These pulses corresponds to a 1.77 MeV gamma depositing 447 keV through Compton scattering, following a ^{56}Co decay in the copper layer.

Table 9.9 shows the resulting γ background in the gas from the copper C10100 SPC shell and shielding layer, and the first layer of lead. The contamination rate was calculated in the sub-keV region as it matches the CEνNS detection range. From the simulation, it was found that the copper

SPC shell produces 9.03±1.0 dru γ below 1 keV after 1 year and 9.56±1.03 dru after 2 years. The copper layer of the shielding creates 9.91±1.14 dru γ below 1 keV after 1 year and 10.76±1.24 dru after 2 years. Finally, the first lead layer produces 1.37±0.40 dru. Overall, it was found that the SPC shell, the copper layer of the shielding and the first layer of lead shielding produce 20.31±2.54 dru γ below 1 keV and 21.69±2.67 dru after 1 and 2 years, respectively.

	Isotopes	dru $\gamma \leqslant 1$ keV 1 year	dru $\gamma \leqslant 1$ keV 2 years
Copper SPC	^{60}Co	0.18±0.012	0.30 ± 0.020
	^{57}Co	1.12±0.062	1.49 ± 0.082
	^{58}Co	4.37±0.20	4.37 ± 0.20
	^{56}Co	0.40±0.025	0.40 ± 0.025
	^{54}Mn	0.11 ± 0.016	0.15 ± 0.022
	^{210}Pb	2.79 ± 0.68	2.79± 0.68
	^{238}U	0.023 ± 0.00077	0.023 ± 0.00077
	^{232}Th	0.040 ± 0.0013	0.040 ± 0.0013
Total: Copper SPC		9.03 ± 1.0	9.56±1.03
Copper layer	^{60}Co	0.78 ± 0.079	1.36±0.14
	^{57}Co	0.22 ± 0.028	0.29±0.037
	^{58}Co	6.10 ± 0.76	6.10 ± 0.76
	^{56}Co	2.09 ± 0.17	2.09 ± 0.17
	^{54}Mn	0.58 ± 0.083	0.78 ± 0.11
	^{210}Pb	0.048±0.019	0.048± 0.019
	^{238}U	0.015 ± 0.0011	0.015 ± 0.0011
	^{232}Th	0.080 ± 0.0083	0.080 ± 0.0083
Total: Copper layer		9.91 ± 1.14	10.76±1.24
1st lead layer	^{210}Pb	0.013 ± 0.006	0.013 ± 0.006
	^{238}U	1.26 ± 0.35	1.26 ± 0.35
	^{232}Th	0.10 ± 0.051	0.10 ± 0.051
Total: 1st lead layer		1.37 ± 0.4	1.37 ± 0.4
Total		20.31 ± 2.54	21.69±2.67

Table 9.9: Background event rates from the different radioactive isotopes in the SPC copper shell, first layer of copper, and first layer of lead shielding in 10.6 bar of neon. We provide the backgrounds of the different isotopes mentioned in the previous sections. For the cosmogenic background, we consider both 1 and 2 years of the copper shell and shielding exposure at the surface.

These results should be compared with our estimations of CEνNS event rate in our detector filled with 10.6 bar of neon gas. With load factors of 100 % and considering both PWR and PHWR the event rate was calculated to be 11.2 dru and 13.22 dru, respectively.

In the light of this preliminary background estimation, it seems that detecting CEνNS in a neon based gas mixture would be more difficult than with an argon based gas mixture.

9.3.3 Background in xenon based gas mixture

Finally, we simulated the background from the radionuclides in a xenon based mixture. The parameters used in the drift-pulse formation simulation are shown in Table 9.10. As for the previous simulations, the electric field was assumed ideal. The W-value and minimum ionization energy were found in [128]. The mobility of the ions was found in [104]. To this day, the NEWS-G collaboration never tested a xenon based gas mixture in an SPC. From a private conversation with I. Giomataris, the voltage necessary to obtain a similar gain to an argon based gas mixture at the same pressure, should be 20 % higher with xenon. Hence, we calculated that a realistic HV on the sensor should be 2520 V for a pressure of 1.6 bar. Because electrons are more subject to diffusion in xenon than in the other gas mixtures we are using, the size of the traces had to be adjusted to contain the events. Hence, the number of sample per events had to be increase to 73000, resulting in 35 ms long time windows.

Examples of pulses obtained with the simulation and these parameters can be found in Figure 9.11. A typical pulse in xenon looks like the first pulse (on the left). Figure 9.12 shows the corresponding trajectories of these events in the SPC. From the simulation, we estimated that the maximum drift time in a 60 cm diameter SPC filled with 1.6 bar of xenon was 18 ms, which is 9 times larger than the drift time in argon and neon gas mixtures.

Table 9.11 shows the resulting γ contamination in the xenon gas from the copper C10100 SPC shell and layer of the shielding, and the first lead layer. As for argon, we calculated the contamination rate below two energy threshold: 0.3 and 1 keV.

Considering the events below 1 keV the SPC produces 4.46±0.59 dru after 1 year and 4.74±0.61 dru after 2 years. The copper layer of the shielding produces a γ rate of 6.95±1.09 dru after 1 year and 7.46±1.16 dru after 2 years. Finally, the lead layer produces 0.695±0.29 dru. Hence, the overall

Parameters	Values
Gas and fraction	Xe - 0.98
Gas and fraction	CH_4 - 0.02
Pressure	1.6 bar
W-value	22.6 eV
Minimum ionization energy	12.13 eV
Mobility	0.57 $(\mathrm{cm}^2/\mathrm{V}/\mu\mathrm{s})$bar
Detector Geometry	SEDINE
Electrode radius	0.315 cm
SPC radius	30 cm
Voltage sensor	2520 V
Voltage umbrella	0 V - Ideal
Preamplifier decay time	47 000 ns
Sampling period of digitizer	480 ns
Samples per event	73000

Table 9.10: Table summarizing the parameters used to simulate pulses in xenon with our simulation. Note: the HV on the umbrella was set to 0 V as we assumed an ideal electric field in the SPC.

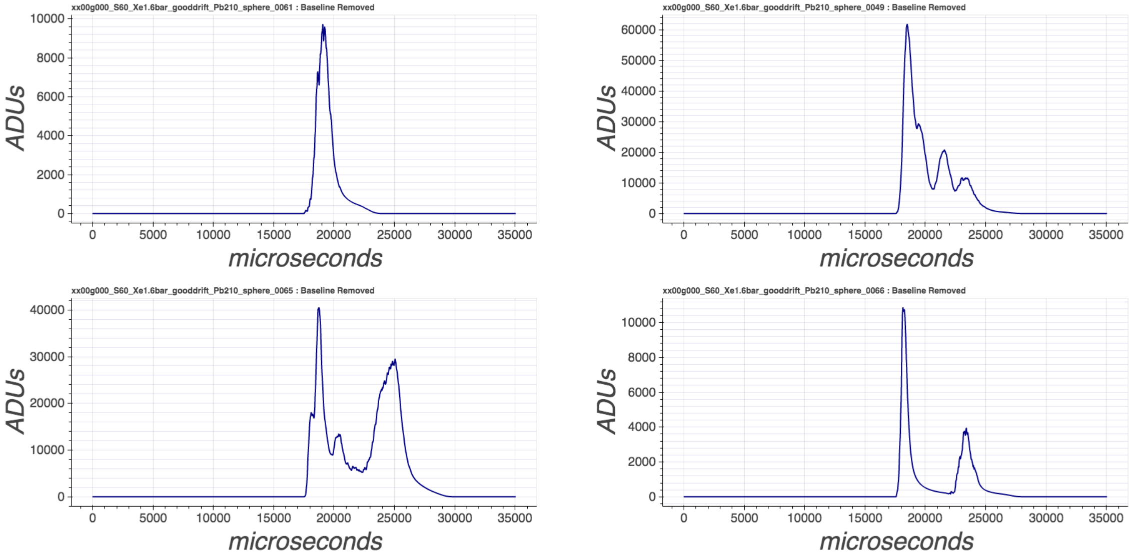

Figure 9.11: Examples of simulated pulses in 1.6 bar of xenon. The first pulse on the upper left is a 7.98 keV event, the second pulse on the upper right is a 653 keV event, and the third pulse on the bottom left is a 908 keV event. The last event, which has two pulses, is a 46.5 keV event. The first pulse was generated by a γ of 29.5 keV and the second pulse corresponds to and electron depositing 12 keV. The corresponding trajectories of these events in the SPC is shown in Figure 9.12.

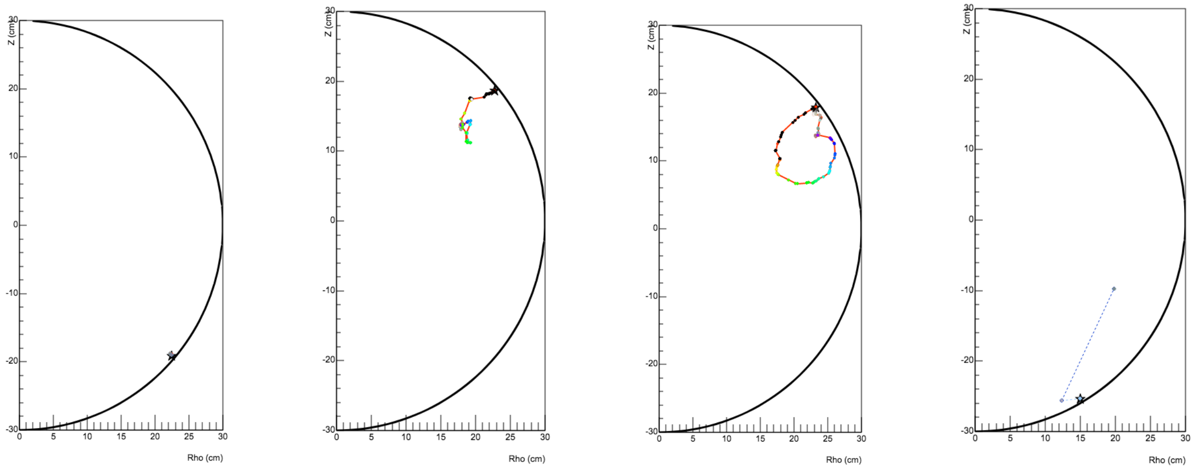

(a) Energy deposition in the gas: event 61. It corresponds to a 425 keV β depositing by photoelectric effect 7.98 keV.

(b) Energy deposition in the gas: event 49. It corresponds to ^{210}Bi β decay depositing 653 keV in the gas through ionization.

(c) Energy deposition in the gas: event 65. It corresponds to ^{210}Bi β decay depositing 908 keV in the gas through ionization.

(d) Energy deposition in the gas: event 61. It corresponds to ^{210}Pb γ decay depositing 46.5 keV in the gas by photoelectric effect.

Figure 9.12: Corresponding trajectories of the events shown in Figure 9.11. Courtesy of F. Vazquez de Sola Fernandez.

event rate below 1 keV is 12.10±1.97 dru after 1 year and 12.89±2.06 dru after 2 years.

We also looked at the event rate below 300 eV. As we have shown in Section 8.3.2, the maximum observable energies in xenon are below that threshold. Hence, the γ event rate produced below 300 eV by the SPC is 1.14±0.29 dru after 1 year and1.21± 0.31 dru after 2 years. The copper layer produces 1.14±0.95 dru after 1 year and 2.09±0.97 dru after 2 years. Finally, the lead layer produces 0.64±0.63 dru. The total contamination rate below 300 eV is 3.73±1.87 dru after 1 year and 3.941.91 dru after 2 years. For these last calculations, the statistical errors reported is of the same order of magnitude as the background rates, hence, simulations with a higher number of trials need to be computed. Despite, the order of magnitudes of the errors, the background event rates below 0.3 keV provides a good estimate of the background rates.

These contamination rates have to be compared with the CEνNS event rate calculated in Section 8.3.2. The event rates were 13.5 dru and 17 dru for PWR and PHWR with LF of 100 %, respectively. Hence, the CEνNS signal is 3.6 and 4.4 times larger than the expected background in the same energy region. As for the argon target, this preliminary study is encouraging in view of a

CEνNS experiment using xenon.

	Isotopes	dru $\leqslant$ 1 keV 1 year	dru $\leqslant$ 1 keV 2 years	dru $\leqslant$ 0.3 keV 1 year	dru $\leqslant$ 0.3 keV 2 years
Copper SPC	^{60}Co	0.10 ± 0.0092	0.18 ± 0.016	0.026 ± 0.0045	0.045 ± 0.0078
	^{57}Co	0.53 ± 0.042	0.69 ± 0.056	0.16 ± 0.023	0.21 ± 0.031
	^{58}Co	2.79 ± 0.17	2.79 ± 0.17	0.71 ± 0.088	0.71 ± 0.088
	^{56}Co	0.27 ± 0.021	0.27± 0.021	0.055 ± 0.010	0.055 ±0.010
	^{54}Mn	0.091 ± 0.015	0.13 ± 0.020	0.028 ± 0.0083	0.038 ± 0.011
	^{210}Pb	0.66 ± 0.33	0.66 ± 0.33	0.16 ± 0.16	0.16 ± 0.16
	^{238}U	0.0029 ± 0.00028	0.0029 ± 0.00028	0.00087 ± 0.00015	0.00087 ± 0.00015
	^{232}Th	0.021 ± 0.0010	0.021 ± 0.0010	0.005 ± 0.00051	0.005 ± 0.00051
Total: Copper SPC		4.46 ± 0.59	4.74 ± 0.61	1.14 ± 0.29	1.56± 0.31
Copper layer	^{60}Co	0.51 ± 0.064	0.89 ± 0.060	0.14 ± 0.034	0.25 ± 0.060
	^{57}Co	0.080 ± 0.017	0.10 ± 0.022	0.028 ± 0.033	0.037 ± 0.013
	^{58}Co	4.26 ± 0.64	4.26 ± 0.64	0.97 ± 0.31	0.97 ± 0.31
	^{56}Co	1.38 ± 0.14	1.38 ± 0.14	0.25 ± 0.060	0.25 ± 0.060
	^{54}Mn	0.34 ± 0.064	0.45 ± 0.086	0.061 ± 0.027	0.081 ± 0.036
	^{210}Pb	0.32 ± 0.16	0.32 ± 0.16	<0.49	<0.49
	^{238}U	0.0093 ± 0.00087	0.0093 ± 0.00087	0.0021 ± 0.00043	0.0021 ± 0.00043
	^{232}Th	0.056 ± 0.007	0.056 ± 0.007	0.014 ± 0.0035	0.014 ± 0.0035
Total: Copper layer		6.85 ± 1.09	7.46 ± 1.16	1.95 ± 0.95	2.09± 0.97
1^{st} lead layer	^{210}Pb	0.0065 ± 0.0046	0.0065 ± 0.0046	<0.49	<0.49
	^{238}U	0.59± 0.24	0.59± 0.24	0.099 ± 0.099	0.099 ± 0.099
	^{232}Th	0.10 ± 0.052	0.10 ± 0.052	0.052 ± 0.037	0.052 ± 0.037
Total: 1^{st} lead layer		0.695	0.695	0.64±0.63	0.64±0.63
Total		12.10 ± 1.97	12.89±2.06	3.73 ± 1.87	3.23 ± 1.91

Table 9.11: Gamma background from the different radioactive isotopes in the SPC copper shell, first layer of copper, and first layer of lead shielding in 1.6 bar of xenon. We provide the background of the different isotopes mentioned in the previous sections. For the cosmogenic background, we consider both 1 and 2 years of the copper shell and shielding exposure at the surface.

The upper plot of Figure 9.14 and Figure 9.15a show the locations of the simulated interactions, following ^{238}U decays, depending on the nature of the interacting particle: β vs γ. As shown with the argon gas mixture, the electrons and γ events are interacting within two distinct regions of the detector. The γ interact in the volume of the detector, while the electrons interact within the first few cm of gas. Hence, a rise time cut will be necessary to reject the β events. Figure 9.13 shows the rise time as a function of the *true* energy of the events from the ^{238}U present in the copper layer of the shielding. In blue are shown the location of the β interactions and in orange the γ interactions. We see that the β interact rarely at low rise times, hence, in the volume, and prefer to interact on the surface of the detector. A feature of the rise times that was noticed in the TUNL data and the simulation in argon, however, less obvious, is the rise time correlation with the energy below

30 keV. Indeed, while this behavior was already observed in the sub-keV region by the NEWS-G collaboration in several data sets, this strong correlation will impact the volume loss. To illustrate our argument, we selected the events with a rise time below 600 μs, which is the strongest rise time cut we could choose. The resulting impact on the distribution of events within the SPC is shown in Figures 9.14 and 9.15b. We show that not only the electrons were removed, but also γ events within the first 6 cm of the SPC. Naturally, this is just an example, but it also illustrate that the optimization of the rise time cut will be necessary in order to maximize the signal over background ratio.

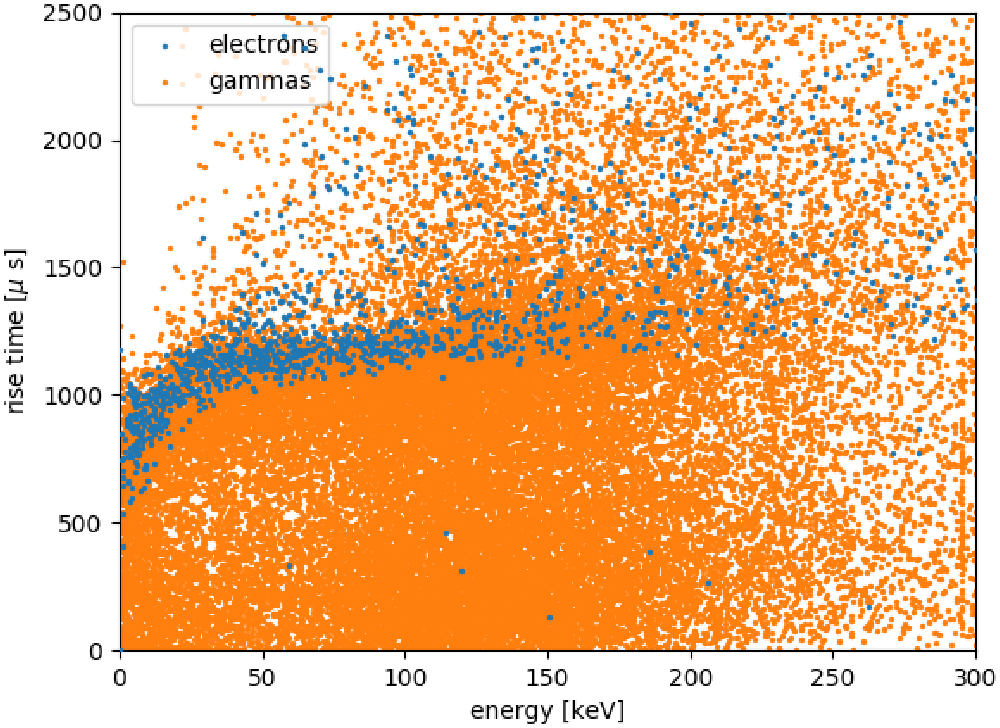

Figure 9.13: Rise times as a function of the *true* energy of the events in xenon. The blue data dots are the electron events and the orange dots are the gammas events. The behavior of the rise time decreasing with the energy, which was observed with our data at TUNL, and also reproduced with the simulated argon data, starts at 30 keV, instead of the sub-keV region. The rise time range of the electrons is quite large, which will result in a larger volume loss than with argon.

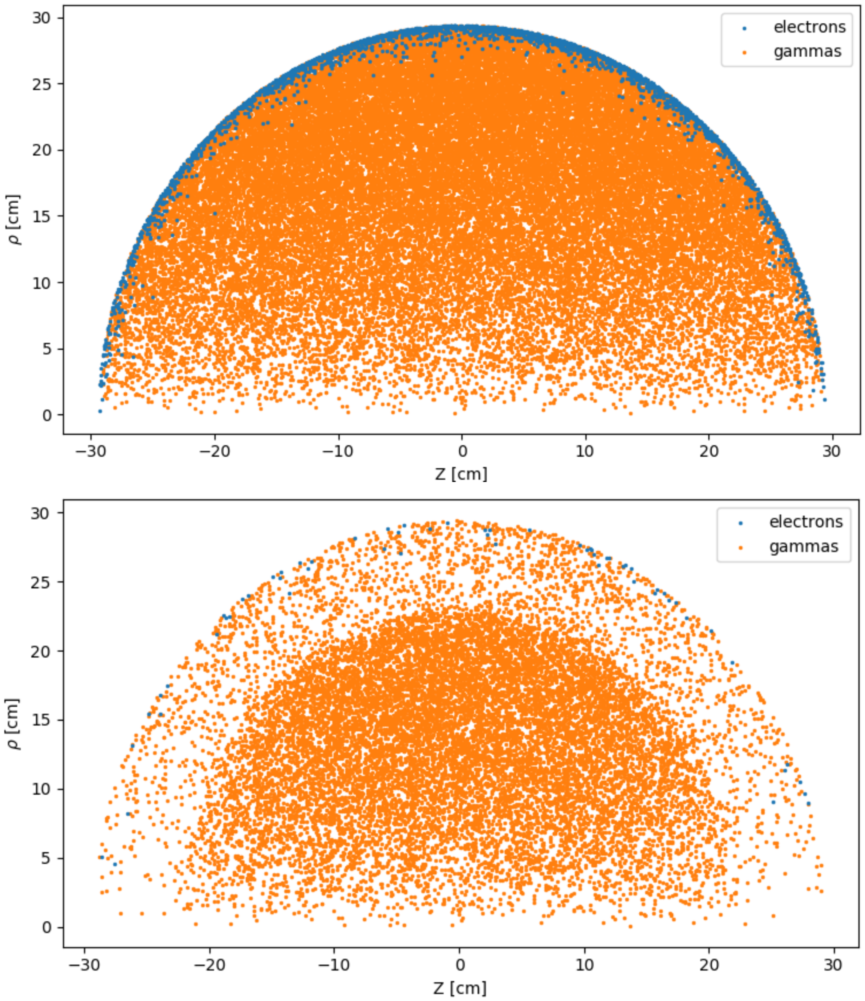

Figure 9.14: Spacial distribution of the events in cylindrical coordinates. The top plot shows the distribution of the electrons and the gammas events from ^{238}U in the copper layer of the shielding in the gas. The bottom plot shows the events passing a rise time cut of 600 μs. The electrons being mostly on the surface were cut out. On the contrary to the rise time cut in argon, the rise time cut does not only cut out electrons, but also the gammas. We can see how much of an impact such a cut would have on the fiducial volume, which is significant: 51 %.

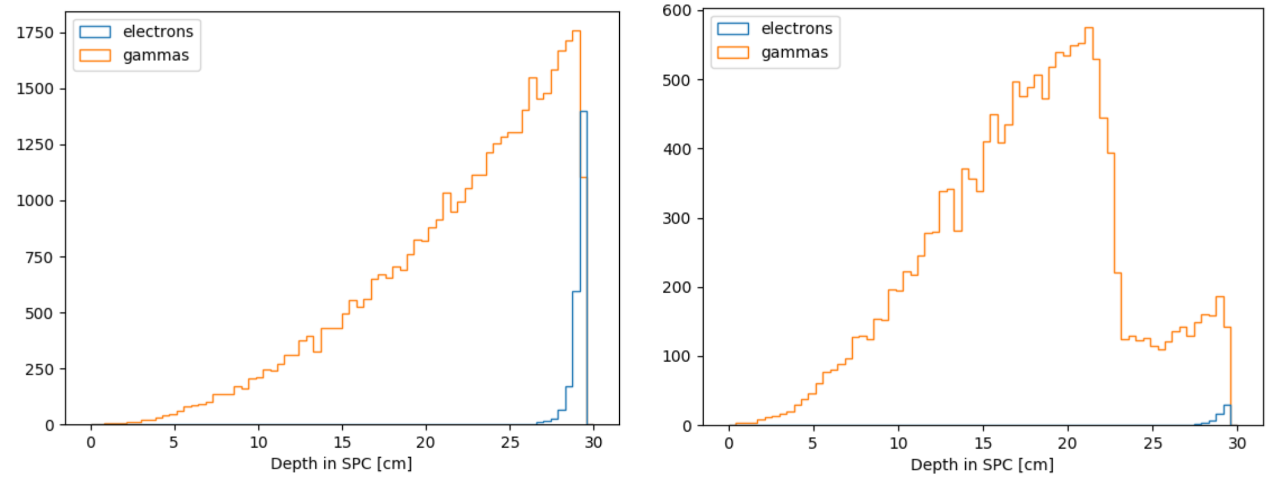

(a) The interactions of the electrons in the SPC take place in the first few cm after entering the gas. On the other hand, the γ are interacting in the whole volume of the gas.

(b) Same quantity with a rise time cut above 600 μs applied on the simulated data. The rise time rejected the most part of the electrons, but also the γ events.

Figure 9.15: Histograms showing the location of the interactions in the xenon based gas mixture.

9.4 Other backgrounds

Other external backgrounds include the background from the nuclear reactor, which produces gammas and neutrons, and cosmic muons. In this section, we will summarize in what way these particles are background events to our future CEνNS experiment and present proposed solutions to reject them.

9.4.1 Background from nuclear reactor

As aforementioned, fissions are taking place in the core of a nuclear reactor, creating a high flux of neutrons, β, and γ. While β particles are not a problem for our experiment, γ and fast neutrons escaping from the core can interact in our detector.

Gammas

Gamma rays are produced within the core of the nuclear reactor. The energy range produced is wide, going up to few MeVs. The high energy gammas can travel through the moderator and concrete structure, which is generally used as shielding to protect against both internal and external hazards from the core, and thus be attenuated.

To prevent this background in the gas of the SPC, our detector is surrounded by four lead layers. Each layer is 5 cm thick, hence, adding up to 20 cm of lead, which is typically used for such experiment [61] [58]. However, an exact characterization of such background will be necessary, in particular in the CEνNS region of interest. For this study, the gamma spectrum from a typical thermal reactor can be used for a preliminary estimation of the background. The gamma spectrum from the nuclear reactor chosen to conduct the experiment will be required to estimate the background accurately.

Neutrons

The typical average neutron energy created during a fission is 2 MeV. PWR and PHWR, which are thermal reactors, these neutrons are slowed down by the moderator, and reach average energies of 0.025 eV. However, the reactor neutron spectrum covers a wide range of energies across eight orders of magnitude. The fast neutrons escaping the nuclear core vessel slow down by going through concrete. Hence, these neutrons have intermediate energies, which can produce nuclear recoils in the CEνNS energy region if their energies are of the order of hundreds of keVs.

In response to this background, many experiment choose to shield their detector with polyethylene (PE), which is a thermoplastic polymer rich in hydrogen atoms: $(C_2H_4)_n$. Hence, this material is ideal to slow down neutrons down to thermal energies, which do not induce nuclear recoils above our energy threshold. As previously mentioned, the NEWS-G3 experiment has two layers of PE, 5 cm thick and one layer of polystyrene (muon veto). A dedicated study of the reactor neutrons contamination in the SPC detector will be required once a suitable experimental site will be found. This study will allow to estimate the efficiency of the PE panels as well as the contamination from such background in our detector.

9.4.2 Cosmic muons

The interactions of cosmic rays with nuclei of the upper atmosphere create showers of particles such as hadrons and leptons. In particular, the muons created during such process travel far and easily reach the surface of the Earth. On the ground the cosmic muon flux is about few hundred muons /m^2/s.

When cosmic muons interact with matter they can create new particles, and in particular neutrons by spallation. In turn, these neutrons will interact by elastic or inelastic scattering. Nuclear recoils produce by neutron elastic scattering constitute a background mimicking perfectly nuclear recoils induced by neutrinos in the energy range of interest. Hence, we imperatively want to prevent these kind of events in our detector. As a response to this background, the detector will be surrounded by a muon veto stopping the acquisition for a given time when a muon is detected. The detection efficiency of the muons and the “dead time” have to be estimated in order to reject successfully such background.

A study to estimate the dead-time due to muon interactions in the detector was performed by summer student C. Mitchinson. For this study, a Geant4 simulation was developed with the same geometry as the NEWS-G3 shield detector. Two muon veto panels, 5 cm thick, cover each face of the shielding. The detector is filled with 1 bar of a neon gas based mixture with 2 % of CH_4. The simulation considered the source of the muons to be a plane of 10×10 m above the shielding and detector. The number of muons simulated corresponded to about 3 h long data taking.
The active time in the SPC was estimated considering two different conditions. The first condition used a single panel interaction above threshold in order to be detected. The impact of the energy threshold, from 0 up to 4 MeV, had a negligible impact on the efficiency of the muons to be detected. The second condition considered coincidence interactions in 2 panels above energy threshold to be detected. The energy threshold impacted by 1 % the detection efficiency between 0 and 4 MeV, with 98 and 96.8 %, respectively. Finally, the active time was estimated as a function of the dead time after a pulse. The best and worst case scenarios were estimated with: 1 panel interaction with no energy threshold (96.8 % detection efficiency) and coincidence interactions in 2 panels with 4 MeV threshold (99.994 % detection efficiency) to be detected. The study showed that considering a maximum dead time of 1000 μs in both scenarios give similar results for both conditions with an active time of about 50 % at sea level.

9.4.3 Cosmogenic activation of the gas

The target gas can also be subject to cosmogenic activation from cosmic ray neutron interactions. The long-lived isotopes produced in xenon have half-lives too great to create a background of interest to us. At last but not least, we need to investigate the possible contamination of the gases to the long-lived isotope tritium.

Cosmogenic activation of argon

The argon extracted from the Earth's atmosphere consists of three stable isotopes: ^{40}Ar, ^{36}Ar, and ^{38}Ar with typical abundances of 99.60 %, 0.33 %, and 0.06 %, respectively [147]. However, the atmospheric argon also contains three unstable radioisotopes: ^{39}Ar, ^{37}Ar, and ^{42}Ar. The activities of each isotopes for 1 kg of atmospheric argon is given in Table 9.12. The isotopes which are the most relevant in terms of background are ^{39}Ar and ^{37}Ar. The first isotope, ^{39}Ar, decays by β emission with a continuous energy spectrum going up 565 keV. The ^{37}Ar emits two X-ray lines at 270 eV and 2.82 keV. Hence, these two isotopes constitute a background in our region of interest for CEνNS detection. Additional studies have to be performed in order to estimate what the induced background would be in our detector for using atmospheric argon.

If atmospheric argon is a source of too great background, then, underground argon could be an option as a gas target. In [148], the authors provide the number of production rate from cosmic ray neutrons at sea-level for ^{39}Ar and ^{37}Ar in argon. They measured 759 ± 128 atoms/kg and 51.0 ± 7.4 atoms/kg for ^{39}Ar and ^{37}Ar, respectively. Considering these results, the cosmogenic activation of the target gas would produce 6.2×10^{-8} Bq/kg/day and 1.17×10^{-4} Bq/kg/day ^{39}Ar and ^{37}Ar, respectively. Figure 9.16 shows the activity as a function of time of the ^{39}Ar and ^{37}Ar isotopes. ^{37}Ar reaches equilibrium in less than a year, at 0.6 mBq/kg. The X-ray line that is in the CEνNS region of interest, 270 eV, has a branching ratio of 0.0872 [154]. Hence, we can estimate that the background rate from such contamination is 4.52 dru, which is not negligible.

Isotopes	Abundances	Half-life	Activity [Bq/kg]
^{40}Ar	0.9960	stable	stable
^{36}Ar	0.0033	stable	stable
^{38}Ar	0.0006	stable	stable
^{39}Ar	8.2×10^{-16}	269 years	1.0 [150] [151]
^{37}Ar	1.3×10^{-20}	35.1 days	4.5×10^{-2} [152]
^{42}Ar	6.8×10^{-21}	32.9 years	6.8×10^{-5} [153]

Table 9.12: Table summarizing the stable and radioisotopes of argon. We provide the abundances [147], the half-lives [149], and the activities.

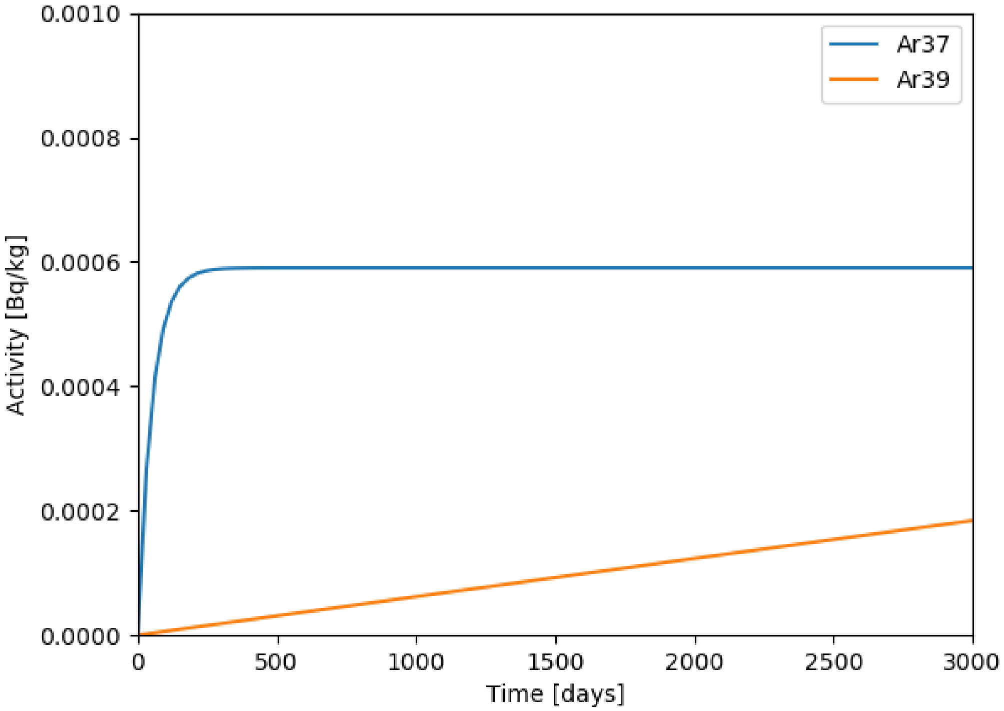

Figure 9.16: Activity of the argon isotopes ^{39}Ar and ^{37}Ar as a function of time. The largest contamination is coming from ^{37}Ar.

Presence of tritium in the gas

Finally, due to the exposition to cosmic rays, tritium can be produced in the various gas targets. This long-lived isotopes has a half-life of 12.32 years, and decays by emitting β particles with $Q = 18.59 \pm 0.001$ keV. In this section, we cover the contaminations expected from such isotope in our gas mixtures.

For neon, the production rate of ^{3}H from cosmogenic activation is 228 ± 16 atoms/kg/day [155]. It was calculated by former Ph.D student A. Brossard, that the tritium activity in neon after 1 year of exposure at the surface would be 0.14 ± 0.01 mBq/kg. Figure 9.17 shows the activity of tritium a function of time in argon.

In the same paper [155], the authors estimated the production rate of tritium from cosmogenic activation in argon. The estimated rate it 146 ± 31 atoms/kg/day. The corresponding tritium activity in argon after 1 year of exposure at the surface would be 0.09 ± 0.02 mBq/kg.

Finally, the authors in [156] calculated the production rate of tritium in xenon based on the work presented in [140]. Their estimate is 35.6 atoms/kg/day, resulting in an activity in xenon after 1 year of exposure of 0.023 mBq/kg. Figure 9.17 shows the activity of tritium a function of time in neon. Figure 9.17 shows the activity of tritium a function of time in xenon.

We acknowledge these possible sources of backgrounds for a CEνNS experiment. Hence, future studies will be conducted as to estimate their background rate in the region of interest for CEνNS detection.

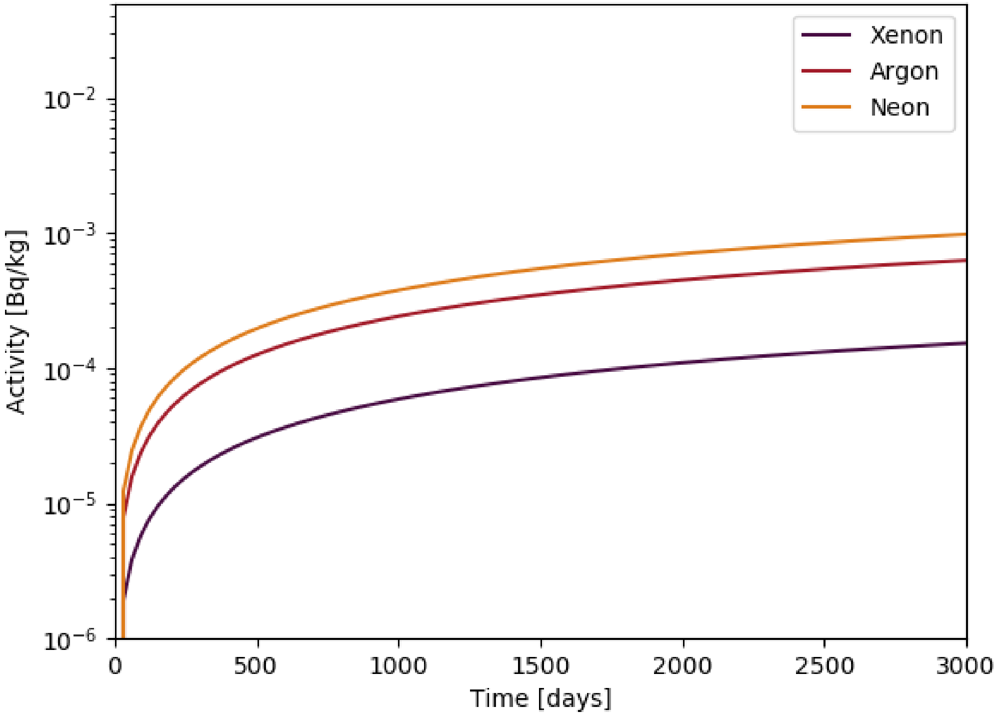

Figure 9.17: Activity of tritium in argon, neon and xenon as a function of time, induced by cosmic rays.

9.5 Conclusion on the preliminary background estimation for a CEνNS experiment

We investigated the background contaminations from the SPC shell and copper layer, and first lead layer, following the NEWS-G3 shielding design. As to complete our study on the CEνNS event rate presented in Section 8.3.2, we estimated the background in the three targets that produced an event rate above 10 events/day/kg/GW. These targets are: argon, neon, and xenon. With these preliminary estimations of the background contaminations, we can propose argon and xenon as serious candidates for a CEνNS experiment using a SPC at a nuclear reactor. The signal from CEνNS is about 4 and 1.5 times larger than the estimation of the background, after 2 years of material exposure, for xenon and argon, respectively. However, the background contamination in the neon based gas mixture is about 1.7 times larger than the expected CEνNS signal.

Further studies of the background will be necessary, accounting for the complete ensemble of layers of the compact shielding, the copper holder of the SPC, and so on. Moreover, background contaminations from external sources will require dedicated studies, such as the reactor neutrons and gammas contaminations. A preliminary study of the impact of the dead-time induced by muons interacting in the muon veto was performed. It was shown that the active time of the detector would be impacted by about 50 % with a worst case scenario dead-time of 1000 μs. The cosmic muon study is still underway. The next steps will allow to estimate an optimization between the dead-time and the active time in the detector, and lead to a corresponding background estimation in our detector.

Chapter 10

Summary and conclusion

The context of this thesis was to estimate the feasibility of an experiment; detecting Coherent Elastic Neutrino-Nucleus Scattering with an SPC detector at a nuclear reactor. In our study we considered a nuclear power plant having a thermal power of 1 GW, our detector to be 10 m away from the nuclear core, and a 60 cm diameter SPC detector. We investigated the signals induced by neutrinos in four gas targets: argon, helium, neon, and xenon, to determine the best candidate for a successful CEνNS experiment. The event rates were determined by a Monte Carlo simulation, taking into account the response of our detector and the nuclear quenching factor. From this study, we found that helium was not a competitive target for a CEνNS experiment, as a pressure of 53 bar would be required to reach 1 kg of target material, and hence, 3.6 events/kg/day/GW. We also explored two kinds of nuclear reactors: Pressurized Water Reactors and Pressurized Heavy Water Reactors, to estimate the neutrino flux's impact on the CEνNS event rate. It was found that the kind of reactors impacts between 15 and 20 % the CEνNS event rate in argon, neon, and xenon, in favor of PHWR. Hence, PHWR are proposed to conduct a CEνNS experiment, instead of a PWR. Finally, we looked at the background contamination induced from the intrinsic radioactivity of the materials used to build an SPC detector and appropriate shielding for a CEνNS experiment. For this study, we developed a simple Geant4 simulation using the geometry of the NEWS-G3 experiment, which aims at assessing the background on the surface. For the background sources, we considered the copper SPC vessel, the copper shielding, and the first lead layer of the shielding. We found that argon and xenon were promising candidates with about 1.5 and 5 times more CEνNS events than background events, respectively. However, we estimated that a neon based CEνNS experiment would be dominated by the background, having twice as many background events as CEνNS events in the region of interest. Additional studies will be performed, taking into account the complete design of the detector and compact shielding in order to estimate accurately the expected background in the detector. Furthermore, studies dedicated to external backgrounds, such as cosmic muons, or reactor neutrons and gammas, are either under way or will be performed in the near future.

A nuclear quenching factor measurement was performed between 0.43 and $11\,\mathrm{keV_{nr}}$ in a neon based gas mixture using a SPC exposed to a neutron beam. We investigated eight nuclear recoil energy "points", whose distributions overlapped significantly and were not Gaussian-like. In response to this, we developed a new analysis technique to extract the quenching factor. We developed a model to describe the nuclear recoils, taking into account the scattering angle distribution, the neutron energy distribution, the response of the detector, the resolution of the detector and the quenching factor. We performed an unbinned-joint fit to the data in a Bayesian framework to extract the most likely values of the quenching factor parametrization variables. The available statistics provided by the joint fit allowed to set excellent uncertainties on the quenching factor, no larger than 5 % in the sub-keV region. We have demonstrated the feasibility of measuring the quenching factor of a gas target using a neutron beam.

Future nuclear quenching factor measurements will see an improvement of the sensor design, and use a new generation sensor with an electric field corrector. This improvement will allow to reduce the uncertainties related to the energy response of the detector. The uniform response of the detector will allow *in situ* energy calibrations with ^{37}Ar, providing X-rays at 270 eV and 2.82 keV, in addition to the existing 5.9 keV calibration point obtained from an ^{55}Fe source. Future measurements will explore various gas mixtures and pressures in order to broaden our knowledge to the nuclear recoil response in gases, and extend the reach of the NEWS-G collaboration to various physics programs, amongst others CEνNS searches.

Appendices

A Preliminary quenching factor experiment: 2018

Prior to the quenching factor measurements presented in this work, we performed a preliminary campaign as to assess the feasibility of a quenching factor experiment using a neutron beam in a SPC filled with gas at the TUNL facility. For a period of about ten days we performed the first step of our quenching factor experiment, in the target room 4. In this appendix, we will present amongst others the experimental set up and the nuclear recoil data obtained.

A.1 Experimental set up

Neutron beam

During this preliminary campaign, we aimed at investigating nuclear recoil energies above $5\,\mathrm{keV_{nr}}$, hence, the neutron beam energy targeted was of a few MeV. The choice of accelerated particles and target were chosen carefully in order to reach such neutron energies. We used a deuteron beam of 1.9 MeV on a deuterium gas cell:

$$\mathrm{D^+ + D \longrightarrow n + {}^3Be + \gamma} \tag{1}$$

The neutron energy was measured using the time of flight method (TOF) presented in Section 5.1.2 of this work. After analysis of the TOF data, our collaborators at TUNL calculated the neutron energy to be $3.68 \pm 0.295\,\mathrm{MeV}$. A scan of the neutron beam was performed, estimating the cross section of the beam to be $3\,\mathrm{cm} \times 3\,\mathrm{cm}$.

Experiment

For the experiment, we used a 15 cm diameter SPC, 2 mm thick, made with stainless steal. The sensor was a 2 mm diameter metallic ball set to a positive voltage of 850 V, with an electric field corrector, or umbrella, set to 0 V. The detector was filled with 480 mbar of Ne + CH_4 (3 %). The digitized pulses from the CANBERRA preamplifier [99] were recorded using a Struck SIS3316 digitizer [100].

The SPC was exposed to the neutron beam: the south hemisphere was aligned with the neutron beam line to avoid the presence of the sensor and the rod in the north hemisphere. The scattered neutrons were detected by 11 backing detectors (BDs). The backing detector were on an annulus structure, allowing the record the same same scattering angle for all BDs. The annulus structure had a 29.4 cm radius. The BDs were the same as the BDs used in the 2019 campaign: they consisted in a combination of Hamamatsu R7724 photomultiplier tubes [101] and liquid scintillator, made by Eljen [102], allowing for pulse shape discrimination between gamma and neutron events. Figures 1a and 1b show the experimental set up.

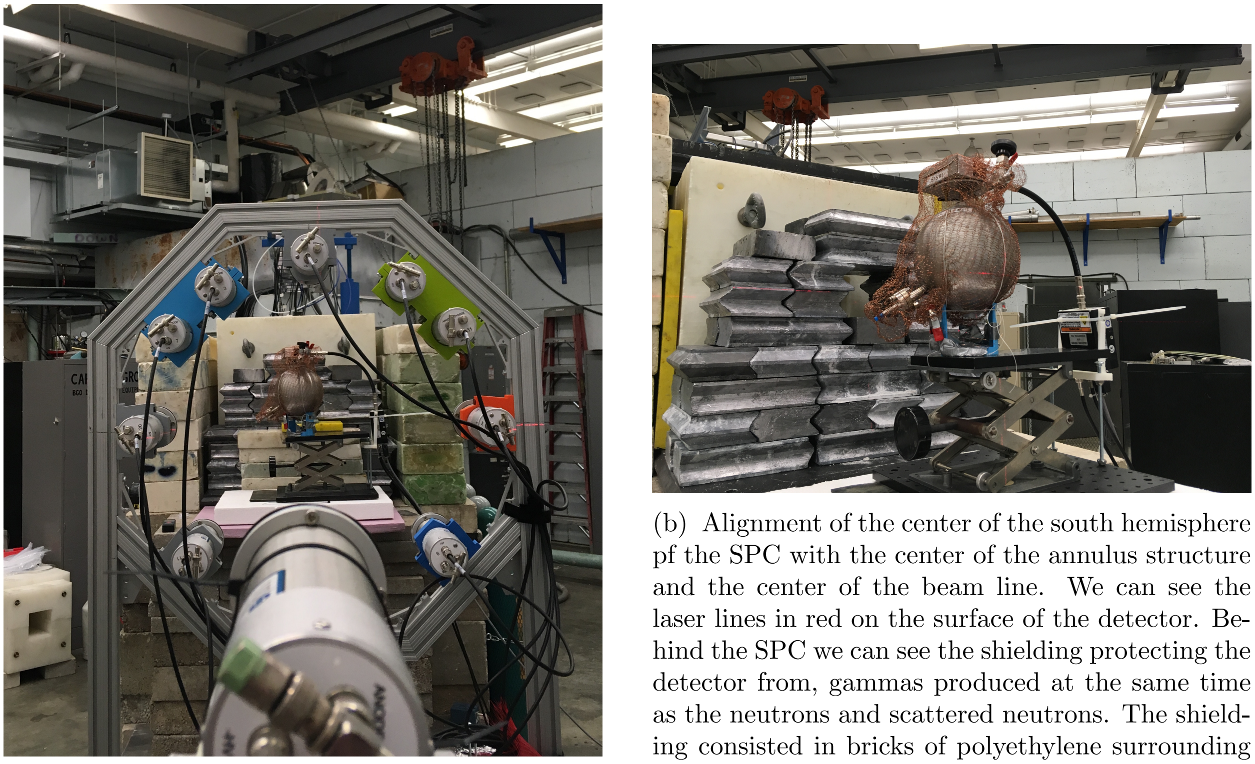

(a) The annulus structure holds 11 BDs, the center of the structure is aligned with the neutron beam line and the south hemisphere of the SPC.

(b) Alignment of the center of the south hemisphere pf the SPC with the center of the annulus structure and the center of the beam line. We can see the laser lines in red on the surface of the detector. Behind the SPC we can see the shielding protecting the detector from, gammas produced at the same time as the neutrons and scattered neutrons. The shielding consisted in bricks of polyethylene surrounding the beam line and a wall of lead bricks between the polyethylene shielding and the SPC.

Figure 1: Experimental set up for the 2018 quenching factor campaign. The annulus structure holds 11 BDs, the center of the structure is aligned with the neutron beam line and the

Using this experimental set up, we recorded four nuclear recoil energies, from about 5 up to 30 $\mathrm{keV_{nr}}$. The details about each run configuration is given in Table 1. The nuclear recoil energy means were not calculated using the Monte Carlo simulation that generates the scattering angle distribution. The reason being that we did not take as many measurements of the SPC within its environment, for example the distance between the exit of the collimator and the SPC. Hence, to calculate the nuclear recoils we considered that the interactions of the neutrons in the SPC were taking place in the center of the south hemisphere and at the surface of the BDs.

Run number	Recoil energies [keV$_{nr}$]	Angle [^{o}]	Distances [m]	Exposure [h]
6	28.74	22.83 ± 0.69	69.83 ± 0.12	8
5	14.95	16.40 ± 0.52	99.90 ± 0.081	12
3	8.76	12.53 ± 0.41	132.30 ± 0.14	8
4	4.75	9.22 ± 0.31	181.033 ± 0.047	16

Table 1: Table with the chosen nuclear recoil energies, their corresponding angles, the distance between SPC detector and annulus, and time exposures.

A.2 Energy calibration

The energy calibration of the experiment was performed using and ^{55}Fe source located at the south pole of the SPC. The calibration window was made of an aluminum foil As aforementioned, the ^{55}Fe emits X-rays of 5.9 keV. This calibration gave an electron ionization energy scale within the range of nuclear recoil energies that we investigated, and provided a source of monitoring for eventual gain drifts.

The source was left on the detector during data taking (triggering on the BDs), but calibration data were also taken every hour for 5 min (triggering on the SPC). Figure 2a shows the rise time as a function of the energy of the events. We can see the ^{55}Fe events with energies between 20000 and 25 000 ADC. In order to select the ^{55}Fe events, we applied a rise time cut between 1 and 1.51 μs. An example of resulting energy spectrum of the ^{55}Fe is shown in Figure 2b.

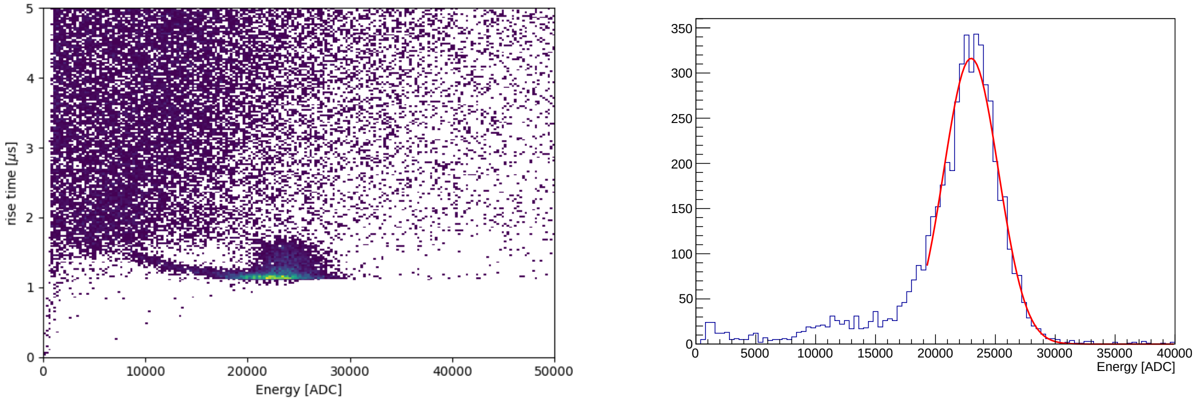

(a) Rise time as a function of energy for a calibration data set. The ^{55}Fe events are the population of events between 20000 and 25 000 ADC.

(b) Energy spectrum of the ^{55}Fe obtained by applying a rise time cuts between 1 and 1.51 μs. The red curve represent the truncated Gaussian fit to the data.

Figure 2: Energy calibration performed with an ^{55}Fe source placed on the south pole of the SPC.

To obtain the energy scale, we fitted the spectrum to a Gaussian (truncated) with the following function:

$$f(x) = \frac{N}{\sigma\sqrt{2\pi}} exp\left(- \frac{x\mu - 5.9\,(keV)^2}{2\sigma^2} \right) \tag{2}$$

where N and σ are the height and the standard deviation of the ^{55}Fe peak, respectively, μ is the energy scale provided from the mean of the ^{55}Fe peak.

Figure 3 shows the energy scale as a function of time, for the calibration data and the beam data. We can see that the gain of the detector was decreasing with time. In order to scale the data from ADC to keV and to correct for the gain drop, we fitted the energy scale time evolution with a quadratic function.

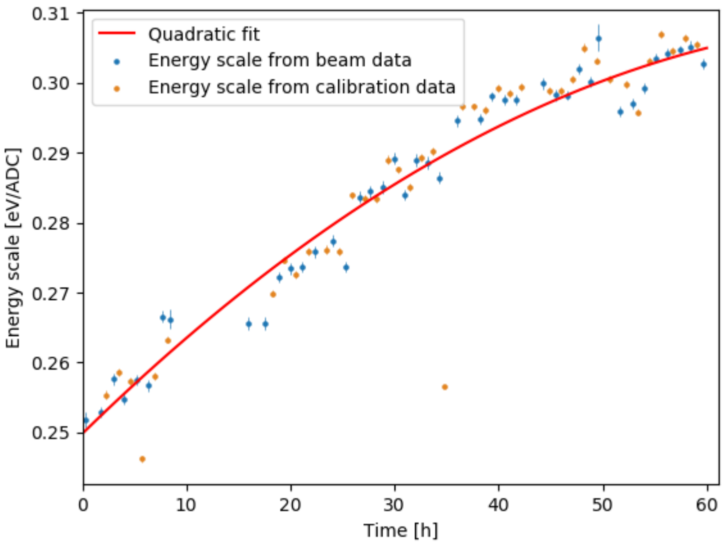

Figure 3: Energy scale of the ^{55}Fe as a function of time. In blue we show the energy scale extracted from the beam data. In orange we show the energy scale extracted from the beam data. In red, we show the quadratic fit to the data. We see that both energy scales have the same trend: the gain of the detector is decreasing with time.

Prior to our experiment at TUNL, we investigated the response in energy in our detector. We took data in the NEWS-G laboratory, at Queen's University, with the same detector, filled with 700 mbar of Ne+CH_4 (2 %). The high voltage applied on the anode was 800 V, and the voltage applied on the umbrella 0 V. To test the energy linearity of our detector we used an ^{55}Fe source and an ^{37}Ar gas source, hence, providing two calibration points at 5.9 keV and 2.82 keV, respectively. Figure 4a shows the rise time as a function of energy of such data set. We can clearly see the two population of events interacting in the volume of the detector, with rise times comprised between 0.3 and 5 μs. We selected the two populations by applying a rise time cut between 0.3 and 4 μs. The resulting energy spectrum is shown in Figure 4b, we can see clearly the two peaks corresponding to the ^{37}Ar and the ^{55}Fe. By fitting a Gaussian to the peaks, we were able to extract their means. The results of the fits are shown in Table 2. We used the ^{55}Fe as the energy scale. Hence, by calculating the mean energy of the ^{37}Ar peak from the result of the fit, we found that the energy mean was 2.838 keV, thus, being 0.6 % away from 2.82 keV. The uncertainty on the peaks position is dominated by the statistic available, and are larger than the possible non-linearities. From these data, we can conclude that our detector has its energy response linear, with an upper limit of 0.6 %, which is in agreement with the limit given by [66].

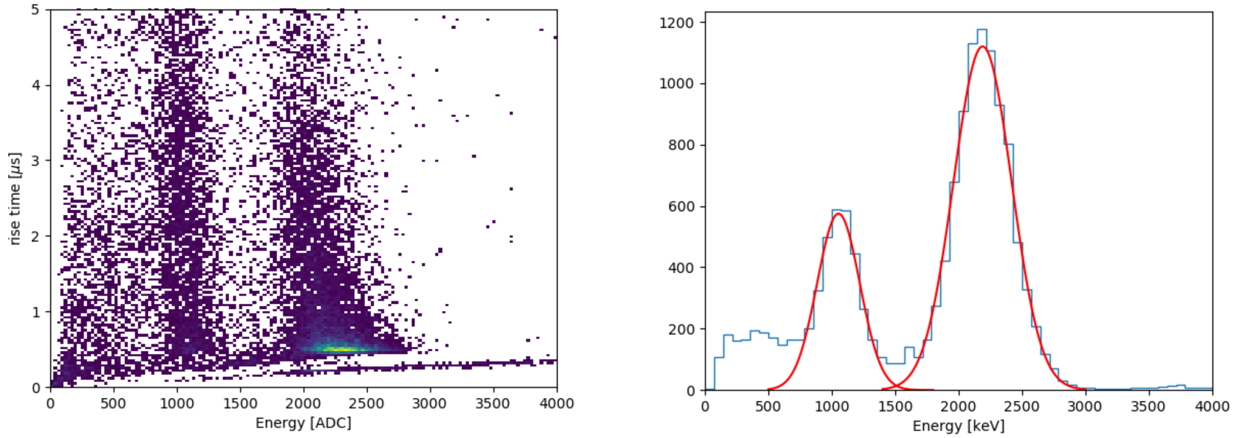

(a) Rise time as a function of the energy of two energy calibrations. The peak at highest energy is the ^{55}Fe peak and the lowest peak is the ^{37}Ar peak.

(b) Energy spectrum of the ^{55}Fe and ^{37}Ar calibrations with rise time cuts between 0.3 and 4 μs. In red we show the Gaussian fits performed to each peak.

Figure 4: Investigation of the energy response of our SPC detector by using an ^{55}Fe and ^{37}Ar sources providing calibration points at 5.9 keV and 2.82 keV, respectively.

	Energy mean [ADC]	Standard deviation [ADC]	Energy mean [keV]
^{55}Fe	2189 ± 24	229 ± 21	5.9
^{37}Ar	1053 ±34.5	168 ± 38.6	2.838

Table 2: Values of the Gaussian fit to the ^{55}Fe and ^{37}Ar peaks. For the last column we use the ^{55}Fe as the energy scale and calculate what is the corresponding energy mean of the ^{37}Ar.

A.3 Data taking and processing

The data taking configuration for the 2018 campaign was the same as for the 2019 experiment. The beam data, or nuclear recoil data, were triggered on the BDs. The calibration data triggered on the SPC.

The processing procedure was the same for the two campaigns. The data were twice processed. Once with a simple trapezoidal filter on the SPC pulses, and pulse profile for the BDs pulses, so that we could reject gamma events using the PSD parameter. Then, a second time with the double deconvolution method.

For more details about the processing and the data taking see Section 5.4.2.

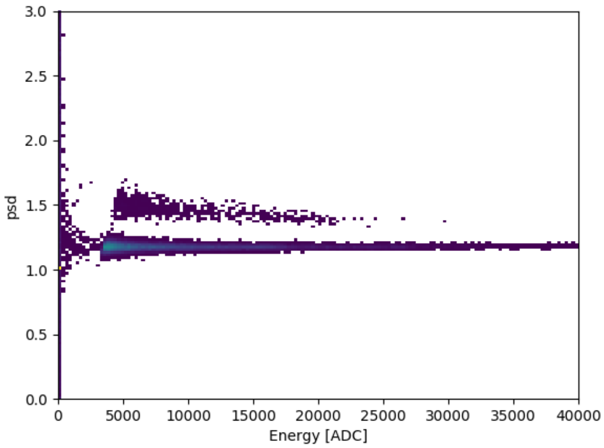

(a) PSD as a function of the energy of the events in the BDs, for 1 h of data of run 6. The events having a PSD above 1.3 were selected.

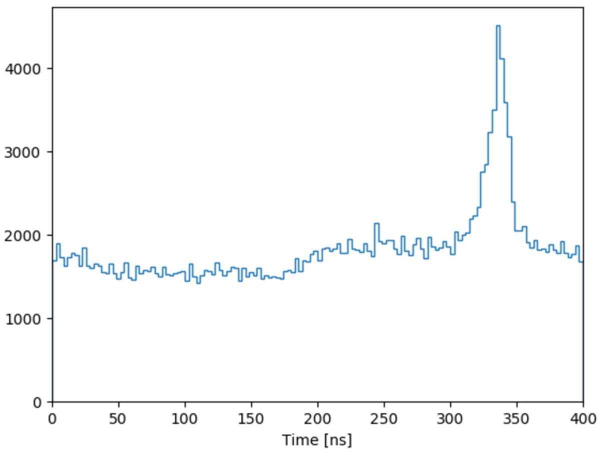

(b) Time of flight (TOF) spectrum of the neutrons for the run 6 between the Beam Pick Off Monitor and the triggering BD. Spectrum obtained after PSD cut.

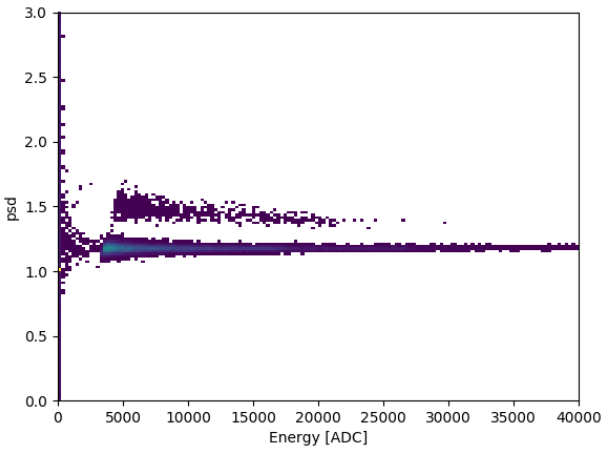

(c) PSD as a function of the energy of the events in the BDs, for 1 h of data of run 6. The events having a PSD above 1.3 were selected.

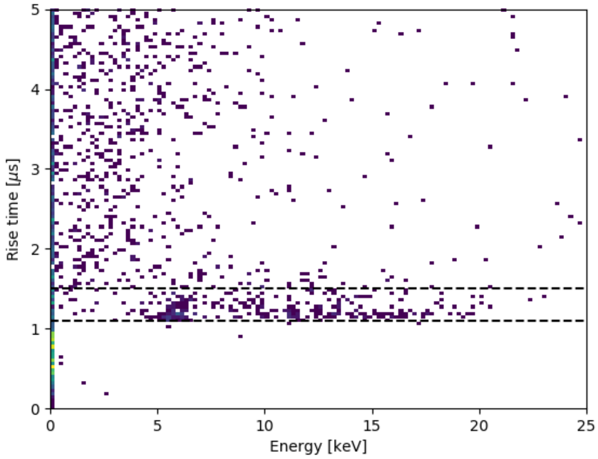

(d) Rise time as a function of the energy of the events in the SPC, for run 6. At 5.9 keV we can observe the ^{55}Fe events and the population at higher energies corresponds to neon nuclear recoils. We selected the events having rise times between 1 and 1.51 μs

Figure 5: Sets of cuts performed to the data.

A.4 Data selection

In order to select the recoil events, we applied different sets of cuts to the data. These cuts were explained in details in Section 6.1. First, we applied a PSD cut to reject gamma events. Figure 5c shows the PSD as a function of the energy of the events in the BDs. We can see two distinct

Run number	TOF cut [ns]
3	315-360
4	320-375
5	310-345
6	295-340

Table 3: Table summarizing the TOF cut for the different runs.

population of events, the neutrons centered at a PSD of 1.5, and the gammas centered at a PSD of 1.2. We can see that the shape of the populations changed in comparison to the populations of the 2019 campaign. In particular we can see that the discrimination between neutron and gamma events is easier at higher neutron energies. Hence, the events having a PSD above 1.3 were selected.

Then, to select the neutrons coming from the beam, we performed a TOF cut. The TOF varies with the distance between the SPC and the annulus structure. The different values of the TOF cuts are shown in Table 3.

Finally, two other cuts were performed on the SPC related quantities. We cut on the onset time, which represent the time difference between the BD and the start of the pulse in the SPC. Based on the onset time spectrum we defined the onset time signal window between 40 and 50 μs. The last cut applied to the data allowed to select events occurring in the volume of the SPC and to reject background events occurring at the surface of the SPC. Figure 5d shows the rise time as a function of the energy of the events in the SPC. We can observe three population of events. The first, at high rise time correspond to track events induced by comic muons or high energy gammas coming from the beam. The second population of events centered at 5.9 keV correspond to the ^{55}Fe events. And the last population, with energies at about 10 keV, corresponds to neon nuclear recoils. To select this particular population we applied rise time cuts between 1 and 1.51 μs.

A.5 Nuclear recoil energy spectra

After applying the cuts mentioned above, we obtained the energy spectra of the 2018 QF campaign. Figure 6 shows such energy spectra. We can see the ^{55}Fe peak in all spectra, and the nuclear recoil signal moving from high to low energies. For run 5 and 3, we can see that the recoils are located in an energy region overlapping with the ^{55}Fe events. Hence, the extraction of the recoils and thus the quenching factor from these two energy runs has to take into account the ^{55}Fe peak. Learning from that experience, during the 2019 quenching factor experiment, the ^{55}Fe source was removed while taking data, as to avoid this situation. Looking at the recoil peaks we can observe the best: run 6 and 4, the first one has a rather symmetric shape, while we can guess an asymmetry in recoil shape of run 4. Asymmetry that we find in the 2019 energy spectra. Thus, it seems that the asymmetry is driven by two factors: the geometry of the experiment, but also the energy response of the detector. In terms of statistics available for each run, they seem to be reasonable except for run 3, where the recoil events are embedded in the ^{55}Fe and environmental background. The time exposure of 8 h was not long enough in order to have satisfactory statistics.

We do not present a QF results for these data, as the analysis methodology to extract the quantity was rather naive in comparison to the technique proposed in Chapter 6.

A.6 Conclusion and discussion of the 2018 preliminary campaign

Despite the fact that this preliminary campaign did not provide final results of the quenching factor of neon ions in neon gas at 480 mbar, we showed the feasibility of a successful quenching factor measurements using an SPC filled with gas and using a neutron beam. This preliminary campaign allowed us to identify areas of improvements for the following QF experiment, which took place in 2019 and is presented in this thesis. We decided to have dedicated calibration times, and to remove the ^{55}Fe source during the data taking. Our collaborators at TUNL designed and built a new shielding around the target and the neutron beam line in order to reduce backgrounds coming from the beam in the detector target. We found that the current of the beam could fluctuate, which impacts the event rate in the SPC. In response to this, we developed a quick analysis to perform on site, in order to estimate the statistics available for each run and adapt the time exposure accordingly.

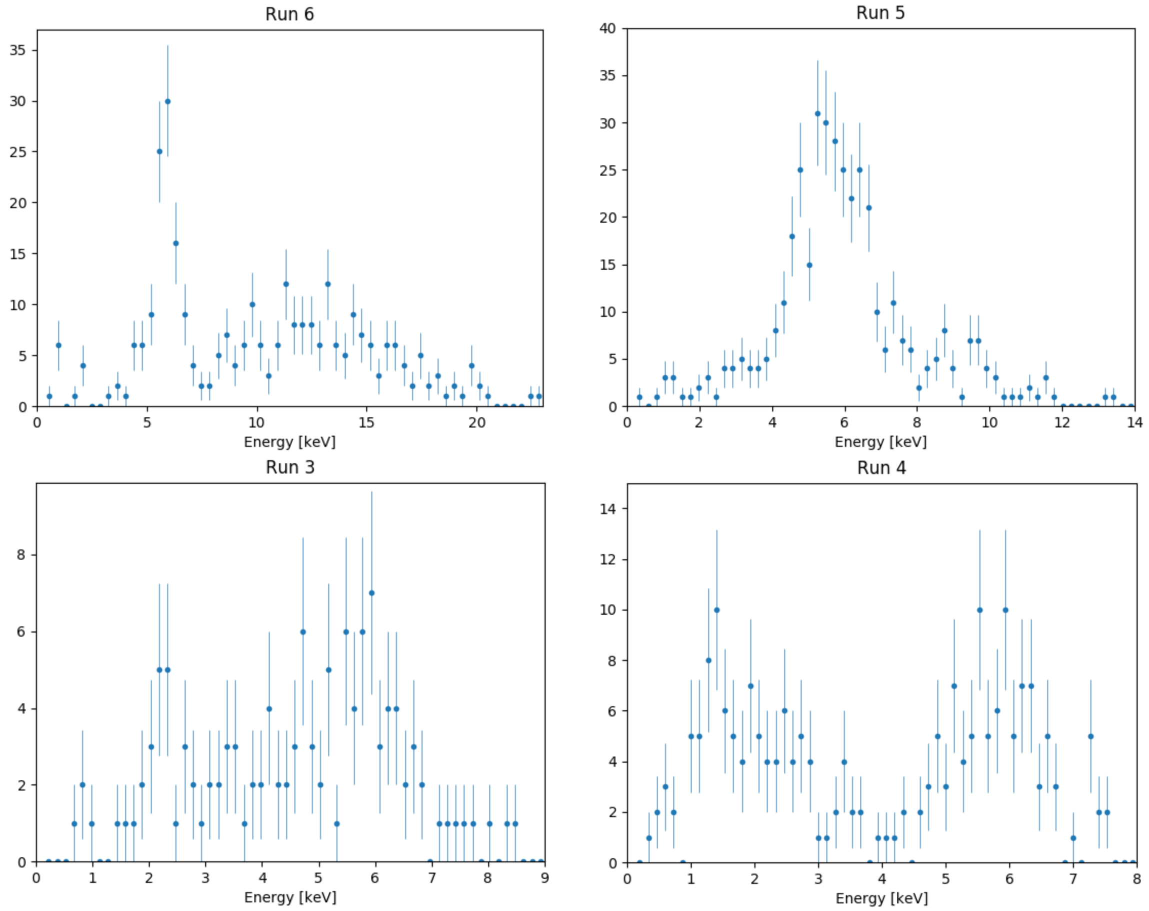

Figure 6: Energy spectra from the 2018 QF campaign, after applying cuts: PSD, TOF, onset and rise times. The mean nuclear recoil energies are: $28.74\,\mathrm{keV_{nr}}$, $14.95\,\mathrm{keV_{nr}}$, $8.76\,\mathrm{keV_{nr}}$, and $4.75\,\mathrm{keV}$, moving from left to right and top to bottom. We can observe the ^{55}Fe events are $5.9\,\mathrm{keV}$ and the nuclear recoil signal.

B Covariance and correlation matrices

The covariance matrix is provided to the reader as is it necessary to compute the correct errors on α and β for a given nuclear recoil energy. The correlation matrix is also provided to allow the reader to observe which variables have strong correlation together.

Parameters	f_{s8}	f_{s7}	f_{s9}	f_{s10}	f_{s11}	$\mathrm{f}_{s14,0.34\,\mathrm{keV}}$	$\mathrm{f}_{s14,1\,\mathrm{keV}}$	$\mathrm{f}_{s14,2\,\mathrm{keV}}$	α	β	θ_8	θ_7	θ_9	θ_10	θ_11	$\theta_{14,0.34keV}$	$\theta_{14,1keV}$	$\theta_{14,2keV}$	σ_a
f_{s8}	4.12e-4	7.65e-5	6.88e-5	6.98e-5	5.65e-5	1.99e-5	6.37e-5	8.07e-5	-1.27e-5	3.38e-5	-4.67e-4	-4.60e-5	8.60e-6	1.11e-5	2.86e-6	-2.94e-6	8.68e-5	-4.86e-5	7.03e-5
f_{s7}	7.65e-5	4.91e-4	9.69e-5	1.02e-4	9.32e-5	3.68e-5	8.99e-5	1.09e-4	-7.63e-6	1.01e-5	-2.63e-4	8.20e-5	-1.33e-5	-4.04e-6	-5.97e-7	-3.79e-5	-1.60e-6	-1.49e-4	9.68e-5
f_{s9}	6.87e-5	9.69e-5	3.42e-4	1.08e-4	1.11e-4	4.83e-5	9.15e-5	1.05e-4	4.03e-6	-4.04e-5	3.23e-4	-2.42e-5	6.64e-5	-2.55e-5	-6.18e-6	-3.50e-5	-1.43e-4	-2.23e-4	9.61e-5
f_{s10}	6.98e-5	1.025e-4	1.08e-4	5.40e-4	1.37e-4	6.21e-5	1.02e-4	1.13e-4	1.38e-5	-8.25e-5	7.73e-4	-8.95e-6	-6.24e-5	7.16e-5	-1.12e-5	-3.60e-5	-2.71e-4	-3.12e-4	1.05e-4
f_{s11}	5.65e-5	9.32e-5	1.11e-4	1.36e-4	1.23e-3	8.41e-5	1.06e-4	1.08e-4	3.45e-5	-1.78e-4	1.92e-3	6.20e-5	-1.01e-4	-8.32e-5	6.88e-5	-3.18e-5	-5.23e-4	-4.29e-4	1.05e-4
$\mathrm{f}_{s14,0.34\,\mathrm{keV}}$	1.99e-5	3.67e-5	4.83e-5	6.21e-5	8.41e-5	1.53e-3	4.66e-5	4.45e-5	2.11e-5	-1.07e-4	1.21e-3	5.29e-5	-5.44e-5	-4.68e-5	-1.23e-5	2.94e-3	-3.01e-4	-2.15e-4	4.55e-5
$\mathrm{f}_{s14,1\,\mathrm{keV}}$	6.36e-5	8.99e-5	9.15e-5	1.02e-4	1.06e-4	4.66e-5	1.13e-3	9.91e-5	3.70e-6	-4.68e-5	4.88e-4	3.80e-6	-2.84e-5	-2.23e-5	-6.07e-6	-3.38e-5	1.88e-3	-1.82e-4	9.12e-5
$\mathrm{f}_{s14,2\,\mathrm{keV}}$	8.07e-5	1.09e-4	1.05e-4	1.13e-4	1.08e-4	4.45e-5	9.91e-5	8.67e-4	-6.82e-6	-1.48e-5	1.81e-4	-1.13e-6	-4.00e-6	-4.10e-6	-2.02e-6	-4.29e-5	-1.75e-5	-3.00e-4	1.07e-4
α	-1.26e-5	-7.63e-6	4.04e-6	1.38e-5	3.45e-5	2.11e-5	3.70e-6	-6.82e-6	2.48e-5	-7.96e-5	6.71e-4	-1.54e-5	-7.20e-5	-5.06e-5	-1.10e-5	-8.51e-6	-3.07e-4	-2.41e-4	-3.13e-6
β	3.38e-5	1.01e-5	-4.04e-5	-8.25e-5	-1.78e-4	-1.07e-4	-4.68e-5	-1.48e-5	-7.96e-5	4.30e-4	-5.61e-3	-4.23e-4	1.21e-4	1.41e-4	4.22e-5	1.07e-6	9.91e-4	3.55e-4	-3.95e-5
θ_8	-4.67e-4	-2.63e-4	3.23e-4	7.73e-4	1.92e-3	1.21e-3	4.88e-4	1.81e-4	6.72e-4	-5.61e-3	1.15e-1	9.25e-3	3.72e-4	-8.76e-4	-4.23e-4	-2.16e-4	-8.12e-3	2.58e-3	5.78e-4
θ_7	-4.60e-5	8.20e-5	-2.42e-5	-8.95e-6	6.20e-5	5.29e-5	3.80e-6	-1.12e-6	-1.54e-5	-4.23e-4	9.25e-3	8.01e-3	3.85e-4	1.10e-4	-8.49e-6	-6.87e-5	2.65e-4	1.53e-3	4.37e-5
θ_9	8.60e-6	-1.33e-5	6.64e-5	-6.24e-5	-1.02e-4	-5.44e-5	-2.84e-5	-4.00e-6	-7.20e-5	1.21e-4	3.73e-4	3.85e-4	3.06e-3	1.69e-4	2.91e-5	-2.76e-6	9.26e-4	1.07e-3	-1.09e-6
θ_{10}	1.10e-5	-4.04e-6	-2.55e-5	7.16e-5	-8.32e-5	-4.68e-5	-2.23e-5	-4.10e-6	-5.06e-5	1.41e-4	-8.76e-4	1.10e-4	1.69e-4	2.29e-3	2.23e-5	1.36e-5	6.44e-4	5.96e-4	-7.40e-6
θ_{11}	2.86e-6	-5.97e-7	-6.18e-6	-1.12e-5	6.88e-5	-1.23e-5	-6.07e-6	-2.02e-6	-1.10e-5	4.22e-5	-4.23e-4	-8.50e-5	2.90e-5	2.23e-5	1.13e-3	1.51e-6	1.39e-4	9.90e-5	-3.74e-6
$\theta_{14,0.34keV}$	-2.94e-5	-3.79e-5	-3.50e-5	-3.60e-5	-3.18e-5	2.94e-3	-3.38e-5	-4.29e-5	8.51e-6	1.07e-6	-2.16e-4	-4.87e-5	-2.76e-5	1.36e-5	-1.51e-6	6.87e-2	-7.21e-2	-6.38e-5	-3.96e-5
$\theta_{14,1keV}$	8.68e-5	-1.60e-6	-1.43e-4	-2.71e-4	-5.23e-4	-3.01e-4	1.88e-3	-1.75e-5	-3.07e-4	9.91e-4	-8.12e-3	2.65e-4	9.27e-4	6.44e-4	1.39e-4	-7.21e-5	3.21e-2	3.20e-3	-5.18e-5
$\theta_{14,2keV}$	-4.86e-5	-1.49e-4	-2.23e-4	-3.12e-4	-4.29e-4	-2.15e-4	-1.82e-4	3.00e-4	-2.41e-4	3.55e-4	2.58e-3	1.52e-3	1.07e-3	5.95e-4	9.90e-5	-6.38e-5	3.20e-3	2.32e-2	-9.08e-5
σ_a	7.03e-5	9.68e-5	9.61e-5	1.05e-4	1.06e-4	4.55e-5	9.12e-5	1.07e-4	-3.13e-6	-3.94e-5	5.78e-4	4.37e-5	-1.1e-6	-7.40e-6	-3.74e-6	-3.96e-5	-5.18e-5	-9.08e-5	9.94e-5

Table 4: Covariance matrix for the joint fit performed to the data.

Parameters	f_{s8}	f_{s7}	f_{s9}	f_{s10}	f_{s11}	$\mathrm{f}_{s14,0.34\,\mathrm{keV}}$	$\mathrm{f}_{s14,1\,\mathrm{keV}}$	$\mathrm{f}_{s14,2\,\mathrm{keV}}$	α	β	θ_8	θ_7	θ_9	θ_10	θ_11	$\theta_{14,0.34keV}$	$\theta_{14,1keV}$	$\theta_{14,2keV}$	σ_a
f_{s8}	1.000	0.170	0.183	0.148	0.079	0.025	0.093	0.135	-0.125	0.080	-0.068	-0.025	0.008	0.011	0.004	-0.006	0.024	-0.016	0.347
f_{s7}	0.170	1.000	0.236	0.199	0.120	0.042	0.121	0.168	-0.069	0.022	-0.035	0.041	-0.011	-0.004	-0.001	-0.007	-0.000	-0.044	0.438
f_{s9}	0.183	0.236	1.000	0.252	0.171	0.067	0.147	0.194	0.044	-0.105	0.051	-0.015	0.065	-0.029	-0.010	-0.007	-0.043	-0.079	0.521
f_{s10}	0.148	0.199	0.252	1.000	0.168	0.068	0.131	0.165	0.119	-0.171	0.098	-0.004	-0.048	0.064	-0.014	-0.006	-0.065	-0.088	0.453
f_{s11}	0.079	0.120	0.171	0.168	1.000	0.061	0.090	0.105	0.197	-0.244	0.161	0.020	-0.052	-0.050	0.058	-0.003	-0.083	-0.080	0.302
$\mathrm{f}_{s14,0.34keV}$	0.025	0.042	0.067	0.068	0.061	1.000	0.035	0.039	0.108	-0.132	0.091	0.015	-0.025	-0.025	-0.009	0.286	-0.043	-0.036	0.117
$\mathrm{f}_{s14,1keV}$	0.093	0.121	0.147	0.131	0.090	0.035	1.000	0.100	0.022	-0.067	0.043	0.001	-0.015	-0.014	-0.005	-0.004	0.312	-0.036	0.272
$\mathrm{f}_{s14,2keV}$	0.135	0.168	0.194	0.165	0.105	0.039	0.100	1.000	-0.046	-0.024	0.018	-0.000	-0.002	-0.003	-0.002	-0.006	-0.003	0.067	0.367
α	-0.125	-0.069	0.044	0.119	0.197	0.108	0.022	-0.046	1.000	-0.770	0.397	-0.035	-0.261	-0.212	-0.066	0.007	-0.343	-0.317	-0.063
β	0.080	0.022	-0.105	-0.171	-0.244	-0.132	-0.067	-0.024	-0.770	1.000	-0.797	-0.228	0.105	0.142	0.060	0.000	0.266	0.112	-0.191
θ_8	-0.068	-0.035	0.051	0.098	0.161	0.091	0.043	0.018	0.397	-0.797	1.000	0.305	0.020	-0.054	-0.037	-0.002	-0.133	0.050	0.171
θ_7	-0.025	0.041	-0.015	-0.004	0.020	0.015	0.001	-0.000	-0.035	-0.228	0.305	1.000	0.078	0.026	-0.003	-0.002	0.017	0.112	0.049
θ_9	0.008	-0.011	0.065	-0.048	-0.052	-0.025	-0.015	-0.002	-0.261	0.105	0.020	0.078	1.000	0.064	0.016	-0.002	0.093	0.127	-0.002
θ_10	0.011	-0.004	-0.029	0.064	-0.050	-0.025	-0.014	-0.003	-0.212	0.142	-0.054	0.026	0.064	1.000	0.014	-0.001	0.075	0.082	-0.016
θ_11	0.004	-0.001	-0.010	-0.014	0.058	-0.009	-0.005	-0.002	-0.066	0.060	-0.037	-0.003	0.016	0.014	1.000	-0.000	0.023	0.019	-0.011
$\theta_{14,0.34keV}$	-0.006	-0.007	-0.007	-0.006	-0.003	0.286	-0.004	-0.006	0.007	0.000	-0.002	-0.002	-0.002	-0.001	-0.000	1.000	-0.002	-0.002	-0.015
$\theta_{14,1keV}$	0.024	-0.000	-0.043	-0.065	-0.083	-0.043	0.312	-0.003	-0.343	0.266	-0.133	0.017	0.093	0.075	0.023	-0.002	1.000	0.117	-0.029
$\theta_{14,2keV}$	-0.016	-0.044	-0.079	-0.088	-0.080	-0.036	-0.036	0.067	-0.317	0.112	0.050	0.112	0.127	0.082	0.019	-0.002	0.117	1.000	-0.060
σ_a	0.347	0.438	0.521	0.453	0.302	0.117	0.272	0.367	-0.063	-0.191	0.171	0.049	-0.002	-0.016	-0.011	-0.015	-0.029	-0.060	1.000

Table 5: Correllation matrix for the joint fit performed to the data.

Bibliography

[1] W. Pauli, *Dear radioactive ladies and gentlemen*, Phys. Today, 31N9: **27**, 1978

[2] F. Reines and C. L. Cowan, Jr., *The Neutrino*, Nature **178**, 446, 1956

[3] G. Danby and J. Gaillard and K. Goulianos and L. Lederman and N. Mistry and M. Schwartz and J. Steinberger, *Observation of High-Energy Neutrino Reactions and the Existence of Two Kinds of Neutrinos*, Physical Review Letters, **9**, 36-44, 1962

[4] K. Kodama *et al.*, *Observation of tau-neutrino interactions*, Phys. Lett. B **504**, 218-224, 2001

[5] R. Hofstadter, *Nuclear and Nucleon Scattering of High-Energy Electrons*, Annu. Rev. Nucl. Sci. **7**.1, 1957

[6] D. Z. Freedman, *Coherent effects of a weak neutral current*, Phys. Rev. D **9**.5, 1974

[7] D. Z. Freedman, D. N. Schramm and D. L. Tubbs, *The weak neutral current and its effects in stellar collapse*, Ann. Rev. Nucl. Sci. **27**, 1977

[8] I. Giomataris *et al.*, *A novel large-volume spherical detector with proportional amplification read-out*, J. Instrum. 3, 2008

[9] J.L. Feng, *Dark matter candidates from particle physics and methods detection*, Annu. Rev. Astron. Astrophys. **48**, 495 - 545, 2010

[10] D. Santos, arXiv: 0810.1137v1 [astro-ph], 2008

[11] B. Tampon, D. Santos, O. Guillaudin, J.-F. Muraz, L. Lebreton, T. Vinchon and P. Querre, *Ionization Quenching Factor measurement of 1 keV to 25 keV protons in Isobutane gas mixture*, DOI: 10.1051/epjconf/201715301014, EPJ Web of Conferences 153, 01014 (2017)

[12] A. Drukier and L. Stodolsky, *Principles and applications of a neutral-current detector for neutrino physics and astronomy*, Phys. Rev. D. **30** 11, 1984

[13] J.D. Lewin, P.F. Smith, *Review of mathematics , numerical factors, and corrections for dark matter experiments based on elastic nuclear recoil*, Astroparticle Physics **6** (1996) 87-112

[14] R.H. Helm, Phys. Rev. **104** (1956) 1466.

[15] COHERENT Collaboration, *Observation of coherent elastic neutrino-nucleus scattering*, Science, 10.1126/science.aao0990, 2017

[16] J. Billard, E. Figueroa-Feliciano, and L. Strigari, *Implication of neutrino backgrounds on the reach of next generation dark matter direct detection experiments*, Phys. Rev. D **89**:023524, 2014

[17] L. E. Strigari, *Neutrino coherent scattering rates at direct dark matter detectors*, New J. Phys. **11** 105011, 2009

[18] J. Monroe and P. Fisher, *Neutrino Backgrounds to Dark Matter Searches*, Phys. Rev., D **76**:033007, 2007

[19] G. Battistoni, A. Ferrari, T. Montaruli, and P. R. Sala, *The atmospheric neutrino flux below 100-MeV: The FLUKA results*, Astropart. Phys., **23**:526?534, 2005

[20] M. Th. Keil, G. G. Raffelt, and H.-T. Janka, *Monte Carlo study of supernova neutrino spectra formation*, Astrophys. J., **590**:971?991, 2003

[21] The Borexino Collaboration, *Comprehensive measurement of pp-chain solar neutrinos*, Nature **562**, 505-510, 2018

[22] J. Beringer *et al.* (Particle data group), Phys. REv. D **86**, 010001, 2012

[23] https://novaexperiment.fnal.gov.

[24] https://www.dunescience.org/.

[25] J. I. Collar, Phys. Rev. D 100, 033003 (2019)

[26] W. Hampel *et al.*, *Final results of the Cr-51 neutrino source experiments in GALLEX*, Phys.Lett., B **420**:114?126, 1998

[27] J.N. Abdurashitov *et al.*, *Measurement of the response of the Russian-American gallium experiment to neutrinos from a Cr-51 source*, Phys.Rev., C **59**:2246?2263, 1999

[28] P. Coloma, E. Figueroa-Feliciano, J. A. Formaggio, P. Huber, J. M. Link, J. Newby, K. Ni, and X-J Xu, *Physics with Electron Capture Neutrino Sources*, Snowmass 2021, 2020

[29] J.A. Formaggio, E. Figueroa-Feliciano, and A.J. Anderson, *Sterile Neutrinos, Coherent Scattering and Oscillometry Measurements with Low-temperature Bolometers*, Phys. Rev. **D**, 85, 013009, 2012

[30] K. Scholberg, *Coherent elastic neutrino-nucleus scattering*, J. Phys.: Conf. Ser. 606 012010, 2015

[31] A.S. Cucoanes *et al.*, *The Nucifer experiment*, https://doi.org/10.1016/j.nds.2014.07.033, 2014

[32] , K. Fujikawa and R. E. Shrock, *Magnetic moment of a massive neutrino and neutrino-spin rotation*, Phys. Rev. Lett **45**: 963-966, 1980

[33] J. Billard, J. Johnston, B. J. Kavanagh, *Prospects for exploring New Physics in Coherent Elastic Neutrino-Nucleus Scattering*, JCAP 11 016, arXiv:1805.01798 [hep-ph], 2018

[34] J. Barranco, D. Delepine, M. Napsuciale, and A. Yebra, *New upper bound for the neutrino magnetic moment from its Dirac/Majorana nature and Borexino data*, arXiv: 1704.01549 [hep-ph], 2017

[35] A. G. Beda, V. B. Brudanin, V. G. Egorov, D. V. Medvedev, V. S. Pogosov, M. V. Shirchenko and A. S. Starostin, *The Results of Search for the Neutrino Magnetic Moment in GEMMA Experiment*, Adv. High Energy Phys., doi:10.1155/2012/350150, 2012

[36] L. B. Auerbach et al. [LSND Collaboration], Phys. Rev. D **63**, doi:10.1103/PhysRevD.63.112001 [hep-ex/0101039], 2001

[37] B. Kayser, *Majorana neutrinos and their electromagnetic properties*, Phys. Rev. D 26.7, 1982

[38] K. Patton, J. Engel, G. C. McLaughlin, and N. Schunck, *Neutrino-nucleus coherent scattering as a probe of neutron density distributions*, Phys. Rev. C 86.2, arXiv:1207.0693 [nucl-th], 2012

[39] H.A. Bethe and J.R. Wilson, *Revival of a stalled supernova shock by neutrino heating*, Astrophys. J. 295, 1985

[40] H.-T. Janka, F. Hanke, L. Hudepohl, A. Marek, B. Muller, and M. Obergaulinger, *Core-collapse supernovae: Reflections and directions*, Progress of Theoretical and Experimental Physics, Volume **2012**, 2012

[41] A. B. Balantekin and G. M. Fuller, *Neutrinos in Cosmology and Astrophysics*, arXiv:1303.3874 [nucl-th], 2013

[42] L. Wolfenstein, *Neutrino oscillations in matter*, Phys. Rev. D **17**, 2369, 1978

[43] S. P. Mikheev and A. Y. Smirnov, *Resonance enhancement of oscillations in matter and solar neutrino spectroscopy*, Sov. J. Nucl. Phys. *42*, 913, 1985

[44] G. Fernandez-Moroni, P. A.N. Machado, I. Martinez-Soler, Y. F. Perez-Gonzalez, D. Rodrigues, S. Rosauro-Alcaraz, *The physics potential of a reactor neutrino experiment with Skipper CCDs: Measuring the weak mixing angle*, arXiv:2009.10741 [hep-ph], 2020

[45] Particle Data Group Collaboration, P. Zyla *et al.*, *Review of Particle Physics*, PTEP no. 8, 083C01, 2020

[46] A. de Gouvea, P. A. Machado, Y. F. Perez-Gonzalez, and Z. Tabrizi, *Measuring the Weak Mixing Angle in the DUNE Near Detector Complex*, Phys. Rev. Lett. **125**, no. 5, 051803 2020

[47] G. Mention, M. Fechner, Th. Lasserre, Th. A. Mueller, D. Lhuillier, M. Cribier, A. Letourneau, *The Reactor Antineutrino Anomaly*, Phys. Rev. D **83**: 073006, 2011

[48] P. Anselmann *et al.*, *First results from the ^{51}Cr neutrino source experiment with the GALLEX detector*, Phys. Lett. B **342**: 1-4, 1995

[49] J.N. Abdurashitov *et al.*, *The Russian-American Gallium Experiment (SAGE) Cr Neutrino Source Measurement*, Phys. Rev. Lett. 77.23, 1996

[50] A. Aguilar et al. *Evidence for neutrino oscillations from the observation of $\bar{\nu}_e$ appearance in a $\bar{\nu}_\mu$ beam*, Phys. Rev. **D** 64.11, 2001

[51] A.A. Aguilar-Arevalo *et al.*, *Event Excess in the MiniBooNE Search for $\bar{\nu}_\mu \rightarrow \bar{\nu}_e$ Oscillations*, Phys. Rev. Lett. 105.18, 2010

[52] COHERENT Collaboration, *COHERENT 2018 at the Spallation Neutron Source*, arXiv:1803.09183v2 [physics.ins-det], 2018

[53] COHERENT Collaboration, *First detection of Coherent Elastic Neutrino-Nucleus Scattering on Argon*, Phys. Rev. Lett. **126**, 012002 (2021)

[54] CONUS Collaboration, *Constraints onElastic Neutrino Nucleus Scattering in the Fully Coherent Regime from the CONUS Experiment*, Phys. Rev. Lett. **126**, 041804, 2021

[55] Alexis Aguilar-Arevalo *et al.* (CONNIE Collaboration), *Exploring low-energy neutrino physics with the Coherent Neutrino Nucleus Interaction Experiment*, Phys. Rev. D **100**, 092005, 2019

[56] E. Aprile*et al.*(XENON Collaboration), *Search for Coherent Elastic Scattering of Solar ^{8}B Neutrinos in the XENON1T Dark Matter Experiment*, Phys. Rev. Lett.126, 091301, 2021

[57] C. Buck *et al.*, *A novel experiment for coherent elastic neutrino nucleus scattering: CONUS*, J. Phys.: Conf. Ser. 1342 012094, 2020

[58] CONNIE Collaboration, *The CONNIE experiment*, arXiv:1608.01565 [physics.ins-det], 2016

[59] MINER Collaboration, *Background studies for the MINER Coherent Neutrino Scattering Reactor Experiment*, arXiv :1609.02066 [physics.ins-det], 2016

[60] R. Strauss *et al.*, *The ν-cleus experiment: A gram-scale fiducial-volume cryogenic detector for the first detection of coherent neutrino-nucleus scattering*, arXiv:1704.04320 [physics.ins-det], 2017

[61] Ricochet Collaboration, *Coherent Neutrino Scattering with Low Temperature Bolometers at Chooz Reactor Complex*, arXiv:1612.09035v2 [physics.ins-det], 2017

[62] Workshop: The Magnificent CEνNS, `https://indico.cern.ch/event/943069/`

[63] E. Rutherford and H. Geiger, Proc. Royall Soc. A81, 1908

[64] F. Sauli, *Gaseous Radiation Detectors: Fundamentals and Applications*, Cambridge University Press, 2014. 33

[65] Bttner, H., *The Initial Characteristics of the Townsend Discharge in Noble Gases*, Z. Physik **111**, 750-769, 1939

[66] Q. Arnaud et al., *Precison laser-based measurements of the single electron response of SPCs for the NEWS-G light dark matter search experiment*, arXiv:1902.08960v1 [physics.ins-det], 2019

[67] F. A. Vazquez de Sola Fernandez, *Solar KK axion search with NEWS-G*, Ph.D. dissertation, Queen's University, 2020

[68] COMSOL Multiphysics, `https://www.comsol.com/products`

[69] W. Shockley, *Currents to conductors induced by a moving point charge*, J. Appl. Phys., 9:635?636, 1938

[70] Zhong He, *Review of the Shockley-Ramo theorem and its application in semiconductor gamma-ray detectors*, Nucl. Intruments and Methodes in Physics Research A **463**, 2001

[71] J. Derré, *Pulse shape in the SPC prototype*, Technical report, 2007

[72] U. Fano, *Ionization Yield of Radiations. II. The Fluctuations of the Number of Ions.*, Phys. Rev. **72** 1: 26-29, 1947

[73] D. Durnford, Q. Arnaud, G. Gerbier, *Novel approach to assess the impact of the Fano factor on the sensitivity of low-mass dark matter experiments*, Phys. Rev. D. **98**, 103013, 2018

[74] J. Derré, Y. Giomataris , Ph. Rebourggeard, H. Zaccone, J.P. Perroud and G. Charpak, *Fast signals and single electron detection with a MICROMEGAS photodetector*, Nucl. Instrum. Methods Phys. Res., Sect. A 449, 314-321, 2000

[75] T. Zerguerras, B. Genolini, V. Lepeltier, J. Peyre, J. Pouthas and P. Rosier, *Single-electron response and energy resolution of a Micromegas detector*, Nucl. Instrum. Methods Phys. Res., Sect. A 608, 397-402, 2009

[76] M. Kobayashi, T. Ogawa, T. Kawaguchi, K. Fujii, T. Fusayasu, K. Ikematsu, Y. Kato, S. Kawada, T. Mat- suda, R.D. Settles, et al., *A novel technique for the mea- surement of the avalanche fluctuation of gaseous detectors*, Nucl. Instrum. Methods Phys. Res., Sect. A 845, 236-240, 2017

[77] R. Bellazzini, G. Spandre, A. Brez, M. Minuti, L. Baldini, L. Latronico, M.M. Massai, N. Omodei, M. Pesce-Rollins, C. Sgrò, et al., *Imaging with the invisible light*, Nucl. Instrum. Methods Phys. Res., Sect. A 581, 246 ? 253, 2007

[78] Q. Arnaud *et al.*, *First results from the NEWS-G direct dark matter search experiment at the LSM*, Astropart. Phys. J. C, 97:54?62, 2018. 45, 108

[79] L. Balogh *et a.*, *Copper electroplating for background suppression in the NEWS-G experiment*, Nucl. Instrum. Methods Phys. Res A **988**, 164884, 2021

[80] A. Giganon *et al.*, *A multiball read-out for the spherical proportional counter*, JINST, 12:P12031, 2017. 36, 54.

[81] `https://geant4.web.cern.ch/`.

[82] A. Brossard, *Optimization of spherical proportional counter background and response for low mass dard matter search*, PhD dissertation, Queen's University, 2020

[83] J. Lindhard, V.Nielsen, M.Scharff and P. V. Thomsen, *Integral equations governing radiation effects*, 1963

[84] J. F. Ziegler, M. D. Ziegler, J. P. Biersack, Nucl. Instrum. Methods Phys. Res. B 268 (2010) 1818 - 1823, doi: 10.1016/j.nimb.2010.02.091, 19^{th} International Conference on Ion Beam Analysis.

[85] P. Sorensen, *Atomic limits in the search for galactic dark matter*, arXiv:1412.3028v1 [astro-ph.IM], 2014.

[86] D. M. Mei, Z. B. Yin, L. C. Stonehill and A. Hime, *A Model of Nuclear Recoil Scintillation Efficiency in Noble Liquids*, arXiv:0712.2470v2 [nucl-ex], 2008

[87] J. Lindhard, M. Scharff and H.E. Schiott, *Range concepts and heavy ion ranges*, Mt. Fys. Medd. Dan. Vid. Selsk. **36** 14, 1963

[88] W.H. Bragg, R. Kleeman, Phil. Mag., 10 (1905), p. 318.

[89] D. Pershey, *New CEvNS Results from the COHERENT CsI[Na] Detector*, Fermilab JETP Seminar, 2020

[90] J. B. Albert *et al.*, *Measurement of neutron capture on* ^{136}Xe, Phys. REv. C **94**: 034617, 2016

[91] D. Durnford, *phenomelological studies and analysis techniques to search for light dark matter with NEWS-G*, Master dissertation, Queen's University, 2018

[92] I. Savvidis and D. Durnford, *Low energy calibration and neutron capture calibration of the spherical proportional counter*, Internal report from NEWS-G collaboration meeting, 2017

[93] I. Katsioulas, P. Knights and K. Nikolopoulos, *Estimation of the ionisation quenching factor in gases from W-value measurements*, arXiv:2105.01414 [hep-ex], 2021

[94] U. Kneissl, H. H. Pitz and A. Zilges, *Investigation of Nuclear Structure by Resonance Fluorescence Scattering*, Prog. Part. Nucl. Phys., Vol. 37, pp 349-433, 1996.

[95] Tenzing H. Y. Joshi, *A nover source of tagged low-energy nuclear recoils*, Nucl. Instrum and Meth. A, 656 51-54, 2011

[96] `https://tunl.duke.edu/`

[97] C. R. Howell, *Neutron scattering from* ^{28}*Si and* ^{32}*S: cross sections and analyzing powers from 8 to* 40 MeV, Ph.D. Thesis, Duke University 1984

[98] C. Iliadis, *Nuclear Physics of Stars*, Wiley-VCH, 2015

[99] `https://www.mirion.com/products/2006-proportional-counter-preamplifier`

[100] `https://www.struck.de/sis3316.html`

[101] `https://www.hamamatsu.com/resources/pdf/etd/R7723_R7724_R7725_TPMH1315E.pdf`

[102] `https://eljentechnology.com/products/liquid-scintillators/ej-301-ej-309`

[103] D. G. Kelly et al., *The production of Ar-37 using a thermal neutron reactor flux*, J Radioanal Nucl Chem 318, 279?285, 2018

[104] W. Blum, W. Riegler, and L. Rolandi, *Particle detection with drift chambers; 2nd ed.*, Berlin: Springer, 2008

[105] V. Sanglard *et al.* (EDELWEISS Coll.), *Final results of the EDELWEISS-I dark matter search with cryogenic heat-and-ionization Ge detectors* Phys. Rev. D 71, 2005

[106] `https://iminuit.readthedocs.io/en/stable/about.html`

[107] F. James, *Reference Manual - Function Minimization and Error Analysis*, 1998

[108] F. James and M. Roos, *Minuit - A system for function minimization and analysis of the parameter errors and correlations.*, 1975

[109] https://en.wikipedia.org/wiki/Freedman%E2%80%93Diaconis_rule

[110] https://numpy.org/

[111] A. Raue, C. Kreutz, F.j. Theis and J. Timmer, *Joining forces of Bayesian and frequentist methodology: a study for inference in the presence of non-identificability*, Phil. Trans. R. Soc. A **371**: 20110544, 2013

[112] G. Curie Rich, *Measurement of low-energy nuclear recoil quenching factors in CsI[Na] and statistical analysis of the first observation of coherent , elastic neutrino-nucleus scattering*, Ph.D. dissertation, University of North Carolina, 2017

[113] D. S. Akerib *et al.*, LUX Collaboration, *Low-energy (0.7-74 keV) nuclear recoil calibration of the LUX dark matter experiment*, arXiv:1608.05381, 2016

[114] NEST Collaboration, https://zenodo.org/record/4262416#.X7PvxS2ZO8o

[115] X. B. Ma, W. L. Zhong, L. Z. Wang Y. X. Chen ad J. Cao, Physical Review C **88**, 014605, (2013).

[116] P. Huber and T.Schwetz, *Precision spectroscopy with reactor anti-neutrinos*, Phys. rev., D**70**:053011, 2004.

[117] https://en.wikipedia.org/wiki/Nuclear_chain_reaction

[118] Z. Djuric, J. A. Detwiler, A. Piepke, V. R. Foster, L. Miller and G. Gratta, *Uncertainties in the anti-neutrino production at nuclear reactors*, J. Phys. G: Nucl. Part. Phys. **36**, 2009

[119] G. Bellini *et al.* (Borexino Collaboration), Phys. Letters B **687**, 299, 2010.

[120] P. Vogel and J. Engel, *Neutrino electromagnetic form factors*, Phys. Rev. D **39** 11, 1989.

[121] V. I. Kopeikin, *Flux and Spectrum of reactor antineutrinos*, Phys. of Atommic Nuclei **75** 2, 2012.

[122] T. A. Mueller, D. Lhuillier, M. Fallot, A. Letourneau, S. Cormon, M. Fechner, L. Giot, T. Lasserre, J. Martino, G. Mention, A. Porta and F. Yermia, *Improved Predictions of Reactor Antineutrino Sprectra*, Phys. Rev. C **83**, 054615, 2011.

[123] P. Huber, *Determination of anti-neutrino spectra from nuclear reactors*, Phys.Rev.C **84**:024617, 2011.

[124] M. Baldoncini, I. Callegari, G. Fiorentini, F. Mantovani, B. Ricci, V. Strati and G. Xhixha, *Reference worldwide model for antineutrinos from reactors*, arXiv:1411.6475 [physics.ins-det], 2014.

[125] J. Mandula, *Nuclear Power Engineering Section*, Inter. Atom. Energy Agency, IAEA-PRIS database, 2014.

[126] `https://www.world-nuclear.org/reactor/default.aspx/DARLINGTON-1`

[127] P. Barbeau, J.I. Collar, J. Miyamoto, I. Shipsey, *Towards Coherent Neutrino Detection Using Low-Background Micropattern Gas Detectors*, IEEE Trans. Nucl. Sci. **50**: 1285-1289, 2003

[128] *Journal of the International Commission on Radiation and Unit Measurements*, **11**, 31-31, 04 2011.

[129] I. K. Bronic, *W-values and Fano factors for electrons in rare gases and rare gas mixtures*, Ionizing Radiation, **24**, 1998.

[130] J.I. Collar, A.R.L. Kavner, C.M. Lewis, *Response of CsI[Na] to nuclear recoils: Impact on Coherent Elastic Neutrino-Nucleus Scattering (CEνNS)*, Phys. Rev. D **100**, 033003, 2019

[131] H.W.Joo, H.S.Park, J.H.Kim, S.K.Kim, Y.D.Kim, H.S.Lee, S.H.Kim, *Quenching factor measurement for NAI(Tl) scintillation crystal*, arXiv:1809.10310, 2019

[132] B. Lenardo, Member, IEEE, K. Kazkaz, A. Manalaysay, J. Mock, M. Szydagis and M. Tripathi, *A global analysis of light and charge yields in liquid xenon*, arXiv:1412.4417v3, 2014

[133] B. Lenardo et *al.*, *Measurement of the ionization yield from nuclear recoils in liquid xenon between 0.3* - 6 keV *with single-ionization-electron sensitivity*, arXiv:1908.00518, 2019

[134] G. Heusser, W. Weber, J Hakenmuller, M. Laubenstein, M. Lindner, W. Maneschg, H. Simgen, D. Stolzenberg and H. Strecker, *GIOVE: a new detector setup for high sensitivity germanium spectroscopy as shallow depth*, The European Physical Journal C **75**: 53, 2015

[135] https://marshield.com/

[136] https://eljentechnology.com/products/plastic-scintillators/ej-200-ej-204-ej-208-ej-212

[137] https://www.hamamatsu.com/us/en/product/type/R8520-406/index.html

[138] https://www.radiopurity.org/rp/rp/_design/persephone/index.html?lead

[139] J. F. Ziegler, *Terrestrial cosmic ray intensities*, IBM J. Res. Dev. **42**: 117-139, 1998

[140] M. S. Gordon, P. Goldhagen, K. P. Rodbell, T. H. Zabel, H. H. K. Tang, J. M. Clem, and P. Bailey, *Measurement of the flux and energy spectrum of cosmic- ray induced neutrons on the ground*, IEEE Transactions on Nuclear Science **51**: 32427-3434, 2004

[141] S. Cebrián, H. Gómez, G. Luzón, J. Morales, A. Tomás, and J. A. Villar, *Cosmogenic activation in germanium and copper for rare event searches*, Astroparticle Physics **33**: 316-329, 2010

[142] O. Dragoun, A. Spalek, A. Koval?ik, E. Yakushev, M. Rysavy, J. Frána, V. Brabec, A. Novgorodov, and D. Liljequist, *Scattering of* 7.3 keV *conversion electrons from a* ^{57}*Co source covered gradually by gold absorbers of various thickness*, Nucl. Instr. and Methods in Phys. R. S. B: Beam Interactions with Materials and Atoms, vol. **194**, no. 2, pp. 112-122, 2002

[143] F. Arneodo et al., *Scintillation efficiency of nuclear recoil in liquid xenon*, Nucl. Instrum. Meth. A, 2000

[144] https://commons.wikimedia.org/wiki/File:Fr_Decay_chain_Uranium_238.svg

[145] https://en.wikipedia.org/wiki/Decay_chain

[146] https://ref.web.cern.ch/ref/CERN/CNL/2000/001/magboltz

[147] J. K. Bohkle, *Variation in the terrestrial isotopic composition and atomic weight of argon (IUPAC Technical Report)*, Pure and Applied Chemistry **84**, 1421-1432, 2014

[148] R. Saldanha, H. O. Back, R. H. M. Tsang, T. Alexander, S. R. Elliott, S. Ferrara, E. Mace, C. Overman, and M. Zalavadia, *Cosmogenic production of* ^{39}Ar *and* ^{37}Ar, Phys. Rev. C **100**, 024608, 2019

[149] R. W. Stoenner, O. A. Schaeffer, S. Katcoff, *Half-lives of Argon-37, Argon-39, and Argon-42*, Science **148**, 1965

[150] H. Loosli, H. Oeschger, *Detection of* ^{39}Ar *in atmospheric argon*, Earth and Planetary Science Letters 5, 1968

[151] P. Benetti, F. Calaprice, E. Calligarich, M. Cambiaghi, F. Carbonara, F. Cavanna, A. Cocco, F. Di Pompeo, N. Ferrari, G. Fiorillo, et al., *Measurement of the specific activity of 39Ar in natural argon*, Nuclear Instruments and Methods in Physics Research Section A: Accelerators, Spectrometers, Detectors and Associated Equipment **574**, 2007

[152] R. Purtschert, M. Kaliowski, J. Wieslander, X. Blanchard, R. Riedmann, L. Raghoo, J. Kusmierczyk-Michulec, H. Gheddou, Y. Tomita, *Ar-37, Be-7 and Xe-133 in the atmosphere*, CTBT Science and Technology Conference, 2017

[153] A. Barabash, R. Saakyan, V. Umatov, *On concentration of* ^{42}Ar *in the Earth?s atmosphere*, Nuclear Instruments and Methods in Physics Research Section A: Accelerators, Spectrometers, Detectors and Associated Equipment **839**, 2016

[154] http://www.nucleide.org/DDEP_WG/Nuclides/Ar-37_tables.pdf

[155] J. Amare *et al.*, *Cosmogenic production of tritium in dark matter detectors*, Astropart. Phys. vol. **97**, pp. 96-105, 2018

[156] C. Zhanga, D.-M. Mei, V.A. Kudryavtsevc, S. Fiorucci, *Cosmogenic activation of materials used in rare event search experiments*, Astrop. Phys. **84**, 62-69, 2016